Dissertation
Submitted to and approved by the

Department of Civil and Environmental Engineering
University of Florence

and the

Department of Civil Engineering
Tongji University

In candidacy for the degree of a
European PhD

Intelligent evaluation for wind-resistant stability of long-span bridges based on dataset and machine learning

DOCTORAL THESIS

by
Neyu Chen

Tutor (s)
Prof. Claudio Borri (Responsible Tutor)
Prof. Yaojun Ge

Reviewer (s)
Prof. Fabio Rizzo
Prof. Shujin Laima

The Coordinator of the PhD Program
Prof. Luca Solari

Submitted on

11 April 2023

Acknowledgements

ACKNOWLEDGEMENTS

First and foremost, I am extremely grateful to my supervisors, Prof. Claudio Borri and Prof. Yaojun Ge for their guidance and valuable advice during my PhD study. I feel particularly grateful to Prof. Claudio Borri for his continuous assistance and patience during my study at the University of Florence, as well as for his invaluable supervision of the progress of my work. I also really appreciate Prof. Yaojun Ge. I have been under his guidance for nearly eight years, he has always been there to support and help me in both scientific research and daily life, so that I will not lose my way. His immense knowledge and ample experience always encourage me. I am also very grateful to Prof. Luca Facchini for providing me with the technical support and Margherita Mellini who has supported me in all the bureaucratic issues during my exchange period in Italy. All my gratitude to Prof. Lin Zhao and Prof. Yongxin Yang from Tongji State Key Laboratory of Disaster Reduction in Civil Engineering for sharing their rich research experience and achievements in the field of bridge wind engineering. Then a great acknowledgement to the China Scholarship Council for financial support during my stay abroad.

I am greatly indebted to several colleagues I have worked with during my PhD. I would like to thank Yizhe Lan, Zihang Liu, Miaomiao Wei and Jinbo Zhu for providing me with a lot of computational assistance. I really enjoyed working with the members of wind engineering research group of Tongji. A special thanks to Dr. Shiyu Zhao, Dr. Qing Xia, Dr. Shengyuan Liu and Dr. Biao Tan for a cherished research time spent together. I feel the strength of the team and believe I am not alone. It is also impossible to forget the warm attention and care I received from Zihan Liu and Jiuyan Gao for making my daily life so interesting in a foreign country.

Lastly, my family deserves endless gratitude. They have always embraced me unconditionally. No matter when and where I am, they always give me the warmest comfort and love.

Abstract

ABSTRACT

With the increase of span length, bridges are characterized by lightweight, high flexibility and low damping, making wind-resistance a key control factor in structural design. Aerodynamic parameters are important for describing the wind-resistant performance of bridges, and all parameters can be obtained by wind tunnel test or numerical simulation. In this study, an intelligent identification method of aerodynamic parameters based on machine learning will be established to provide a new way for the analysis of bridge wind-resistant performance.

A specialized wind-resistance database of 99 long-span bridges has been built based on the experimental results accumulated from the Wind Tunnel Laboratory in Tongji University over the years. The dataset related to wind-resistant stability of 20 long-span suspension bridges with steel closed box girders has been firstly selected. In pursuit of representativeness of closed box girders, 20 numerical simulation results from other studies have been collected in the dataset. In order to make the dataset more uniformly, 15 data samples have been carefully proposed and calculated by computational fluid dynamics (CFD) numerical simulation as the supplementary cross-sections. In total 55 hybrid closed box girder datasets have been derived, and all these data samples have been re-calculated by CFD numerical simulation to make the comparison and contrast between the hybrid datasets and the pure numerical simulation ones.

In combination with some other collected numerical simulation data and supplementary data, the machine learning models for identifying aerostatic coefficients and flutter derivatives of closed box girders are trained and developed via improved error back propagation (EBP) neural network and gradient boosting decision tree (GBDT) respectively after the comparison of several machine learning algorithms. In order to further improve the effectiveness of machine learning training and prediction, all the data samples are re-calculated by CFD numerical simulation to obtain the better data conditions. The results show that machine learning models can explore the underlying distribution of dataset. The intelligent method can provide a feasible option for identifying and expanding data sets of aerodynamic parameters without wind tunnel testing and numerical simulation.

With the aerodynamic parameters intelligently identified by the trained machine learning methods, the two-dimensional and three-dimensional aerostatic stability and flutter stability of long-span suspension bridges can be evaluated respectively. The sensitivity analysis and error analysis of aerodynamic parameters can be realized to further demonstrate the feasibility and effectiveness of machine learning models in wind-resistant stability analysis. At the same time, the variation pattern of wind-resistant stability with the feature dimensions of the closed box cross-section is summarized

through both two-dimensional and three-dimensional calculation methods. It can help preliminarily determine the appropriate shape of the closed box girder cross-section and provide the necessary reference for the aerodynamic shape optimization to evaluate the influence of the section shape on wind-resistant performance.

Keywords: *database, aerostatic coefficients, flutter derivatives, machine learning, aerostatic stability, flutter stability, aerodynamic shape, sensitivity analysis*

List of publications

National and International Journals

1. **Chen, N.Y.**, Chen, X., Zhao, L., and Ge, Y.J. (2018). Parametric study on wind-induced effect of a cooling tower with hyperbolic steel trusses. *Journal of Building Structures*, 39(4), 18-27. (in Chinese)
2. **Chen, N.Y.** and Ge, Y.J. (2019). Aerodynamic parameter identification of typical bridge sections based on artificial neural network. China Civil Engineering Journal, 52(8), 91-97. (in Chinese)
3. Ma, T.T., Zhao, L., **Chen, N.Y.**, Ge, Y.J., and Zhang, D. (2020). Wind-induced dynamic performance of a super-large hyperbolic steel-truss cooling tower. Thin–Walled Structures, 157, 107061.
4. **Chen, N.Y.**, Ge, Y.J., and Borri, C. (2023). Intelligent identification and verification of flutter derivatives and critical velocity of closed box girders using gradient boosting decision tree. *Atmosphere, "submitted".*

International Conferences/Workshops with Peer Review

1. **Chen, N.Y.** and Ge, Y.J. (2019). Intelligent identification of aerodynamic parameters for bridges. Proc. of 2nd IABSE Young Engineers Colloquium in East Asia, Tokyo, Japan.
2. **Chen, N.Y.** and Ge, Y.J. (2022). Aerodynamic parameter identification and flutter performance perdition of closed box girder based on machine learning. Proc. of 2022 IABSE Congress: Connection, Integration and Harmonization, Nanjing, China.
3. **Chen, N.Y.**, Ge, Y.J., Borri, C., and Fang, G.S. (2023). Flutter derivatives identification of closed box girders based on gradient boosting decision tree. The 16th International Conference of Wind Engineering, Florence, Italy. (abstract submitted)

Table of contents

List of Figures

List of Tables

CHAPTER 1

1 Introduction

1.1 Wind-induced responses of bridges

With the increase of span length, bridges are characterized by light weight, high flexibility and low damping, making wind-resistance a key control factor in structural design. At the beginning, wind load was regarded as static load in bridge design, and the phenomenon and mechanism of wind-induced responses were not thoroughly explored. However, the old Tacoma suspension bridge in the United States with a main span of 853m collapsed only under the wind speed of 19m/s on 7th November 1940 (as shown in Figure 1.1). The cause of the collapse was attributed to a phenomenon of self-excited vibration due to fluid-structure interaction commonly known as torsional flutter (Bisplinghoff et al., 1957; Fung, 1955). Then the study of wind-induced response of long-span bridges was kicked off.

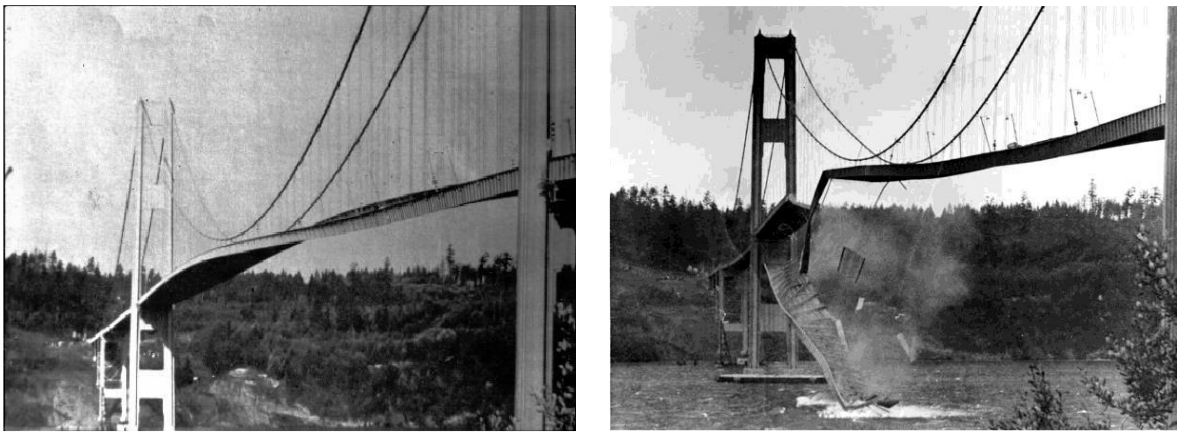

Figure 1.1: The collapse of the Tacoma Bridge

The research on wind-induced response of bridges involves numerous contents. In general, it can be divided into wind environment and wind loading simulation, aerodynamic force expression and aerodynamic parameter identification, wind-induced vibration analysis and so on. Each aspect contains many subdivisions, and the following describes these major directions of the whole process of bridge wind-resistant performance analysis.

1.1.1 Wind environment and wind loading

Wind environment refers to the wind field formed by outdoor natural wind under the influence of landform. In the field of bridge and structural wind engineering, the following concepts are usually involved in the description and research of wind environment:

• Basic wind speed

The average wind speed is of great significance to determine the wind force. The basic wind speed is also called the reference wind speed or standard wind speed, which refers to the annual average maximum wind speed that meets the specified time interval and return period at the standard height on the standard landform.

• Basic wind pressure

Basic wind pressure is also called reference wind pressure or standard wind pressure, which is defined as:

$$P = \frac{1}{2}\rho U^2 \tag{1.1.1}$$

where P is the basic wind pressure, ρ=1.225kg/m3, is the air density, and U is the basic wind speed.

• Wind direction and wind speed

The wind direction is expressed as angle. At present, the wind scale standard recommended by the World Meteorological Organization is Beaufort scale, which is divided into 18 scales (0-17) mainly according to the impact of wind on ground objects or sea surface.

• Wind profile

In the atmospheric boundary layer, the airflow velocity is related to the height. This is because when the airflow moves horizontally near the surface, it will be subject to the horizontal resistance imposed by the surface, resulting in the reduction of the airflow velocity (Aboshosha et al., 2015; Elshaer et al., 2017). With the increase of height, the friction effect of the surface will gradually weaken, and the wind speed will increase. Finally, when the airflow reaches the top of the boundary layer, the wind speed will reach the maximum. At present, the law of average wind speed changing along the height mainly includes exponential wind profile model and logarithmic wind profile model. The calculation results of these two models are similar, and the exponential wind profile model is simpler (Zhang, 2003).

• Turbulence intensity

The turbulence intensity is the most important character of the turbulence (Ayata et al., 2018). It describes the degree of wind speed changing with time and space, and reflects the relative intensity of fluctuating wind speed. Turbulence will occur when the air flow is subjected to the friction action of the ground. The turbulence intensity at a certain height Z is defined as follows:

$$I_z = \frac{\sigma_z}{v_z} \tag{1.1.2}$$

where σ_Z is the root mean square of fluctuating wind speed, and $\overline{v_z}$ is the average wind speed at height Z. Turbulence intensity is mainly affected by the ground roughness and height. The greater the ground roughness, the stronger the pulsation of the airflow near the ground will be, and the larger the root mean square of the pulsating wind speed will be, resulting in the increase of turbulence intensity. As the root mean square of fluctuating wind speed will gradually decrease with the increase of height and the average wind speed will gradually increase with the increase of height, the turbulence intensity will decrease with the increase of height (Zhou, 2012).

• Turbulence integral scale

The turbulence integral scale represents the average size of the turbulent vortex in the airflow,

which can determine the basic characteristics of the turbulence field macroscopically. The larger the turbulence integral scale, the stronger the diffusion ability of turbulence (Wang, 2017). In the atmospheric boundary layer, the turbulence integral scale is mainly affected by height, temperature and some other factors.

Wind loading refers to the pressure on the surface of the structure when the wind formed by the airflow meets the structure. The magnitude of wind loads is mainly related to the wind speed, wind direction, landform and surrounding environment where the structure is located, as well as the height and shape of the structure itself. Usually, the structure will be in a static or micro vibration state. When the structure that can be regarded as a rigid body, the aerostatic effect on the structure can be expressed in the form of lift, drag and moment. The lift and drag are produced by the pressure difference, and the moment is produced by the fact that the resultant force action point does not coincide with the centroid of the cross-section.

The bridge will not always be in a completely static state, and it will be in a micro vibration state in most cases. When the structure in the micro vibration state is coupled with the aerodynamic airflow, the airflow and the micro vibration structure will interact, which is usually called aeroelastic effect (Chen, 2005). This coupling will make the micro vibrating structure leave the current equilibrium state, and change its amplitude and form of vibration with the airflow. The boundary conditions of the airflow will also change with the vibration. In the process of vibration, the external wind load will provide aerodynamic self-excited force for the structure. The constantly changing structural vibration is repeated and superimposed, resulting in the increase or divergence of structural vibration.

1.1.2 Aerodynamic forces and aerodynamic parameters

Complex air force is created when wind bypasses the structure. When the stiffness of bridge is large and the structure remains stationary, the force is equivalent to the static force. To be precise, the static force refers to the effect of the static pressure exerted on the structure by the part of mean wind velocity, which can be divided into along-wind force (F_D), cross-wind force (F_L) and torsional moment (M) as shown in Figure 1.2. In the practical engineering application, sometimes for convenience, the static forces under the body-axis (F_x, F_y, M) can also be used. M in two kinds of coordinate systems is the same, and the forces can be converted as follows:

$$F_x = F_D \cos\alpha - F_L \sin\alpha \tag{1.1.3a}$$

$$F_y = F_D \sin\alpha + F_L \cos\alpha \tag{1.1.3b}$$

where α is the wind attack angle and is positive when the lower surface is facing the wind. When the wind attack angle is 0°, the wind-axis and body-axis coincide.

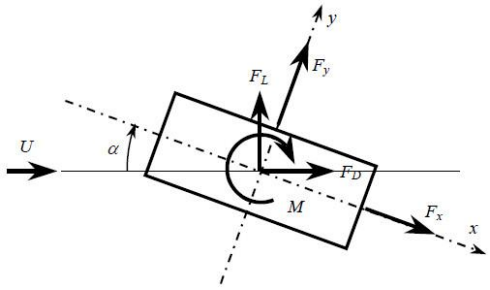

Figure 1.2: Static forces acting on the structure

The aerostatic coefficients are dimensionless parameters used to describe the static wind load a structure is subjected to. The drag coefficient (C_D), lift coefficient (C_L) and moment coefficient (C_M) under the wind axis system are defined as follows:

$$C_D = \frac{F_D}{\rho U^2 B/2} \tag{1.1.4a}$$

$$C_L = \frac{F_L}{\rho U^2 B/2} \tag{1.1.4b}$$

$$C_M = \frac{M}{\rho U^2 B/2} \tag{1.1.4c}$$

where ρ is the air density, U is the mean wind velocity, B is a certain characteristic dimension of the cross-section.

When the stiffness of the bridge is small, the structural vibration is excited and the effect of air force is not only static, but also dynamic. In general, the bridge undergoes amplitude limiting vibration under fluctuating wind load. When a certain wind speed is reached, the vibrating bridge continuously absorbs energy through the feedback of air flow, so that the amplitude gradually increases until the structure is damaged. In the research of wind-induced vibration response of bridges, the accurate expression of aerodynamic force is the basis of analysis.

In the field of aerofoil flutter has been paid attention to for a long time. Theodorson (1935) used the potential flow theory to derive the analytical expression of unsteady aerodynamic forces acting on a flat plate making a simple harmonic vibration with circular frequency w in a uniform flow field with velocity, that is, Theodorson self-excited force model. This model is only applicable to thin aerofoils or flat plate cross-sections, and is no longer applicable to non-streamlined cross-sections with obvious airflow separation (Wu, 2013).

Davenport and Scanlan were pioneers in introducing aerodynamic models from the aviation into bridge and structural wind engineering. The self-excited force model of bluff body is a semi-theoretical and semi-empirical formula, and the aerodynamic parameters must be obtained by wind tunnel test or numerical simulation, of which Scanlan self-excited force model is the most widely used. Scanlan and

Tomko (1971) proposed a linear expression of aerodynamic self-excited force expressed by 6 flutter derivatives, the first derivative of vertical displacement of the structure, torsion angle and the first derivative of it:

$$L_{se} = \rho U^2 B\left[K_h H_1^* \frac{\dot{h}}{U} + K_\alpha H_2^* \frac{B\dot{\alpha}}{U} + K_\alpha^2 H_3^* \alpha \right]$$

(1.1.5a)

$$M_{se} = \rho U^2 B^2\left[K_h A_1^* \frac{\dot{h}}{U} + K_\alpha A_2^* \frac{B\dot{\alpha}}{U} + K_\alpha^2 A_3^* \alpha \right] \quad (1.1.5b)$$

where B is the bridge width and $K = B\omega/U$ is the reduced frequency. Flutter derivatives are dimensionless functions of K. H_1^*, A_2^*, A_3^* are called positive derivatives or direct derivatives, which represent the aerodynamic force in one degree of freedom generated by the motion in that direction of degree-of-freedom. H_2^*, H_3^*, A_1^* are called deputy derivatives or cross derivatives, which represent the aerodynamic force in one degree of freedom generated by the motion in the other directions of degree-of-freedom.

Huston (1986) considered the influence of vertical displacement on the basis of the above formula, and obtained the expressions including 8 flutter derivatives:

$$L_{se} = \rho U^2 B\left[K_h H_1^* \frac{\dot{h}}{U} + K_\alpha H_2^* \frac{B\dot{\alpha}}{U} + K_\alpha^2 H_3^* \alpha + K_h^2 H_4^* \frac{h}{B} \right] \quad (1.1.6a)$$

$$M_{se} = \rho U^2 B^2\left[K_h A_1^* \frac{\dot{h}}{U} + K_\alpha A_2^* \frac{B\dot{\alpha}}{U} + K_\alpha^2 A_3^* \alpha + K_h^2 A_4^* \frac{h}{B} \right] \quad (1.1.6b)$$

With the increase of bridge span, the lateral displacement gradually becomes non-negligible. Sarkar et al. (1994) considered the flutter derivative related to lateral displacement and the first derivative of it, and extended the self-excited force model to three degrees of freedom:

$$D = \rho U^2 B\left[K_p P_1^* \frac{\dot{p}}{U} + K_\alpha P_2^* \frac{B\dot{\alpha}}{U} + K_\alpha^2 P_3^* \alpha + K_p^2 P_4^* \frac{p}{B} + K_h P_5^* \frac{\dot{h}}{U} + K_h^2 P_6^* \frac{h}{B} \right] \quad (1.1.7a)$$

$$L = \rho U^2 B\left[K_h H_1^* \frac{\dot{h}}{U} + K_\alpha H_2^* \frac{B\dot{\alpha}}{U} + K_\alpha^2 H_3^* \alpha + K_h^2 H_4^* \frac{h}{B} + K_p H_5^* \frac{\dot{p}}{U} + K_p^2 H_6^* \frac{p}{B} \right] \quad (1.1.7b)$$

$$M = \rho U^2 B^2\left[K_h A_1^* \frac{\dot{h}}{U} + K_\alpha A_2^* \frac{B\dot{\alpha}}{U} + K_\alpha^2 A_3^* \alpha + K_h^2 A_4^* \frac{h}{B} + K_p A_5^* \frac{\dot{p}}{U} + K_p^2 A_6^* \frac{p}{B} \right] \quad (1.1.7c)$$

Flutter derivative identification is the key to the application of the above self-excited force model. For thin aerofoils or ideal thin plate cross-sections, Theodorsen self-excited force can be expressed by Scanlan self-excited force model, and Scanlan flutter derivatives can be expressed by the real and

imaginary parts of Theodorsen cycle function (Simiu and Scanlan, 1996). The flutter derivatives of non-streamlined cross-sections can be determined by sectional model wind tunnel test or CFD numerical simulation.

Davenport (1962) established a quasi-steady buffeting force model based on the quasi-steady assumption. The quasi-steady assumption holds that the buffeting force at the current time is only related to the fluctuating wind speed at that time, and has nothing to do with the fluctuating wind speed at the previous time, that is, the fluctuating wind of various frequencies has the same ability to produce buffeting force. Under this assumption, the buffeting force can be expressed in the form of the following formula:

$$D_b = \frac{1}{2}\rho U^2 B\left[C_D(\alpha_0)\left(2\frac{u}{U}\right)+C_D^{'}(\alpha_0)\frac{w}{U}\right] \tag{1.1.8a}$$

$$L_b = \frac{1}{2}\rho U^2 B\left[C_L(\alpha_0)\left(2\frac{u}{U}\right)+[C_L^{'}(\alpha_0)+C_D(\alpha_0)\frac{w}{U}\right] \tag{1.1.8b}$$

$$M_b = \frac{1}{2}\rho U^2 B^2\left[C_M(\alpha_0)\left(2\frac{u}{U}\right)+C_M^{'}(\alpha_0)\frac{w}{U}\right] \tag{1.1.8c}$$

Davenport quasi-steady buffeting force model assumes that the bridge cross-section is an ideal two-dimensional strip. In order to modify the quasi-steady assumption, 6 aerodynamic admittances are required, and the modified model is:

$$D_b = \frac{1}{2}\rho U^2 B\left[2C_D\chi_{Du}\frac{u}{U}+C_D^{'}\chi_{Du}\frac{w}{U}\right] \tag{1.1.9a}$$

$$L_b = \frac{1}{2}\rho U^2 B\left[2C_L\chi_{Lu}\frac{u}{U}+(C_L^{'}+C_D)\chi_{Lu}\frac{w}{U}\right] \tag{1.1.9b}$$

$$M_b = \frac{1}{2}\rho U^2 B^2\left[2C_M\chi_{Mu}\frac{u}{U}+C_M^{'}\chi_{Mu}\frac{w}{U}\right] \tag{1.1.9c}$$

where $\chi_{Lu}, \chi_{Lw}, \chi_{Du}, \chi_{Dw}, \chi_{Mu}, \chi_{Mw}$ are aerodynamic admittances, which are functions of reduced frequency.

Another assumption of Davenport buffeting force model is that the bridge structure is rigid, ignoring the aeroelastic phenomenon, and that the structural vibration and wind load do not affect each other. In fact, the structural vibration and the flow field will interact. The structural vibration is equivalent to changing the airflow boundary conditions, resulting in the change of wind load. Scanlan considered the participation effect of aerodynamic self-excited force in buffeting and modified Davenport buffeting force model as follows:

$$D = D_b + D_{se} \tag{1.1.10a}$$

$$L = L_b + L_{se} \tag{1.1.10b}$$

$$M = M_b + M_{se} \tag{1.1.10c}$$

The traditional linear unsteady self-excited force and buffeting force models can not consider the aerodynamic nonlinear phenomenon. With the increase of bridge span, the aerodynamic nonlinear characteristics become increasingly prominent, and the impact on the structural response cannot be ignored. Due to the influence of nonlinear factors, the uncertainty of critical flutter wind speed of long-span bridges in turbulence field increases.

1.1.3 Wind-induced vibration

In general, bridges have limited amplitude vibration under fluctuating wind load, that is, buffeting or vortex induced vibration. Buffeting refers to the forced vibration caused by the turbulent components in the airflow. It may cause structural fatigue. Excessive buffeting amplitude will cause discomfort and even endanger the speeding vehicles on the bridge. Vortex induced vibration is due to the vortex shedding that may occur when the wind flows through bluff-body structures with various cross-section shapes (circular, rectangular, polygonal, etc.). When the vortex shedding frequency is close the natural frequency of the structure, the resonance will be excited.

In some cases, when the wind speed reaches a certain degree, the negative damping will increase the amplitude until the structure is unstable. There are two possibilities of aerodynamic instability of bridges: flutter and galloping. Flutter is a dangerous self-excited divergent vibration. When it reaches the critical wind speed, the vibrating bridge continuously absorbs energy through the feedback of airflow, so that the amplitude gradually increases until the structure is damaged. Galloping refers to a decentralized cross wind single degree of freedom bending self-excited vibration formed by the energy absorbed by the structure overcoming the energy consumed by the structural damping when the critical wind speed is reached for a blunt body. It occurs when the energy absorbed by the structure from the airflow exceeds the energy consumed by the structural damping, and it is a kind of cross-wind single degree-of-freedom bending self-excited vibration.

1.1.3.1 Buffeting

The forced vibration caused by the fluctuating wind on the structure is called buffeting, also known as turbulent wind response. According to the source of fluctuating wind, it can be roughly divided into three types: wake buffeting caused by the wake of the structure itself, buffeting caused by the wake of upstream adjacent structures, and buffeting caused by the turbulence in airflow. Among them, buffeting caused by the turbulence in airflow plays a major role. Buffeting is a kind of limited amplitude vibration

but it may cause structural fatigue. Excessive buffeting amplitude will cause discomfort and insecurity. Therefore, buffeting analysis has become an increasingly important topic in the wind-resistant design of bridges.

There are two research methods of buffeting: frequency domain and time domain. The frequency domain method cannot consider structural nonlinearity, aerodynamic nonlinearity and other factors, while the time domain analysis does not have these limitations. The buffeting response of bridge is mainly analyzed in the frequency domain by the buffeting theory proposed by Scanlan. Chen (1993) proposed the buffeting response spectrum method for long-span bridges by integrating the characteristics of Davenport and Scanlan buffeting theory and referring to the idea of response spectrum method in seismic analysis. Ding (2001) developed the finite element CQC method for the coupled buffeting response analysis of long-span bridges based on the natural modal coordinates of the structure, which can comprehensively consider the multimodal and modal coupling effects of buffeting response. Hu (2006) developed the WIND-RESPONSE analysis program of bridge including the bridge buffeting time domain analysis module on the platform of ANSYS.

The buffeting response analysis of bridges has made great progress in the frequency domain and time domain, but there are still many unsatisfactory aspects: 1) the error between theoretical analysis, wind tunnel test and engineering measurement is still large, and the main reason is the determination and simulation of wind characteristics parameters. 2) Most of the current aerodynamic force expressions are linear, but many studies show that the aerodynamic force acting on the structure has nonlinear characteristics. Moreover, the aerodynamic admittance function which is widely used in the analysis of bridge buffeting response is the Sears function suitable for airfoils. Its application in the buffeting response analysis of long-span bridges has been questioned. Therefore, there is still a long way to go for the study of bridge buffeting.

1.1.3.2 Vortex induced vibration

When the airflow passes through the bluff body, separation will inevitably occur, so the periodic vortex shedding is formed and the periodic aerodynamic force acting on the bridge is generated. When the vortex shedding frequency is close to the natural frequency of the structure, the vortex induced vibration will be excited. Vortex induced vibration of bridge is usually vertical or torsional. Although vortex induced vibration will not cause destructive damage to bridges, frequent and continuous vortex induced vibration will cause fatigue damage and discomfort. Therefore, avoiding vortex induced vibration is also one of the key points of wind-resistant design of bridges.

As early as 1898, Strouhal found the relationship among cylinder diameter, incoming wind speed and wake vortex shedding frequency through the cylinder flow test:

$$S_t = \frac{f_v \cdot D}{U} \tag{1.1.11}$$

where f_v is the wake vortex shedding frequency, D is the cylinder diameter, and U is the incoming wind speed. For a specific type of cross-section, within a certain range of Reynolds number, S_t is basically constant. The onset wind speed of vortex induced vibration can be calculated by the Strouhal formula above.

As for the study of vortex induced vibration locking interval phenomenon, the most direct way is to establish a mathematical model that can accurately describe the vortex induced force. In recent decades, researchers have proposed several mathematical models to describe vortex induced force, which can be mainly divided into two types: single degree of freedom and two degrees of freedom.

The dynamic equation of the structure under the action of single degree of freedom vortex induced force model is as follows (Billah, 1989):

$$m \cdot \ddot{y} + c \cdot \dot{y} + k \cdot y = F\left(\ddot{y}, \dot{y}, y, C_L, U, t\right) \tag{1.1.12}$$

where m is the equivalent mass of the structure, c is the damping factor, k is the structural stiffness, y is the structural displacement response, F is the vortex induced force which is a function of the structural acceleration response, velocity response, displacement response, lift coefficient of cross-section, incoming wind speed and time.

The two degrees of freedom vortex induced force model regards the wake vortex shedding as a vibrator coupled with the structural vibration. The structural dynamic equation and the dynamic equation of wake vibrator are coupled through the structural response, as shown below:

$$m \cdot \ddot{y} + c \cdot \dot{y} + k \cdot y = \frac{1}{2} \rho U^2 D \cdot C_L \tag{1.1.13a}$$

$$K_1 \ddot{C}_L + K_2 \dot{C}_L + K_3 C_L = F\left(\ddot{y}, \dot{y}, y, U, t\right) \tag{1.1.13b}$$

where the wake vibrator response C_L is a function of the structural response, and K_1, K_2, K_3 are aerodynamic parameters to be identified.

Vortex induced vibration can be studied through wind tunnel tests. Sato and Tanaka conducted the wind tunnel test of the full bridge aeroelastic model to study the aerodynamic stability of the Akashi Kaikyo Bridge in Japan (Yamada and Katsuchi, 2004). Ge has made a series of experimental studies on the characteristics and influence parameters of vortex induced vibration based on the actual bridge engineering project, and put forward the wake test method and the estimation method of vortex induced vibration on the bridge cross-section wind speed locking range (Li et al., 2003; Du et al., 2003). Diana et al. (2006) carried out a sectional model wind tunnel test based on the main beam cross-section of the Messina Strait Bridge, and measured the phenomenon of two separated vortex locking intervals. Wang et al. (2007) studied the vortex induced vibration characteristics of the E'dong Bridge through large-scale sectional model wind tunnel test.

1.1.3.3 Flutter

Flutter is an unstable vibration phenomenon that occurs when an elastic body is subjected to the combined action of aerodynamic force, inertial force, elastic force and damping force in a uniform flow. Flutter is a dangerous self-excited divergent vibration. When the wind speed reaches the critical flutter wind speed the vibrating bridge continuously absorbs energy from the wind through the feedback of airflow, so that its amplitude continues to increase until the structure is completely destroyed as a whole. With the increasing span of bridges, the structure is becoming lighter and softer. For the super long-span suspension bridge, its flutter stability has become a key factor that directly affects the further growth of span (Ge, 2011).

Researchers have proposed a variety of empirical models to describe the self-excited force acting on the bridge. Scanlan self-excited force model is a classic empirical model. There may be some differences between the calculated self-excited force and the self-excited force of the actual structure because the cross-section types of bridges are diverse. There are mainly two kinds of differences. One is that Scanlan assumes that the self-excited force is a linear function of structural displacement and velocity, but the experimental research shows that there are obvious high-order harmonics in the self-excited force of some bluff body cross-sections, that is, the relationship between the self-excited force and structural motion is not completely linear. Moreover, the flutter derivative in Scanlan self-excited force model is a function of dimensionless reduced frequency. For two degrees of freedom or three degrees of freedom models, there are multiple reduced frequencies corresponding to the vibration frequencies of each degree of freedom, but there are different views on whether the flutter derivative is a function of a certain reduced frequency or multiple reduced frequencies (Simiu and Scanlan, 1996). The existing solution is to use the reduced frequency of its degree of freedom, which needs to be further verified.

People have done a lot of research on the flutter phenomenon of bridges, but the recognized flutter driving mechanism is mainly divided into two types: damping driving type and stiffness driving type. The driving mechanism of separated flow flutter is damping driving, that is, with the increase of wind speed, the total damping of the vibration system will change from positive to negative, and the negative aerodynamic damping offsets the structural damping so that the system energy cannot be dissipated, resulting in the structural vibration divergence. When this kind of flutter occurs, torsional deformation is the main vibration form, and the vertical bending vibration is not obvious. The flutter frequency is very close to the torsional natural vibration frequency of the structure. Generally, the bending-torsional coupling flutter of streamlined cross-section is attributed to the stiffness driving type. Its principle is that the aerodynamic stiffness effect brought by the airflow changes the frequency of bending vibration and torsional vibration of the system, which makes the bending frequency increase and the torsional

frequency decrease, so that a unified flutter frequency is coupled at the flutter critical point, and drives the structural vibration divergence. The main characteristic of this kind of flutter is that the structural motion contains obvious vertical bending vibration and torsional vibration when flutter occurs, and the value of flutter frequency is in the middle of vertical bending and torsional natural frequencies. About the mechanism of flutter, there is still some controversy. Zhang (1998) and Yang (2002) both believe that the flutter divergence mechanism of streamlined cross-section and bluff body cross-section is essentially the same, which is caused by a certain modal damping of structural vibration changing from positive to negative.

1.1.3.4 Galloping

The research on galloping began as early as people found that the airfoils are often damaged by airflow. After Birnbaum first proposed the expression of aerodynamic lift, more and more scholars began to study the galloping of flat plates. The essence of galloping is a pure bending large amplitude vibration of slender objects due to the self-excited effect of airflow, which can be divided into wake galloping and cross flow galloping, and their mechanisms are different. There is a critical wind speed for galloping. When this wind speed is reached, the structural amplitude will suddenly increase, that is, enter the critical state, and continue to increase with the increase of wind speed. Therefore, one of the key problems of galloping is to determine the critical wind speed.

In 1932, Den Hartog first expounded the galloping phenomenon and its mechanism by studying how freezing rain caused the oscillation of transmission lines, and introduced its famous Den Hartog criterion. Until now, the prediction of galloping critical wind speed of sectional model is still based on it, but Den Hartog criterion ignores the nonlinear component of aerodynamic force, and it is necessary to further analyze the steady-state response after galloping.

1.2 Wind-resistance study of bridges

Generally, there are three methods to study the wind-induced response of bridges: theoretical analysis, wind tunnel test and numerical simulation. Theoretical analysis refers to the study of aerodynamic performance of structure from the wind-resistant mechanism, but it is quite difficult to solve the wind-induced vibration response acting on the bridge by pure theoretical analysis because of the aeroelastic effect of bridge. Therefore, the wind tunnel model test has become the most effective and reliable means of wind-resistant design. Wind tunnel test is to study the airflow and its interaction with the model, so as to research the aerodynamic characteristics of the structure in the actual situation. Sometimes, it will cooperate with the on-site measurement and other means to conduct multi-scale evaluation of aerodynamic performance. With the rapid development of computer technology and the improvement of computational fluid dynamics (CFD), numerical simulation has become a common method to study the wind-induced response of bridges and other structures in recent years, but its

calculation accuracy remains to be verified.

1.2.1 Theoretical analysis

The effect of wind on long-span bridges is very complex, which is constrained by the wind characteristics, the aerodynamic characteristics of structure and the interaction between wind and structure. At present, there are many advancements in the theoretical research of bridge wind-resistance, but due to the complexity of wind environment and bridge structure, the theoretical analysis is still not mature.

Long-span bridges have the common characteristics of light weight, low stiffness and low damping, so it is necessary to carry out wind-resistant design and evaluation according to these characteristics. At present, the general practice is to divide the wind-induced effect into two parts: aerostatic effect and aerodynamic effect. The aerostatic effect includes torsional instability and lateral buckling, and the aerodynamic effect includes flutter, galloping, vortex induced vibration and buffeting. Among them, vortex induced vibration and buffeting do not have divergent effect, which belongs to limited amplitude vibration, and usually occur when the wind speed is low. Flutter and galloping are aeroelastic unstable vibration caused by aerodynamic self-excited force, which belong to divergent vibration. In addition, the interaction between the aerostatic wind and flutter or buffeting response is also included in the scope of study.

Wind-induced vibration of structure is random. From the perspective of engineering design, the research often does not need to accurately know the response of structure at all times. People usually only care about statistical information such as mean value, variance, extreme value, etc. The random vibration analysis of engineering structures can be divided into two types: the time-domain method based on direct integration and the frequency-domain method based on mode decomposition.

The time-domain method is to act the time history of wind load directly on the structure, and then obtain the time history of dynamic response of structure through gradual integration, and then carry out statistical analysis on the time history to determine the mean value, root mean square and other information of response. The advantage of time-domain method is that it has a wide range of applications. In principle, it is suitable for any system and any excitation, and it can obtain more complete information of the whole process of structural dynamic response with high accuracy. Its disadvantage is that the amount of calculation is large, but this problem is gradually being overcome with the development of computer technology.

The frequency-domain method is to obtain the wind load power spectrum through the fluctuating wind speed power spectrum, and then use the transfer function to establish the relationship between the displacement response power spectrum and the generalized wind load power spectrum, so as to obtain the mean square response of the structure. The advantages of frequency domain method are: 1) The

concept is clear, which can directly reflect the action law of fluctuating wind. 2) The amount of calculation is small because the statistical value of the random response of structure is directly solved in the frequency domain. The disadvantages of the frequency domain method are: 1) It assumes that the incoming airflow is a stationary random process, which is not applicable to some wind climates with short duration and violent wind speed changes (such as thunderstorm, tornado, etc.). 2) It is difficult to consider the influence of high-order mode shapes and mode coupling of the structure. 3) It is difficult to consider the influence of geometric nonlinearity and material nonlinearity. Nevertheless, the frequency-domain analysis method still plays a very important role in the theory of structural wind engineering.

1.2.2 Wind tunnel test

Wind tunnel test is a kind of aerodynamic test method. During the test, in addition to ensuring the geometric similarity between the model and the real object, it should also ensure the similarity between the test flow field and the real flow field. Although wind tunnel test has its limitations, it also has advantages that cannot be ignored:

- The wind tunnel can accurately control the test conditions, such as the velocity, pressure and temperature of the airflow.
- The test is carried out indoors, which is less affected by climate and time.
- The test contents are diverse and the accuracy of the test results is high.
- The test is safe and efficient.

The first wind tunnel recognized in the world was built by British Wenham from 1869 to 1871.A large number of wind tunnels appeared in the middle of the 20th century. Now the total number of wind tunnels in the world has reached more than 1000.

The bridge wind tunnel test belongs to the low-speed wind tunnel aerodynamic test, which can provide reference for the wind-resistant design of long-span bridges, and can also be used to study the wind-induced vibration of bridges. The University of Washington has specially built a wind tunnel to study the cause of Tacoma Bridge collapse with a 1/50 full bridge model. After finding out the cause of the destruction of the bridge, the wind-resistance of new Tacoma Bridge was studied and verified by wind tunnel test. In the 1960s, Britain built the Forth Highway Bridge with a main span of 1006m and the Severn Bridge with a main span of 988m. The beam cross-sections of these two suspension bridges have been model tested in the wind tunnel of the National Physical Laboratory in the UK. The streamlined cross-section of Severn bridge comes from the wind tunnel test. Later, the wind tunnel test of cable-stayed bridges was also considered as a necessary means after the wind-induced vibration problems occurred in the Saint-Nazaire Bridge in France (a steel cable-stayed bridge with a main span of 404m) and the Faro Bridge in Denmark (a steel cable-stayed bridge with a main span of 287m). In 1965, the world's first atmospheric boundary layer wind tunnel was built at the University of Western

Ontario and many boundary layer wind tunnels of different sizes have been built around the world. In China, the State Key Laboratory of Disaster Reduction in Civil Engineering of Tongji University took the lead in developing a special wind tunnel for bridges. In October 1994, a large bridge wind tunnel for full bridge model test was built with a test section size of 14m×15m×2m, filling the gap for bridge construction industry in China (Zhang and Xiang, 1997).

The wind tunnel test of bridge involves the aerostatic effect, wind-induced vibration response, vibration control, etc., which can be divided into sectional model test, full bridge aeroelastic model test, strip model test, wind environment test of the bridge site and so on. In addition, the bridge wind tunnel can also carry out pressure and vibration measurement tests of building structures, pressure and force measurement tests of vehicle models.

1.2.2.1 Sectional model test

In general, the aerodynamic performance of long-span bridges should be tested by sectional model test. It is an economical and effective means to use the sectional model test to select the optimal cross-section and preliminarily evaluate the wind-resistant characteristics of bridges because the test cycle of sectional model test and its cost is low. According to the different suspension methods, the sectional model test can be divided into rigid suspension test, elastic suspension test, forced vibration test and free vibration test.

1.2.2.2 Full bridge aeroelastic model test

The sectional model test has advantages in the cross-section selection and flutter analysis in the preliminary design stage of bridges, but in order to comprehensively reflect the aerodynamic characteristics and wind-resistance of the actual bridge, the full bridge aeroelastic model wind tunnel test plays an irreplaceable role. The full bridge aeroelastic model test can carry out flutter and buffeting test in the construction state and the operation state under the uniform flow field and turbulent flow field. It can make up for the deficiency of the simulation of atmospheric boundary layer turbulence and the aerodynamic response of bridges under the action of turbulent wind in the sectional model test. It can more truly reflect the aerodynamic stability and wind-induced vibration response of bridges in the actual atmospheric boundary layer. For particularly important or novel long-span bridges, full bridge aeroelastic model test are generally carried out.

1.2.2.3 Strip model test

Due to the difference between the test results of sectional model and the full bridge aeroelastic model, the strip model is produced in order to eliminate the interference of the tower, cable, etc. on the aerodynamic characteristics of the main beam and consider the three-dimensional effect of space. The strip model test is used to measure the vortex induced vibration, buffeting response and flutter of the bridge girder under uniform and turbulent flow. It can consider the two-dimensional and three-

dimensional vibration effect.

1.2.3 Numerical simulation

In recent years, with the rapid development of computer technology and the improvement of computational fluid dynamics (CFD), numerical simulation method based on CFD technology has gradually become one of the main methods to study the aerodynamic performance of bridges.

CFD is the analysis of systems containing physical phenomena such as fluid flow and heat conduction through computer numerical calculation and image display. The basic idea of CFD can be summed up in that the fields of continuous physical quantities in the time domain and space domain, such as velocity field and pressure field, are replaced by a set of variable values of a series of finite discrete points. The algebraic equations of the relationship between the field variables of these discrete points are established according to some certain principles, and then the approximate values of the field variables are obtained by solving the algebraic equations. CFD can be regarded as a numerical simulation of flow under the control of the basic equations of fluid (conservation equations of mass, momentum and energy). Through this simulation, the distribution of basic physical quantities (such as velocity, pressure, temperature, etc.) at various positions in the flow field of extremely complex problems can be obtained, as well as the changes of these physical quantities with time (Wang, 2004).

CFD appeared in 1931 and originated from the study of flow characteristics around airfoil in the field of aeronautical engineering. It is also known as the numerical wind tunnel (Xiang and Chen, 2003). For more than 50 years after its emergence, it has been mainly devoted to the development of computational conditions and numerical methods. It has gradually entered the field of wind engineering since the 1980s, and was initially used to simulate the flow around a cylinder in a uniform flow field. In the late 1980s, in order to study the problem of bluff body flow in turbulent field, a variety of turbulence models were developed and established. These turbulence models were used to analyze the flow around two-dimensional and three-dimensional rectangular bluff bodies, and the results were consistent with the experiments. In 1993, Walther of Denmark first calculated the flutter derivatives of the flat plate section by CFD, and then calculated the two-dimensional critical flutter wind speed, which took an important step in the "numerical wind tunnel". Then Walther and Larsen took the lead in developing the DVMFLOW software based on the discrete vortex method, which was successfully used for the wind-induced vibration analysis of the Great Belt Bridge (Lin and Ariaratnam, 1980). Since then, countries around the world have followed suit and improved the algorithm. Subsequently, the emergence of commercial software finally made CFD gradually mature and become an easy-to-use analysis tool that can truly meet the needs of practical engineering. Through the accumulation and merger of hundreds of CFD software, the world's best and most powerful CFD software has been produced: Fluent, CFX, Phoenix, STAR-CD, the FLOTRAN CFD module in ANSYS, etc.

Although the application of CFD technology in aeronautical engineering has achieved success, numerical simulation in the field of bridge and structural wind engineering is much more complex than the problems of pipe flow and airfoil flow that people have studied more in the past because civil engineering structures are mostly in the shape of bluff bodies, and the flow around them is inevitably accompanied by complex flow phenomena such as separation, reattachment, vortex shedding, etc. Although it is impossible to make CFD replace the full bridge wind tunnel test for the whole process simulation at present and in the near future, CFD technology not only provides parameters for theoretical analysis, but also reproduces complex flow phenomena and study the mechanism of aerodynamic measures, so as to preliminarily optimize the cross-section of bridges under the existing conditions. Therefore, CFD technology is a very effective tool and important process for aerodynamic shape optimization, independent design review, wind vibration mechanism research and the transition to "numerical wind tunnel" in the future (Xiang, 2002).

1.3 Wind-resistant stability analysis of bridges

1.3.1 Aerostatic stability theory

The aerostatic instability of bridge structure refers to the lateral and vertical linear displacement and torsional angular displacement of the main girder under wind load. Linear displacement can cause the change in structural stiffness, while angular displacement can cause the change in wind load. The changed wind load may further exacerbate the deformation of the main girder, leading to the aerostatic instability of the structure. In terms of the relationship between static wind and wind-resistance of structure, aerostatic instability refers to the divergence phenomenon where the additional aerodynamic force caused by structural deformation exceeds the increment of wind-resistance of structure and the deformation continues to increase. It can be vividly illustrated in Figure 1.3. For long-span bridges, aerostatic instability may precede aerodynamic instability (Boonyapinyo et al., 2006; Zhang, 2007), so the aerostatic stability performance of most long-span bridges cannot be ignored.

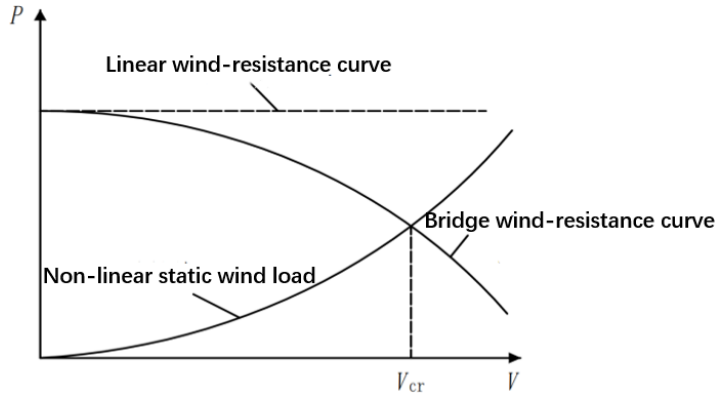

Figure 1.3: Diagram of the relationship between structural wind-resistance and wind speed

Because the static wind load is strongly dependent on the deformation, the research on the

mechanism of aerostatic instability of long-span bridge needs to track its instability process. The aerostatic instability generally starts from the equilibrium state and as the wind speed increases, the static wind load will also continue to increase, leading to an increase in the displacement of the main girder. The change in displacement will in turn affect the magnitude of the static wind load. Before reaching the critical wind speed, the deformation of the structure will eventually converge. After the critical wind speed, the vertical and torsional displacement of the structure will increase exponentially, leading to obvious softening of some components, and eventually leading to non-convergence of the structural deformation. At this time, the structure will suffer from aerostatic instability (Cheng et al., 2000).

As early as 1967, Prof. Hirai of the University of Tokyo in Japan observed the aerostatic torsional divergence phenomenon in the full model wind tunnel test of a suspension bridge (Boonyapinyo et al., 1994). The wind tunnel laboratory of Tongji University also found the bending torsional instability phenomenon in the test of the Second Shantou Bay Bridge. Nagai et al. (1998) also showed the possibility of this phenomenon through calculation.

The early aerostatic stability analysis is mainly linear, which can be divided into torsional divergence and lateral instability according to the different modes of structural instability. Trigonometric series method is another practical method to analyze the aerostatic stability. This method considers the geometric nonlinearity of the structure and the nonlinear influence of the combined action of the lift force and lift moment of the aerostatic load. If only the geometric nonlinearity of the structure is considered, the instability wind speed will be high. Only when the geometric nonlinearity and the nonlinearity of aerostatic load are fully considered, can the whole process of the instability be truly reflected. Wind-resistant design guidance for highway bridges in China (Xiang et al., 1996) adopts a combination of incremental method and iterative method to carry out the finite element analysis of the second type of aerostatic stability of long-span bridges. This method can better track the whole process of instability, but there is a problem of error accumulation because it uses the incremental method to calculate the geometric nonlinearity of the structure. In addition, if we want to get the critical wind speed of aerostatic instability of the structure, we can only load the wind speed step by step, which will cause the disadvantage of slow calculation. Cheng and Xiao (2001) proposed an improved incremental dual iteration method, which can obtain the critical wind speed of aerostatic instability of the structure without step-by-step loading of wind speed, and the accuracy is high. Zhang et al. (2013) analyzed the entire process of aerostatic instability and added turbulence to study the response of bridge structure. In addition, Li et al. (2012) studied the effect of aerostatic coefficient and some other parameters on aerostatic stability.

1.3.2 Flutter stability theory

1.3.2.1 Classical coupled flutter theory

Before studying the flutter of bridge, people first conducted research on the flutter phenomenon of airfoil. Theodorsen (1935) first studied the aerodynamic forces acting on an ideal flat plate in theory and derived an expression for the unsteady aerodynamic forces generated by the motion of an ideal flat plate in incompressible flow. In 1938, von Karman also achieved the same result. In a horizontally uniform flow field, the unsteady aerodynamic lift force and aerodynamic torque on a two-dimensional ideal flat plate undergoing small vibrations can be expressed as:

$$L = -2\pi\rho bU^2\left\{C(k)\left[\alpha+\frac{\dot{h}}{U}\right]+[1+C(k)]\frac{b}{2}\frac{\dot{\alpha}}{U}\right\} \tag{1.3.1a}$$

$$M = \pi\rho b^2U^2\left\{C(k)\left[\alpha+\frac{\dot{h}}{U}\right]+[1-C(k)]\frac{b}{2}\frac{\dot{\alpha}}{U}\right\} \tag{1.3.1b}$$

where ρ is air density; b is half width of the plate; U is incoming wind speed; h is vertical displacement of the cross-section; α is torsional angle of the cross-section; k is reduced frequency, $k=\omega b/U$ and ω is the circular frequency of the vibration; $C(k)$ is Theodorson cyclical function.

The Theodorson expression of self-excited aerodynamic force lays the foundation for the study of airfoil flutter problem. Bleich (1949) first applied Theodorson flutter theory of flat plate to suspension bridge and established two-dimensional flutter differential equation:

$$m\ddot{h}+m\omega_h^2(1+ig_h)\cdot h = L \tag{1.3.2a}$$

$$I\ddot{\alpha}+I\omega_\alpha^2(1+ig_\alpha)\cdot\alpha = M \tag{1.3.2b}$$

where L and M represent the aerodynamic lift force and aerodynamic torque of flat plate, respectively; m and I represent the mass and inertia moment of main girder per meter, respectively; ω_h and ω_α are the vertical bending fundamental frequency and torsion fundamental frequency, respectively; g_h and g_α are the plural damping factor of vertical bending and torsional vibration, respectively.

Bleich uses the natural modal coordinates of the structure to transform the flutter differential equation into a homogeneous equation set with variable parameters, and iteratively calculates k_c and ω_c at the critical state to obtain the critical flutter wind speed, which is the semi-inverse method that has been widely used later.

The classical coupled flutter theory is based on the flat plate flutter theory, but the aerodynamic forces of bridge cross-sections with obvious bluff body characteristics are different from those of flat plates in uniform flow. Therefore, the applicability of classical flutter theory to bridges has significant limitations.

1.3.2.2 Separation flow flutter theory

In 1971, Scanlan published a paper on flutter derivatives of cross-sections of bridge and airfoil, and proposed an unsteady model of aerodynamic forces combining theory with experiment to reasonably describe self-excited aerodynamic forces of non-streamlined cross-sections. This model contains 6 dimensionless flutter derivatives (Equation 1.1.5). In 1986, Huston derived the self-excited aerodynamic force expression with 8 flutter derivatives (Equation 1.1.6) based on Scanlan theory, taking into account the effect of vertical displacement h. Scanlan model of self-excited aerodynamic forces can better reflect the aerodynamic characteristics of non-streamlined cross-sections and the of bending-torsional aerodynamic coupling effect, so it has been widely used since it was proposed and has been used as a classical formula for bridge flutter analysis until now.

As the span of bridge continues to increase, researchers are becoming aware of the effect of lateral vibration on the aerodynamic performance of main girders. Sarkar and Jones extended the Scanlan self-excited force model to three dimensions, proposing a self-excitation model expressed in terms of 18 flutter derivatives (Equation 1.1.7). However, in practical applications, it is difficult to fully identify the 18 flutter derivatives, and it is generally simplified to a certain extent according to the specific situation.

The above research theories on flutter are all based on the two-dimensional cross-section of bridge, and the experiment also uses the sectional model of main girder to represent the entire bridge without considering the changes in the aerodynamic characteristics of the main girder along the bridge span, which is called the two-dimensional flutter theory.

1.3.2.3 Three-dimensional frequency domain flutter analysis

Scanlan (1978) used a semi-inverse method to obtain the flutter frequency and critical wind speed, pushing flutter analysis from two-dimensional to three-dimensional. Subsequently, based on the Scanlan self-excited aerodynamic force model, researchers conducted extensive research on bridge flutter issues and proposed various three-dimensional frequency domain flutter analysis methods. These three-dimensional frequency domain flutter analysis methods can be roughly classified as multi-modal methods and full-modal methods.

The multi-modal flutter analysis method uses modal decomposition technology to establish aerodynamic equations for the natural modal coordinates of the structure, and performs flutter analysis on the structure by solving matrix eigenvalues. Namini et al. (1992) proposed the *p-KF* method for multi-modal flutter analysis of bridge structures, drawing on analytical methods from the aviation field. Chen and Agar (1994) proposed the multi-modal and single-parameter method for the flutter analysis of bridge, which transforms flutter analysis into a generalized eigenvalue problem for plural matrices. Ding et al. (2002) proposed a multi-modal analysis method for aerodynamic coupled flutter of long-span bridges, which is a non-iterative single-parameter search method with strong automaticity.

Full-modal flutter analysis methods are also known as direct flutter analysis methods or full-order flutter analysis methods. This type of method is based on the full-order physical coordinates of the structural finite element model, which was first proposed by Miyata and Yamada (1990) in Japan based on a full finite element model of bridge. It ignores the effect of structural damping and does not require an iterative search. However, this method is very computationally intensive, resulting in a low analysis efficiency. Ge et al. (2000) proposed a three-dimensional full-modal flutter analysis method of long-span bridges, which better considered the effect of structural damping and further improved the computational efficiency.

1.3.2.4 Three-dimensional time domain flutter analysis

Frequency domain analysis is simple, practical and computationally efficient, and is widely used in the analysis of bridge structural vibrations. However, the frequency domain analysis method is based on the linear superposition of the modalities, which determines that it cannot fully reflect the influence of non-linear factors such as the non-linearities of structure and aerodynamic force. The time domain flutter analysis method is based on numerical integration, which can overcome the shortcomings of the frequency domain analysis method. It can effectively consider the influence of various non-linear factors and analyze the flutter stability of bridges more accurately.

Scanlan (1974) first introduced the concept of the classical step function proposed by Wagner in his aeronautical research into the study of bridge flutter, proposing a step function to describe the aerodynamic force expression acting on the bridge at arbitrary vibrations. Taking pure torsional vibration as an example, its time-domain expression can be written as

$$M_\alpha = \frac{1}{2}\rho U^2(2B^2)\frac{dC_M}{d\alpha}\left[X_{M\alpha}\dot{\alpha}(s)+\int_0^s \Phi_{M0}(s-\tau)\dot{\alpha}(\tau)d\tau\right] \tag{1.3.3}$$

where $dC_M/d\alpha$ is the gradient of the moment coefficient to the torsional angle; $X_{M\alpha}$ is the undetermined parameter; s is dimensionless time, $s=Ut/B$; $\Phi_{M0}(s)$ is the step function of aerodynamic force, which can be expressed by Wagner function in aviation.

For bridge flutter analysis, Scanlan constructed the step function expression:

$$\Phi_{M0}(s)=1+C_1e^{C_2 s}+C_3e^{C_4 s} \tag{1.3.4}$$

where C_1, C_2, C_3, C_4 are undetermined parameters that can be determined by fitting the flutter derivatives of the bridge cross-section using Fourier transform.

Drawing on the idea of expressing aerodynamic forces in terms of step functions, Lin and Yang (1983) proposed an expression for self-excited forces expressed by unit impulse response function:

$$L_{se}(t)=\int_{-\infty}^{t} f_{Lh}(t-\tau)h(\tau)d\tau+\int_{-\infty}^{t} f_{Lp}(t-\tau)\,p(\tau)d\tau+\int_{-\infty}^{t} f_{L\alpha}(t-\tau)\alpha(\tau)d\tau \tag{1.3.5a}$$

$$D_{se}(t)=\int_{-\infty}^{t} f_{Dh}(t-\tau)h(\tau)d\tau+\int_{-\infty}^{t} f_{Dp}(t-\tau)\,p(\tau)d\tau+\int_{-\infty}^{t} f_{D\alpha}(t-\tau)\alpha(\tau)d\tau \tag{1.3.5b}$$

$$M_{se}(t)=\int_{-\infty}^{t} f_{Mh}(t-\tau)h(\tau)d\tau+\int_{-\infty}^{t} f_{Mp}(t-\tau)p(\tau)d\tau+\int_{-\infty}^{t} f_{M\alpha}(t-\tau)\alpha(\tau)d\tau \quad (1.3.5c)$$

where $f_{ij}(t-\tau)$ $(i=L,D,M,\ j=h,p,\alpha)$ denote the unit impulse response function in the corresponding direction respectively.

On the basis of quasi-steady aerodynamic forces, Lin derived the aerodynamic force expression using the Roger rational function of unsteady aerodynamic forces in aviation (using $M_{\alpha}(t)$ as an example):

$$M_{\alpha}=\frac{1}{2}\rho U^{2}(2B^{2})\left[C_{1}\alpha(t)+\frac{C_{2}B}{U}\dot{\alpha}(t)+\sum_{k=3}^{n}C_{k}\int_{-\infty}^{t}e^{-\frac{d_{k}U}{B}(t-\tau)}\dot{\alpha}(\tau)d\tau\right] \quad (1.3.6)$$

where C_1, C_2, C_k, d_k are undetermined parameters that can be determined by fitting the measured flutter derivatives.

Based on the time domain aerodynamic force model mentioned above, many researchers have begun to use time domain analysis methods to study the flutter stability of long-span bridges (Chen et al., 2000; Costa and Borri, 2006; Wilde et al., 1996).

1.4 Machine learning in wind engineering

In recent years, artificial intelligence has been widely used in engineering. Artificial intelligence is a new science that researches the theory, technology and application used to simulate and extend human intelligence. Artificial intelligence is not human intelligence, but it can think like human beings and may even exceed human intelligence. It is a branch of computer science, which can simulate the process of human consciousness, and the technological products of artificial intelligence are the "containers" of human intelligence. Research in this field includes automatic programming, robotics, language recognition, image recognition, character recognition, natural language processing, intelligent search, gambling, expert system and so on. Since the birth of artificial intelligence, the application field has been expanding, and the theory and technology have become increasingly mature.

Machine learning is a method to realize artificial intelligence, which has been widely used in many fields of wind engineering. There have been many successful machine learning applications in the field of structural wind engineering. The existing literature can be reviewed and categorized into three main traits: (1) integration of previous on-site measurement data with machine learning models for the prediction of natural and extreme winds, (2) prediction of wind load/pressure or aerodynamic force on different structures, and (3) assessment of the wind-induced vibration response of structures. Among them, typical application examples in the last few years include: Wu and Kareem (2011) analyzed the hysteretic nonlinear behavior in bridge aerodynamics by cellular automata nested neural network; Jin et al. (2018) realized the prediction of velocity field around circular cylinder based on pressure on cylinder through convolutional neural network; Li et al. (2018) used support vector regression and decision tree

to identify the eigenvalues of vortex-induced vibration of bridge and analyze the influencing parameters of response; Yu et al. (2018) forecasted short-term wind speed by using wavelet packet decomposition and Elman neural network; Hu and Kwok (2020) and Tian et al. (2020) both achieved the prediction of surface wind pressure of bluff bodies using machine learning techniques; Li et al. (2021) successfully used long short-term memory neural network to predict the buffeting response at the time domain level. The other application examples of machine learning methods in the field of structural and bridge wind engineering are summarized in Table 1.1.

In recent years, machine learning methods have also been successfully applied to aerodynamic parameters identification and wind-resistant performance analysis. Li and Yang (2000) took the lead in realizing the prediction of aerostatic coefficients of bridges by artificial neural network; Jung et al. (2004) realized the estimation of six flutter derivatives of a rectangular section using artificial neural network based on 17 sets of experimental data; The artificial neural network was utilized by Chen et al. (2008) to predict eight flutter derivatives of bluff-body sections; The support vector machine was introduced by Lute et al. (2009) to identify flutter derivatives of the main girder before estimating the critical flutter wind speed of cable stayed bridges; Chung et al. (2012) used numerical simulations and forced-vibration test in a wind tunnel to estimate eight flutter derivatives of rectangular section by back propagation neural network; Abbas et al. (2020) used the normalized lift force and torsional moment coefficients at current time step as the output of artificial neural network to predict the aeroelastic response of bridge decks; The artificial neural network model based on Levenberg-Marquardt algorithm was derived and trained by Rizzo and Caracoglia (2020) using various geometrical and mechanical parameters of the bridge deck cross-section, and critical flutter wind speed of suspension bridge with closed box deck sections can be predicted directly; Mei (2021) proposed a machine learning strategy for flutter prediction based on four widely-used machine learning algorithms; Li et al. (2022) applied artificial neural networks to establish the relationship between aerostatic coefficients and flutter performance for fast prediction of critical flutter wind speed. Table 1.2 summarized the application examples of the intelligent identification for bridge aerodynamic parameters and wind-resistant performance.

Table 1.1: Summary of machine learning applications in bridge and structural wind engineering

Researcher	Application	Method	Data source
Fu et al. (2002)	Prediction of wind loads on a large flat roof	FNN	Wind tunnel test
Chen et al. (2003)	Prediction of pressure coefficients on roofs of low buildings	ANN	Wind tunnel test
Gu and Zhou (2003)	Prediction of the average wind pressure on the long-span roof surface of a hall	ANN	Wind tunnel test
Xie et al. (2004)	Identification of the wind-induced interference effect of two high-rise buildings	ANN	Wind tunnel test

Zhang and Zhang (2004)	Prediction of building interference effects	ANN	Literature
Chen et al. (2008)	Prediction of dynamic responses of rectangular bridge sections	ANN	Wind tunnel test
Wu and Kareem (2011)	Modeling hysteretic nonlinear behavior of bridge aerodynamics	ANN	Wind tunnel test
Wang and Cheng (2013)	Estimation of the wind force coefficients on a rectangular building	GRNN	Wind tunnel test
Elshaer et al. (2017)	Aerodynamic shape optimization of tall buildings	ANN	Numerical simulation
Huang et al. (2017)	Prediction of wind loads on high-rise building	ANN	Wind tunnel test
Jin et al. (2018)	Prediction of velocity field around circular cylinder	CNN	Wind tunnel test
Li et al. (2018)	Identification of the eigenvalues of vortex-induced vibration of bridge	SVM	On-site measurement
Yu et al. (2018)	Forecast of short-term wind speed	RNN	On-site measurement
Zhu and Zhang (2018)	Estimation of the fatigue damage of coastal bridges under coupled loads	SVM	Numerical simulation
Oh et al. (2019)	Wind-induced response estimation for tall buildings	CNN	Wind tunnel test
Castellon et al. (2020)	Estimation of the buffeting response speed of a bridge	SVM	On-site measurement
Hasegawa et al. (2020)	Modeling for unsteady flows around bluff bodies of various shapes	LSTM	Numerical simulation
Hu and Kwok (2020)	Predicting wind pressures around circular cylinders	GBDT	Literature
Le and Caracoglia (2020)	Performance assessment of a vertical structure subjected to nonstationary tornadic wind	ANN	Monte Carlo simulation
Li et al. (2020)	Prediction of nonlinear unsteady bridge aerodynamics	LSTM	Numerical simulation
Tian et al. (2020)	Prediction of the mean and the peak pressure coefficient on a low-rise gable building	DNN	Wind tunnel test
Li et al. (2021)	Prediction of the buffeting response time history	LSTM	On-site measurement

Notes: FNN-fuzzy neural network, ANN-artificial neural network, GRNN-general regression neural network, CNN-convolutional neural network, RNN-recursive neural network, SVM-support vector machine, LSTM-long short term memory, GBDT-gradient boosting decision tree, DNN-deep neural network.

Table 1.2: Summary of machine learning applications in aerodynamic parameter identification

Researcher	Application	Method	Data source
Li and Yang (2000)	Identification of aerostatic coefficients of bridges	ANN	Wind tunnel test
Yang (2000)	Identification of aerostatic coefficients and flutter critical wind speed of bridges	ANN	Wind tunnel test
Wang et al. (2001)	Identification of 8 flutter derivatives of bridges by using acceleration response	ANN	Wind tunnel test
Li (2003)	Identification of aerodynamic parameters of bridge section	ANN	Wind tunnel test
Jung et al. (2004)	Estimation of aeroelastic parameters of bridge decks	ANN	Wind tunnel test
Chen et al. (2008)	Prediction of flutter derivatives of a rectangular section model	ANN	Wind tunnel test
Lute et al. (2009)	Prediction of flutter derivatives of a cable stayed bridge	SVM	Wind tunnel test
Chung et al. (2012)	Estimation of flutter derivatives of a rectangular section	ANN	Numerical simulation
Abbas et al. (2020)	Prediction of the aeroelastic response of bridge decks	ANN	Numerical simulation
Rizzo and Caracoglia (2020)	Prediction of the flutter velocity of suspension bridges	ANN	Wind tunnel test
Mei (2021)	Unified modeling and parameter identification of nonlinear aerodynamic forces	LSTM	Wind tunnel test
Li et al. (2022)	Relationship between aerostatic coefficients and flutter critical wind speed	ANN	Wind tunnel test

All these studies confirm the feasibility and effectiveness of machine learning methods in bridge and structural wind engineering (Bao and Li, 2020). However, these attempts are not really independent of specially designed wind tunnel tests or supplementary numerical simulation. Current research lacks the integration and data-mining of existing results of wind tunnel tests or numerical simulations. Furthermore, most of the existing research is a direct application of common machine learning methods to a specific scenario in parameter identification or wind-resistance analysis, without illustrating the applicability of the algorithms and improving them accordingly. The existing machine learning applications are mostly to build a black box, lacking the interpretation and extension of the identification model.

1.5 Objectives and scope of research

Based on the data of bridge wind-resistance, this study models and predicts the aerodynamic parameters of typical bridge cross-sections in a data-driven manner, and then analyzes the wind-resistant performance of long-span bridges. This section roughly combs the theoretical framework of the research on the bridge wind-resistance involved in this paper. The main objectives of this research are as follows:

1) Database establishment

In Chapter 2, a self-built wind-resistance database of long-span bridges based on the existing wind tunnel test results will be described in detail, including all the data source, the setting of the underlying database management system and the development of foreground visualization application, as well as the connection between them.

2) Dataset collection

In Chapter 3, several cross-sections of long-span bridges with closed box girder in the database will be selected as a part of the data sample set used for data-driven in this paper. Some numerical simulation data of closed box girder from open-source literature and another some supplementary data are also added as hybrid dataset to jointly drive the training process of machine learning. In addition, CFD numerical simulation will be carried out to calculate the aerostatic coefficients and flutter derivatives of all selected cross-sections to further improve the accuracy of machine learning models, and the calculation results will be compared with the wind tunnel test results or theoretical solutions to verify the effectiveness of numerical simulation.

3) Machine learning prediction of aerodynamic parameters

The Chapter 4 will introduce and compare the machine learning algorithms used for modeling of aerodynamic parameters, and select the algorithm that is most suitable for the analysis of aerodynamic performance of bridges to realize the machine learning modeling and prediction of aerostatic coefficients and flutter derivatives of closed box girder, so that the identification of aerodynamic parameters of bridges can be separate from wind tunnel test and numerical simulation to a certain extent. At the same time, it also provides a convenient and feasible choice for expanding the aerodynamic parameter dataset. In addition, the post-interpretation of the model will also be implemented, which can further check the validity of trained machine learning models.

4) Two-dimensional wind-resistant stability analysis

In Chapter 5, the two-dimensional wind-resistant stability analysis of bridge will be carried out. Taking a specific bridge as an example, combined with the trained machine learning models, the aerostatic stability and flutter stability of the structure will be analyzed, and the sensitivity of aerostatic coefficients and flutter derivatives will be studied. At the same time, the influence of the feature size of cross-section on aerostatic stability and flutter stability will be evaluated by changing the local

dimensions of the cross-section, which provides a necessary reference for the preliminary aerodynamic shape optimization of closed box girder.

5) Three-dimensional wind-resistant stability analysis

In Chapter 6, the two-dimensional stability analysis in the previous chapter is extended to three-dimensional, and a specific bridge is still taken as an example to carry out three-dimensional finite element modeling, so as to carry out three-dimensional aerostatic stability calculation and three-dimensional multi-modal flutter analysis, and compare the machine learning prediction results under the same conditions. Besides, the two-dimensional and three-dimensional wind-resistant stability calculation and cross-section shape sensitivity analysis results are also compared to make a comprehensive comparative analysis of the two-dimensional and 3-dimensional wind-resistance analysis methods based on machine learning algorithms.

In the last chapter of this paper, all the research work and main conclusions will be summarized, and the shortcomings of this research will also be explained. Moreover, some personal comments and suggestions for further research in the future will be put forward. Figure 1.4 shows the technology roadmap of this study.

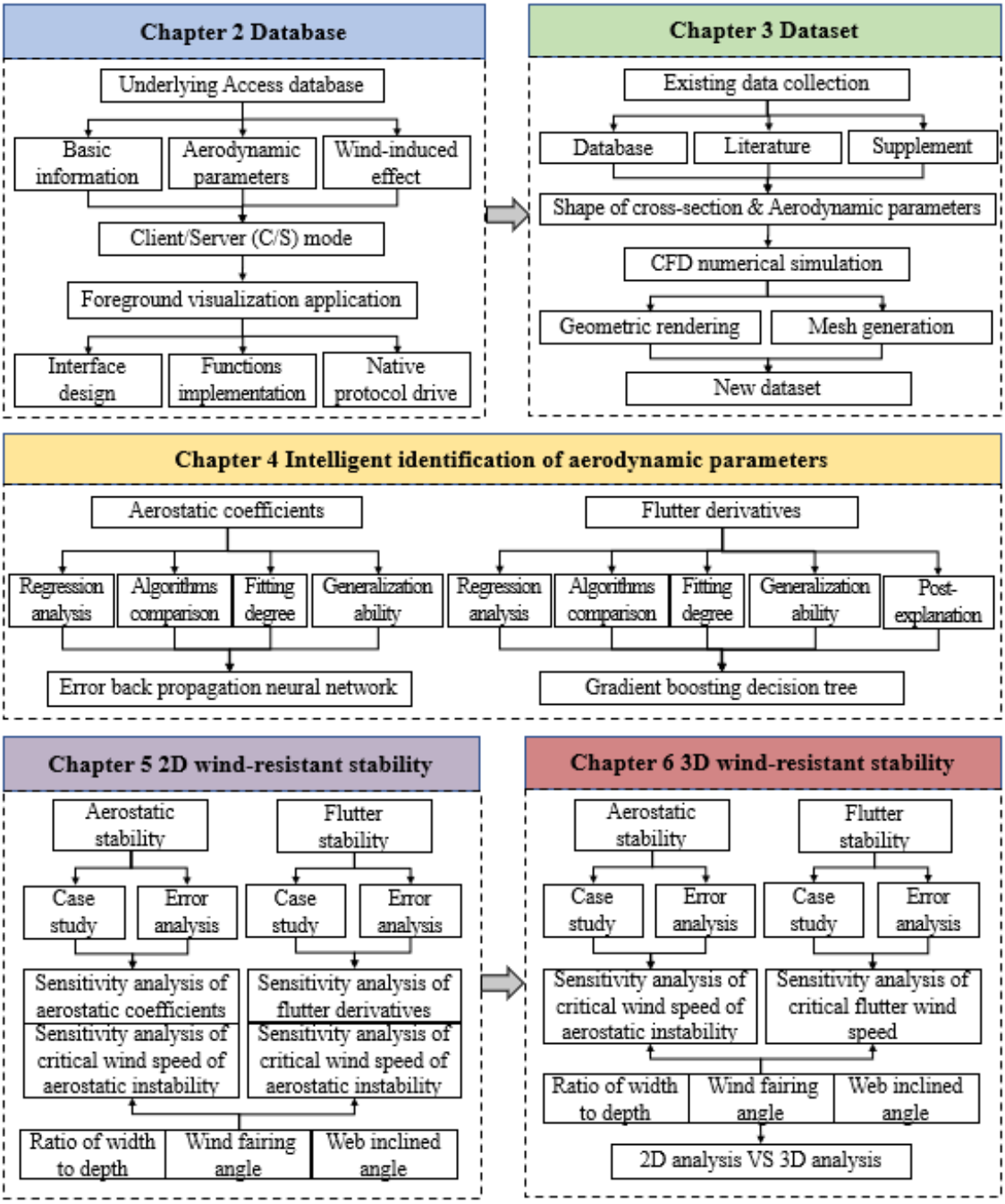

Figure 1.4: Technology roadmap

CHAPTER 2

2 Wind-resistance database of long-span bridges

2.1 Background

Machine learning is a technique of data science that helps computers learn from existing data in order to forecast future behaviors, outcomes, and trends. Therefore, data is the basis of machine learning, and database is a collection of organized and sharable data. In daily work, it is often necessary to put some relevant data into such a "warehouse" and deal with it according to the needs of management.

There are already some mature open-source wind engineering databases, which are mainly established by some wind engineering groups, for example, from Canada, China, Japan, USA, etc. Among them, the United States began to develop the wind tunnel test database in the 1980s, and General Motors Company was the first to establish the wind tunnel test database. In 1985, NASA (National Aeronautics and Space Administration) also established a wind tunnel test database for the transonic wind tunnel. Zhou et al. (2003) established the first online aerodynamic database for tall buildings (http://aerodata.ce.nd.edu/). Then, Ho et al. (2005) built the aerodynamic database from a large number of pressure measuring tests of low-rise building models conducted at the University of Western Ontario for NIST (National Institute of Standards and Technology) in Canada. The database built by Tokyo University of Technology in Japan is comprehensive, which contains model test data of high-rise and low-rise buildings and interference test data of high-rise buildings (http://www.wind.arch.t-kougei.ac.jp/info_center/weic.html) (Quan et al., 2006).

In China, the established wind tunnel test databases include the low-speed wind tunnel test database system developed by China Aerodynamics Research and Development Centre, as well as some other small and medium-sized wind engineering databases developed by laboratories or individuals. For example, Harbin Institute of Technology established a comprehensive wind engineering database, collating wind tunnel test data for several large-span structures and a small amount of high-rise buildings. Zhao et al. (2007) developed a wind load database mainly for large-span roofs based on Access database system. Wang et al. (2003) conducted high-frequency force balance wind tunnel tests on more high-rise building models and built a wind-resistance database for them based on expert system, which can automatically retrieve the corresponding test data according to the information entered by users for online calculation and analysis (http://windexpert.ce.tku.edu.tw/).

The existence of these data and databases is a prerequisite for researchers to carry out wind-resistance analysis using machine learning methods. However, the above databases are mainly for building structures, and are self-contained. Even if they can be used for bridge wind-resistance, the data types may not be matched completely. Actually, a large number of wind tunnel test data of long-span bridges have been accumulated in Tongji University, and various experimental data has been unified to the same criterion. The WindLock software independently developed by Zhao of Tongji University and some other researchers is mainly used for the wind-resistant design of cooling towers and bridges, which

has a variety of functions such as calculation, analysis, automatic plotting and so on. It collates some wind tunnel test data of bridges to fill the gap in the bridge wind engineering database. In 2009, Liu established a set of bridge wind-resistance analysis software, which also collected the wind tunnel test data of some typical cross-sections of long-span bridges, and built a client to facilitate users' access, call and other visual operations (Liu, 2009). In this research, a specialized bridge wind-resistance database is developed based on it, which not only realizes the management, secondary utilization, and sharing of bridge wind tunnel test data, but also provides the necessary data foundation for subsequent machine learning.

2.2 Underlying database

2.2.1 Data source

This research collected the test data of 99 long-span bridges from the wind tunnel laboratory of Tongji University. The list of bridges included is shown in Appendix A. After classification, all the data can be summarized into three modules: basic information, aerodynamic characteristics and aerodynamic parameters. Among them, the basic information includes the type of bridge, span, the material of girder, the type and size of cross-section, mass, stiffness, basic wind speed, critical wind speed, amplitude, etc. The aerodynamic characteristics include the natural frequency and mode of vibration. The aerodynamic parameters only include the aerostatic coefficient and flutter derivative, and the aerodynamic admittance is not involved.

• Basic information

The data involve three types of bridge: cable-stayed bridge, suspension bridge and arch bridge. The types of cross-sections include closed box girder, π-shaped girder, cantilever box girder, slotted box girder, etc. The architectures of these cross-sections are shown in Figure 2.1. The materials of girder include concrete, steel and steel-concrete composite. The data retrieval and viewing functions to be implemented later are filtered and classified by the above three types of information. In addition, some other basic information such as bridge span, geometric dimension of cross-section, wind speed and so on are also collected, sorted and displayed accordingly.

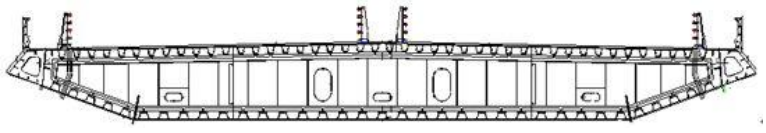

(a) closed box girder

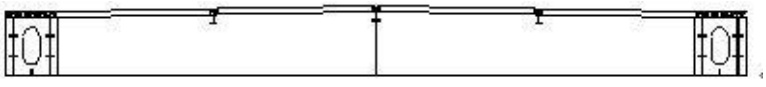

(b) π-shaped girder

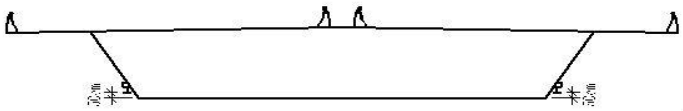

(c) cantilever box girder

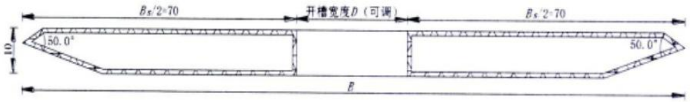

(d) slotted box girder

Figure 2.1: Architecture of various cross-sections

• Dynamic characteristics

The database sorts out the first several vertical bending, lateral bending and torsional frequencies of each long-span bridge, which can be called and viewed by users, and also provides the data basis for the subsequent wind-resistant performance analysis of bridges.

• Aerodynamic parameters

The database collects the aerostatic coefficients and flutter derivatives of 99 long-span bridges under different wind attack angles and eliminates the data with obvious errors. The final results are stored in the database and applied to the machine learning prediction of aerodynamic parameters in Chapter 4, so that these long-span bridge wind tunnel test data can be fully reutilized.

All the parameters involved in each module of database are listed for reference in Table 2.1.

Table 2.1: Parameters of each module of the database

Module	Parameter
Filter	bridge type, section type, girder material
Basic information	basic wind speed, length of main bridge, main span, dimension of cross-section, mass and inertia moment per unit length of girder
Aerodynamic characteristic	first 10 orders vertical bending, lateral bending and torsional frequencies and corresponding vibration modes and damping ratios
Aerodynamic parameter	aerostatic coefficients (-12°~+12° wind attack angles): C_D, C_L, C_M flutter derivatives (-3°~+3 ° wind attack angles): $A_1^*{\sim}A_4^*, H_1^*{\sim}H_4^*$
Other information	critical flutter wind speed, wind speed locking interval and amplitude of vortex induced vibration

2.2.2 Database management system

After completing the data collation, the data needs to be managed in the database for viewing, calling and editing. In this study, the wind-resistance database of long-span bridges uses Microsoft Access as the underlying database system. Access database is a very representative relational database

based on Windows Desktop launched by Microsoft company. After years of improvement, it has become one of the most mainstream database products in the world and is widely used in various fields.

Access database management system adopts the concept of Windows programming to design user interface, data storage, data query, report generation, etc. With the unique technology of Windows, it can also use the programming language VBA (Visual Basic for Applications) shared by the whole Office suite for advanced operation control and complex data manipulation. Access makes it easy to build a fully functional database management system because its integrated development environment and standardised processing. Compared to other database management system software, Access is much simpler to learn. It is powerful enough to cope with general data management and processing needs, and is suitable for small and medium-sized data management requirements. An average computer user, even with no programming skills, can still quickly master and use it to build complex reports, interfaces, etc. It will automatically generate SQL code and efficiently perform most data management tasks. The main advantages of Access are also evident in the following:

- It is stored in the form of a file (with the file extension *.mdb), which is easy for the user to manipulate and manage.

- It is an object-oriented development tool with a user-friendly interface that is very intuitive and convenient, which can greatly simplify the user's development work.

- The Windows-based development environment incorporates a variety of tools that greatly improve the efficiency of the user and make it easier to create databases in an organised manner.

- It creates both data objects (e.g. datasheets) and a database management system with a user interface, and the link between the interface and the data can be achieved through wizards in the software.

- It allows the application to be applied to the web and connected to dynamic data, using database access objects to generate HTML files to easily build applications for the Internet/Intranet.

Access was used as the underlying database system for the creation of specialised wind-resistance database for long-span bridges in this study, and the design and use of which is described below.

2.2.3 Access datasheet design

This research selects the 'datasheet' function of Access to store all data as shown in Figure 2.2. 'Field' is the basic unit of datasheet in Access. In the process of creating a sheet, the data type of field needs to be set in advance. There are 10 available field data types: auto-number, text, number, note, currency, date and time, yes/no, OLE object, attachment and hyperlink. If some data can be stored with multiple data types, it needs to be determined by comprehensively considering the size and purpose of data. In the process of creating a sheet or after creating the sheet, fields can be added or deleted under this view, and the data and attributes of fields can also be reset.

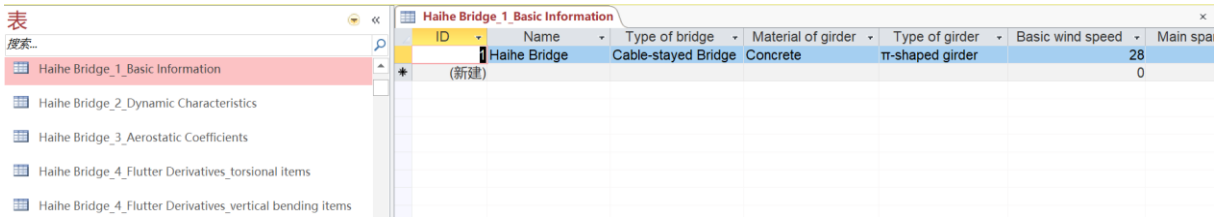

(a) basic information

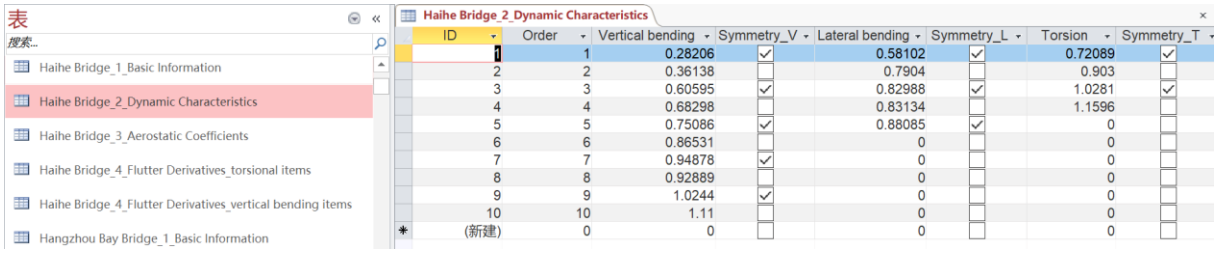

(b) dynamic characteristics

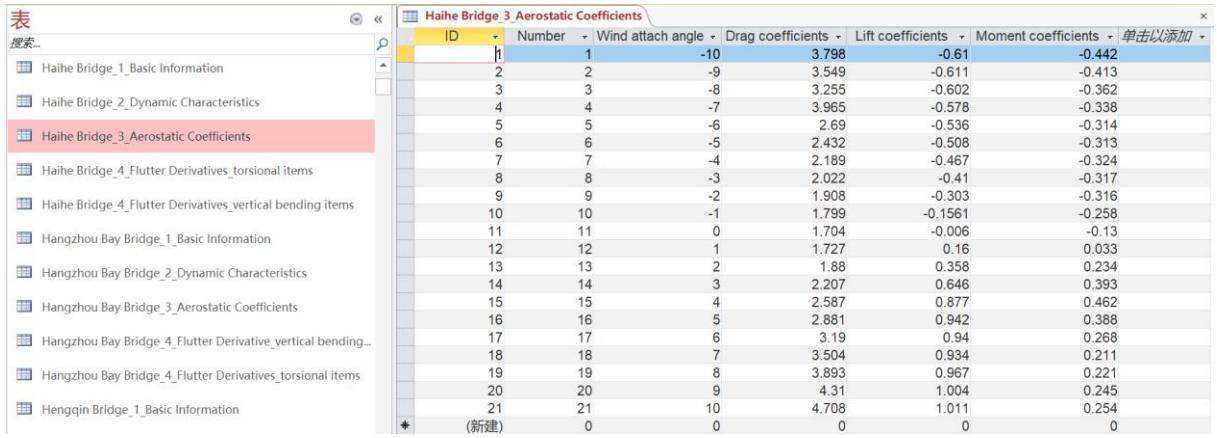

(c) aerostatic coefficients

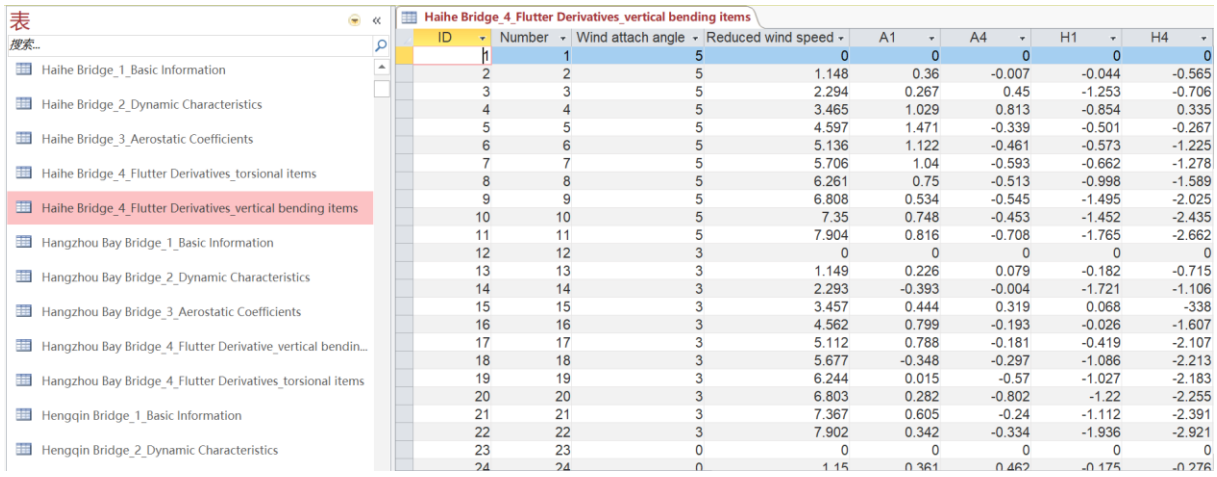

(d) flutter derivatives- vertical bending terms

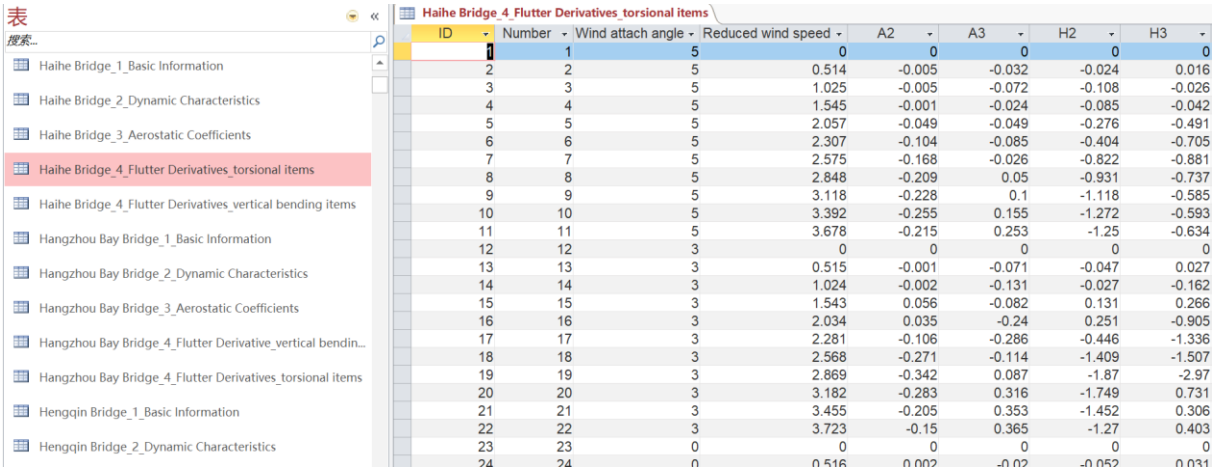

ID	Number	Wind attach angle	Reduced wind speed	A2	A3	H2	H3
1	1	5	0	0	0	0	0
2	2	5	0.514	-0.005	-0.032	-0.024	0.016
3	3	5	1.025	-0.005	-0.072	-0.108	-0.026
4	4	5	1.545	-0.001	-0.024	-0.085	-0.042
5	5	5	2.057	-0.049	-0.049	-0.276	-0.491
6	6	5	2.307	-0.104	-0.085	-0.404	-0.705
7	7	5	2.575	-0.168	-0.026	-0.822	-0.881
8	8	5	2.848	-0.209	0.05	-0.931	-0.737
9	9	5	3.118	-0.228	0.1	-1.118	-0.585
10	10	5	3.392	-0.255	0.155	-1.272	-0.593
11	11	5	3.678	-0.215	0.253	-1.25	-0.634
12	12	3	0	0	0	0	0
13	13	3	0.515	-0.001	-0.071	-0.047	0.027
14	14	3	1.024	-0.002	-0.131	-0.027	-0.162
15	15	3	1.543	0.056	-0.082	0.131	0.266
16	16	3	2.034	0.035	-0.24	0.251	-0.905
17	17	3	2.281	-0.106	-0.286	-0.446	-1.336
18	18	3	2.568	-0.271	-0.114	-1.409	-1.507
19	19	3	2.869	-0.342	0.087	-1.87	-2.97
20	20	3	3.182	-0.283	0.316	-1.749	0.731
21	21	3	3.455	-0.205	0.353	-1.452	0.306
22	22	3	3.723	-0.15	0.365	-1.27	0.403
23	23	0	0	0	0	0	0
24	24	0	0.516	0.002	-0.02	-0.052	0.031

(e) flutter derivatives- torsional terms

Figure 2.2: Underlying Access database

After establishing the underlying data table, the logical relationship between data operations, that is, the query function, can be formulated. The query function should extract data from the table according to the actual needs of users and some certain rules, which is the most important operation of database design (Sa and Tu, 1997). The main purpose of database is to store information and extract relevant information according to users' requirements. Access can query the information of one or more tables in a database, and it can also edit data. Access supports many different types of queries, and the query relationship should be established according to the users' requirements.

2.3 Foreground visualization application

2.3.1 Computer language

In this study, the database management system uses the Client/Server (C/S) mode, which means that after the underlying database is established, a suitable computer language should be used to develop the foreground application for users' convenient visual operation. A comparison of the various computer languages available shows that object-oriented languages are more suitable for the development of functionally complex programs because the use of objects encapsulates the code and makes it easier to maintain (Liu, 2009).

Considering the actual needs of users, Java programming language is used to develop the foreground visualization application in this research. Java is an object-oriented programming language that is both powerful and easy to use, and its cross-platform nature makes it popular with many developers and has a wide range of applications. As a representative of static object-oriented programming language, Java can well implement object-oriented theory, allowing programmers to complete complex programming tasks in a very elegant way of thinking. Java can be used to write desktop applications, web applications, embedded system applications and so on. It can be compiled or

interpreted, and it only needs to be compiled once to interpret and execute when the program is running (Phipps, 1999). Because of its good design philosophy, Java has become a standard development language in recent years, and its features and advantages can be summarized as follows (Zhao, 2005):

- Java language doesn't need pointers, so developers don't have to worry about storage management.
- It is a distributed language that supports various levels of network connectivity and applications.
- Java environment is portable to new hardware platforms and operating systems.
- It is designed to be a highly reliable and robust language, ensuring that the compiler successfully catches call errors.
- It is a dynamic language, which is capable of adapting to changing environments.

Java programs must be compiled and run in two steps: (1) compile the source file into bytecode; (2) interpret the bytecode independent of the execution platform. These two steps require the java and javac commands. For Windows operating systems, finding the commands according to the Path environment variable is needed, i.e. add the paths where the java and javac commands are located to the Path environment variable to compile and run the Java program.

Moreover, there are four ways to realize Java-DataBase Connectivity (JDBC): JDBC-ODBC bridge, native API driver, network protocol driver and native protocol driver. This project uses a native protocol driver to translate JDBC calls into requests that meet the requirements of database system specification directly in order to achieve the independence of platform. The core code is as follows:

```
public static void connetAccessDB() throws Exception {
    Class.forName("com.hxtt.sql.access.AccessDriver").newInstance();
    Properties prop = new Properties();
    String dbur1 = "jdbc:Access:///F:/大跨桥梁数据库.mdb";
    con = DriverManager.getConnection(dbur1, prop);
    sql = con.createStatement();
}
public static void connetDBAbsolute(String dbname) throws Exception {
    Class.forName("com.hxtt.sql.access.AccessDriver").newInstance();
    Properties prop = new Properties();
    String dbur1 = "jdbc:Access:///" + dbname;
    con = DriverManager.getConnection(dbur1, prop);
    sql = con.createStatement();
}
private static void executeSql(String query) throws Exception {
    rs = sql.executeQuery(query);
```

```
}
public static void closeConnection() throws Exception {
    sql.close();
    con.close();
}
```

Any text editor can be used to edit Java source code, but do not use a formatted editor because hidden formatting characters will prevent the program from compiling and running properly. For this paper, IntelliJ software has been chosen as the development environment for Java programs, as it offers the most useful combination of tools and has been hailed by many developers and experts as the best Integrated Development Environment (IDE). IntelliJ frees developers from some time-consuming routines and therefore significantly improves development efficiency. It is easy to code, fast to run, continuously redesigned and integrates perfectly with other tools.

2.3.2 Visualization application interface design

The design of the interface and the functions of application should fully consider the data that needs to be managed and displayed, as well as the actual needs of users. The page should be as concise and clear as possible. This study needs to design the interface and realize the corresponding functions according to the classification of data to display the wind tunnel test results of 99 long-span bridges. The whole user interface is designed in Chinese and composed of four windows: basic information, aerodynamic characteristic, aerostatic coefficient and flutter derivative. Three filters are set in the basic information window of the home page, which are bridge type, cross-section type and girder material. The filters have no sequence. Only the bridges that meet these filters at the same time will be shown below. When a bridge is selected, the interface will show its corresponding information. The contents displayed in the other three windows (aerodynamic characteristic, aerostatic coefficient and flutter derivative) will also change with the selected bridge at the same time. Figure 2.3 shows the design effect of each window.

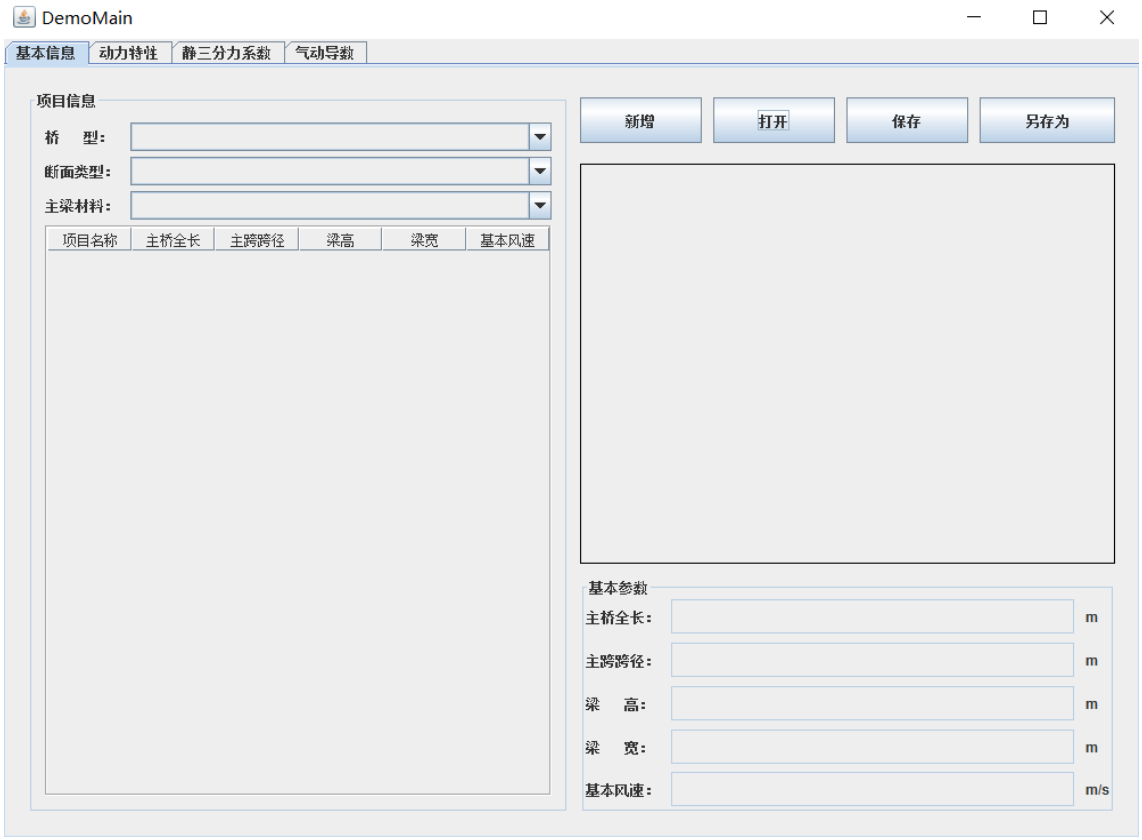

(a) Home page

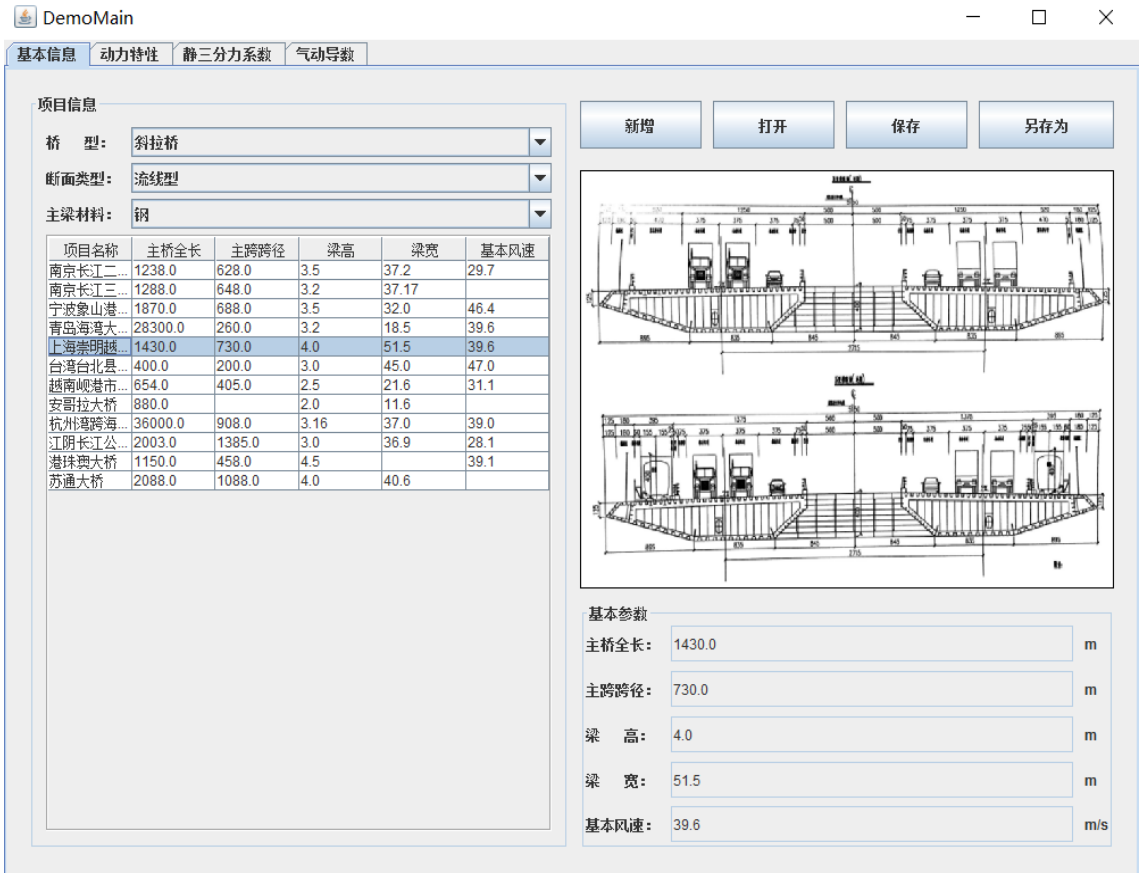

(b) Window of basic information

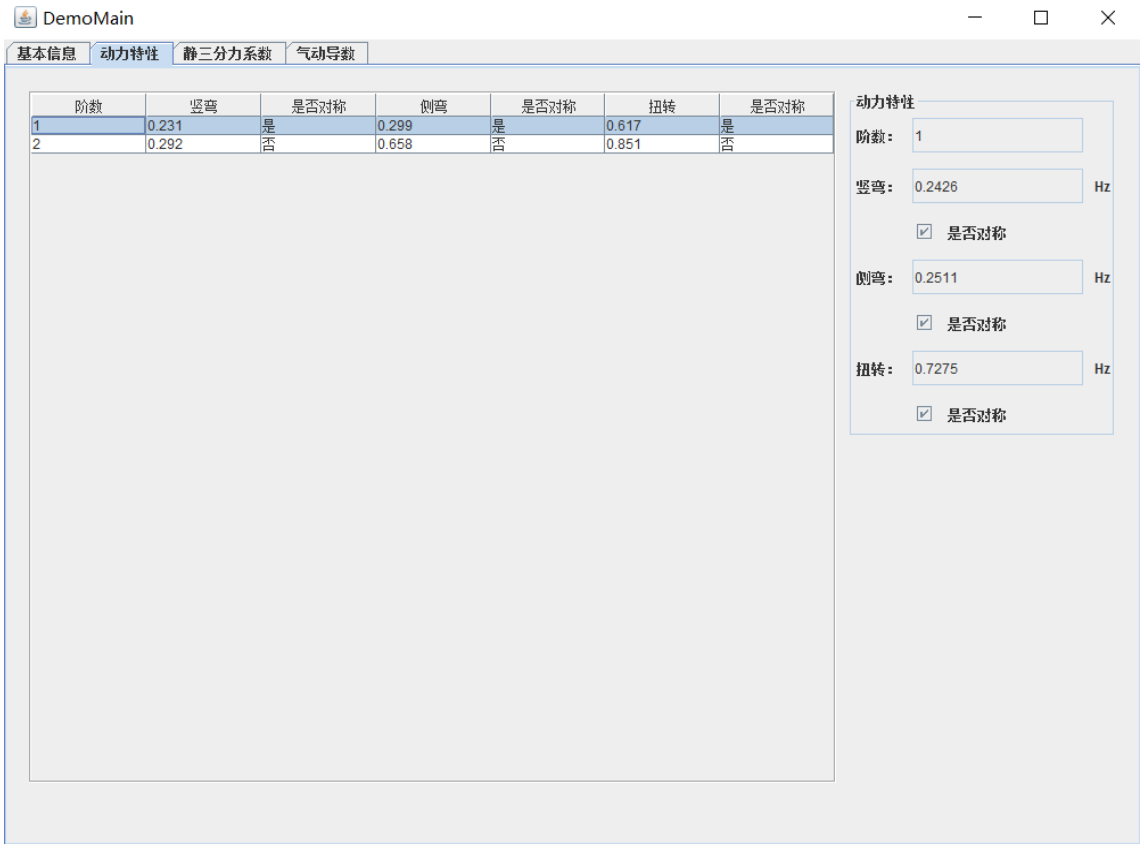

(c) Window of dynamic characteristics

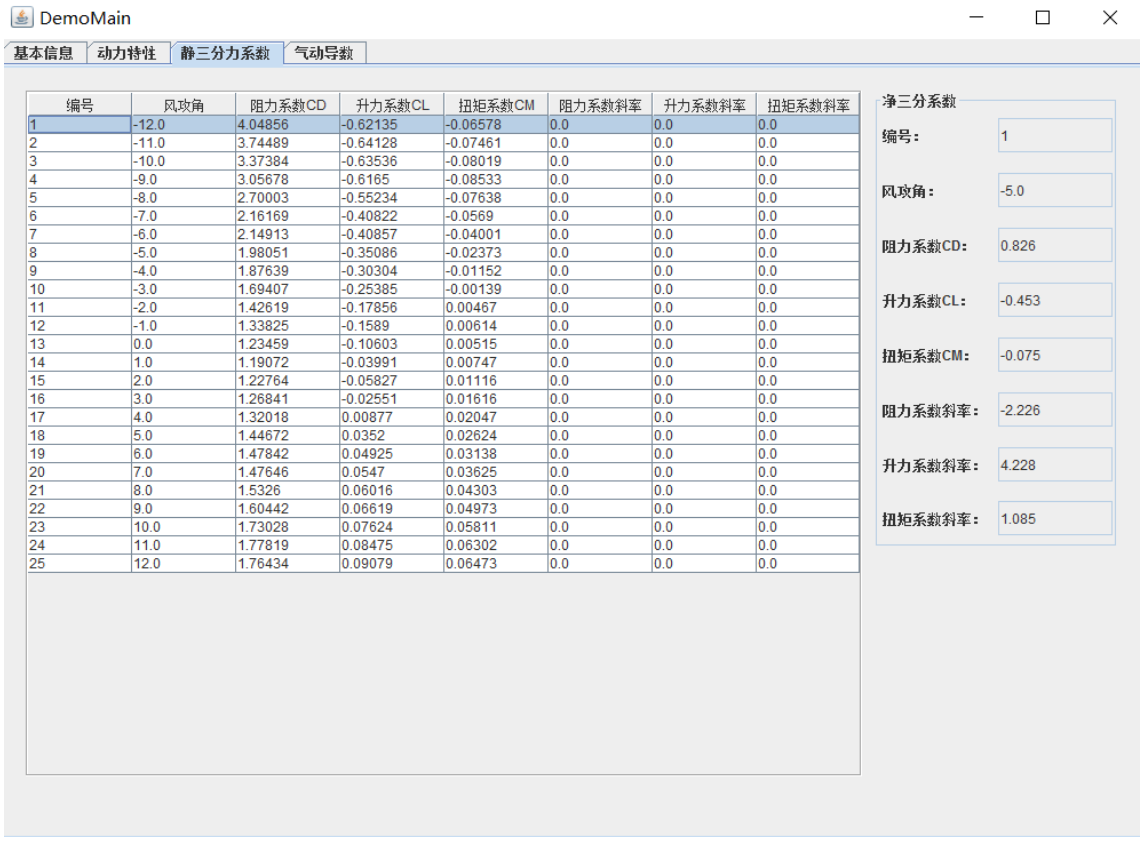

(d) Window of aerostatic coefficients

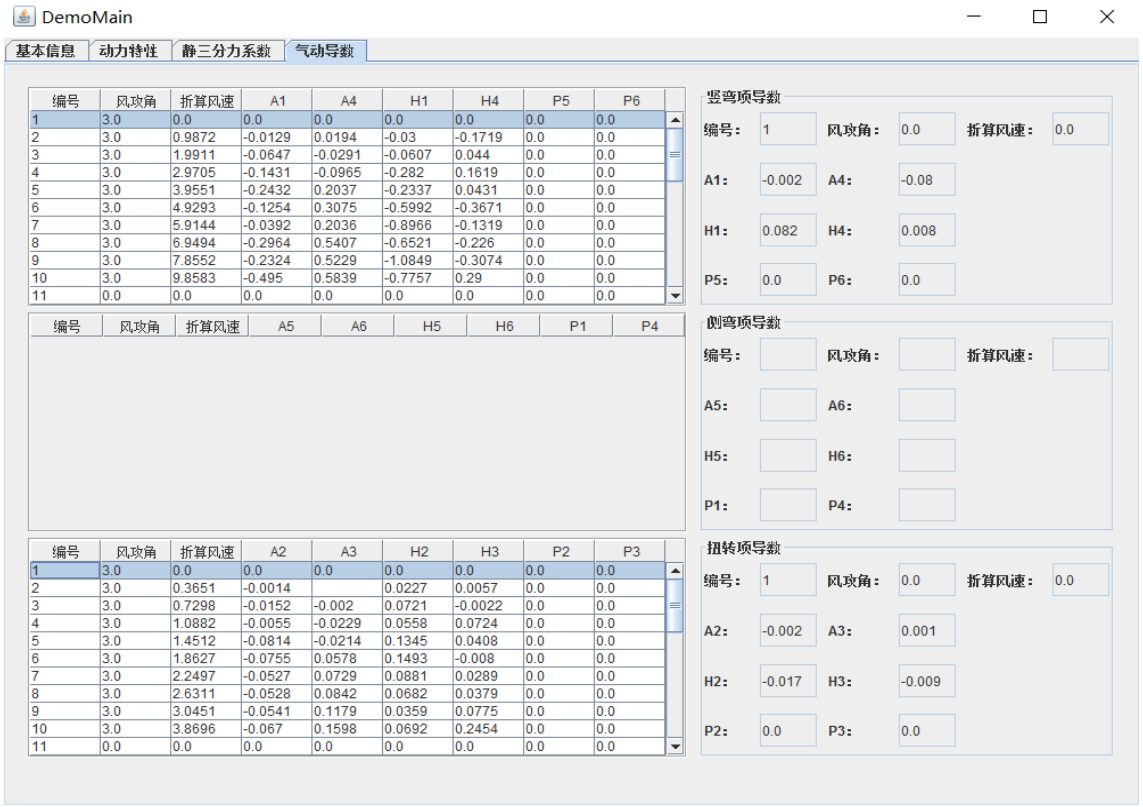

(e) Window of flutter derivatives

Figure 2.3: Design effect of each window

2.3.3 Application functions implementation

The application for this project contains mainly functions for viewing, modifying and saving data. After running the published program, the underlying Access database file will first need to be loaded (there is no requirement for a file path), as shown in Figure 2.4. After successfully selecting the matching underlying database, the data needs to be filtered for display. There are three filtering conditions, as explained above, and the program will filter the data to meet the requirements based on the conditions selected by the user.

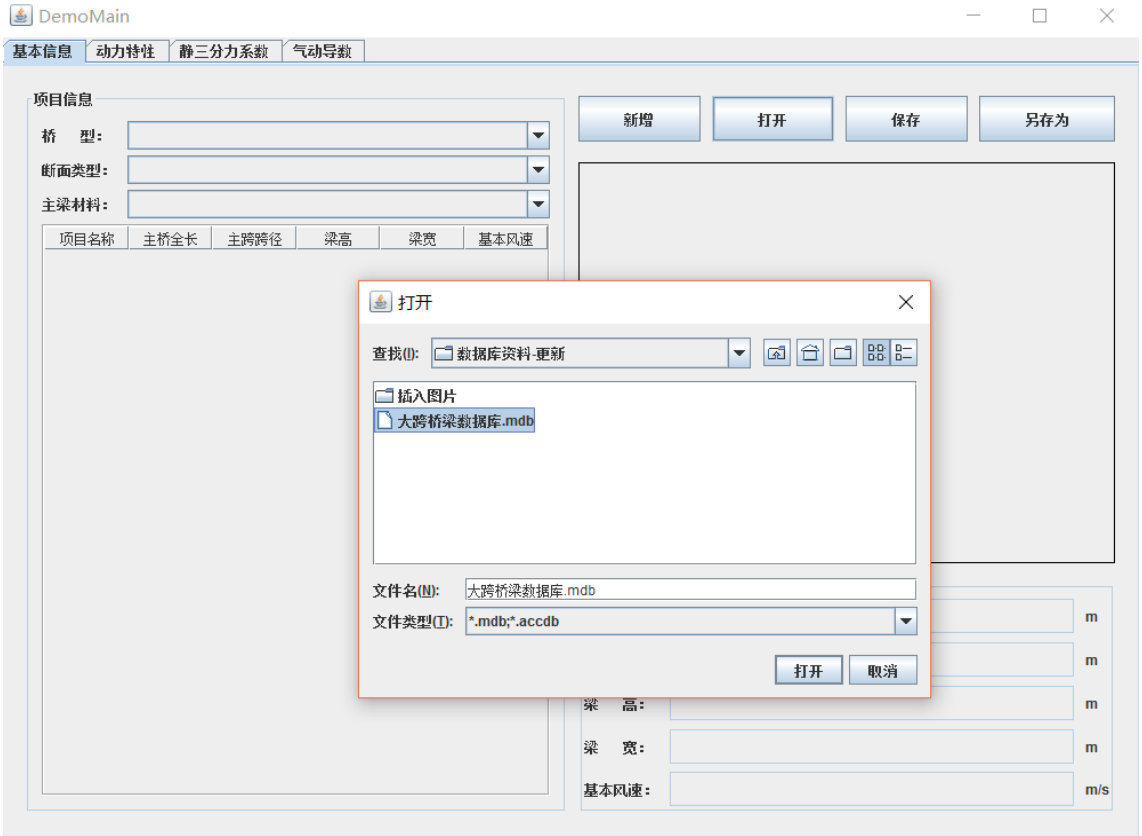

Figure 2.4: Data loading interface

At present, the modification of data can only be carried out in the underlying Access database. The modification operations in the application interface are not supported. Data can be saved in part or in full. The program has a default save path, and the user can also save the data as any specified path. The main code for Java to manipulate the database is shown below:

```
public static JSONArray ListInformation(String dbname,String query) {
    try {
        JSONArray array = new JSONArray();
        connetDBAbsolute(dbname);
        executeSql(query);
        ResultSetMetaData metaData = rs.getMetaData();
        int columnCount = metaData.getColumnCount();
        while (rs.next()) {
            JSONObject jsonObj = new JSONObject();
            for (int i = 1; i <= columnCount; i++) {
                String columnName = metaData.getColumnLabel(i);
                String value = rs.getString(columnName);
                jsonObj.put(columnName, value);
```

```
                }
                array.add(jsonObj);
            }
            closeConnection();
            return array;
        } catch (Exception e) {
            e.printStackTrace();
            return null;
        }
}
public static void insert(String dbname,JSONObject jsonObject) {
        try {
            Object key,value;
            connetDBAbsolute(dbname);
            System.out.println("另存为数据库成功");
            String sqlquery1 = "INSERT into  表 1(";
            String sqlquery2 = ") values(";
            String sqlquery3 = ");";
            Iterator iterator = jsonObject.keys();
            while(iterator.hasNext()){
                key = iterator.next();
                value = jsonObject.get(key);
                sqlquery1+=key+",";
                sqlquery2+="'"+value+"',";
            }
            sqlquery1 =sqlquery1.substring(0,sqlquery1.length()-1);
            sqlquery2 = sqlquery2.substring(0,sqlquery2.length()-1);
            String sqlquery=sqlquery1+sqlquery2+sqlquery3;
           sql.executeUpdate(sqlquery);
            closeConnection();
        } catch (Exception e) {
            e.printStackTrace();
        }}
```

2.4 Conclusion

The wind-resistance database of long-span bridges involved in this study was developed in a C/S mode using Access as the underlying database system and Java programming language for the development of foreground visualization application. The test data of 99 long-span bridges from the wind tunnel laboratory of Tongji University were collected and stored in the database after sorting and filtering. All the data can be summarized into three modules: basic information, aerodynamic characteristics and aerodynamic parameters. The development of foreground application was carried out, which mainly implemented the functions of filtering, viewing, modifying and saving data for the user's visualization. The foreground application is connected to the database using a local protocol driven approach to achieve the independence of platform.

CHAPTER 3

3 Dataset of Closed Box Girders

3.1 Background

In this section, the aerodynamic parameters and wind-resistant performance of a typical cross-section, steel closed box girder, of long-span bridges are studied. The architecture of the cross-section of the standard closed box girder is shown in Figure 3.1, which can be described by five dimensions, including box width B, box depth H, wind fairing width b, wind fairing angle θ and web inclined angle β. In 1966, closed box girder cross-section was firstly adopted in Seven Bridge in UK. In the following 50 more years, this type of cross-section was widely used in the design and construction of long-span bridges, in particular in long-span suspension bridges. For later machine learning modeling, it is necessary to establish a special sample set of aerodynamic parameters of closed box girder, including the dimension of cross-section, wind attack angle, wind speed, aerodynamic parameters, etc. In this chapter, two types of sample sets will be established: hybrid dataset and pure numerical simulation dataset. The hybrid dataset includes 20 sets of wind tunnel test data of long-span bridges with closed box girders from the self-built wind-resistance database, and 20 sets of numerical simulation data from open-source literature, as well as another 14 sets of supplementary data. All these samples will be re-calculated by CFD numerical simulation to form the pure numerical simulation dataset, so as to obtain the better data condition.

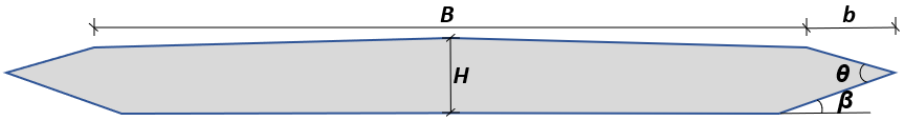

Figure 3.1: Architecture of standard closed box girder

3.2 Dataset collection

3.2.1 Wind tunnel test data

In this study, wind tunnel test data for 20 bridges with closed box girder were selected from the self-built wind-resistance database of long-span bridges introduced in Chapter 2. Specific dimensions involved are listed in Table 3.1 and covered with box width B=18-50m, box depth H =2.0-5.8m, wind fairing length b=0.6-5.5m, wind fairing angle θ=39-79° and web inclined angle β=8-26°, and the aerostatic coefficients and the flutter derivatives under different wind attack angles and different reduced wind speeds are listed in Appendix B.

In general, based on the vibration state of the sectional model, there are three methods of identifying flutter derivatives in the wind tunnel tests: forced vibration (Li et al., 2022), free vibration (Fang et al., 2020) and random vibration (Qin and Gu, 2005). Each of these methods can be divided into two types: time domain and frequency domain. Commonly, the coupled free vibration method was the preference to extract the bridge flutter derivatives in wind tunnel tests due to its instrumental simplicity and operational convenience (Ding et al., 2010; Sarkar et al., 1994; Xu et al., 2014). A series of methods

were developed over the past several decades based on the free decay time histories of the bridge deck at various wind speeds (Chowdhury and Sarkar, 2003; Yamada et al., 1992).

Table 3.1: Geometric size of collected 20 sets of cross-sections with wind tunnel tests

Section No.	B (m)	H (m)	b (m)	θ (°)	β (°)
1	35.2	3.535	1.79	40	15
2	28.5	3.0	0.97	60	8
3	30.0	3.5	2.0	39	14
4	46.7	5.83	1.66	63	18
5	40.8	3.5	0.6	72	13
6	33.5	2.875	2.9	50	20
7	36.2	3.8	0.9	71	20
8	40.0	3.74	2.25	48	21
9	45.2	3.0	1.15	64.8	18.6
10	43.0	2.0	1.0	55.8	10.8
11	30.0	5.0	5.5	49	24
12	36.9	3.6	1.0	66	14
13	43.0	3.0	1.0	62	16
14	30.4	3.5	0.6	73	23
15	18.0	2.5	1.8	48	22
16	50.0	2.5	0.8	60	10
17	44.0	4.5	1.0	79	26
18	33.5	3.0	1.7	48.1	19.9
19	38.0	4.0	1.3	59	15
20	28.6	3.5	0.7	72.6	17.6
Range	**18.0-50.0**	**2.0-5.8**	**0.6-5.5**	**39-79**	**8-26**

The 20 sets of experimental data selected in this paper are all derived from the free vibration wind tunnel tests of sectional models, and the unifying least square method developed by Gu et al. (2000) and improved by Bartoli et al. (2009), Ding et al. (2010) and Li et al. (2003) was utilized to extract the flutter derivatives in wind tunnel tests, which was referred to as the modified unifying least square (MULS) approach. At each wind speed, the two DOFs free decay displacements, that is, *h(t)* and *α(t)* were mathematically superposed with two displacement modes as

$$h(t)=\sum_{i=h,\alpha}h_i(t)=\sum_{i=h,\alpha}A_{hi}e^{-\omega_i\zeta_i t}\cos\left(\omega_i\sqrt{1-\zeta_i^2}t+\theta_{hi}\right) \tag{3.2.1a}$$

$$\alpha(t)=\sum_{i=h,\alpha}\alpha_i(t)=\sum_{i=h,\alpha}A_{\alpha i}e^{-\omega_i\zeta_i t}\cos\left(\omega_i\sqrt{1-\zeta_i^2}t+\theta_{\alpha i}\right) \tag{3.2.1b}$$

where A_{di} and θ_{di} ($d = h, \alpha$; $i = h, \alpha$) = the amplitudes and phases information for each mode, which were determined by the initial conditions; ω_i and ζ_i = the natural frequencies and damping ratios.

3.2.2 Numerical simulation data

Due to the significant fluctuation of the flutter derivatives changing with the reduced wind speed measured by wind tunnel tests, and sometimes different test conditions or identification methods will produce very different results, machine learning method is difficult to extract potential input-output relationship from only 20 sets of wind tunnel test data. Therefore, another 20 sets of numerical simulation data of flutter derivatives from open-source literatures are collected to jointly drive the training process of machine learning. The specific dimensions of these 20 sets of cross-sections are listed in Table 3.2 and covered with box width B=12-45.2m, box depth H =2.0-4.39m, wind fairing length b=0.15-4.2m, wind fairing angle θ=30-101.4° and web inclined angle β=9.8-27.1°. The flutter derivatives under different reduced wind speeds are listed in Appendix B. These 20 sets of collected numerical simulation results are mainly for flutter derivatives, and only a small number of them also provide numerical simulation results for the aerostatic coefficients.

Table 3.2: Geometric size of collected 20 sets of cross-sections with numerical simulation results

Section No.	***B*** (m)	***H*** (m)	***b*** (m)	***θ*** (°)	***β*** (°)
21 (Wang, 2018)	38.5	4.39	1.25	65.3	12.26
22 (Wang, 2003)	38.0	3.5	1.3	59.1	17.2
23 (Zhu, 2014)	12.0	2.0	0.9	50.8	22.2
24 (Zhang, 2016)	29.7	3.9	0.15	101.4	17.84
25 (Qi, 2013)	27.0	4.3	2.0	53.6	27.1
26 (Bai et al., 2011)	45.2	3.1	2.44	36.4	9.8
27 (Hong, 2012)	35.5	3.5	3.1	34.7	18.5
28 (Zhu, 2017)	29.9	3.0	0.8	79.1	19.95
29 (Bai and Ou, 2009)	26.0	2.8	1.7	40.9	15.7
30 (Hao, 2011)	35.5	3.5	2.18	44	21
31 (Jiao, 2009)	35.0	3.5	1.8	48.6	20.77
32 (Fu, 2016)	41.0	3.5	0.5	76.7	13.12
33 (Peng, 2012)	23.2	3.36	1.92	48.1	19.28
34 (Gao, 2013)	35.3	3.54	4.2	30	15.6
35 (Pang, 2007)	45.2	3.0	1.152	65	19
36 (Hong, 2019)	31.1	2.8	1.8	43.1	16.5
37 (Lv et al., 2011)	39.0	2.0	3.0	37	18
38 (Zhang, 2008)	33.9	3.0	1.8	47.7	21.14
39 (Xia, 2011)	35.5	3.54	3.12	38.2	18.15
40 (Chao, 2015)	35.9	3.5	1.3	59.5	11.42
Range	**12.0-45.2**	**2.0-4.39**	**0.15-4.2**	**30-101.4**	**9.8-27.1**

The CFD numerical simulation method is to discretize the calculation domain and realize the solution of fluid control equation, so as to carry out the numerical calculation for various fluid problems.

Similar to wind tunnel test, there are also three methods of identifying flutter derivatives in CFD numerical simulation: free vibration (Zhu and Gu, 2007), forced vibration (Xu and Zhang, 2017) and random vibration (Wang, 2008). Among them, the free vibration method belongs to the bidirectional fluid-structure coupling. Firstly, the aerodynamic characteristics of structure and the boundary conditions of flow field are defined and an initial condition is imposed. The time domain is discretized into multiple time steps. The dynamic equation is solved in each time step and the motion state and force condition at the end of each step are taken as the initial conditions of the next time step. In this way, the motion state and force time history of the cross-section during the whole vibration process can be obtained (Ding et al., 2012; Xu, 2015; Xu and Zhang, 2017). There are some difficulties in the realization of the free vibration method, and there are also great difficulties in the identification of flutter derivatives. The forced vibration method is to solve the flow field characteristics by vibrating the cross-section according to the established motion pattern. At the same time, the time history of the unsteady aerodynamic self-excited force of the cross-section is monitored so as to solve and fit the aerodynamic force expression to obtain the results (Niu and Chen, 2014; Zhang, 2016; Zhu, 2017; Zhu et al., 2005). The forced vibration method avoids solving the motion equation, which saves time and is easy to realize by software. Therefore, the numerical identification of flutter derivatives is mainly based on the sub-state forced vibration method at present. The structure is forced to vibrate at a certain frequency in the single DOF. The aerodynamic forces can be obtained and the least square method is used for the exaction of flutter derivatives.

3.2.3 Supplementary data

Figure 3.1 shows the geometric shape parameters of a standard closed box girder: box width B, box depth H, wind fairing width b, wind fairing angle θ and web inclined angle β. These parameters can determine a unique shape of closed box girder. Since this study focuses on the machine learning prediction of aerostatic coefficients and flutter derivatives of closed box girders. The value range of shape parameters of cross-sections in the sample set will have a decisive impact on the prediction results. The existing 40 sets of data are not uniform in terms of dimensions such as box width, box depth, etc. Besides, considering the actual requirements of the bridge structure, each aerodynamic shape parameter has a concentrated distribution range, so the representativeness of the existing data is also not good enough. For example, most of wind fairing angles used in projects are between 45° and 60°; Most of web inclined angles are between 15° and 25°, and 11° and 32° are also often used in engineering (Chen, 2016). Based on the above considerations, additional 14 sets of cross-sections are added in this study, whose size distributions remain within these concentrated distribution ranges and fill in the gaps in some size ranges. The specific dimensions of these 14 sets of cross-sections are listed in Table 3.3 and covered with box width B=25.5-59.5m, box depth H =12-28m, wind fairing length b=0.6-2.1m, wind fairing

angle θ=37-70° and web inclined angle β=12-28°. Therefore, a total of 54 sets of closed box girder cross-sections form a data sample set for machine learning training. The distribution of these 54 sets of cross-sections is shown in Figure 3.2.

Table 3.3: Geometric size of supplementary 14 sets of cross-sections

Section No.	B (m)	H (m)	b (m)	θ (°)	β (°)
41	30.5	3.0	1.7	57	28
42	29.5	3.0	1.5	57	17
43	34.3	3.2	1.5	50	13
44	26.2	2.8	0.7	70	20
45	25.5	3.0	1.5	51	19
46	51.4	5.0	1.5	57	14
47	54.0	5.8	2.0	65	15
48	32.8	3.2	0.6	60	12
49	39.1	4.6	2.1	53	23.5
50	42.8	4.5	2.0	53	17.5
51	41.8	4.4	2.0	53	16.5
52	58.1	4.3	1.9	43	16.5
53	56.7	4.2	1.9	43	11.5
54	59.5	4.1	1.8	37	16.5
Range	**25.5-59.5**	**2.8-5.8**	**0.6-2.1**	**37-70**	**12-28**

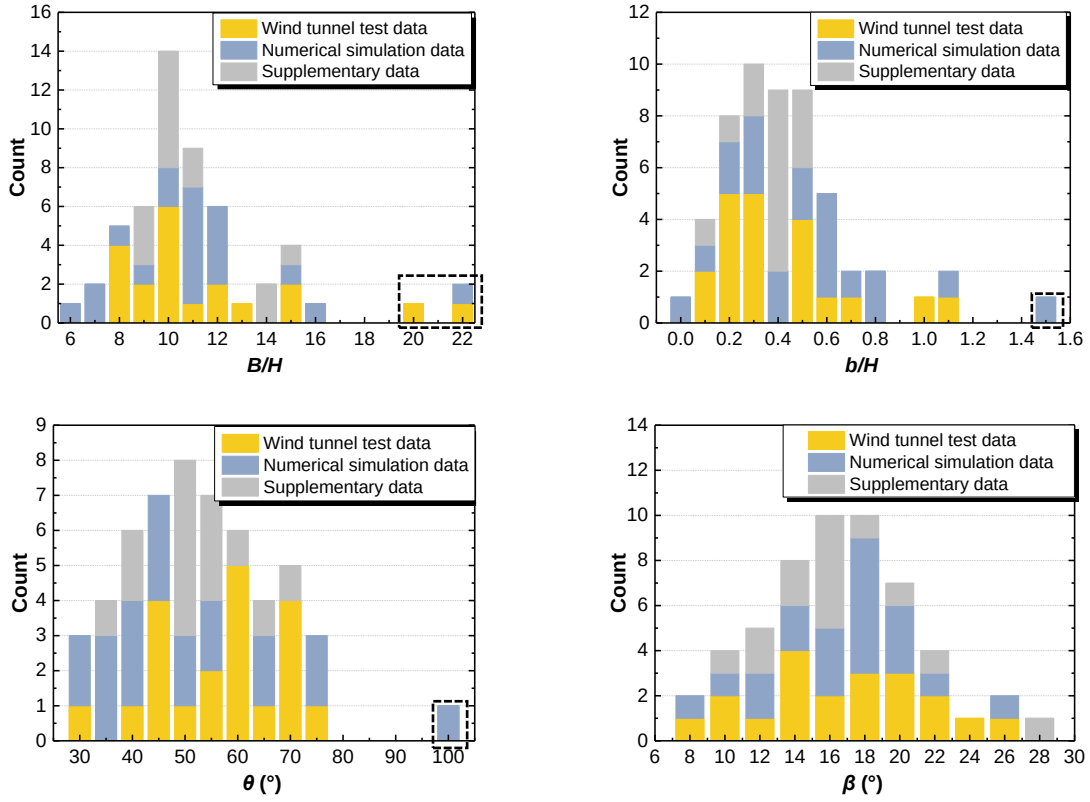

Figure 3.2: Cross-section distribution histogram of sample set

3.3 CFD numerical simulation

In order to obtain better machine learning effect of training and prediction, all collected and supplemented closed box girder cross-sections were calculated by CFD numerical simulation to obtain the aerostatic coefficients and flutter derivatives with good data conditions. This research uses single degree of freedom step-by-step forced vibration with multi frequencies, that is, the two degrees of freedom of cross- section motion are decoupled, and the model is designated to perform vertical and torsional motions respectively. Based on Scanlan's theoretical framework of superposition of linear self-excited forces, it is assumed that the model performs multi frequency forced vibration of single degree of freedom:

$$h(t) = \sum_{i=1}^{n} h_0 \sin(2\pi f_i t) \tag{3.3.1a}$$

$$\alpha(t) = \sum_{i=1}^{n} \alpha_0 \sin(2\pi f_i t) \tag{3.3.1b}$$

where h_0 and α_0 are the vertical bending and torsional amplitudes, respectively. The flutter derivatives are obtained by identifying the amplitude of aerodynamic force and the phase difference between force and displacement through frequency domain method.

3.3.1 Models and parameters

The numerical calculation domain is a two-dimensional flow field. Pointwise is used for geometric rendering and mesh generation, and ANSYS Fluent is used for numerical simulation. The Reynolds number of each sectional rigid model is the same as that of the corresponding wind tunnel test. The calculation domain is shown in Figure 3.3. The numerical calculation domain is 15B in depth and 28B in width. The center of the closed box girder cross-section is 10.5B away from the inlet, 17.5B from the exit, and 7.5B from the upper and lower boundaries. The left inlet boundary of the computational domain is set as the velocity inlet and the right outlet boundary is set as the pressure outlet.

The identification of flutter derivatives requires the use of the dynamic mesh technique. Considering that the number of the mesh should be controlled to reduce the computational resources, the computational domain is divided into three sub-regions and different mesh types are used in different regions. The body-fitted mesh around the closed box girder is the fine structured mesh with high computational accuracy. This region contains the main turbulent boundary layer near the cross-section, which can more accurately capture the flow characteristics in the near-wall region. Unstructured mesh is used for the transition region. The outermost region extending to the boundary of the computational domain is the sparse structural quadrilateral mesh. According to different cross-sections and flow fields, the number of the mesh of different models varies from 550000 to 650000. Figure 3.4 shows some

details of mesh meshing by zooming in the mesh around the cross-section. The tests of independence for mesh size and time step are performed to verify that the numerical simulation results are unaffected by mesh and time discretization.

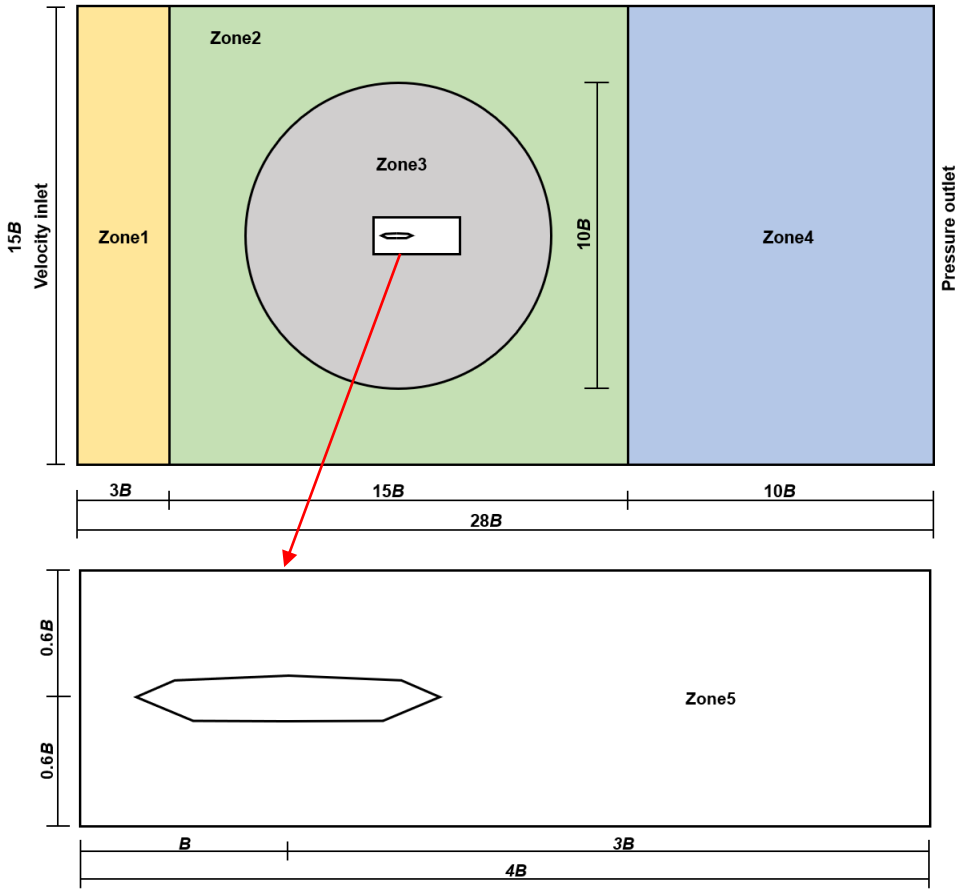

Figure 3.3: Design scheme of computing domain

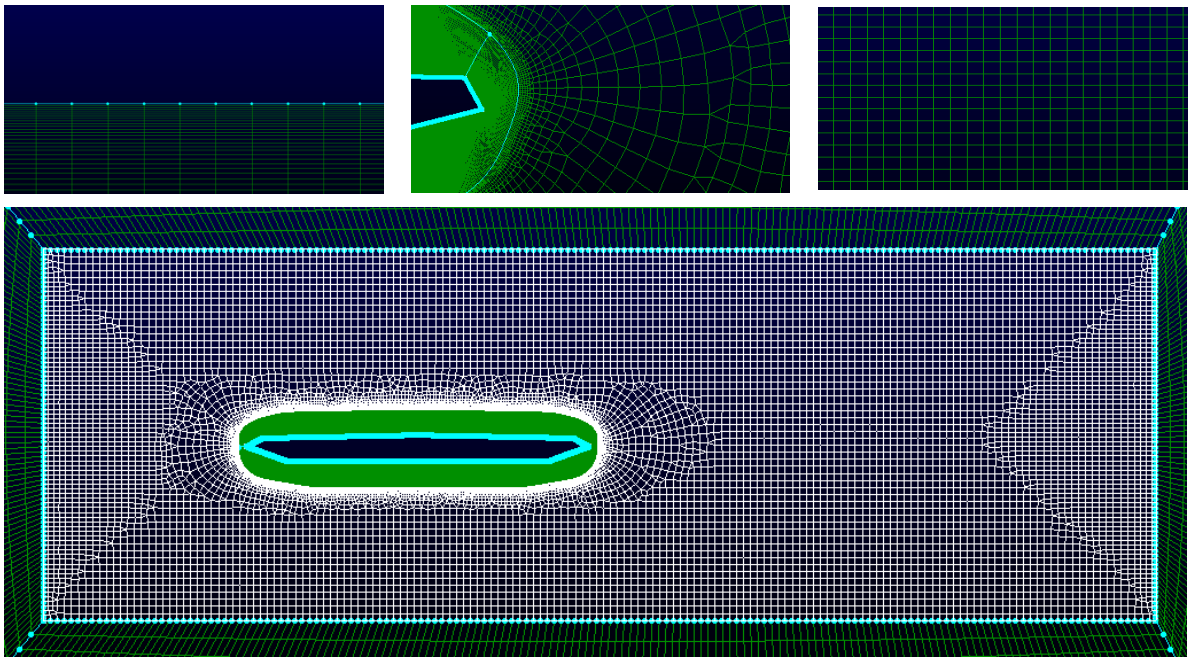

Figure 3.4: Flow field meshing

SST K-ω turbulence model is used in this study because the external flow field simulation requires high accuracy in the near wall region of the structure. SST k-ω turbulence model can not only make full use of the characteristics of k-ω model sensitive to inverse pressure, but also overcome the defect of k-ω model sensitive to free flow conditions, so as to improve the stability of the model (Yakhot and Orszag, 1986). The SIMPLEC algorithm is adopted for the coupling of pressure and velocity. The second-order upwind scheme is adopted for the convection term, and the second-order central difference scheme is adopted for the diffusion term. Firstly, the steady-state calculation is adopted, and then the stable results are obtained iteratively as the initial values of the transient calculation. In this paper, the aerostatic coefficients at -6°~6° wind attack angle and the flutter derivatives at 0° wind attack angle of each cross-section are calculated, and all the numerical simulation results are compared with the wind tunnel test or other calculation results to check the validity of the data.

3.3.2 Calculation results and verification

3.3.2.1 Aerostatic coefficients

The numerical simulation of 55 closed box girder cross-sections was carried out in this study. Figure 3.5 shows of the change of drag coefficient, lift coefficient and moment coefficient under the wind axis within the range of -6°~6° wind attack angle of two of the cross-sections. Figure 3.5(a) shows the comparison between the numerical simulation results and the wind tunnel test results of cross-section 1 (as shown in Table 3.1) from database. Figure 3.5(b) shows the comparison between my numerical simulation results (CFD1) and other researcher's calculation results (CFD2) (Wang, 2018) of cross-section 21 (as shown in Table 3.2) from literature.

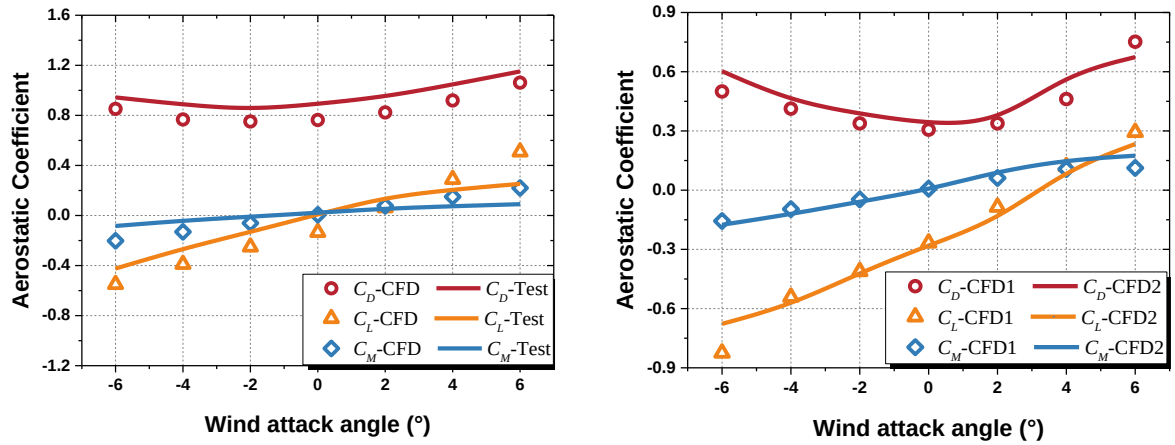

(a) Cross-section 1 (b) Cross-section 21

Figure 3.5: Trend of aerostatic coefficients changing with wind attack angle

It can be seen from Figure 3.5 that the results calculated by fluent are in good agreement with the wind tunnel test results and other researcher's calculation results. The drag coefficients are all in the positive range, which is consistent with the actual situation. The lift coefficient increases with the increase of wind attack angle in the range of -6°~6° and the change trend is almost linear. The order of

magnitude of moment coefficient is small, and the value range is between -0.3 and 0.3. The change trend of moment coefficient shows a symmetrical trend. The cross-section within the negative wind attack angle is subject to negative bending moment, and the cross-section within the positive wind attack angle is subject to positive bending moment.

3.3.2.2 Flutter derivatives

Figure 3.6 shows the trend of 8 flutter derivatives of two cross-sections changing with the reduced wind speed under 0° wind attack angle. Like the aerostatic coefficients, Figure 3.6(a) shows the comparison between the numerical simulation results and the wind tunnel test results of cross-section 1 (as shown in Table 3.1) from database. Figure 3.6(b) shows the comparison between my numerical simulation results (CFD1) and other researcher's calculation results (CFD2) (Wang, 2018) of cross-section 21 (as shown in Table 3.2) from literature. It can be seen from the figures that the numerical simulation results of section 1 fit well with the wind tunnel test results. Except for the slight deviation between the calculation results and the test results of H_2^* and H_4^* (which is caused by the test error is not excluded), the calculation results of the other flutter derivatives are consistent with the test results. The numerical simulation results of section 21 are compared with those of other researchers. The overall trend of each flutter derivatives in both is consistent.

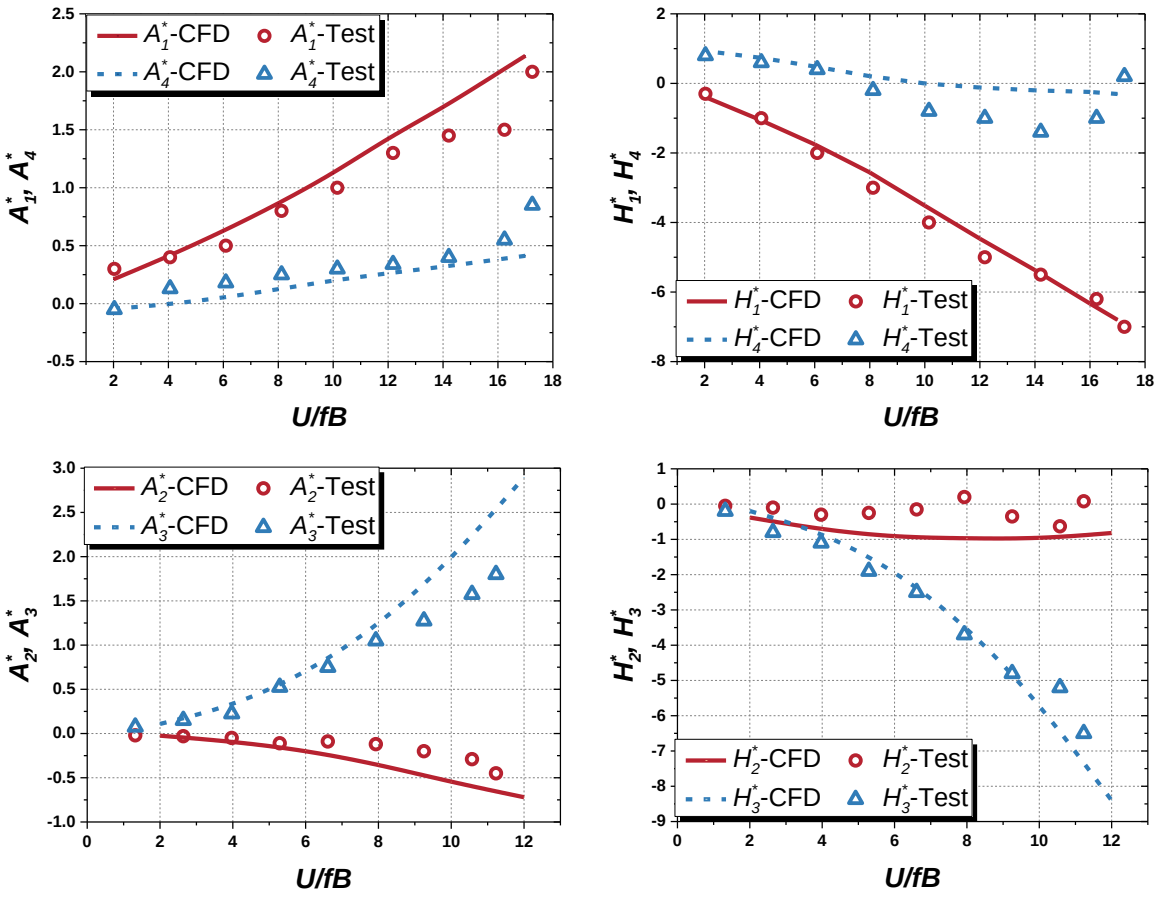

(a) Cross-section 1

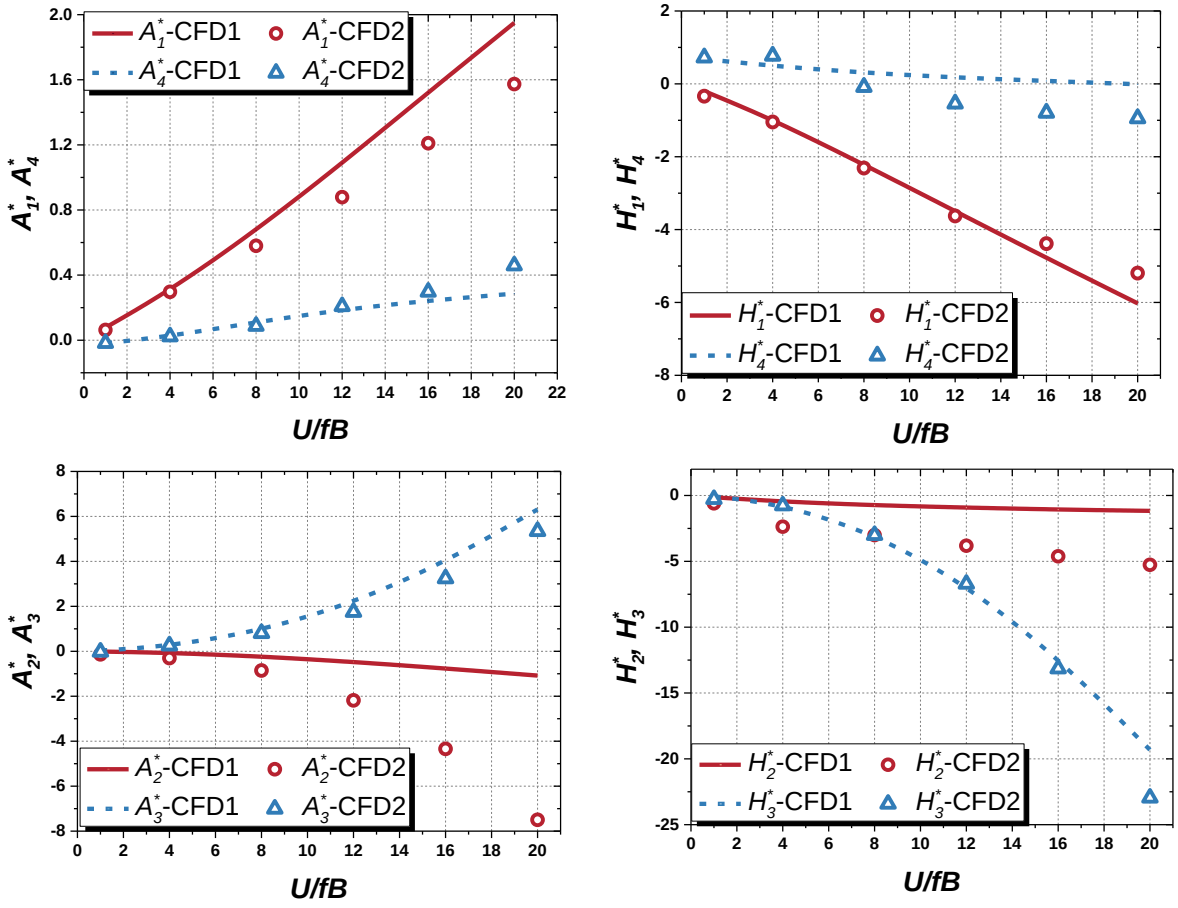

(b) Cross-section 21

Figure 3.6: Trend of flutter derivatives changing with reduced wind speed

The above verification and analysis process is applicable to all other selected or designed cross-sections. All the calculation results are shown in Appendix C. In the following, these numerical simulation data will be used for machine learning training and prediction, so as to form an intelligent identification method for aerodynamic parameters.

3.4 Conclusion

There are two types of training samples for the machine learning prediction of aerodynamic parameters of bridges to be carried out later. One type of sample sets contains hybrid data, which includes of 20 sets of wind tunnel test data from database, and 20 sets of numerical simulation data from open-source literature, as well as 14 sets of supplementary data.

In order to obtain a better machine learning prediction effect, these 54 sets of samples are re-calculated by CFD numerical simulation based on the shape of cross-section and quality system of structure to obtain the aerostatic coefficients and flutter derivatives so as to form another type of sample set with good data conditions. The re-calculation results are compared with the wind tunnel test results or other researchers' calculation results to check the validity of the new dataset.

CHAPTER 4

4 Intelligent identification of aerodynamic parameters

4.1 Background

This study deals with the analysis of aerostatic stability and flutter stability of bridges, and this chapter focuses on intelligent identification of aerostatic coefficients and flutter derivatives. The traditional means of identifying aerodynamic parameters are wind tunnel test or numerical simulation. There are three methods of identifying aerodynamic parameters by wind tunnel tests: forced vibration, free vibration and random vibration. Each of these techniques falls into one of two categories: time domain or frequency domain. The numerical simulation approach is the other technique to examine wind-induced effects of bluff bodies by discretizing the calculation domain and realizing the solution of fluid control equations. The identifications of aerodynamic parameters can all be made similarly to wind tunnel tests using CFD.

In this chapter, machine learning methods will be used for intelligent identification of aerostatic coefficients and flutter derivatives, rather than traditional identification methods with wind tunnel or numerical simulation. Typical machine learning methods mainly include decision trees, random forests, artificial neural networks and Bayesian learning. Deep learning algorithms, which have been widely used in recent years, can actually be regarded as deep machine learning methods. As the data samples relied on this study do not fit the characteristics of big data, serious overfitting problems would arise if deep learning methods were used, the modelling and analysis in this paper are only in a shallow machine learning framework. A variety of shallow machine learning algorithms are attempted in this study, involving error artificial neural network, support vector machine, decision tree, etc. This chapter will focus on the improved error back propagation (EBP) neural network, support vector regression (SVR), gradient boosting decision tree (GBDT) and their comparison.

4.2 Machine learning methods

4.2.1 Artificial neural network (ANN)

An artificial neural network is an operational model consisting of a large number of nodes (neurons) connected to each other. Each node represents a particular output function, which can be called the excitation function, and the connection between every two nodes represents a weight. The network is usually an approximation of an algorithm, or it can be an expression of some expression of a logical strategy. The output of the whole network depends on the connections, weights and excitation functions. Macroscopically, an artificial neural network consists of an input layer, one or more hidden layers and an output layer, as shown in Figure 4.1. Its most important feature is the ability to learn, which is recorded in the connection weights, and the algorithm for correcting the weights is called a learning rule.

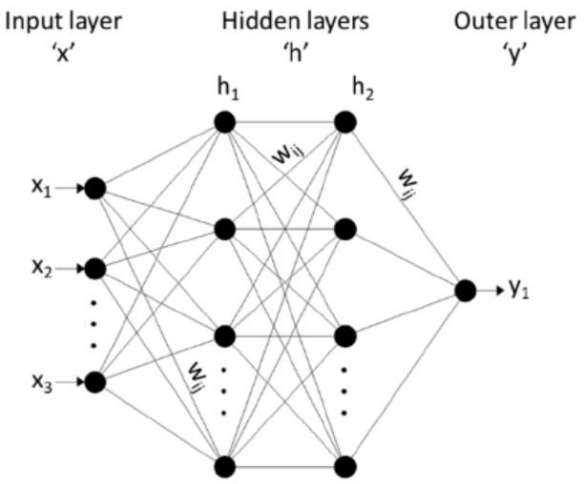

Figure 4.1: Architecture of artificial neural network

The most common learning rule used today is the error back propagation (EBP) algorithm. It was proposed by Rumelhart and McClelland (1986), and it has been mathematically proven that a three-layer EBP neural network with a hidden layer can approximate any mapping function. The basic idea of EBP neural network is to continually modify the connection weights between the various artificial neurons that make up the forward multi-layer network, so that the network can convert the input information into expectations. The reason why it is called back learning algorithm is that when it modifies the connection weight of neurons, it is based on the difference between the actual output and the expected output, and the difference is back-propagated layer by layer to modify the connection weight. The process of continuously adjusting the weights is also the training process of neural network. The key to the EBP algorithm lies in the training rules of the hidden layer, which is equivalent to a feature extractor for the input information. This whole training process continues until the output error given by the network is reduced to an acceptable range, or until the preset training time.

The key to the EBP algorithm lies in determining an approach or principle for adjusting the connection weights so that the error of the network follows a reduced direction. Specifically, an appropriate excitation function, for example, sigmoid function, needs to be applied to the output N of a neuron to obtain the output signal U:

$$U = 1/(1+e^{-N}) \tag{4.2.1}$$

The target value of a neuron is subtracted from its actual output and multiplied by the derivative of the excitation function to obtain the value of δ:

$$\delta = U(1-U)(T-U) \tag{4.2.2}$$

where T is the target value for the neuron. The weights of the output layer are adjusted as follows:

$$\Delta W_{pq}^{(2)} = \eta \delta_q^{(2)} U_p^{(1)} \tag{4.2.3a}$$

$$\Delta W_{pq}^{(2)}(n+1) = W_{pq}^{(2)}(n) + \Delta W_{pq}^{(2)} \tag{4.2.3b}$$

where $\Delta W_{pq}^{(2)}$ and $\Delta W_{pq}^{(2)}(n+1)$ denote the values of the connection weights from the pth neuron in the hidden layer to the q^{th} neuron in the output layer at the nth and $(n+1)^{\text{th}}$ steps. $\delta_q^{(2)}$ is the value of δ for the q^{th} neuron in the output layer, $U_p^{(1)}$ is the value of U for the p^{th} neuron in the hidden layer, and η is the training speed factor to adjust the magnitude of the change in weights.

These weights are back propagated to produce the δ values of the neurons in previous layer:

$$\delta_p^{(1)} = U_p^{(1)}(1-U_p^{(1)})(\sum_q \delta_q^{(2)} W_{pq}^{(2)}) \tag{4.2.4}$$

Then errors are back propagated layer by layer until the adjustment of weights for each layer is completed.

4.2.2 Support vector machine (SVM)

The basic theory of support vector machine (SVM) was established by Vapnik in 1995 and it is welcomed and developed rapidly for its good generalization ability. The SVM algorithm is based on the principle of structural risk minimization. This principle has been proven to be superior to the traditional principle of empirical risk minimization. The empirical risk minimization is to minimize the error of the model to the training set, but the structural risk minimization is to minimize the upper bound of the expected risk. This difference makes SVM have better generalization ability, which is also the ultimate goal of statistical learning. The basic idea of SVM in solving nonlinear problems is to map the input vector x to a high-dimensional feature space through some nonlinear mapping, and construct the optimal separation plane in this high-dimensional feature space Z, as shown in Figure 4.2. SVM was originally created to solve the classification problem, known as support vector classification (SVC). Its purpose is to find an optimal hyperplane to separate the sample points and maximize the interval. In recent years, the research on SVM has been extended to regression problems. It is called support vector regression (SVR), and its goal is to find a linear regression equation to fit all sample points and minimize the total variance of the sample points from the hyperplane.

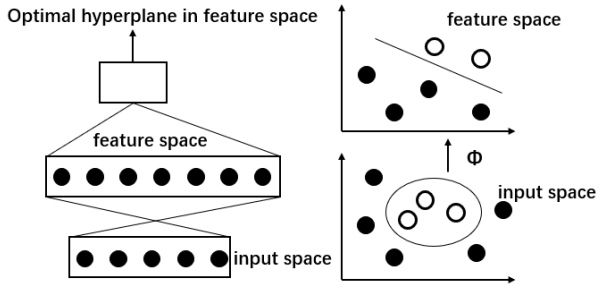

(a) Mapping relationship between input space and high-dimensional feature space

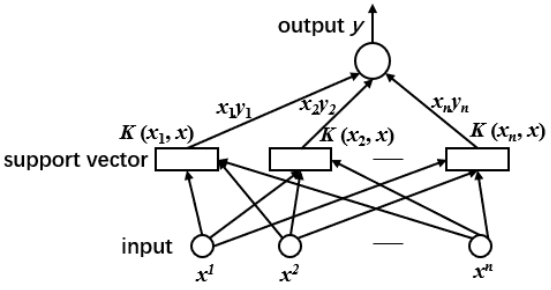

(b) Support vector machine structural network

Figure 4.2: Architecture of support vector machine

When performing support vector regression fitting, the data sample can be expressed as $\{(x_1, y_1),...,(x_n, y_n)\}$, $x_i, y_i \in R$, and the learning goal is to use the training data set regression to obtain

the optimal estimation of the objective function f_0. The linear regression function form is used in the regression equation $f(x)$ first:

$$f(x) = \langle w, \Phi(x) \rangle + b \tag{4.2.5}$$

where $w \in R^d$, $b \in R$, d is the dimension of the feature space, < , > represents the dot product, and Φ represents the nonlinear mapping. The coefficient vector w determines the direction of the partition plane, and b determines the offset of the partition plane from the original position. The goal of this algorithm is to find appropriate w and b to minimize the following ε-loss function:

$$\min \ \frac{1}{2}\|w\|^2 + C\sum_{i=1}^{M}(\xi_i + \xi_i^*) \tag{4.2.6}$$

The constraints are as follows:

$$y_i - \langle w, \Phi(x) \rangle - b \le \varepsilon + \xi_i \tag{4.2.7a}$$

$$\langle w, \Phi(x) \rangle + b - y_i \le \varepsilon + \xi_i^* \tag{4.2.7b}$$

$$\xi_i, \xi_i^* \ge 0 \tag{4.2.7c}$$

where $y = A_{rms}^n$ is the measured objective function, C is a penalty parameter that needs to be specified and plays a role in adjusting the fitting error and the smoothness of the function, $\varepsilon \ge 0$ is an error limit to be specified and the obtained regression function should have an error no greater than that for any given sample. Each training sample has a set of relaxation factors $\xi_i = (\xi_1, \xi_2, ..., \xi_i)^T$ and $\xi_i^* = (\xi_1^*, \xi_2^*, ..., \xi_i^*)^T$ to determine whether the training sample is within or outside the error limit.

For nonlinear regression, the input vector xi of the input space is mapped to the vector of the high-dimensional feature space Z by using the nonlinear mapping $\phi: x_i \to z_i$, and then the optimal separation hyperplane is constructed in the high-dimensional feature space to obtain the effect of nonlinear regression in the original space. This requires computing the inner product in the high-dimensional feature space and defining the inner product as the kernel function. The linear classification after nonlinear transformation can be realized by using appropriate kernel function in the optimal classification plane, and the computational complexity does not increase (Chen and Guestrin, 2016).

4.2.3 Gradient boosting decision tree (GBDT)

The gradient boosting decision tree (GBDT) is an enduring model in machine learning since it has the advantages of good training effect and less overfitting on small and low-dimensional data. It is not sensitive to the absence of some features and its framework allows post-interpreters to be run for model representation and improvement. Its main idea is to use weak classifiers (decision trees) to iteratively train input data before obtaining the optimal model. The architecture is shown in Figure 4.3.

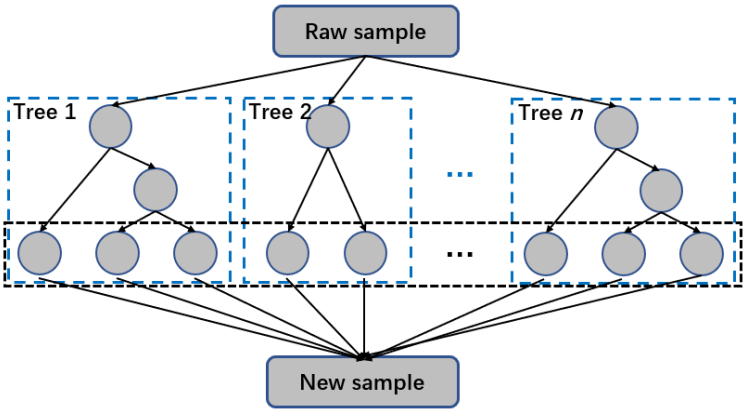

Figure 4.3: Architecture of gradient boosting decision tree

GBDT accomplishes the task of classification by defining a logarithmic loss function for logistic regression. To solve the problem of measuring the approximation of the loss function, gradient boosting algorithm uses the negative gradient of the loss function to fit the approximation of the loss and fits a classification and regression tree so that the loss in each round becomes as small as possible.

The minimum value of the loss function is:

$$C_{ij} = \arg\min \sum_{x_i \in R_{ij}} L(y_i, f_{t-1}(x_i) + c) \tag{4.2.8}$$

where the function L is a logarithmic loss function. x_i is the eigenvalue of the input, y_i is the output, and c is a constant. R_{mj} is the zone of the decision tree j domain and I, m, j are counting variables.

The decision tree fitting function is:

$$h_t(x) = \sum_{j=1}^{J} C_{mj} I(x) \quad (x \in R_{tj}) \tag{4.2.9}$$

where the function $I(x)$ is an indicator function that returns 0 when the equation in parentheses is false and 1 otherwise. J is the number of iterations.

The updated boosting decision tree is the sum of the previously fitting decision trees and the latest fitting function:

$$f(x) = f_{t-1}(x) + h_t(x) \tag{4.2.10}$$

GBDT can be used for classification and regression, and the principles of both are similar. A weak learner is generated in each round, and finally, we will get a strong predictive model through continuous accumulation. Based on the above definition of negative gradient loss function and update process, the entire GBDT regression process can be expressed as:

(1) Initialization:

$$f_0(x) = \arg\min \sum_{i=1}^{N} L(y_i, c) = \frac{1}{2} \log \frac{1+\bar{y}}{1-\bar{y}} \tag{4.2.11}$$

where $f_0(x)$ is the initial value of the algorithm, N denotes the length of the training set, $\bar{y}$ represents

the mean of outputs, and the others are defined as above.

(2) For each number of iteration rounds， m=1,2,…,M:

For training set: i=1,2,…,N, compute negative gradients:

$$r_{mi} = -\left[\frac{\partial L(y_i, f(x_i))}{\partial f(x_i)}\right]_{f(x)=f_{m-1}(x)} \tag{4.2.12}$$

Get the leaf node region of the m-th tree.

For j=1,2,…,J, compute:

$$C_{mj} = \arg\min \sum L(y_i, f_{m-1}(x_i) + c) \tag{4.2.13}$$

(3) Updating:

$$f(x) = f_M(x) = \sum_{m=1}^{M}\sum_{j=1}^{J} C_{mj} I \tag{4.2.14}$$

4.3 Identification of aerostatic coefficients

4.3.1 Input and output

The input of machine learning model represents the influencing factors of the problem, and the output is the prediction or classification result. When the machine learning method is used to study the aerodynamic characteristics of bridge, the section geometry is a key factor and the geometric dimensions of the cross-section must be used as the input of model. For closed box girders, five parameters can determine the unique cross-section, including B, H, b, θ and β as shown in Figure 3.1. Since the amount of data is not big in this study, without being able to increase the amount of data significantly, the dimensionality of the input parameters should be reduced as much as possible. Considering that aerodynamic parameters are dimensionless parameters that are only related to the shape of cross-section and are independent of the absolute size of cross-section, four shape feature parameters (B/H, b/H, θ, β) are finally used as input parameters for the model. Since the aerostatic coefficients are also closely related to the angle of wind attack, it is also necessary to add the wind attack angle as input. The total number of input layer neurons is therefore five. As the aerostatic coefficients are interchangeable between body-axis and wind-axis (the conversion modes between two axes are shown in Equation 1.1.3 and Figure 1.3), only one output is required in either case, which means that the number of neurons in the output layer is three. In this study, the aerostatic coefficients are identified separately, so the number of neurons in the output layer is actually only one. In general, the prediction results under wind-axis are better than those under body-axis, this is because the drag coefficient under wind-axis is always positive, while the drag coefficient under body-axis may be negative, so the regularity of aerostatic coefficients under wind-axis is better, and using the aerostatic coefficients under body-axis will increase the

difficulty of machine learning identification (Li, 2003). Therefore, the aerostatic coefficients under wind-axis, i.e. drag coefficient C_D, lift coefficient C_L and moment coefficient C_M, are used in this paper for further study.

Before starting the machine learning training, a regression analysis was first performed by creating an equation of how the dependent variable varies with multiple independent variables and testing the equation and parameters for statistical significance. The T-test is used here for significance testing of parameters, which can also be regarded as a parameter sensitivity analysis.

A regression model with k independent variables can be expressed as:

$$y = \beta_0 + \beta_1 x_1 + \beta_2 x_2 + \cdots + \beta_k x_k + \varepsilon \tag{4.3.1}$$

where β_0, β_1, β_2, …, β_k are the parameters of the regression model, and ε is the random error in the y-axis. It is generally assumed that ε obeys the normal distribution with the mean of zero and variance of σ^2. For n sets of data, the following vector β consisting of the estimated values of the parameters in the regression model can be obtained.

$$\beta = (X^T X)^{-1} X^T Y \tag{4.3.2}$$

where X^T is the transposed matrix of X (design matrix). $\beta=(\beta_0, \beta_1, \cdots, \beta_k)^T$ and $Y = (y_1, y_2, \cdots, y_n)^T$ are both column vectors.

In the multiple linear regression model, the test statistic t_j for parameter β_j obeys a t-distribution with n-k-1 degrees of freedom (Montgomery et al., 2012):

$$t_j = \frac{\beta_j - \beta_j}{\sqrt{\sigma^2 C_{ij}}} = \frac{\beta_j - \beta_j}{se(\beta_j)} \sim t(n-k-1) \tag{4.3.3}$$

where C_{jj} is the element of the j-th row and j-th column of the k-order matrix $(X^TX)^{-1}$.

$$\sigma^2 = \frac{SSE}{n-k-1} = \frac{\sum_{i=1}^{n}(y_i - y_i)^2}{n-k-1} \tag{4.3.4}$$

When $\beta_j = 0$ there is $t_j = \beta_j / se(\beta_j)$ obeying the t-distribution with n-k-1 degrees of freedom. The difference between β_j and 0 can be considered statistically significant when $|t_j| > t_{0.025}(n-k-1)$ or the p-value corresponding to t_j is less than 0.05. A query of the t-distribution table shows that for a given significance level α=0.05, the critical value $t_{\alpha/2}$ is basically close to 2 when the degree of freedom is greater than 10. That is when judging the regression analysis results, the effect of the corresponding variable is significant when $|t|>2$, and the probability of error will not exceed 0.05. If $|t|$ is much greater than 2, the probability of error is even smaller. Table 4.1 gives the t-statistics of each input feature for the output parameter (aerostatic coefficients). It can be seen that most of the values of $|t|$ are greater than 2, which proves that when the machine learning method is used to study the aerodynamic characteristics of bridges, the dimensions of cross-section and wind attach angle are very important factors, and these

geometric dimensions given must be used as the input of the model.

Table 4.1: T-test of regression analysis (aerostatic coefficients)

***t*-statistic**	***B/H***	***b/H***	***θ***	***β***	***α***
C_D	3.286	1.109	2.626	-2.402	2.147
C_L	5.384	2.252	-0.793	-1.763	92.019
C_M	-2.156	-1.123	-4.181	4.740	168.293

4.3.2 Comparison of algorithms

Actually, in the case of big data, the existing machine learning methods show insignificant difference in accuracy that can be achieved. However, in the face of a small amount of data, it is necessary to compare various machine learning algorithms before selecting the most favorable one. In this study, three machine learning algorithms are compared: EBP neural network, support vector regression and gradient boosting decision tree.

The comparison is based on the wind tunnel test data of 20 sets of aerostatic coefficients of closed box girders by wind tunnel tests from the database. The fitting degree (R^2 statistic) of the model is used as the evaluation index to select the optimal algorithm. R^2 is defined as:

$$R^2(y, y_i) = 1 - \frac{\sum_{i=1}^{n}(y_i - y_i)^2}{\sum_{i=1}^{n}(y_i - \bar{y})^2} \tag{4.3.5}$$

where y_i is the true value of the sample, y_i is the predicted value, and n is the number of samples. R^2 reflects the proportion of the variation in the dependent variables that can be explained by the independent variables through the regression relationship, and R^2 takes a value between [0,1]. The larger the R^2, the better the model is. It can be seen from Figure 4.4 that the fitting degree of three methods is not significantly different (R^2>0.95). All three algorithms can obtain the potential input-output transfer relationship of the training set, and either algorithm is sufficient for good identification of aerostatic coefficients.

To judge the prediction effect of trained machine learning models, the extrapolation ability of the test set should also be evaluated, which is also called the generalization ability evaluation. By inputting the data in the test set, the predicted aerostatic coefficients can be obtained through the trained model. The predicted values by three algorithms are compared with the true values (wind tunnel test results). Figure 4.5 gives the prediction results for the cross-section 1 as the test set. The prediction accuracy can be reflected by the mean relative error (MRE) which is defined as:

$$MRE(y, y) = \frac{1}{n}\sum_{i=1}^{n}\left|\frac{y_i - y_i}{y_i}\right| \tag{4.3.6}$$

where y_i is the true value of the sample, y_i is the predicted value, and n is the number of samples. The

smaller the value of MRE, the more accurate the prediction is. Table 4.2 gives the specific values of MRE under different algorithms. The analysis shows that the training and prediction effect of EBP and GBDT are significantly better than that of SVR. In this paper, the EBP neural network, which is the most widely used, is ultimately chosen for the intelligent identification of aerostatic coefficients.

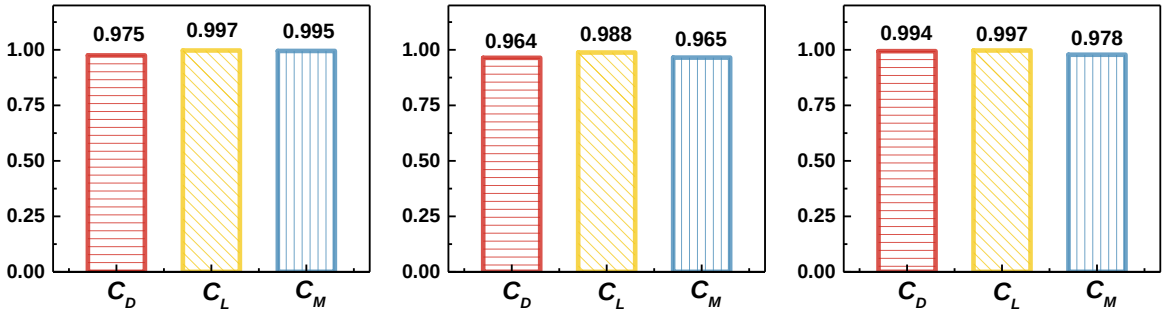

(a) EBP (b) SVR (c) GBDT

Figure 4.4: Fitting degree of three algorithms (aerostatic coefficients)

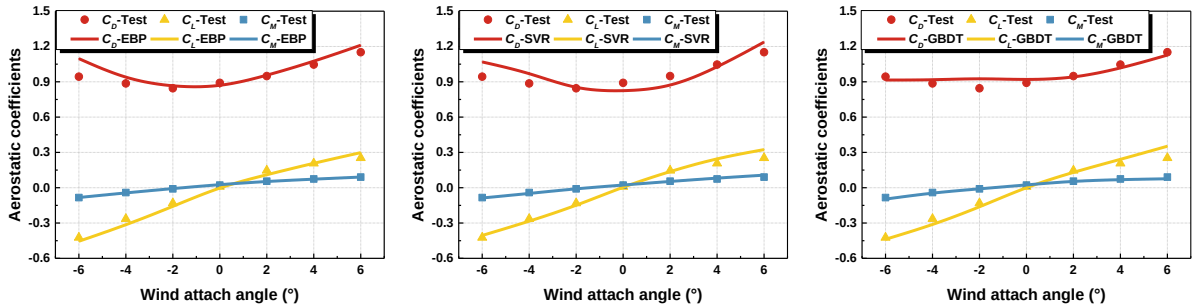

(a) EBP (b) SVR (c) GBDT

Figure 4.5: Generalization ability of three algorithms (aerostatic coefficients)

Table 4.2: Comparison of prediction errors under three algorithms (aerostatic coefficients)

MRE	C_D	C_L	C_M	Mean
EBP	0.0484	0.1531	0.0831	0.0949
SVR	0.0771	0.1292	0.1038	0.1034
GBDT	0.0377	0.1872	0.0783	0.1011

4.3.3 Model construction

In order to further improve the prediction effect of machine learning, the machine learning modeling and optimization conducted in this section will be based on the 54 sets of CFD re-calculated results. A four-layer EBP neural network is developed for the intelligent identification of aerostatic coefficients of closed box girders. The model contains one input layer, two hidden layers and one output layer. The number of nodes in hidden layer is determined based on the dimensionality of input and output, as well as the iterative trial calculations. A small number of nodes in hidden layer does not reflect the underlying distribution of sample set well, while a large number of nodes results in an overly complex non-linear model to represent the transfer relationship between input and output, and the

corresponding training time will be greatly extended. Taking into account the mapping capability of model and the training time, the number of nodes in each of the two hidden layers was finally determined to be 20. The structure of the whole EBP neural network is shown in Figure 4.6.

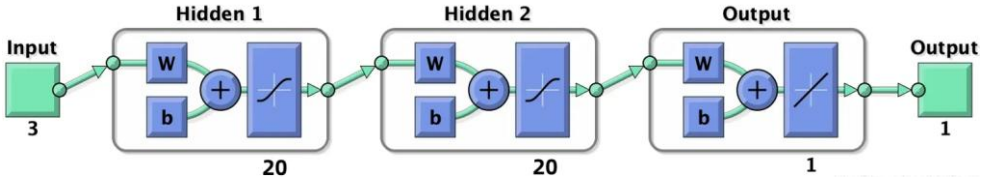

Figure 4.6: Architecture of EBP neural network

Since EBP algorithm is actually a gradient descent method, there are inevitably certain limitations, such as a slow convergence rate and a local extremum. In order to prevent these problems, Levenberg-Marquardt algorithm is used for the optimization of model, which can provide numerical solutions for minimizing nonlinear function problems. It combines the advantages of the steepest descent method and the Gauss-Newton algorithm.

The steepest descent method is a first-order algorithm. Normally, gradient g is defined as the first-order derivative of total error function, then the update rule of the steepest descent algorithm could be written as

$$w_{k+1} = w_k - \alpha g_k \tag{4.3.7}$$

where α is the learning constant (step size).

Newton's method assumes that all the gradient components g_1, g_2, …, g_n are functions of weights and all weights are linearly independent. The update rule for Newton's method is

$$w_{k+1} = w_k - H_k^{-1} g_k \tag{4.3.8}$$

As the second-order derivatives of total error function, Hessian matrix H gives the proper evaluation on the change of gradient vector. In order to get Hessian matrix H, the second-order derivatives of total error function have to be calculated and it could be very complicated. In order to simplify the calculating process, Jacobian matrix J is introduced, so the update rule of the Gauss–Newton algorithm is presented as

$$w_{k+1} = w_k - (J_k^T J_k)^{-1} J_k e_k \tag{4.3.9}$$

In order to make sure that the approximated Hessian matrix J^TJ is invertible, Levenberg–Marquardt algorithm introduces another approximation to Hessian matrix:

$$H \approx J^T J + \mu I \tag{4.3.10}$$

where μ is always positive and called combination coefficient, I is the identity matrix.

By combining Equations (4.3.8) and (4.3.9), the update rule of Levenberg–Marquardt algorithm can be presented as

$$w_{k+1} = w_k - (J_k^T J_k)^{-1} J_k e_k \tag{4.3.11}$$

As the combination of the steepest descent algorithm and the Gauss–Newton algorithm, the Levenberg–Marquardt algorithm switches between the two algorithms during the training process. When the combination coefficient μ is very small (nearly zero), Equation (4.3.13) is approaching to Equation (4.3.11) and Gauss–Newton algorithm is used. When combination coefficient μ is very large, Equation (4.3.13) approximates to Equation (4.3.9) and the steepest descent method is used.

The improved EBP neural network based on Levenberg-Marquardt algorithm is constructed using MATLAB software to identify aerostatic coefficients in this paper. The main code is shown below:

```
% Training set
load data.txt;
input_train = (data (30:384,1:5))';
output_train = (data (30:384,6))';
% Test set
input_test = (data (1:29,1:5))';
output_test = (data (1:29,6))';
% Normalization of input and output data
[inputn,inputps] = mapminmax (input_train,-0.9,0.9);
[outputn,outputps] = mapminmax (output_train,-0.9,0.9);
% EBP neural network construction
% Initialization
net = newff (inputn,outputn, [20 20], {'tansig','purelin'}, 'trainlm');
net.trainParam.epochs = 10000;
net.trainParam.lr = 0.01;
net.trainParam.goal = 0.00004;
% Training
[net,tr] = trainlm (net, inputn, outputn);
% Prediction
% Normalization of prediction data
inputn_test = mapminmax ('apply', input_test, inputps);
% Result output
an = sim(net,inputn_test);
% Denormalization
BPoutput=mapminmax('reverse',an,outputps)
```

4.3.4 Training and prediction effects

The ultimate goal of machine learning is to deploy trained models into real environments, with the hope that the models can achieve good prediction effect in real scenarios. For this purpose, the sample set is usually divided into three parts: training set, validation set and test set. Training set is a set of samples used for learning, which is to fit the parameters (i.e. weight) of the classifier; Validation set is a set of samples used to tune the parameters (i.e. architecture, not weight) of a classifier, for example to choose the number of hidden units in a neural network; Test set is a set of samples used only to assess the performance (generalization) of a fully specified classifier (Lecun and Bengio, 1995). In this study, cross validation is used to evaluate the accuracy and stability of the model through different data division patterns. Each sample will be used as the training set, validation set and test set in turn. Cross validation method can help to monitor the changes of training effect under different patterns, and avoid overfitting problems.

In this section, a total of 54 sets of CFD re-calculation numerical simulation data will be used as the sample set for machine learning. Among them, 4 samples far from the mean of datasets (samples in the dashed box in Figure 3.2, i.e. cross-section 10, 16, 24 and 37), they will be removed from the sample set according to the statistical results. Therefore, a total of 50 sets of data can be available in the sample set finally. These 50 sets of data will be used as the test set one by one, resulting in 50 working conditions; Under each working condition, take any one of the remaining 49 sets of samples as the validation set, and the remaining 48 sets as the training set, resulting in 49 working conditions. It will ultimately result in a total of 50*49=2450 working conditions. Each working condition will be randomly assigned 100 times and each assignment will be followed by 500 training sessions. Then, the best and worst working conditions are displayed below.

Improved EBP neural networks are trained under 2450 working conditions depending on the data division. The average training effect of aerostatic coefficients is shown in Figure 4.7. Generally speaking, all the models are trained successfully because the values of fitting degree (R^2) are all above 0.99. To judge the prediction effect of trained machine learning models, the extrapolation ability of the test set should also be evaluated, which is called the generalization ability evaluation. The predicted aerostatic coefficients by improved EBP neural network under different wind attack angles are compared with the true values (CFD re-calculation results), which is shown in Figure 4.8. Figure 4.8 shows that the prediction errors of C_D are slightly larger than that of C_L *and* C_M, but the error mainly occurs under the large wind attack angles. The prediction effect of aerostatic coefficients under small wind attack angles is good enough. This is because there are errors between different experiments, and the distribution of the collected aerostatic coefficients at large wind attach angles is divergent. It means the distribution pattern of data under large wind attach angles is not obvious especially for C_D, so the prediction errors

of C_D under large wind attach angles are slightly larger. Table 4.3 shows the specific values of mean relative error (MRE). The MRE of the best prediction result is only 0.0355, and the worst one is 0.0778, which indicates that the model has good generalization ability to the data outside the training set.

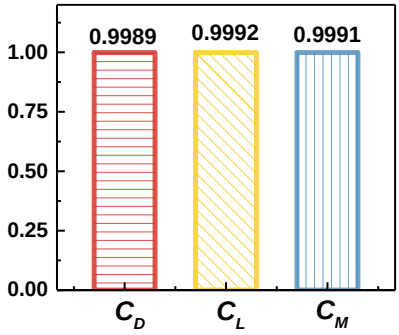

Figure 4.7: Fitting accuracy of training set (aerostatic coefficients)

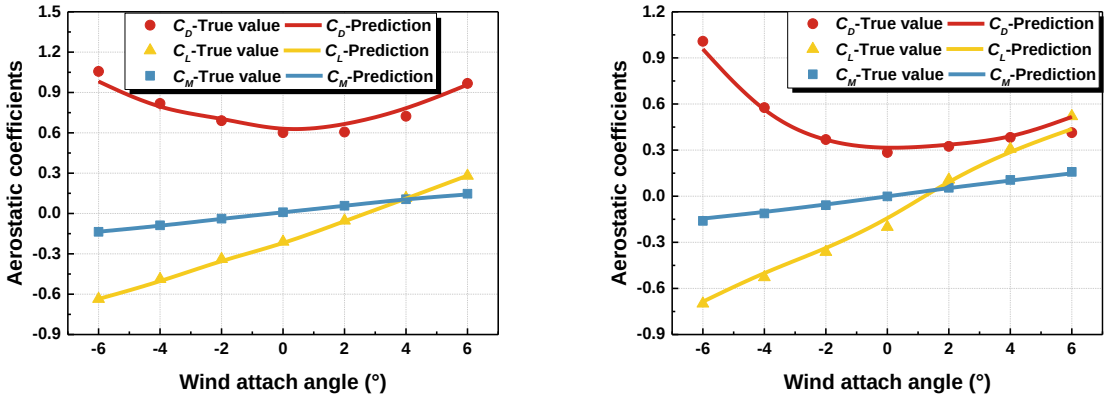

(a) The best prediction results (cross-section 19) (b) The worst prediction results (cross-section 26)

Figure 4.8: Generalization ability of test set (aerostatic coefficients)

Table 4.3: Prediction errors of aerostatic coefficients

MRE	C_D	C_L	C_M	Mean
Best	0.0462	0.0352	0.0250	0.0355
Worst	0.0827	0.0879	0.0628	0.0778

4.4 Identification of flutter derivatives

4.4.1 Input and output

Similar to the intelligent identification of aerostatic coefficients, the input to machine learning modelling of flutter derivatives is also five parameters, including the dimensions of cross-section (*B/H, b/H, θ, β*) shown in Figure 3.1 and reduced wind speed. The outputs of the model are flutter derivatives, but only one flutter derivative at a single reduced wind speed is output each time. Regression analysis between input and output is shown in Table 4.4, which demonstrates that the dimensions of cross-section and wind speed are also very important factors in the identification of flutter derivatives.

Table 4.4: T-test of regression analysis (flutter derivatives)

t-statistic	*B/H*	*b/H*	θ	β	*U/fB*
A_1^*	2.539	-2.351	-4.517	4.147	115.834
A_4^*	1.237	1.601	1.407	-2.478	47.381
H_1^*	-2.950	1.573	1.632	-1.033	-82.835
H_4^*	-3.798	2.648	2.681	-1.609	-27.241
A_2^*	-3.066	2.468	2.802	-2.339	-37.922
A_3^*	2.635	-1.829	-1.210	0.847	38.996
H_2^*	3.267	-1.812	-1.079	0.380	5.875
H_3^*	-2.977	1.989	1.277	-0.815	-37.282

4.4.2 Comparison of algorithms

Same as aerostatic coefficients, before modelling the flutter derivatives, three machine learning algorithms are compared: EBP neural network, SVR and GBDT. Unlike the static three component force coefficient, considering that machine learning is difficult to capture the potential distribution pattern of flutter derivatives only under 20 sets of wind tunnel test data from the database, the comparison of three algorithms is conducted under 54 sets of hybrid original data to obtain accurate comparison results. Figure 4.9 and Figure 4.10 shows the average fitting degree and generalization ability of a test set (cross-section 1) under three algorithms, and Table 4.5 gives the specific prediction accuracies of three algorithms.

It can be found that the fitting degree and generalization ability of GBDT are both superior to the other two methods, which is different from the aerostatic coefficients. Since EBP neural network is actually a gradient descent method which is very easy to fall into local minimums and not suitable for training the depth network with multiple hidden layers. EBP neural network cannot solve complex nonlinear mapping problems and dose not adapt well to small data situation where the underlying distribution is ambiguous even with improvement. This is why EBP neural network can predict aerostatic coefficients well, but cannot achieve the prediction of flutter derivatives. Although SVR has the ability to map complex nonlinear problems to high-dimensional spaces for analysis and it is suitable for small-scale data, the use of SVR requires very rigorous data pre-processing and hyper-parameters tuning because it is very sensitive to data. The SVR model is difficult to check and adjust, especially for the situation with large data dimensionality but few samples, so it is also inapplicable for the intelligent identification of flutter derivatives under current data condition. GBDT can flexibly handle various types of data, including continuous and discrete values, and it can achieve good prediction results with very few parameters tuning even in the case of small-scale data. It is not sensitive to the absence of some features, and its framework allows post-interpreters to be run for model representation and improvement. Therefore, GBDT is chosen for learning and prediction of flutter derivatives in this study. However, as

GBDT is an integrated algorithm based on sequence, a new decision tree needs to be established for each iteration and each decision tree needs to be optimized, which results in the long training time. Moreover, the GBDT model is prone to overfitting, which leads to poor generalization ability. To solve this problem, the use of appropriate regularization methods or other strategies is necessary.

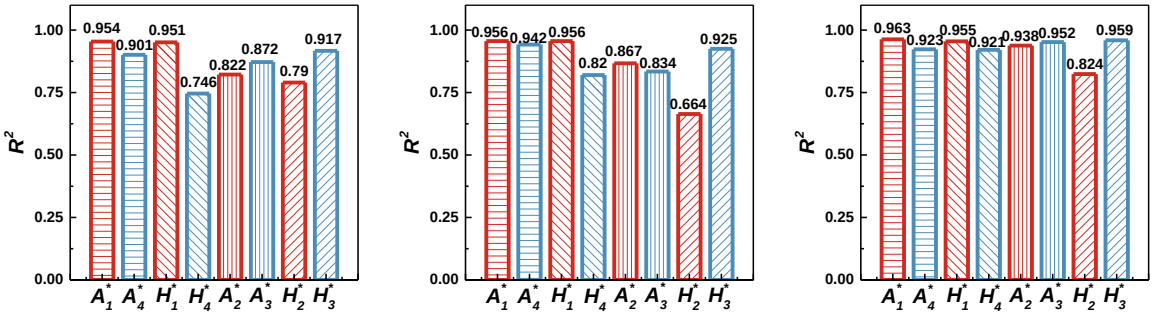

(a) EBP (b) SVR (c) GBDT

Figure 4.9: Fitting degree of three algorithms (flutter derivatives)

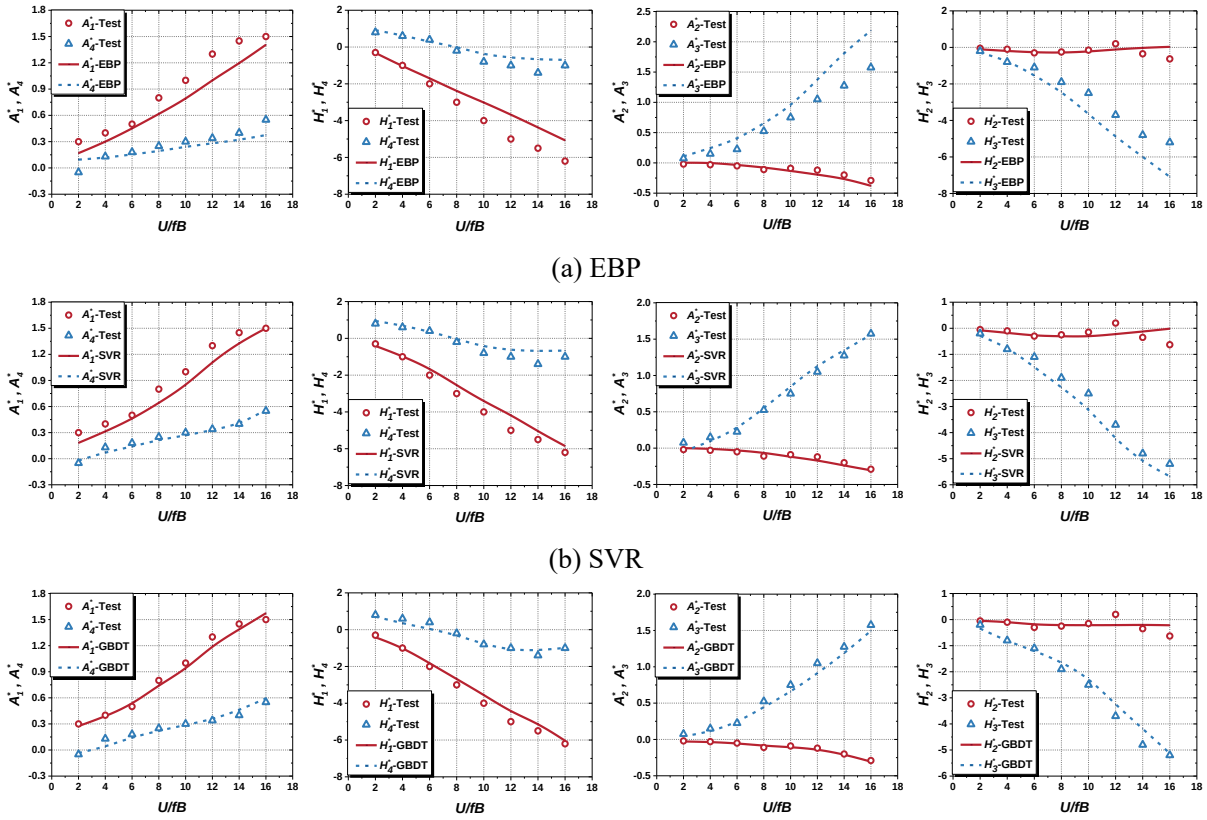

(a) EBP

(b) SVR

(c) GBDT

Figure 4.10: Generalization ability of three algorithms (flutter derivatives)

Table 4.5: Comparison of prediction errors under three algorithms (flutter derivatives)

MRE	A_1^*	A_4^*	H_1^*	H_4^*	A_2^*	A_3^*	H_2^*	H_3^*	Mean
EBP	0.2136	0.5329	0.1702	0.4110	0.5667	0.4239	0.7999	0.3278	0.4307
SVR	0.1604	0.1923	0.1491	0.3608	0.4465	0.3107	0.8019	0.2049	0.3283
GBDT	0.0595	0.2033	0.1150	0.2750	0.1480	0.1624	0.5310	0.1702	0.2081

4.4.3 Model construction

The prediction errors of flutter derivatives under three algorithms in the previous section indicate that using all 54 sets of hybrid original data cannot achieve satisfactory prediction results. Therefore, the machine learning modeling and optimization conducted in this section will be based on the 54 sets of CFD re-calculated results. A hybrid model combining GBDT and linear regression method is used for the training and prediction of flutter derivatives in this study as shown in Figure 4.11. Input features are transformed by means of GBDT which consists of m decision trees. The number of trees and the number of branches (nodes) per tree are determined based on the amount of input data. During the training process of GBDT, a new tree is added to the existing trees to fit the residuals between the predicted values and the true value in each iteration so that GBDT can form a strong predictive model by superimposing multiple weak learners. Finally, the transformed features w_i (i=0,1,2,…,n) are trained in a linear regression model to obtain the final prediction results.

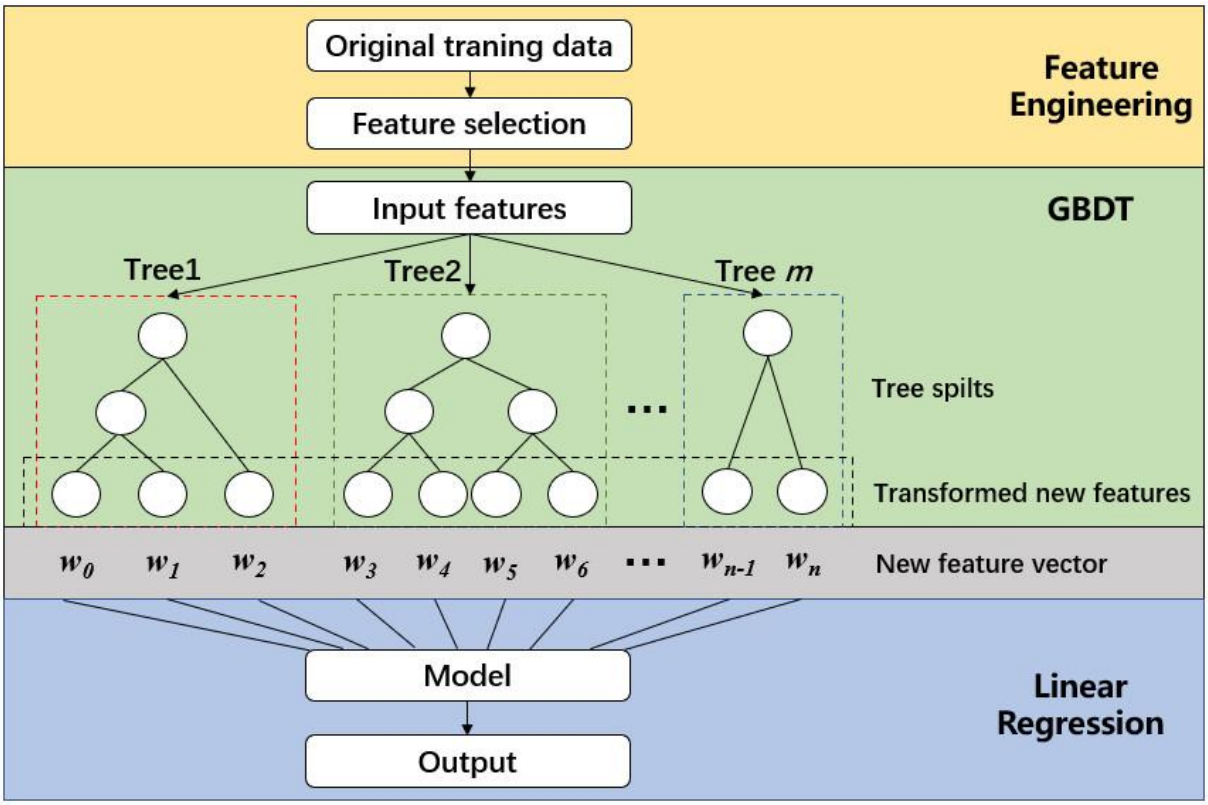

Figure 4.11: Architecture of GBDT and LR

GBDT model has the advantages of robustness, applicability to the low-dimensional, and fast tuning. However, in the case of small samples, it has poor generalization ability and usually faces the problem of overfitting. To solve this issue, a regular term is added to the original loss function to improve the generalization ability of the trained model. The loss function after adding the regular term is shown as follows:

$$L' = \sum_{n=1}^{N} L(y_i, f_{m-1}(x_i) + c) + \sum_{m} \Omega(g_m) \tag{4.4.1}$$

where $\Omega(g) = \delta T + \frac{1}{2}\lambda \|w\|^2$, δ and λ are hyperparameters, T is the number of leaf nodes, and w is a vector consisting of all leaf node values.

The GBDT method used to identify flutter derivatives in this study is based on Python and its toolkit. The programming process is conducted on Jupyter Notebook which is a web-based interactive computing platform, and light gradient boosting machine (LightGBM) is used as the engineering implementation of GBDT algorithm. The main code for function implementation is as follows:

```
# Import libraries
import pandas as pd
import numpy as np
import statsmodels.api as sm
from patsy import dmatrices
import lightgbm as lgb
import shap

# Import data
df1 = pd.read_excel (r"D:\python-notebooks\data14.xlsx")
df2 = pd.read_excel (r"D:\python-notebooks\data23.xlsx")
df1 = df1.fillna(method = "ffill")
df2 = df2.fillna(method = "ffill")
df1.columns = ["K1","K2","K3","K4","K5","A1","A4","H1","H4"]
df2.columns = ["K1","K2","K3","K4","K5","A2","A3","H2","H3"]

# Training
df = df1
X_columns = df.columns[:5]
y_column = "A1"
X = df [X_columns]
y = df [y_column]
model = sm.OLS (y, X)
results = model.fit ()
print (results.summary ())

train_data = lgb.Dataset (X.iloc [30:], label = y.iloc [30:], params = {"min_data_in_bin":1})
params = {
```

```
    'objective': 'regression',
    'learning_rate': 0.1,
    'max_depth':4,
    "min_data_in_leaf": 1,
    "min_data_per_group":1,
    "max_cat_threshold": 1,
    "min_data_in_bin": 1,
    "min_sum_hessian_in_leaf": 0,
    "verbose":"-1"
   }
bst = lgb.train (params, train_data, 30)
explainer = shap.Explainer (bst)
shap_values = explainer (X)
shap.plots.beeswarm (shap_values)
```

4.4.4 Training and prediction effects

The CFD re-calculation results of 50 sets of closed box girder sections were used as the sample set (removed 4 samples far from the mean of datasets) for the model of GBDT. In the same way as the identification process of aerostatic coefficients, the best and worst prediction results will be selected from the 2450 working conditions generated by the 50 sets of data. Figure 4.12 gives the average fitting degree (R^2) of each flutter derivatives, showing that the models of GBDT can obtain the potential input-output transfer relationship of training set. All the values of R^2 are larger than 0.9 except for H_2^*. Figure 4.13 gives the best and worst prediction outcomes from all test sets (predicted value means the predicted flutter derivative by the trained model, true value means the re-calculated CFD result). It shows that the machine learning models are able to predict the distribution of flutter derivatives to a large extent under current data condition. Table 4.6 gives the specific values of MRE of test set. The MRE of the best prediction result is 0.1233 and the worst one is 0.1970.

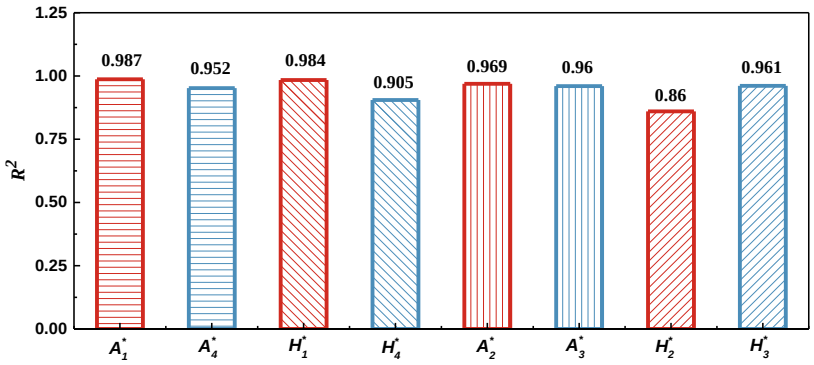

Figure 4.12: Fitting accuracy of training set (flutter derivatives)

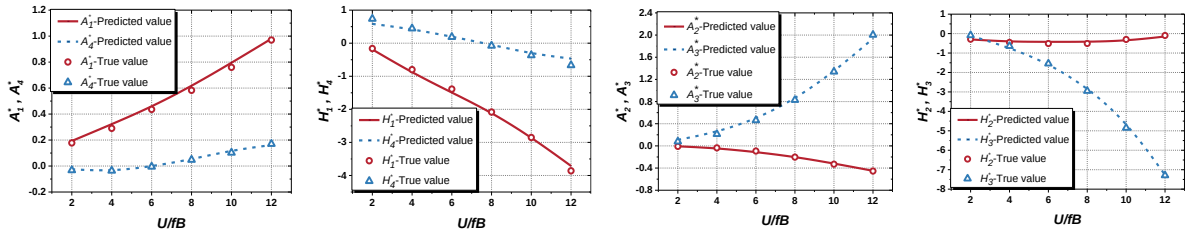

(a) The best prediction results (cross-section 29)

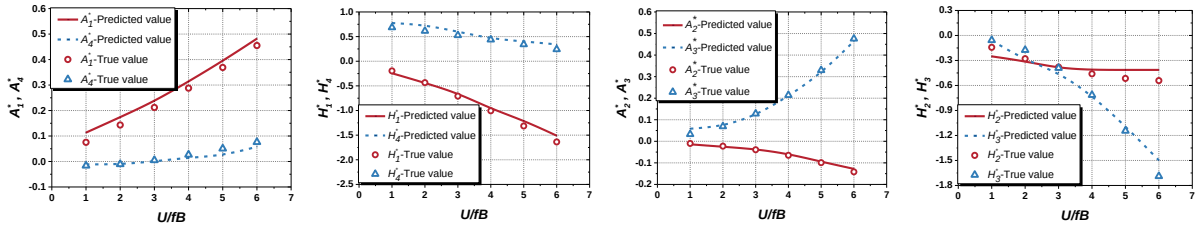

(b) The worst prediction results (cross-section 26)

Figure 4.13: Generalization ability of test set (flutter derivatives)

Table 4.6: Prediction errors of flutter derivatives

MRE	A_1^*	A_4^*	H_1^*	H_4^*	A_2^*	A_3^*	H_2^*	H_3^*	Mean
Best	0.0584	0.1745	0.0662	0.1924	0.0985	0.1089	0.2042	0.0833	0.1233
Worst	0.1755	0.4128	0.0910	0.1851	0.1411	0.1573	0.2400	0.1730	0.1970

4.4.5 Model Interpretation

The process of machine learning is often considered a “black box”. The output is only obtained from the input, and the middle training process is difficult to be explained. To express the machine learning model in some explicit way, the Shapley additive explanation (SHAP) is applied here. SHAP is an additive model interpreter constructed by Lundberg and Lee (2017) inspired by cooperative game theory, which focuses on calculating the SHAP values of each feature as a reflection of how much the feature contributes to the prediction of the model. SHAP interprets the predictive value of the model as the sum of SHAP values of each input feature:

$$y = f_0 + \sum_{i=1}^{M} f_i \tag{4.4.2}$$

where y is the predictive value, f_i is the SHAP value of each feature, and f_0 is the mean predictive value of all training samples. SHAP can reflect the impact of each feature on the final prediction and can show the positivity and negativity of the impact, increasing the interpretability of the model. It also provides powerful data visualization functions to show the model and the prediction results, which are widely used to explain models with complex algorithms.

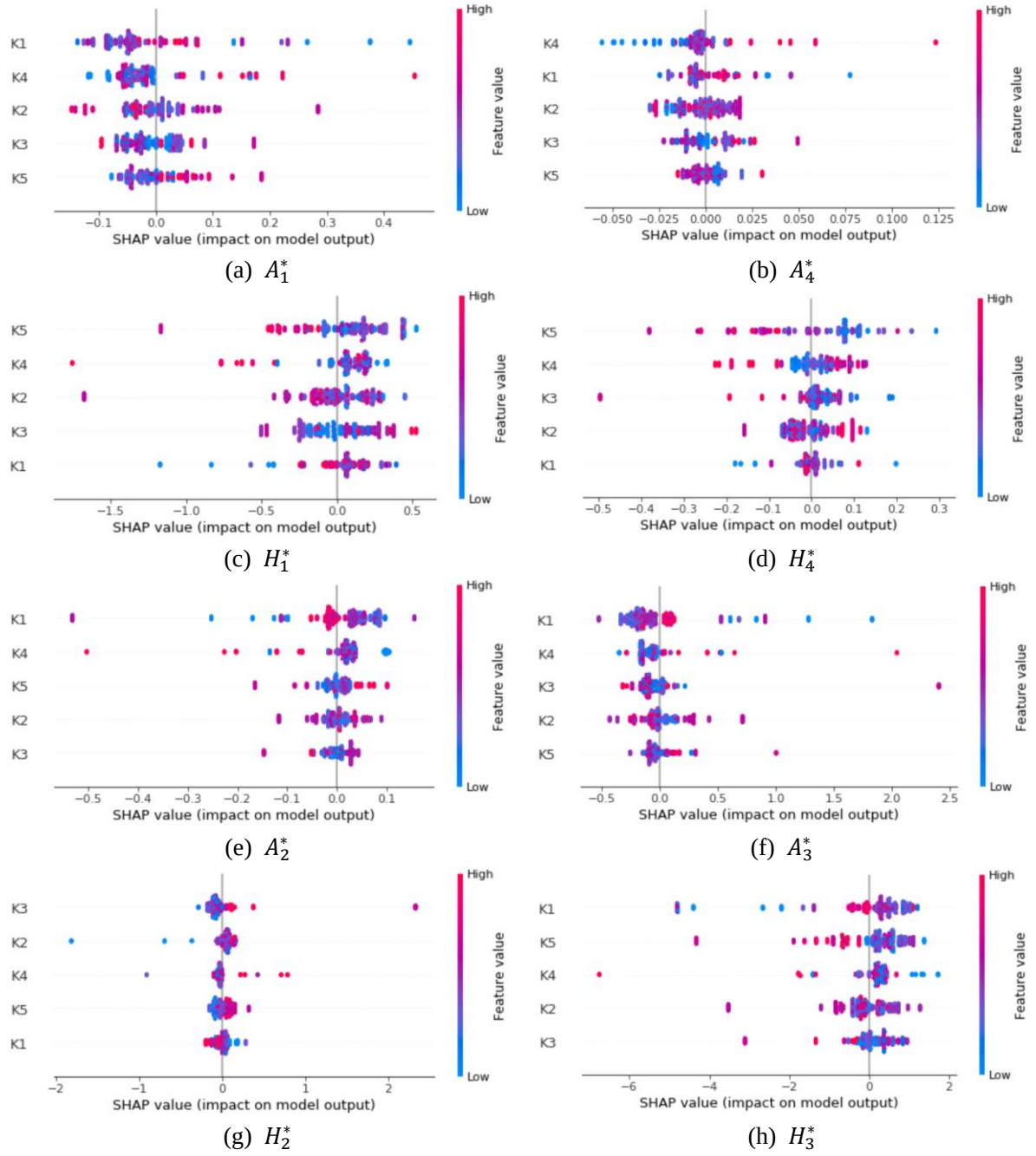

(a) A_1^*

(b) A_4^*

(c) H_1^*

(d) H_4^*

(e) A_2^*

(f) A_3^*

(g) H_2^*

(h) H_3^*

Figure 4.14: SHAP model explanation

Figure 4.14 shows the SHAP values of several dimensions of the cross-section mentioned above for the prediction results of model. (Note: K1, K2, K3, K4 and K5 represent the depth of beam, width of deck, wind fairing extension length, wind fairing angle, and web inclined angle, respectively. They are ranked from top to bottom according to the effect magnitude on each flutter derivative.) Overall, except H_2^*, the influence of these shape parameters on the other flutter derivatives is obvious. K1 (height of beam), K4 (wind fairing angle) and K5 (web inclined angle) play a major role in the flutter derivatives, but the influence direction and the contribution degree of different shape parameters to the flutter derivatives are different. For A_1^*~A_4^*, K1 has the greatest effect on them. They have the same change

direction as K1. It means A_1^*~A_4^* increase with the height of beam, but A_1^*, A_2^* and A_3^* are more likely to be positive and A_4^* is more likely to be negative. For H_1^*~H_4^*, the impact of K5 is large. Except that the situation of H_2^* is unclear, H_1^*, H_3^* and H_4^* all change in the opposite direction to K1, i.e. H_1^*, H_3^* and H_4^* all decrease as the web inclined angle increases and it is more likely that they are all negative. The specific contribution degree of these shape parameters to the flutter derivatives is given in a semi-quantitative form (SHAP values). SHAP analysis enables the interpretability of black box models and it can even provide the necessary reference for further explicit representation of the training process of machine learning.

4.5 Conclusion

In this chapter, aerodynamic parameters of closed box girders are identified by machine learning methods based on the self-built wind-resistance database of long-span bridges and CFD calculation results. The improved EBP neural network and GBDT were selected to train and predict the aerostatic coefficients and flutter derivatives respectively after comparison. The machine learning models can obtain the potential input-output transfer relationship of training set. The prediction error of aerostatic coefficients mainly occurs under the large wind attack angles and the prediction effect under the small wind attack angles is good, which means that the models have the extrapolation capability to the test set to a certain extent. For flutter derivatives, the fitting accuracy and generalization ability are also good through training and improvement The trained models can be used for the preliminary analysis of wind-resistance of bridges. In addition, the distribution analysis of flutter derivatives is realized through the post-interpretation of trained models in a semi-quantitative form (SHAP values). The analysis results show that the depth of beam, wind fairing angle and web inclined angle play a major role in the flutter derivatives. For A_1^*~A_4^*, the depth of beam has the greatest effect on them and they increase with the depth of beam, but A_1^*, A_2^* and A_3^* are more likely to be positive and A_4^* is more likely to be negative. For H_1^*~H_4^*, the impact of web inclined angle is large. Except that the situation of H_2^* is unclear, H_1^*, H_3^* and H_4^* all decrease as the web inclined angle increases and it is more likely that they are all negative. SHAP analysis enables the interpretability of black box models and it can even provide the necessary reference for further explicit representation of the training process of machine learning.

CHAPTER 5

5 Two-dimensional wind-resistant stability evaluation

5.1 Background

The proposed data-driven model in this study can make the identification of aerodynamic parameters of closed box girder without wind tunnel tests and complex numerical simulations to some extent. It can also provide a convenient and feasible option for expanding data sets of aerodynamic parameters. In addition, the aerodynamic parameters predicted by the trained machine learning models can be applied to the rapid analysis of wind-resistant performance of bridges. In this chapter, the aerostatic stability and flutter stability of the structure will be further discussed by applying the modelling results from the previous chapters to the specific example.

5.2 Two-dimensional aerostatic stability evaluation

5.2.1 Two-dimensional linear aerostatic stability analysis model

A linear method means that the research problem is based on very small deformations of structure, assuming that the displacements of the object are so small relative to the size of the structure itself that they are almost negligible, and that the strains in the structure due to external forces are also very small. The establishment of equilibrium conditions for structures using the linear idea ignores the changes in shape and position of structural elements, and therefore disregards the geometric deformations and displacements of the structure after the forces are applied. The two-dimensional linear aerostatic instability model is based on small deformations and assumes that structural displacements and strains are not significant (Chen, 2005; He, 2016). The aerostatic torsional divergence instability of suspension bridges mainly considers the moment factor and ignores the influence of non-linearity of structural geometry, materials and static wind load. The specific instability process is shown in Figure 5.1.

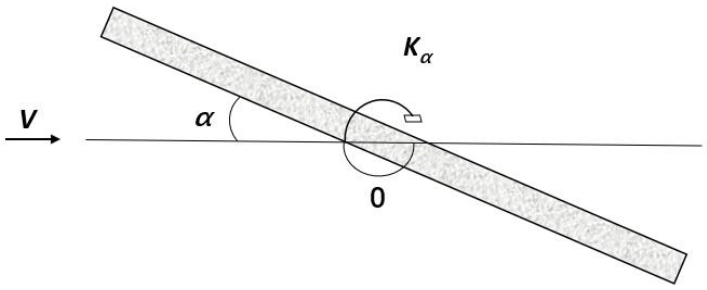

Figure 5.1: Aerostatic instability of flat plate

By simplifying the bridge girder cross-section to a spring-loaded flat plate model with torsional stiffness (Figure 5.1), the structural torsional vibration equation can be expressed as

$$M_\alpha \ddot{\alpha} + c\dot{\alpha} + K_\alpha \alpha = \frac{1}{2}\rho V^2 B^2 C_M(\alpha) \tag{5.2.1}$$

Decompose the lift moment function as

$$C_M(\alpha) = C_{M0}(\alpha) + C_M^{'}\alpha \tag{5.2.2}$$

By substituting Equation (4.2) into Equation (4.1), the following can be obtained:

$$M_\alpha \ddot{\alpha} + c\dot{\alpha} + K_\alpha \alpha = \frac{1}{2}\rho V^2 B^2 \left(C_{M0} + C_M^{'} \alpha\right) \tag{5.2.3a}$$

$$M_\alpha \ddot{\alpha} + c\dot{\alpha} + \left(K_\alpha - \frac{1}{2}\rho V^2 B^2 C_M^{'}\right)\alpha = \frac{1}{2}\rho V^2 B^2 C_{M0} \tag{5.2.3b}$$

$$K_\alpha - \frac{1}{2}\rho V^2 B^2 C_M^{'} = 0 \tag{5.2.3c}$$

$$V_{cr} = \sqrt{\frac{2K_\alpha}{\rho B^2 C_M^{'}}} \tag{5.2.4}$$

where M_α is generalized torsional mass, c is torsional damping, K_α is torsional stiffness, ρ is air density (kg/m^3), V is air volume (m^3); B is the width of cross-section, $C_M(\alpha)$ is the function of lift moment coefficient, and $C_M^{'}$ is the gradient of the lift moment coefficient at 0° wind attack angle.

After introducing the calculation formula for the overall torsional stiffness of bridge structure: $\omega = \sqrt{K_\alpha / I_m} = 2\pi f_t$, $I_m = mr^2$, the critical wind speed of aerostatic torsional divergence can be obtained as follows:

$$V_{crt} = f_t B \sqrt{\frac{\pi^3}{2}\mu\left(\frac{r}{b}\right)^2 \frac{1}{C_M^{'}}} \tag{5.2.5}$$

where f_t is torsional frequency (Hz), which is usually taken as the frequency under the first torsional vibration mode of the structure; M is the mass of main cable and main girder per unit length (kg/m); Im is the mass moment of inertia of main cable and main girder per unit length (kg•m^2/m), which is usually taken as the equivalent mass moment of inertia of the first order torsion of the structure; μ is the ratio of the torsional stiffness to the torsional vibration frequency of the structure, $\mu = \frac{m}{\pi\rho b^2}$; $C_M^{'}$ is the gradient of the lift moment coefficient at 0° wind attack angle.

5.2.2 Intelligent identification of aerostatic coefficients

This paper takes the Runyang Yangtze River Bridge (south branch) as an example, which is a suspension bridge with the span arrangement of 470m+1490m+470m. Figure 5.2 shows the live view, span layout and the cross-section schematic of main girder. Its single main cable consists of 184 strands, each containing 127 galvanized high-strength steel wires. The rise span ratio of the main cable is 1/10, and the center distance in the lateral direction of the bridge is 34.3m. A total of 91 pairs of suspension rods are set up in the main span, with a longitudinal spacing of 16.1m. The connection between the suspension rods, the main cable and the main girder is pin connected. The main girder is a steel closed box girder with a height of 3m and a width of 36.9m. The towers are reinforced concrete portal frame

structures with a height of approximately 210m. In order to avoid bending of the short suspension rod in the middle of the span and improve the overall mechanical performance of the structure, a rigid central buckle for the consolidation of cable and beam is set in the center of the main span.

(a) Live view

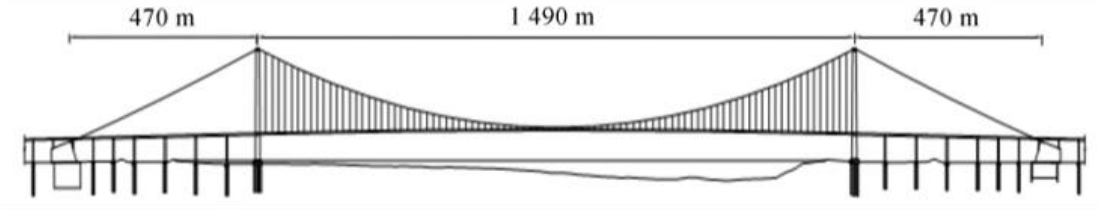

(b) Span layout

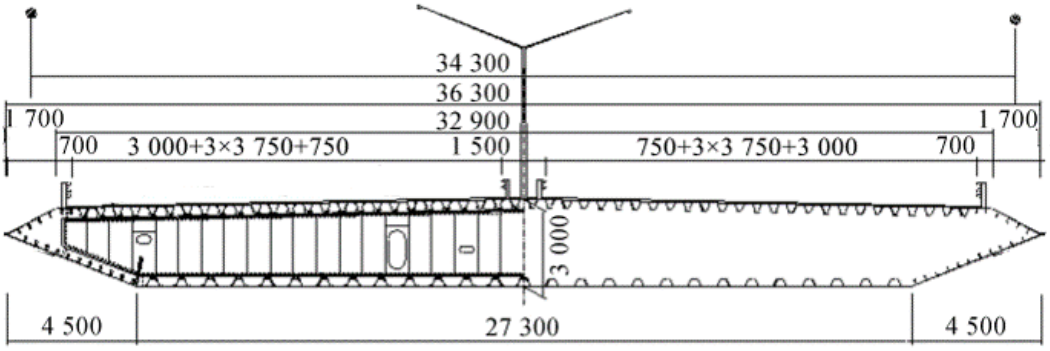

(c) Cross-section schematic of main girder (unit: mm)

Figure 5.2: Architecture of the Runyang Bridge

The trained EBP neural networks are used to obtain the aerostatic coefficients of Runyang Bridge. The comparison of predictions with CFD calculations and experimental results is shown in Figure 5.3, and the specific prediction error (MRE) is shown in Table 5.1.

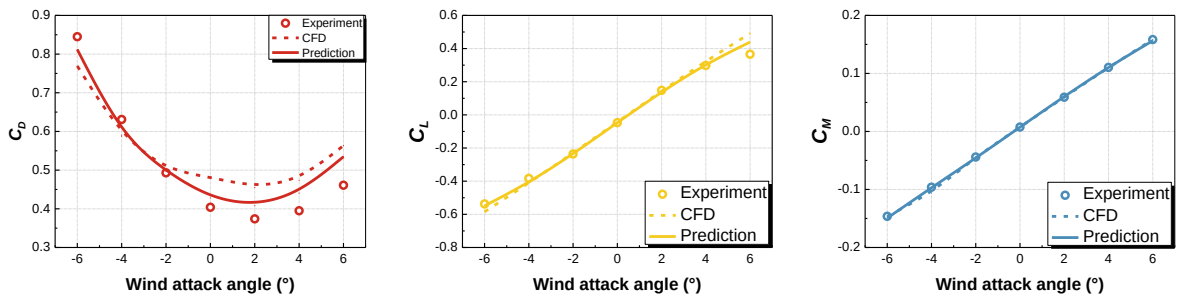

Figure 5.3: Prediction results of aerostatic coefficients for Runyang Bridge

Table 5.1: Prediction accuracy of aerostatic coefficients for Runyang Bridge

MRE	C_D	C_L	C_M	Mean
CFD	0.0579	0.0534	0.0294	0.0469
Experiment	0.0765	0.0563	0.0783	0.0704

5.2.3 Critical aerostatic instability speed analysis based on two-dimensional model

Aerostatic torsional divergence instability refers to the fact that when the wind speed reaches a certain value, the torsional moment that increases with the rotation angle of main girder exceeds the moment of resistance, causing the main girder to develop torsional divergence. Aerostatic torsional divergence can occur on both cable-stayed bridges and suspension bridges. The critical wind speed of aerostatic torsional divergence can be calculated according to Equation 5.2.5. In general, the aerostatic coefficients and their gradients involved in the calculation can be obtained by wind tunnel test or numerical simulation. In this paper, they are predicted by the improved EBP neural network models as shown above, resulting in an estimated critical wind speed (V_{crt}) of 82.4m/s for the aerostatic torsional divergence, which is very close to the result (84.23m/s) calculated through the aerostatic coefficients measured by wind tunnel test with a relative error of only 2.17%.

5.2.4 Sensitivity analysis of aerostatic coefficients to aerostatic instability

In order to further verify the effectiveness and necessity of the aforementioned machine learning method in the calculation of aerostatic stability, the trained models will be used to analyze the impact of the shape of the main girder cross-section on the critical wind speed of aerostatic instability. In this paper, three characteristic dimensions of the cross-section, which are the input parameters of EBP neural network, are mainly considered: ratio of width to depth (B/H), wind fairing angle (θ) and web inclined angle (β). Before that, the EBP neural network was first used to calculate the variation of aerostatic coefficients with wind attach angles (α) under different B/H, θ and β, respectively. Then the predicted aerostatic coefficients were used for the calculation of the critical wind speed of aerostatic torsional divergence in order to analyze the relationship between the critical wind speed for aerostatic instability and the shape of the cross-section.

5.2.3.1 Ratio of width to depth

The trend of the aerostatic coefficients of closed box girder cross-section change with wind attack angles under different ratios of width to depth is shown in Figure 5.4. In the range of -6° to 6°, C_D decreases and then increases, while C_L and C_M increase with wind attack angle (α). For different ratios of width to depth, the variation trends of aerostatic coefficients remain constant.

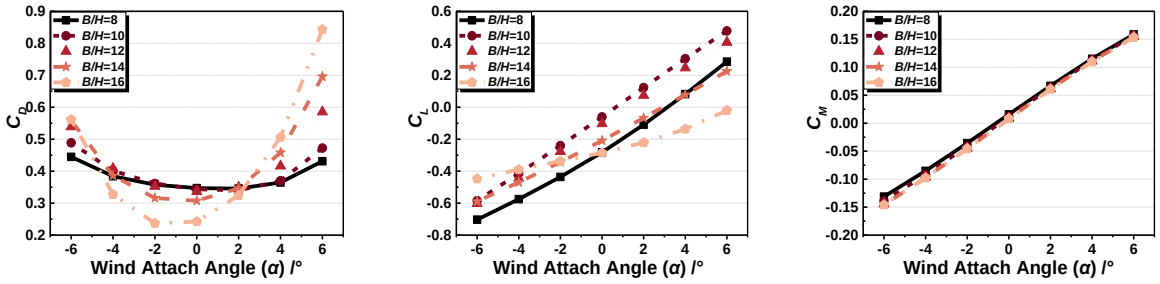

Figure 5.4: Trend of aerostatic coefficients change with wind attach angles under different ratios of width to depth

Figure 5.5 further analyzes the variation of aerostatic coefficients with the ratios of width to depth. Taking the 0° wind attack angle as the main example, it can be analyzed that: 1) C_D decreases with the increase of width to depth ratio. From the perspective of flow field, this is due to the fact that as the width to depth ratio increases, the cross-section of main girder is closer to a flat plate and the shape of flat plate can effectively slow down the separation of flow, which reduces the separation zone and therefore the drag coefficient is smaller. Under other wind attack angles, the state of flow separation changes, so the change trend of C_D with width to depth ratio also varies. 2) When $B/H > 10$, C_L decreases with the increase of width to depth ratio. This is because as the width to depth ratio increases, the vortex shedding decreases and there will be a larger negative pressure zone at the junction of the bottom and the downstream inclined web, which will produce a downward lift, so the lift coefficient gradually decreases; when $B/H < 10$, the change in width to depth ratio no longer plays a major role and the effects of wind fairing angle and web inclined angle are more influential, so the change of C_L with width to depth ratio is different from the situation when $B/H > 10$. The variation trends of C_L under other wind attack angles are similar. 3) The variation of C_M with width to depth ratio is not significant at any wind attack angles. This is due to the simultaneous increase or decrease in pressure at the front and rear ends of the cross-section, which counteracts the change in torque due to pressure, and therefore the change trend in torque is smoother.

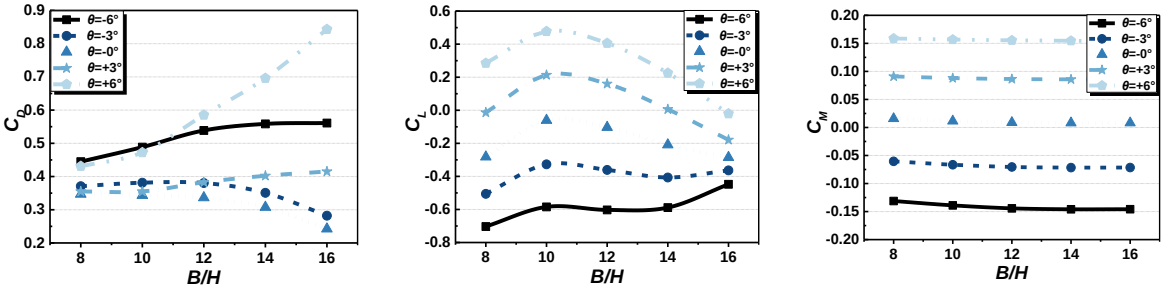

Figure 5.5: Trend of aerostatic coefficients change with ratios of width to depth under different wind attach angles

Figure 5.6 shows the calculation results of two-dimensional aerostatic stability based on the structure of the Runyang Bridge change with the width to depth ratio of main girder cross-section. It can be seen from the figure that the critical wind speed of aerostatic torsional divergence decreases with the increase of width to depth ratio, and the trend is almost linear.

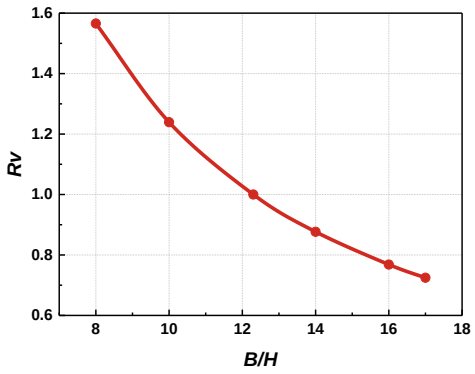

Figure 5.6: Influence of width to depth ratio on critical aerostatic instability wind speed

5.2.3.2 Wind fairing angle

The trend of the aerostatic coefficients change with wind attack angles under different wind fairing angles is shown in Figure 5.7. In the range of -6° to 6°, C_D decreases and then increases, while C_L and C_M increase with wind attack angle (α). Same as the case of width to depth ratio, the variation trends of aerostatic coefficients for different wind fairing angles remain constant.

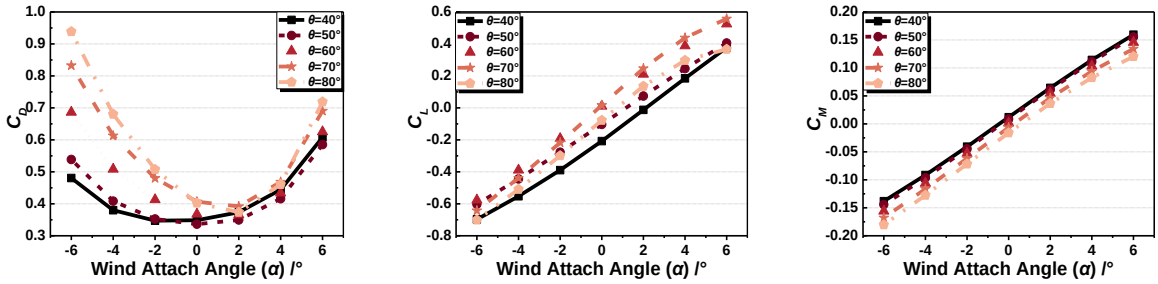

Figure 5.7: Trend of aerostatic coefficients change with wind attach angles under different wind fairing angles

Figure 5.8 further analyzes the variation of aerostatic coefficients with the wind fairing angles: 1) At 0° wind attack angle, C_D increases with the increase of wind fairing angle basically, because when the wind fairing angle increases, the flow separation then increases and therefore the drag coefficient is also increased. The change trends of C_D at other wind attack angles are similar. 2) When $\theta < 60°$, C_L increases with the increase of wind faring angle. This is because as the wind faring angle increases, the vortex shedding strengthens, and the negative pressure zone at the intersection of the bottom and the downstream inclined web gradually disappears, then the lift coefficient gradually increases. When $\theta > 60°$, the change in wind faring angle no longer plays a major role, and the combined effect of other factors leads to the change in the distribution trend of C_L. The variation trends of C_L under other wind attack angles are also similar. 3) C_M decreases with the increase of wind faring angle at any wind attack angles, but all the trends are not obvious. This is also due to the simultaneous increase or decrease in pressure at the front and rear ends of the cross-section, which counteracts the change in torque.

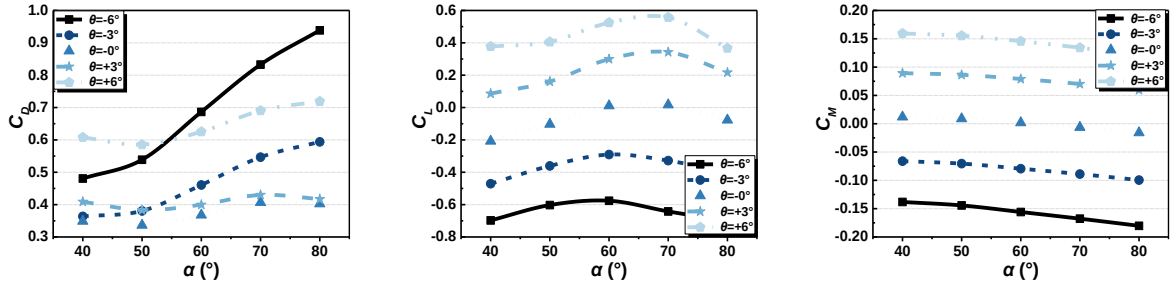

Figure 5.8: Trend of aerostatic coefficients change with wind fairing angles under different wind attach angles

Figure 5.9 shows the calculation results of two-dimensional aerostatic stability change with the wind fairing angle. It can be found that the critical wind speed of aerostatic torsional divergence decreases with the increase of wind fairing angle, but the scope of change is very small (R_V =0.995~1.015).

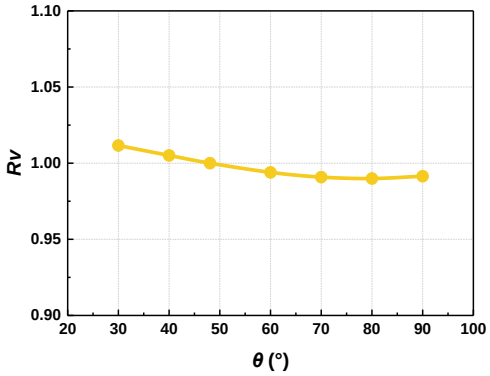

Figure 5.9: Influence of wind fairing angle on critical aerostatic instability wind speed

5.2.3.3 Web inclined angle

For different web inclined angles, the variation trends of C_D, C_L, and C_M remain consistent respectively, as shown in Figure 5.10, which is the same as the above cases.

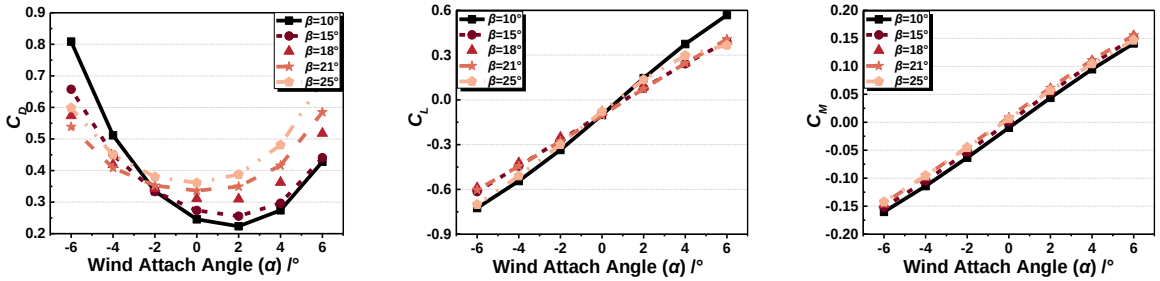

Figure 5.10: Trend of aerostatic coefficients change with wind attach angles under different web inclined angles

Figure 5.11 further analyzes the variation of aerostatic coefficients with the web inclined angles: 1) At 0° wind attack angle, C_D increases with the increase of web inclined angle, because the flow separation increases with the increase of web inclined angle, and therefore the drag coefficient also increases. In the case of other wind attack angles, the state of flow separation is dominated by other factors, thus producing a somewhat different trend in the variation of C_D with the web inclined angle. 2) Neither C_L nor C_M varies significantly with the web inclined angle, especially at 0° wind attack angle,

indicating that C_L and C_M are not sensitive to the change of web inclined angle.

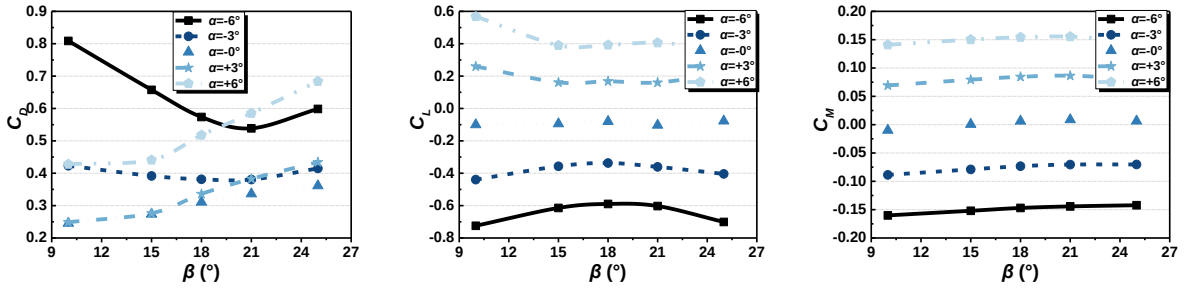

Figure 5.11: Trend of aerostatic coefficients change with web inclined angles under different wind attach angles

Figure 5.12 shows calculation results of two-dimensional aerostatic stability change with web inclined angle. It can be seen from the figure that the critical wind speed of aerostatic torsional divergence increases with the increase of web inclined angle, but the increase rate is slow when $\beta < 18°$.

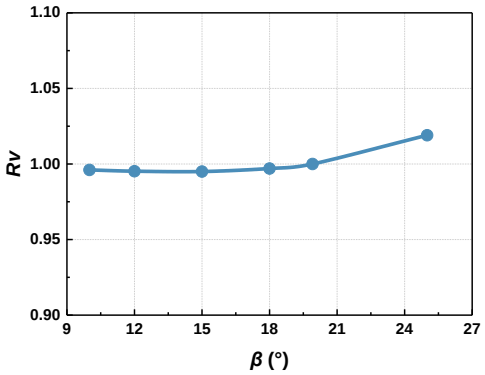

Figure 5.12: Influence of web inclined angle on critical aerostatic instability wind speed

5.3 Two-dimensional flutter stability evaluation

5.3.1 Two-dimensional flutter stability analysis model

For a bridge deck that is immersed in the incoming air flow, the flutter vibration was mainly driven by the self-excited force. The mechanical system of flutter can be described by a two degrees of freedom (DOFs) linear oscillator, free to vibrate in heaving *h(t)* and pitching *α(t)* modes, as shown in Figure 5.13. Based on the study performed by Scanlan and Tomko (1971), the wind-induced linear self-excited force on a bridge deck can be expressed modelled as the function of the vibration state, i.e., displacements and velocities in two DOFs using eight flutter derivatives (as shown in Equation 1.3.5).

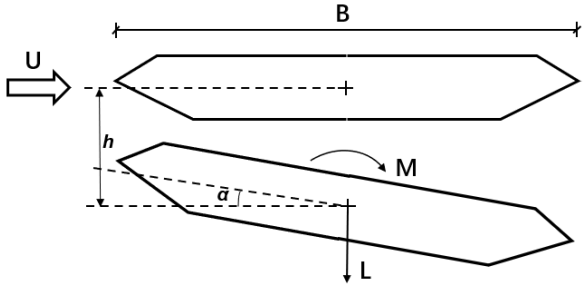

Figure 5.13: Reference system for displacements and self-excited forces

The equation of motion of the bridge deck can be described as:

$$m(\ddot{h}+2\xi_h\omega_h\dot{h}+\omega_h^2 h)=L_{se} \tag{5.3.1a}$$

$$I(\ddot{\alpha}+2\xi_\alpha\omega_\alpha\dot{\alpha}+\omega_\alpha^2\alpha)=M_{se} \tag{5.3.1b}$$

where m and I are the mass and the inertia moment of the bridge per unit length; ω_h and ω_α are the vertical bending and torsional circle frequencies of the model; ξ_h and ξ_α are the damping ratio of vertical bending and torsional modes respectively; L_{se} and M_{se} are the self-excited lift force and self-excited lift moment per unit length of model, respectively.

In the case of small displacement, by substituting Equation 5.3.1 into the frequency domain expressions of self-excited lift force and self-excited lift moment (Equation 1.3.5), the following equation can be obtained:

$$\frac{\ddot{h}}{B}+2\xi_h K_h\frac{\dot{h}}{B}+K_h^2\frac{h}{B}=\frac{\rho B^2}{m}\left[K_h H_1^*\frac{\dot{h}}{B}+K_\alpha H_2^*\dot{\alpha}+K_\alpha^2 H_3^*\alpha+K_h^2 H_4^*\frac{h}{B}\right] \tag{5.3.2a}$$

$$\ddot{\alpha}+2\xi_\alpha K_\alpha\dot{\alpha}+K_\alpha^2\alpha=\frac{\rho B^4}{I}\left[K_h A_1^*\frac{\dot{h}}{B}+K_\alpha A_2^*\dot{\alpha}+K_\alpha^2 A_3^*\alpha+K_h^2 A_4^*\frac{h}{B}\right] \tag{5.3.2b}$$

The dimensionless time parameter $s=tU/B$ is introduced, and the solution of the equation is assumed to be:

$$\frac{h}{B}=\frac{h_0}{B}e^{i\omega t}=\frac{h_0}{B}e^{iKs} \tag{5.3.3a}$$

$$\alpha=\alpha_0 e^{i\omega t}=\alpha_0 e^{iKs} \tag{5.3.3b}$$

By substituting Equation 5.3.3 into Equation 5.3.2, the equations for $\frac{h_0}{B}$ and α_0 can be obtained:

$$\left[-K^2+2i\xi_h K_h K+K_h^2-\frac{\rho B^2}{m}K^2(iH_1^*+H_4^*)\right]\frac{h_0}{B}-\frac{\rho B^2}{m}K^2(iH_2^*+H_3^*)\alpha_0=0 \tag{5.3.4a}$$

$$-\frac{\rho B^4}{I}K^2(iA_1^*+A_4^*)\frac{h_0}{B}+\left[-K^2+2i\xi_\alpha K_\alpha K+K_\alpha^2-\frac{\rho B^4}{I}K^2(iA_2^*+A_3^*)\right]\alpha_0=0 \tag{5.3.4b}$$

Introduce a new unknown number $X=\omega/\omega_h$, then Equation 5.3.4 is rewritten as

$$\left[X^2-2i\xi_h X-1+\frac{\rho B^2}{m}X^2(iH_1^*+H_4^*)\right]+\frac{\rho B^2}{m}X^2(iH_2^*+H_3^*)\alpha_0=0 \tag{5.3.5a}$$

$$\frac{\rho B^4}{I}X^2(iA_1^*+A_4^*)\frac{h_0}{B}+\left[X^2-2i\xi_\alpha\left(\frac{\omega_\alpha}{\omega_h}\right)X-\left(\frac{\omega_\alpha}{\omega_h}\right)^2+\frac{\rho B^4}{I}X^2(iA_2^*+A_3^*)\right]\alpha_0=0 \tag{5.3.5b}$$

To make the above equation has a non zero solution, the determinant of parameters is zero, so a

quadratic polynomial about X can be obtained. Assuming that X is always a real number in the critical flutter state, the real and imaginary parts of the quartic polynomial are both zero:

$$f(X,V_r) = A_{4R}X^4 + A_{3R}X^3 + A_{2R}X^2 + A_{1R}X + A_{0R} = 0 \tag{5.3.6a}$$

$$g(X,V_r) = A_{3I}X^3 + A_{2I}X^2 + A_{1I}X + A_{0I} = 0 \tag{5.3.6b}$$

where

$$A_{4R} = 1 + \frac{\rho B^2}{m}H_4^* + \frac{\rho B^4}{I}A_3^* + \frac{\rho^2 B^6}{mI}(H_4^*A_3^* - H_3^*A_4^* + H_2^*A_1^* - H_1^*A_2^*) \tag{5.3.7a}$$

$$A_{3R} = 2\xi_\alpha \frac{\omega_\alpha}{\omega_h}\frac{\rho B^2}{m}H_1^* + 2\xi_h \frac{\rho B^4}{I}A_2^* \tag{5.3.7b}$$

$$A_{2R} = -\left(\frac{\omega_\alpha}{\omega_h}\right)^2\left(1 + \frac{\rho B^2}{m}H_4^*\right) - \left(1 + \frac{\rho B^4}{I}A_3^*\right) - 4\xi_h\xi_\alpha\frac{\omega_\alpha}{\omega_h} \tag{5.3.7c}$$

$$A_{1R} = 0$$

(5.3.7d)

$$A_{0R} = \left(\frac{\omega_\alpha}{\omega_h}\right)^2 \tag{5.3.7e}$$

$$A_{3I} = \frac{\rho B^2}{m}H_1^* + \frac{\rho B^4}{I}A_2^* + \frac{\rho^2 B^6}{mI}(H_4^*A_2^* - H_2^*A_4^* + H_1^*A_3^* - H_3^*A_1^*) \tag{5.3.7f}$$

$$A_{2I} = -2\xi_\alpha\frac{\omega_\alpha}{\omega_h}\left(1 + \frac{\rho B^2}{m}H_4^*\right) - 2\xi_h\left(1 + \frac{\rho B^4}{I}A_3^*\right) \tag{5.3.7g}$$

$$A_{1I} = -\frac{\rho B^2}{m}H_1^*\left(\frac{\omega_\alpha}{\omega_h}\right)^2 - \frac{\rho B^4}{I}A_2^* \tag{5.3.7h}$$

$$A_{0I} = 2\xi_h\left(\frac{\omega_\alpha}{\omega_h}\right)^2 + 2\xi_\alpha\frac{\omega_\alpha}{\omega_h} \tag{5.3.7i}$$

By assuming different values of K, the solution of each equation is formed into a curve about X~K. The frequency of flutter critical point should satisfy both equations, so the intersection of two curves is the critical point where flutter occurs, i.e. the point (K_f, X_f), as shown in Figure 5.14.

The value of X, flutter frequency ω_f and critical flutter wind speed U_f corresponding to the critical flutter state can be calculated:

$$\omega_f = X_f \cdot \omega_h \tag{5.3.8a}$$

$$U_f = \frac{B \cdot \omega_f}{K_f} \tag{5.3.8b}$$

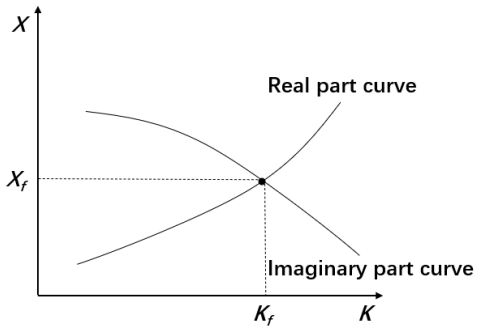

Figure 5.14: Architecture of the flutter critical point solution

5.3.2 Intelligent identification of flutter derivatives

The trained GBDT models are used to obtain the flutter derivatives of Runyang Bridge. The comparison of predictions with CFD calculations and experimental results is shown in Figure 5.15, and the specific prediction error (MRE) is shown in Table 5.2.

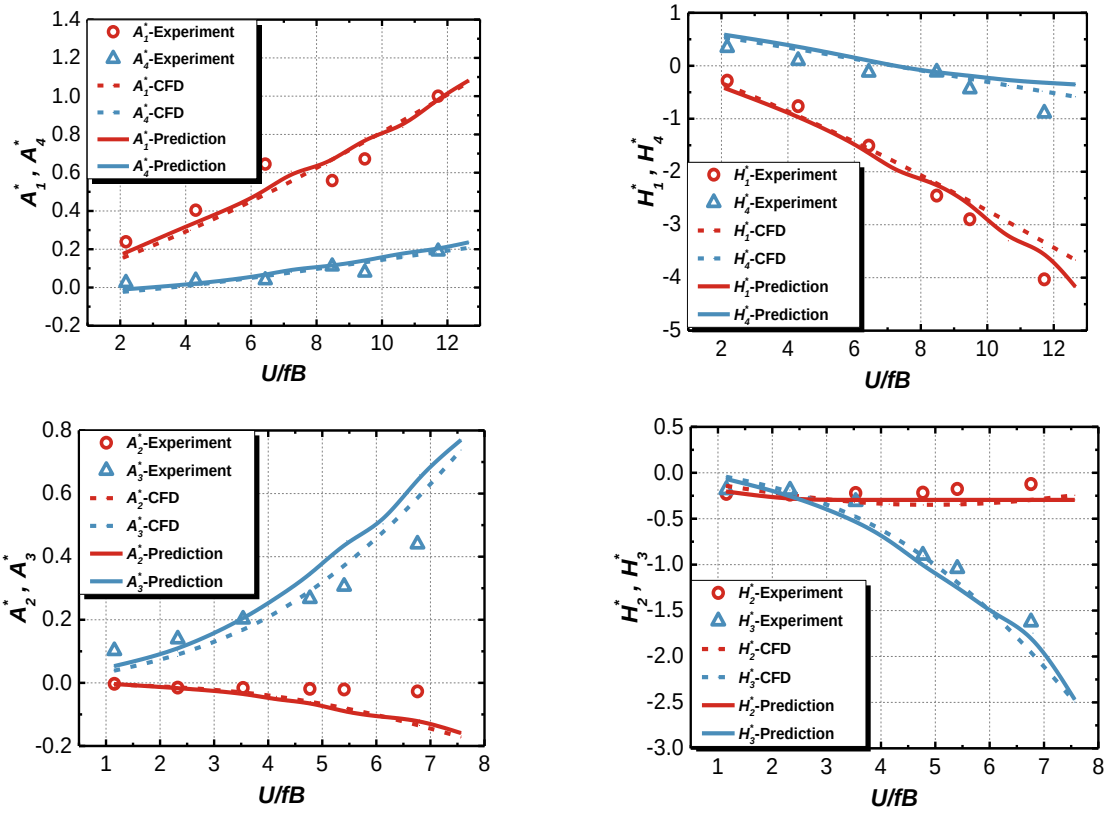

Figure 5.15: Prediction results of flutter derivatives for Runyang Bridge

Table 5.2: Prediction accuracy of flutter derivatives for Runyang Bridge

MRE	A_1^*	A_4^*	H_1^*	H_4^*	A_2^*	A_3^*	H_2^*	H_3^*	Mean
CFD	0.0082	0.1401	0.1383	0.3958	0.0746	0.0435	0.2094	0.0109	0.1520
Experiment	0.1606	0.2113	0.1950	0.2174	0.1812	0.1828	0.2070	0.1445	0.1875

The predicted flutter derivatives are used in the two-dimensional and three-degree-of-freedom flutter numerical calculation (Zhu and Chen, 2004) to obtain the critical flutter wind speed of the structure for further flutter stability analysis. As there are some errors in the flutter derivatives predicted by machine learning, we need to determine the extent to which these errors affect the critical flutter wind speed calculation first. Actually, several machine learning models were trained in this study based on different data division modes. The flutter derivatives prediction results with different errors can be obtained by different trained models and these errors are ultimately reflected in the critical flutter wind speed calculation as shown in Figure 5.16. It can be seen that even with an error of up to 25% in flutter derivatives prediction, the error in critical flutter wind speed calculation is only 10%. When the prediction error of flutter derivatives can be reduced to less than 15%, the calculation result of critical flutter wind speed is very close to the true value (measured by wind tunnel test), and the calculation error is less than 2%. This is due to the fact that different flutter derivatives have a major and minor effect on the critical flutter wind speed. If the prediction accuracy of important flutter derivatives is high, the critical flutter wind speed with high calculation accuracy can be obtained. It means there is no need to predict every flutter derivative accurately in the case of limited computing resource. This analysis further demonstrates that it is entirely feasible to identify flutter derivatives and perform flutter performance analysis by machine learning methods.

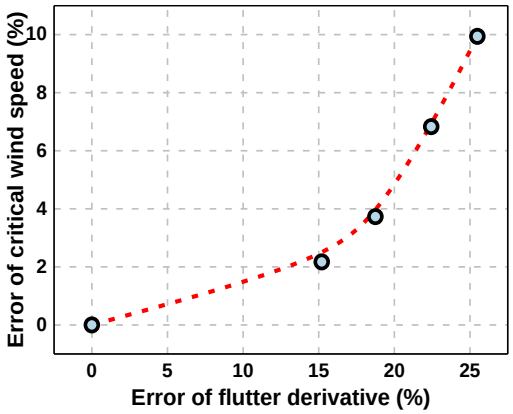

Figure 5.16: Error analysis of critical flutter wind speed

5.3.3 Critical flutter instability speed analysis based on two-dimensional model

For the cross-section shown in Figure 5.2, we can further analyze which flutter derivatives have a major impact on critical flutter wind speed by changing the magnitude of the flutter derivative sequentially. As shown in Figure 5.17, the horizontal axis represents the change ratio of parameters. $R>1$ indicates the parameter increases and $R<1$ indicates the parameter decreases. The longitudinal axis indicates the change of critical flutter wind speed (V) caused by parameter change. $R_V>1$ indicates that the critical flutter wind speed increases after parameter change and $R_V<1$ indicates that the critical flutter wind speed decreases. It can be seen from the figure that the main factors affecting the critical flutter

wind speed are A_1^*, A_2^*, A_3^* and H_3^*. This conclusion is consistent with the test and analysis results of Hong (2020). A_1^* and H_3^* represent the coupled vertical motion speed excited by the aerodynamic lift generated by the torsional motion displacement and the aerodynamic damping formed by the aerodynamic moment caused by the feedback. They make the torsional vibration modal damping decrease from positive to negative, which is the most essential reason for the vibration divergence. A_2^* represents the aerodynamic damping formed by the aerodynamic moment directly generated by the torsional motion speed, and the increase of A_2^* with the increase of wind speed will be beneficial to the stability of the system. The change of A_3^* also affects the critical flutter wind speed, but the influence is smaller than A_1^*, A_2^* and H_3^*. The critical flutter wind speed decreases with the increase of A_1^*, A_3^* and H_3^* and increases with the increase of A_2^*. The other flutter derivatives almost have no effect on the critical flutter wind speed. It should be noted that the conclusion above is not universal, and it is only for the given cross-section and the cross-sections with similar shape and dimension. To obtain accurate results of other structures, it is still necessary to use the trained models to repeat the given operation process, but it is comforting that this process is fast so it is very suitable for the preliminary analysis and design stage of wind-resistant performance.

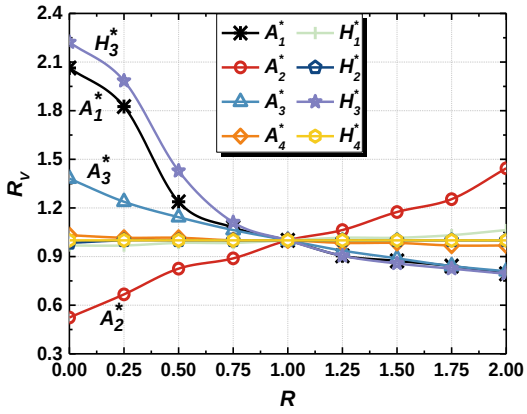

Figure 5.17: Sensitivity analysis of flutter derivatives

5.3.4 Sensitivity analysis of flutter derivatives to flutter instability

Since critical flutter wind speed calculation can be combined with the machine learning prediction process and high calculation accuracy can be obtained, the relationship between the shape of cross-section and the critical flutter wind speed can be analyzed by the trained machine learning models. The analysis results can provide a reference for the aerodynamic shape optimization of closed box girder. For this type of cross-section, there are not many factors affecting the aerodynamic shape without considering the influence of the ancillary facilities on the critical flutter wind speed in the construction stage. It is time-consuming and may not lead to better calculation results if every detail of closed box girder is taken into account. Therefore, this study only discusses three important parameters: ratio of width to depth, wind fairing angle and web inclined angle.

5.3.4.1 Ratio of width to depth

The ratio of width to depth of a closed box girder varies greatly. The width of cross-section varies from 30m to 50m and the height ranges from 2m to 5m. Taking a bridge with the width to depth ratio of 12.3 as an example. In order to reduce the workload of numerical calculation, it is assumed that the critical flutter wind speeds are proportional to different wind fairing angles and web inclined angles, so the wind fairing angle and web inclined angle are kept unchanged. The ratio of width to depth is adjusted only by changing the width of the cross-section.

The flutter derivatives with different ratios of width to depth are identified by the trained machine learning model first, and the results are shown in Figure 5.18. As the ratio of width to depth changes (B/H = 8~16), the flutter derivatives show a certain trend. Among them, the distribution trends of H_2^* and H_4^* under different reduced wind speeds change with the ratio of width to depth. For H_2^*, it decreases with the increase of reduced wind speed when $B/H \leq 12$, but it decreases and then increases with the increase of reduced wind speed when $B/H > 12$. H_4^* is opposite to H_2^*, it decreases with the reduced wind speed when $B/H \geq 12$ while increases first and then decreases with the reduced wind speed when $B/H < 12$. The other flutter derivatives show an increasing or decreasing trend with reduced wind speed, and the change in the ratio of width to depth does not affect the overall distribution trend.

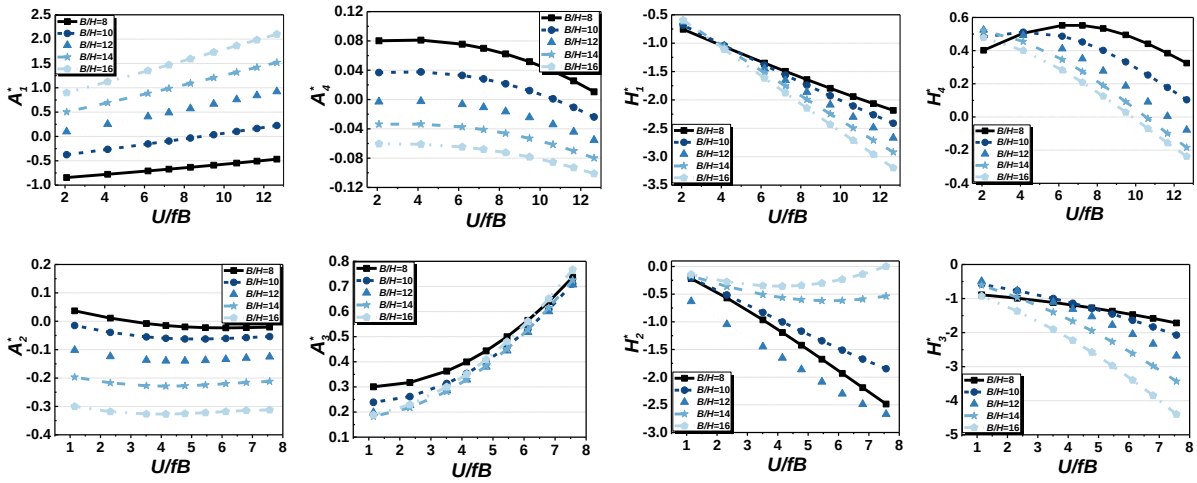

Figure 5.18: Trend of flutter derivatives change with ratios of width to depth

Next, the critical flutter wind speed under different ratios of width to depth is calculated by two-dimensional flutter numerical analysis. The result shows that the critical flutter wind speed decreases with the increase of width to depth ratio, which is consistent with the conclusion obtained by Zhang (2018). The variation law of critical flutter wind speed with the width to depth ratio and the comparison with Zhang's analysis are shown in Figure 5.19. In my study, it can also be found that the critical flutter wind speed decreases sharply when the ratio of width to depth is lower than 11, and the decrease trend of critical flutter wind speed gradually slows down with the increase of width to depth ratio when the ratio is greater than 11.

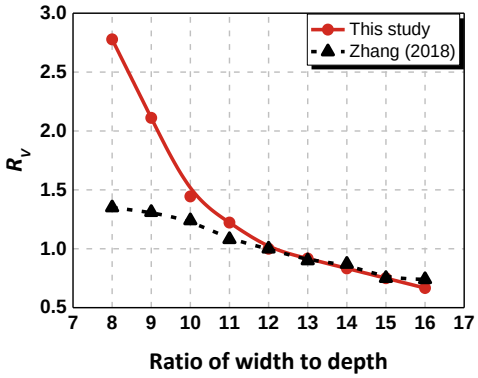

Figure 5.19: Influence of width to depth ratio on critical flutter wind speed

5.3.4.2 Wind fairing angle

Figure 5.20 gives the trend variation of each flutter derivative as the wind fairing angle changes. Different from the trend variation of flutter derivatives with the ratio of width to depth, the distribution trends of A_4^* and H_4^* under different reduced wind speeds change with the wind fairing angle obviously. For A_4^*, it decreases with the increase of reduced wind speed when $\theta < 60°$ and increases with the increase of reduced wind speed when $\theta > 60°$. When θ is around 60°, the distribution of A_4^* belongs to the intermediate transition situation. The distribution trend of H_4^* changes with the wind fairing angle is similar to that changes with the ratio of width to depth. It decreases with the reduced wind speed when $\theta \leq 60°$, and it increases first and then decreases with the reduced wind speed when $\theta > 60°$. The other flutter derivatives show an increasing or decreasing trend with reduced wind speed, and the change in the wind fairing angle does not affect the overall distribution trend.

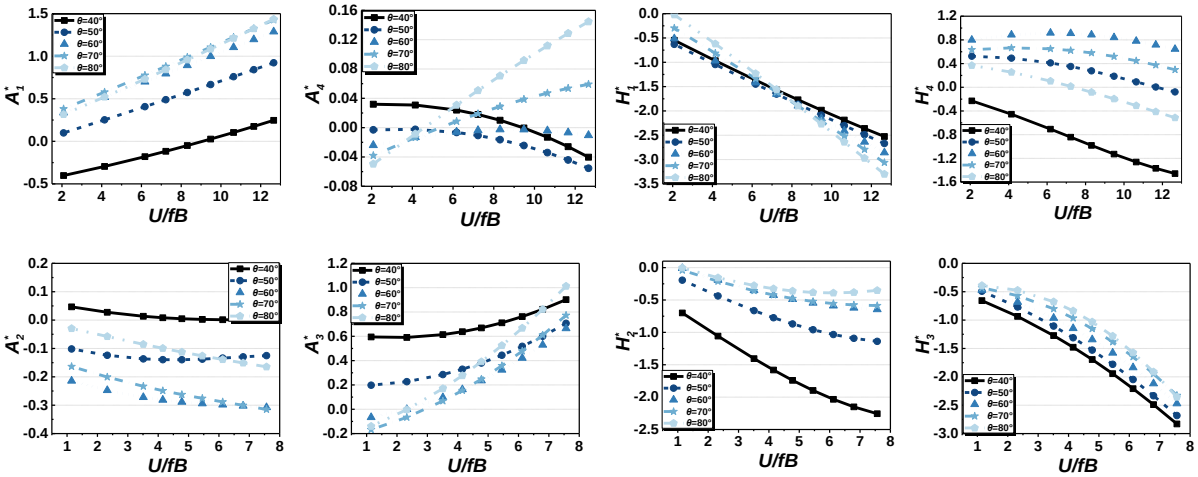

Figure 5.20: Trend of flutter derivatives change with wind fairing angles

The installation of wind fairing can improve the flow pattern around both ends of the cross-section, making the cross-section tend to streamline, which reduces drag force and vortex shedding to improve the flutter stability. Figure 5.21 shows the rule of critical flutter wind speed changing with the wind fairing angle. It can be seen that the critical flutter wind speed first increases and then decreases with

the increase of the wind fairing angle, and reaches the peak at around 60°. Xian and Liao (2008) designed several wind fairings with different angles for a specific cross-section and analyzed the impact of wind fairing angle on the critical flutter wind speed based on wind tunnel test. The result showed that the critical flutter wind speed first increased and then decreased with the increase of wind fairing angle (θ) (from 30° to 60°). This trend is consistent with the results obtained in this study ($40° < \theta < 90°$). The experimental result of wind fairing angle larger than 60° is not given by Xian and Liao. Since the prototype section in their study is somewhat different from the closed box girder in this paper, the optimal wind fairing angles are also different. Although the conclusion is limited, which is only applicable to the closed box girder section with specific width to depth ratio and web inclined angle, the influence regularity of wind fairing angle on critical flutter wind speed can still be used as a reference for the optimization of aerodynamic shape.

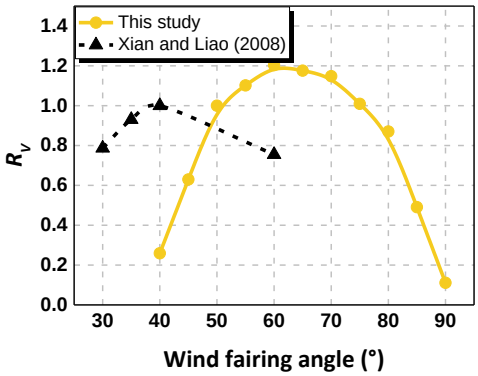

Figure 5.21: Influence of wind fairing angle on critical flutter wind speed

5.3.4.3 Web inclined angle

Different from the trend variation of flutter derivatives with the ratio of width to depth and wind fairing angle, the distribution trends change with the web inclined angles are A_2^*, A_4^* and H_2^*. The overall increasing or decreasing trends of the other flutter derivatives do not change with the web inclined angles. The specific distribution trends and change situations are shown in Figure 5.22.

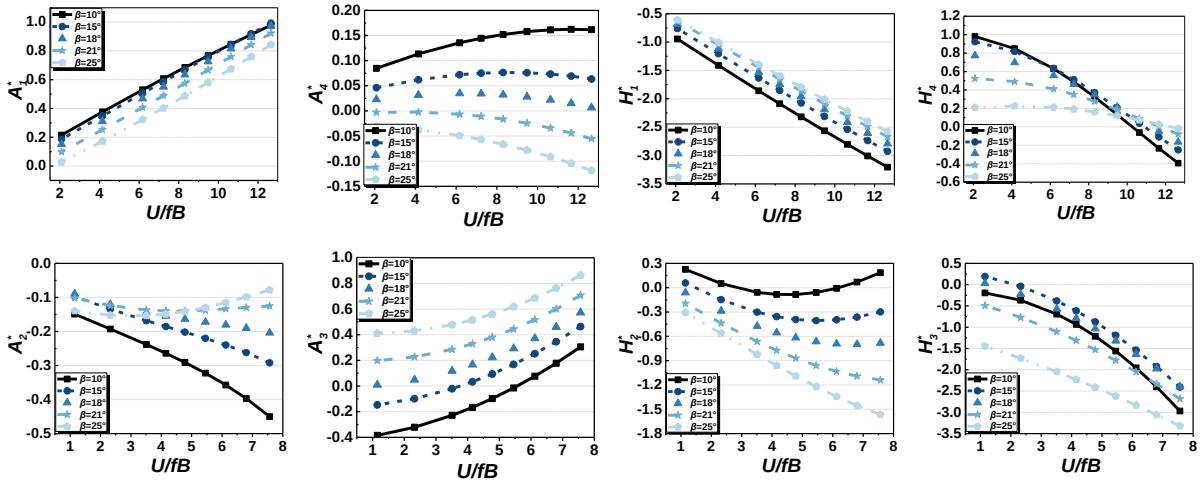

Figure 5.22: Trend of flutter derivatives change with web inclined angles

Li et al. (2018) studied the influence of web inclined angle on critical flutter wind speed by wind tunnel tests. The conclusion is that for a closed box girder with the width to height ratio of 11, the larger the web inclined angle is, the smaller the critical flutter wind speed is. For the closed box girder with the width to height ratio of 7, the influence of web inclined angle on critical flutter wind speed is very small. The width to height ratio of the prototype structure in this paper is 12.3. When the web inclined angle is changed from 10° to 25°, the influence regularity of web inclined angle on critical flutter wind speed is shown in Figure 5.23. It can be seen that the critical flutter wind speed decreases with the increase of web inclined angle, which is consistent with Li's research, and this trend is almost linear. However, during the actual design and construction, the specific web inclined angle should be determined according to the actual engineering because it will significantly increase the manufacturing difficulty if the web inclined angle is too small.

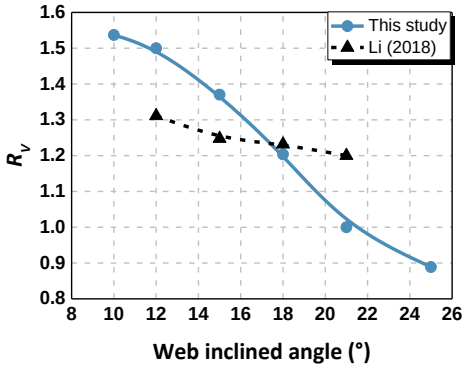

Figure 5.23: Influence of web inclined angle on critical flutter wind speed

5.4 Conclusion

In this chapter, two-dimensional wind-resistant stability analysis is analyzed based on a specific calculation case of a long-span bridge with closed box girder, which further validates the feasibility of applying the machine learning methods and models introduced above to the analysis of wind-resistance of bridges.

In the analysis of two-dimensional aerostatic stability, the trained machine learning models are used to predict the aerostatic coefficients and the sensitivity analysis shows that the trend of C_D of closed box girder decreases and then increases with the change of wind attack angle, while C_L and C_M increase with wind attack angle. The variation trends of aerostatic coefficients remain constant respectively under different ratios of width to depth, wind fairing angle or web inclined angle. In addition, the reason why the aerostatic coefficients change with these characteristic dimensions of cross-section is further analyzed from the perspective of flow field. The two-dimensional aerostatic stability analysis based on the Runyang suspension bridge shows that the shape of the main girder cross-section has a significant impact on the critical wind speed of torsional divergence.

In the analysis of two-dimensional flutter stability, the error analysis of critical flutter wind speed reveals that the machine learning prediction error of flutter derivatives will be weakened in the numerical calculation of critical flutter wind speed. If the prediction error of flutter derivatives can be reduced to less than 15%, the calculation result of critical flutter wind speed will be extremely near to the true value. The sensitivity analysis of flutter derivatives shows that A_1^*, A_2^*, A_3^* and H_3^* have great influence on critical flutter wind speed of closed box girder. The critical flutter wind speed decreases with the increase of A_1^*, A_3^* and H_3^* and increases with the increase of A_2^*. The influence of geometric shape of cross-section on critical flutter wind speed is also analyzed, which provides a reference for the aerodynamic shape optimization of closed box girders. The findings demonstrate that the critical flutter wind speed decreases with the increase of width to depth ratio of the closed box girder. In the range of 30°-100°of wind fairing angles, the critical flutter wind speed first increases and then decreases with the increase of angle, and reaches the peak at around 60°. The critical flutter wind speed decreases with an increase in web inclined angle and is almost linear for a particular ratio of width to depth.

CHAPTER 6

6 Three-dimensional wind-resistant stability evaluation

6.1 Background

Based on the previous chapter, this chapter further discusses the three-dimensional wind-resistant stability of bridges, focusing on the evaluation of aerostatic stability and flutter stability.

Currently, aerostatic stability analysis of long-span bridges is mainly based on two-dimensional methods, but some bridges are located in complex terrain area and the natural wind environment is also very complex, so it is necessary to consider the dual non-linear factors of structure and static wind load. A three-dimensional non-linear aerostatic stability analysis method for long-span bridges is established in this chapter, combining the aerostatic coefficients predicted by the trained machine learning models to calculate the aerostatic displacement and the critical wind speed of aerostatic instability of the Runyang Bridge. The program and calculation process are verified by comparing calculation results with experimental results.

For flutter stability analysis, the limitation of two-dimensional flutter analysis is more obvious. As it considers at most the coupling of two pure modals, vertical and torsional, while many bridges have impure and multiple modals participating in flutter, so three-dimensional flutter theory is needed. By using three-dimensional finite element method and incorporating aerodynamic loads, three-dimensional flutter stability analysis can be carried out. In this chapter, the theoretical basis of three-dimensional multi-modal flutter stability analysis was first introduced, and then the critical flutter wind speed of the Runyang Bridge was then calculated. The effectiveness of the calculation and analysis was verified by comparing it with the results of wind tunnel test and two-dimensional numerical calculation.

6.2 Three-dimensional aerostatic stability evaluation

6.2.1 Three-dimensional non-linear aerostatic stability analysis method

The aerostatic stability for bridge structures belongs stability problem, so the non-linearity of material can be ignored and only the non-linearity of geometric considered, which can be expressed by the equilibrium equation:

$$\left[K_e + K(\delta)\right] \cdot \delta = F(\alpha, U) \tag{6.2.1}$$

where K_e is the inherent linear elastic stiffness matrix of the structure, $K(\delta)$ is the geometric stiffness matrix resulting from the deformation of the structure, δ is the deformation of the structure and $F(\alpha,U)$ is the wind load on the structure when the wind speed is U and the effective wind attack angle is α.

Cheng et al. (2000) considered the non-linearity of the structure and used an iterative method combining internal and external increments to solve for the critical wind speed of aerostatic instability. The set of non-linear incremental equations is:

$$\left(\left[K_e\right] + \left[K_{\sigma_{j-1}}\left(\delta_{j-1}\right)\right]\right) \cdot \left\{\Delta\delta_j\right\} = \left\{F_j\left(\alpha_j, U_i\right)\right\} - \left\{F_{j-1}\left(\alpha_{j-1}, U_{j-1}\right)\right\} \tag{6.2.2}$$

where $\left[K_{\sigma_{j-1}}\left(\delta_{j-1}\right)\right]$ is the geometric stiffness matrix of the element at the (j-1)th iteration; α_j is the effective wind attack angle at the j^{th} iteration; $F_j\left(\alpha_j, U_i\right)$ is the wind load at the j^{th} iteration when the average wind speed is U_i.

A reasonable convergence criterion must be determined for the iterative solution. In this paper, the Euclidean norm of aerostatic coefficients is used as the convergence criterion:

$$\max\left\{\frac{\left\|C_i(\alpha_j, U_j) - C_i(\alpha_{j-1}, U_{j-1})\right\|_2}{\left\|C_i(\alpha_{j-1}, U_{j-1})\right\|_2}\right\} \le \varepsilon \quad (i = 1, 2, ..., m) \tag{6.2.3}$$

where $\|...\|_2$ is the Euclidean norm of the vector; $C_i(\alpha_j, U_j)$ is the vector of aerostatic coefficients for the i^{th} unit subject to static wind action corresponding to the end of the j^{th} iteration step; $C_i(\alpha_{j-1}, U_{j-1})$ is the vector of static wind coefficients for the i^{th} unit subject to static wind action corresponding to the end of the (j-1)th iteration step; ε is the iteration accuracy; m is the number of units subject to static wind action.

Equation (6.2.1) can be understood as the final deformation of the structure under any wind speed, which will achieve stability and reach an equilibrium state before aerostatic instability. After reaching the critical wind speed, this equilibrium state cannot be maintained and Equation (6.2.2) cannot converge, resulting in aerostatic instability of the bridge structure. In practical applications, the nonlinear finite element method of internal and external incremental iteration is often used to calculate the critical wind speed of aerostatic torsional divergence of long-span bridge. The calculation steps are as follows:

(1) Given the initial wind speed and initial wind attack angle, as well as the aerostatic coefficients of the main girder cross-section.

(2) Calculate the wind load and apply it to the structure.

(3) Perform a non-linear solution using the full Newton-Rapson method to obtain the structural displacements, extract the angular displacements and calculate the effective wind attack angle.

(4) Repeat steps (2)~(3) until the Euclidean norm of the aerostatic coefficient is less than the allowable value and the calculation converges. Then the structure can reach equilibrium at this wind speed.

(5) Increase the wind speed in the set step and repeat steps (3)~(4).

(6) If the calculation does not converge, the wind speed in the previous step will be the initial state, and the step size will be subdivided and recalculated.

(7) Continuously reduce the step size and repeat steps (2)~(6). When the wind speed increment is less than the predetermined value, the current wind speed is considered as the critical wind speed for the aerostatic instability of the bridge.

6.2.2 Critical aerostatic instability speed analysis with three-dimensional method

In this part, the Runyang Bridge (south branch suspension bridge) is still used as an example of calculation, and its architecture is shown in Figure 5.2. The three-dimensional finite element model of the bridge was established using the commercial software ANSYS. Beam188 was used to simulate the main girder, tower and pier, Link10 was used to model the cable-stayed wire, and multi-segment cable unit was used to consider the influence of the drape and geometric non-linearity of wires. The finite element model is shown in Figure 6.1, and Table 6.1 gives the calculation results of dynamic characteristics of the bridge.

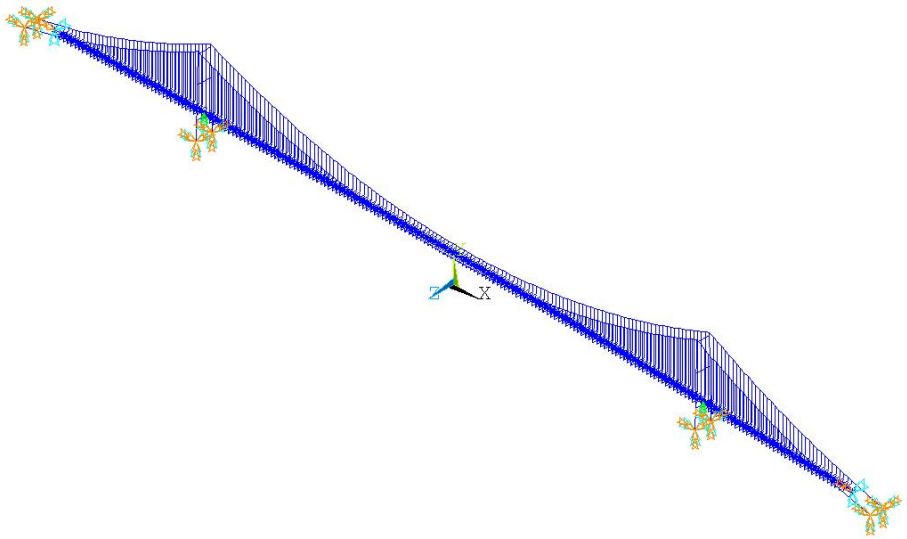

Figure 6.1: Finite element model of the Runyang Bridge

Table 6.1: Dynamic characteristics of the Runyang Bridge

Modal	Natural frequency (Hz)
1st-order anti-symmetrical vertical bending of main girder	0.08843
1st-order symmetrical vertical bending of main girder	0.12412
1st-order symmetric lateral bending of main girder	0.04892
1st-order anti-symmetric lateral bending of main girder	0.12287
1st-order symmetric torsion of main girder	0.23079
1st-order anti-symmetric torsion of main girder	0.26977

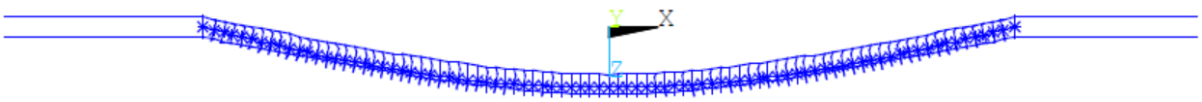

(a) Lateral bending

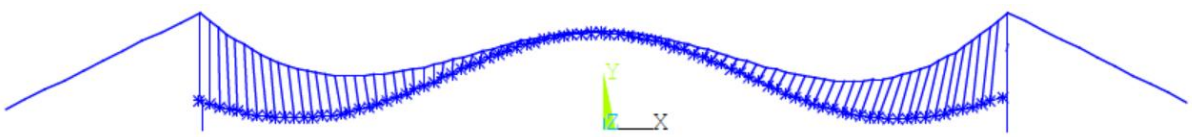

(b) Vertical bending

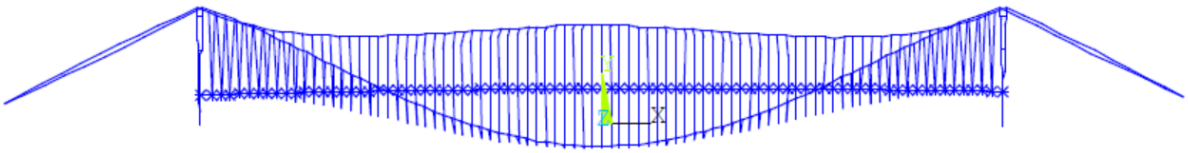

(c) Torsion

Figure 6.2: Vibration mode of main modals of Runyang Bridge

The aerostatic response in the mid-span of the Runyang Bridge was calculated using a three-dimensional non-linear aerostatic stability analysis program. The aerostatic coefficients of main girder involved in the calculation can generally be obtained from wind tunnel test or numerical simulation. In this paper, the aerostatic coefficients of this cross-section, which were predicted based on the aforementioned machine learning models, are used in the three-dimensional non-linear aerostatic stability analysis.

Figure 6.3 shows the variation curves of lateral, vertical and torsional displacements at the mid-span of main girder with increasing wind speed at 0° wind attack angle. As shown in the figure, the aeroelastic instability pattern of this closed box girder has the significant characteristic of spatially coupled deformation, where the lateral, vertical and torsional displacements increase non-linearly with the increase of wind speed, and diverge at critical wind speeds. Figure 6.3 also presents the comparison between the aerostatic instability calculation result based on machine learning prediction and that based on wind tunnel test measurement. The main girder displacements at the mid-span and the variation trend with increasing wind speed are basically the same between two calculation types, and the critical wind speed of aerostatic instability is also similar, which further demonstrates the feasibility of using machine learning methods for wind-resistant stability analysis of bridge structure. Table 6.2 shows the comparison of critical wind speed of aerostatic instability between two-dimensional and three-dimensional methods. It can be seen that two-dimensional analysis overestimates the aerostatic stability of the structure in most cases. In general, using two-dimensional method will bias the wind-resistance design towards insecurity, and the three-dimensional aerostatic stability analysis is more reasonable.

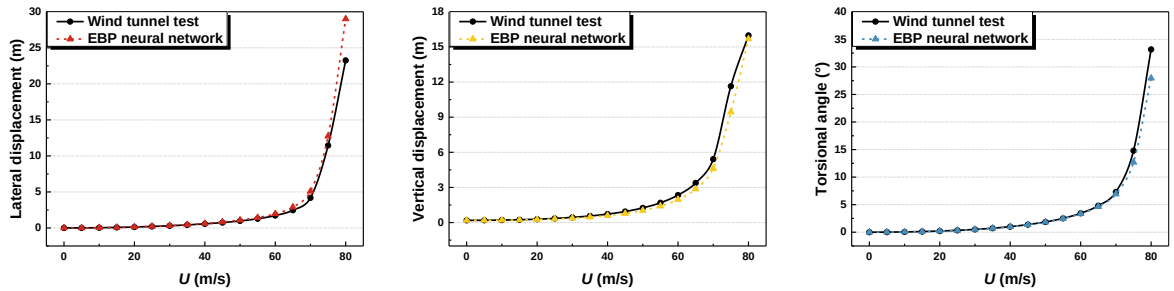

Figure 6.3: Curve of mid-span displacement and wind speed

Table 6.2: Comparison of two-dimensional and three-dimensional aerostatic stability analysis

Section No.	2D critical wind speed of aerostatic instability	3D critical wind speed of aerostatic instability	2D vs 3D
1	82.4m/s	78m/s	-5.64%
2	72.2m/s	80.8m/s	10.64%
3	63.3m/s	87m/s	27.24%
4	81.9m/s	76m/s	-7.76%
5	81.6m/s	80.5m/s	-1.37%
6	82.2m/s	79.6m/s	-3.27%
7	84m/s	81.7m/s	-2.82%

6.2.3 Sensitivity analysis of three-dimensional aerostatic stability

Like the two-dimensional aerostatic stability analysis, the influence of the cross-section shape of main girder on the critical wind speed of aerostatic instability was analyzed in the three-dimensional aerostatic stability calculation. Three important feature sizes of cross-section (H/B, θ and β) were also considered, and the results of two-dimensional and three-dimensional aerostatic torsional divergence analysis are compared.

6.2.3.1 Ratio of width to depth

Figure 6.4 shows the results of the lateral, vertical, and torsional displacements of the main girder at the mid-span, which vary with wind speeds under different ratios of width to depth, based on the three-dimensional aerostatic stability calculation of the Runyang Bridge. It can be seen that the lateral displacement, vertical displacement and torsional angles of the main girder all increase non-linearly with the increase of wind speed from the figure, and show a divergent increase at the critical wind speed. Under different ratios of width to depth, this trend remains unchanged.

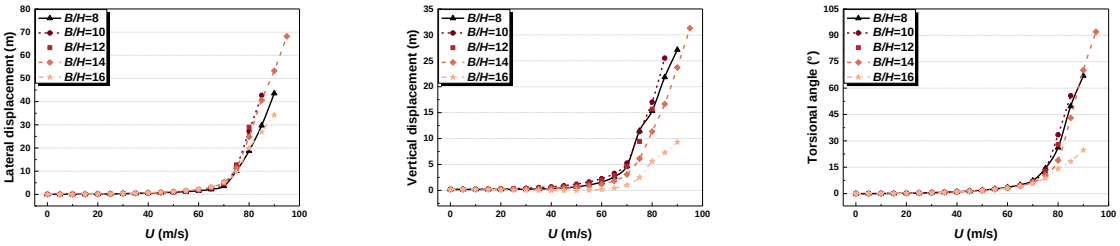

Figure 6.4: Curve of mid-span displacement under different ratios of width to depth

Figure 6.5 shows the variation patterns of lateral, vertical, and torsional divergence critical wind speeds with ratios of width to depth, respectively. It can be found that the aerostatic instability critical wind speed of this structure gradually increases with the increase of width to depth ratio in the range of $10<B/H<16$. When the ratio of width to depth increases, the cross-section is more streamlined, which can effectively reduce the drag coefficient and lift coefficient. The displacement of each wind speed point is also reduced, so as to achieve the purpose of increasing the critical wind speed of aerostatic instability. Figure 6.6 gives the comparison between two-dimensional and three-dimensional aerostatic

torsional divergence calculation results. It shows that the two-dimensional analysis overestimates the aerostatic stability performance of the structure, especially when $B/H < 12$. This is because the lift force and lift moment of the girder are the main factors affecting the aerostatic instability of suspension bridge, and the two-dimensional aerostatic stability analysis does not consider all the gradients of moment coefficient, which will overestimate the aerostatic stability of the structure. The three-dimensional aerostatic stability analysis considers the above factors so the calculation results are more reasonable.

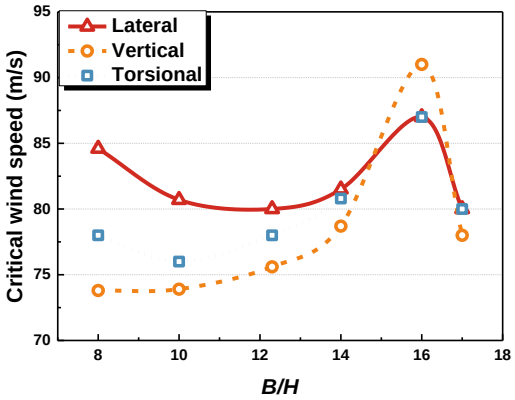

Figure 6.5: Curve of critical wind speed of aerostatic instability change with ratios of width to depth

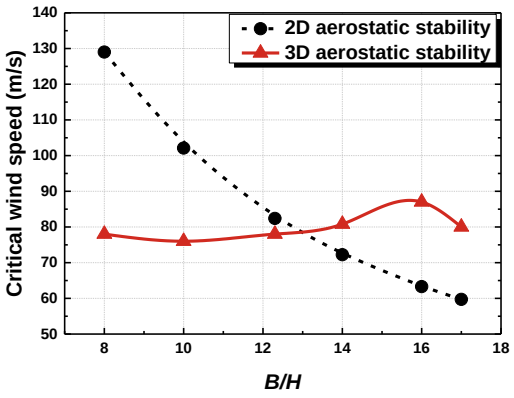

Figure 6.6: Comparison of critical wind speed of aerostatic instability change with ratios of width to depth

6.2.3.2 Wind faring angle

Figure 6.7 shows the results of the lateral, vertical and torsional displacements at the mid-span of the main girder calculated by three-dimensional aerostatic stability analysis, and they vary with wind speed at different wind fairing angles. The displacement in each direction still increases non-linearly with the increasing wind speed and ultimately diverges, and the trend remains unchanged at different wind fairing angles.

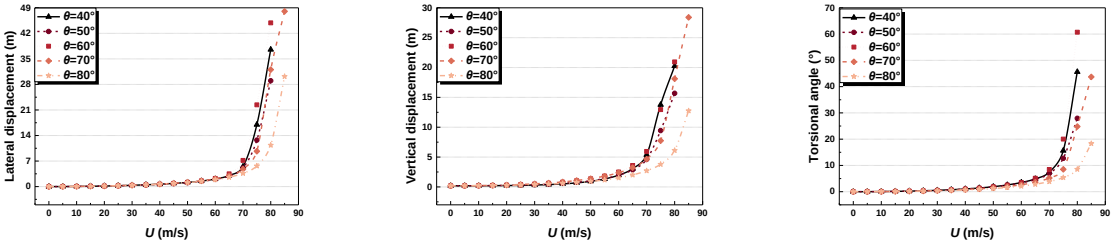

Figure 6.7: Curve of mid-span displacement under different wind fairing angles

Figure 6.8 shows the variation pattern of lateral, vertical and torsional divergence critical wind speeds with wind fairing angles. The aerostatic instability critical wind speed roughly increases with the increase of wind fairing angle. However, due to existing data limitations, machine learning models can only effectively predict the aerostatic coefficients of closed box girder within the range of $30°<\theta<90°$. Therefore, analyzing the variation pattern of aerostatic instability critical wind speed with wind fairing angle is only limited to the range of $30°<\theta<90°$ currently. Figure 6.9 gives the comparison between two-

dimensional and three-dimensional aerostatic torsional divergence calculation results. Consistent with the previous analysis, the two-dimensional analysis overestimates the aerostatic stability of the structure, especially when $\theta < 70°$. Using the two-dimensional calculated critical wind speed of aerostatic instability in wind-resistance design will bias the design towards insecurity, and the three-dimensional aerostatic stability analysis is more reasonable.

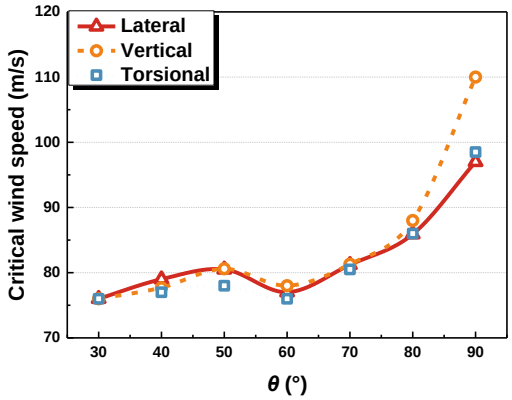

Figure 6.8: Curve of critical wind speed of aerostatic instability change with wind fairing angles

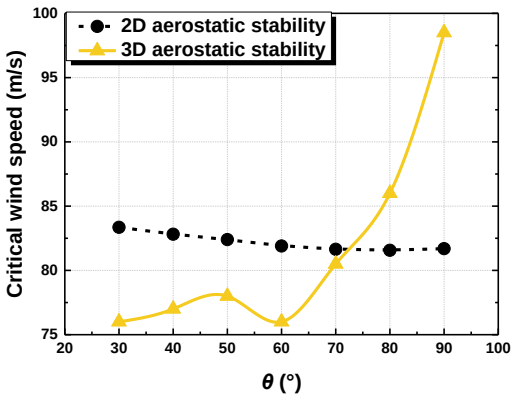

Figure 6.9: Comparison of critical wind speed of aerostatic instability change with wind fairing angles

6.2.3.3 Web inclined angle

The calculation results of the three-dimensional aerostatic stability of the mid-span displacements of the main girder in each direction under different web inclined angles are given in Figure 6.10. The lateral, vertical and torsional displacements increase with the increase of wind speed, and the trend remains unchanged at different web inclined angles, which is consistent with the change trend in width to depth ratio and wind fairing angle.

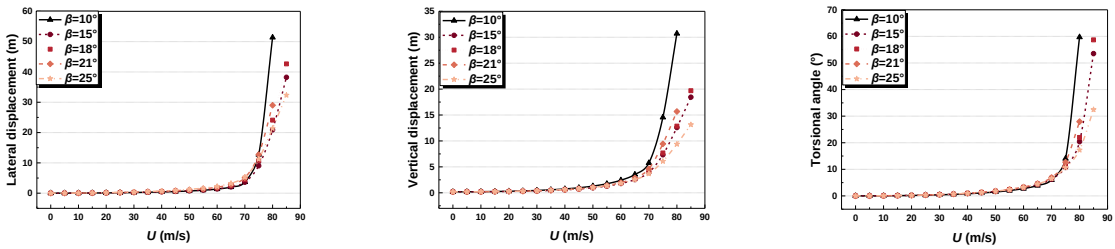

Figure 6.10: Curve of mid-span displacement under different web inclined angles

Figure 6.11 shows that the critical wind speed of lateral, vertical and torsional divergence fluctuates with the web inclined angle, but the fluctuation range is small. According to the previous analysis, the lift coefficient and moment coefficient of closed box girder are not sensitive to the web inclined angle, so the calculated critical wind speed of aerostatic instability is also not obvious to the web inclined angle. Figure 6.12 gives the comparison between two-dimensional and three-dimensional aerostatic torsional divergence calculation results. It can be seen from the figure that two-dimensional analysis overestimates the aerostatic stability of the structure under any setting of web inclined angles.

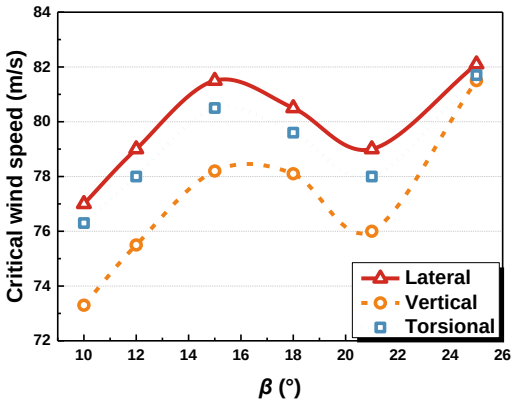

Figure 6.11: Curve of critical wind speed of aerostatic instability change with web inclined angles

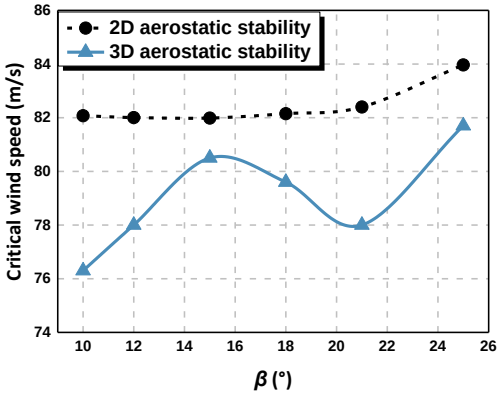

Figure 6.12: Comparison of critical wind speed of aerostatic instability change with web inclined angles

6.3 Three-dimensional flutter stability evaluation

As the span of bridge increases, the influence of lateral vibration of the main girder on aerodynamic performance also increases. The self-excited aerodynamic force per unit length of the main girder can be calculated by Equation (1.3.6), and the three-dimensional flutter analysis diagram is shown in Figure 6.10. The flutter derivatives of the main girder cross-section can be identified through wind tunnel tests, but it is difficult to accurately identify the 18 flutter derivatives through free vibration method. Moreover, the existing wind tunnel test data is insufficient to support the training of machine learning models, so based on the 8 flutter derivatives A_i^* and H_i^* (i=1~4) in this paper, the other 10 flutter derivatives are simplified according to the proposed hydrostatic theory (Chen et al., 2000):

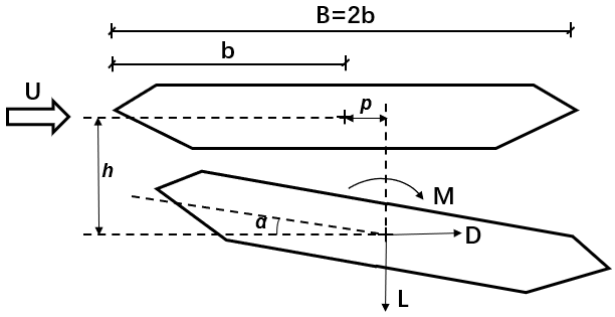

Figure 6.13: three-dimensional flutter analysis model

$$P_1^* = -\frac{1}{K}C_D,\ P_2^* = \frac{1}{2K}C_D^{'},\ P_3^* = \frac{1}{2K^2}C_D^{'},\ P_5^* = \frac{1}{2K}C_D^{'},\ H_5^* = \frac{1}{K}C_L,\ A_5^* = -\frac{1}{K}C_M \tag{6.3.1a}$$

$$P_4^* = P_6^* = H_6^* = A_6^* = 0 \tag{6.3.1b}$$

where C_D, C_L and C_M are the drag coefficient, lift coefficient and moment coefficient respectively; α is the incoming wind attach angle; L, B and H are the length, width and depth of the cross-section respectively; $C_D^{'} = dC_D / d\alpha$.

Equation (1.3.6) can be expressed in plural form as (Casero et al., 1999):

$$D_{se}(t)=\omega^2\rho B^2\left(C_{Dh}h+C_{Dp}p+BC_{D\alpha}\alpha\right) \tag{6.3.2a}$$

$$L_{se}(t)=\omega^2\rho B^2\left(C_{Lh}h+C_{Lp}p+BC_{L\alpha}\alpha\right) \tag{6.3.2b}$$

$$M_{se}(t)=\omega^2\rho B^2\left(BC_{Mh}h+BC_{Mp}p+B^2C_{M\alpha}\alpha\right) \tag{6.3.2c}$$

where $C_{rs}(r=L,M,D;\ s=h,p,\alpha)$ are self-excited force coefficients in plural form:

$$C_{Lh}=H_4^*+iH_1^*, C_{Lp}=H_6^*+iH_5^*, C_{L\alpha}=H_3^*+iH_2^* \tag{6.3.3a}$$

$$C_{Mh}=A_4^*+iA_1^*, C_{Mp}=A_6^*+iA_5^*, C_{M\alpha}=A_3^*+iA_2^* \tag{6.3.3b}$$

$$C_{Dh}=P_6^*+iP_5^*, C_{Dp}=P_4^*+iP_1^*, C_{D\alpha}=P_3^*+iP_2^* \tag{6.3.3c}$$

Using the finite element method for flutter analysis, the motion equation of the structure in the air without considering the buffeting forces can be expressed as

$$M\ddot{X}+C\dot{X}+KX=F_{\text{se}} \tag{6.3.4}$$

where M, C and K are the mass matrix, damping matrix and stiffness matrix of the structure respectively; $\ddot{X}$, $\dot{X}$ and X denote the displacement vector, velocity vector and acceleration vector of the structural system; F_{se} is the vector of self-excited aerodynamic forces in the structural system.

In the finite element analysis, the main girder is discretized into spatial beam units and the self-excited forces F_{se} distributed along the main girder can be equivalently converted to the beam unit nodes as follows:

$$F_{se}^e=\omega^2A_{se}^eX^e \tag{6.3.5}$$

where F_{se}^e is the vector of self-excited forces of the main beam unit and X^e is the displacement vector of main beam unit nodes with the degrees of freedom and positive direction shown in Figure 6.11.

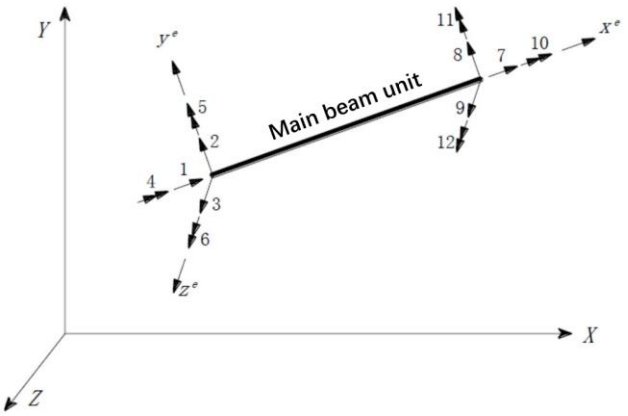

Figure 6.14: Degrees of freedom and positive direction of main beam unit nodes

In Equation (6.3.5), A_{se}^e is the matrix of self-excited forces of the main beam unit, and the matrix of self-excited forces of the main beam unit of length L can be expressed as

$$A_{se}^{e}=\begin{bmatrix} A_1 & 0 \\ 0 & A_1 \end{bmatrix} \tag{6.3.6}$$

where $A_1=\frac{1}{2}\rho B^2 L\begin{bmatrix} 0 & 0 & 0 & 0 & 0 & 0 \\ 0 & C_{Lh} & C_{Lp} & BC_{L\alpha} & 0 & 0 \\ 0 & C_{Dh} & C_{Dp} & BC_{D\alpha} & 0 & 0 \\ 0 & BC_{Lh} & BC_{Lp} & B^2C_{L\alpha} & 0 & 0 \\ 0 & 0 & 0 & 0 & 0 & 0 \\ 0 & 0 & 0 & 0 & 0 & 0 \end{bmatrix}$.

The matrix of self-excited forces of the main beam unit in the local coordinate system is converted to the overall coordinate system to form the matrix of self-excited forces of the structure:

$$F_{se}=\omega^2 A_{se} X \tag{6.3.7}$$

where A_{se} is a plural matrix and it is the total matrix of self-excited forces of the structure.

6.3.1 Three-dimensional multi-mode flutter stability analysis method

Three-dimensional multi-modal flutter analysis method treats the bridge structure and surrounding flow as an interactive whole, thereby transforming the flutter problem of the system into a plural eigenvalue solution problem (Ding, 2001). According to Equation (6.3.4) ~ (6.3.7), the motion control equation of the structure can be expressed by the plural matrix representation of self-excited forces:

$$M\ddot{X}+C\dot{X}+KX=\omega^2 A_{se} X \tag{6.3.8}$$

Introducing $\mathrm{X}=\mathrm{R}e^{st}$, where R represents the plural modal response of the structural system, s represents the corresponding plural frequency, $s=(-\xi+i)\omega$, ξ and ω are the damping ratio and circular frequency of the plural modal of the structural system. Substituting $\mathrm{X}=\mathrm{R}e^{st}$ into Equation (6.3.8), the characteristic equation of the structural system is:

$$\left(s^2M+sC+K-\omega^2 A_{se}\right)\mathrm{R}e^{st}=0 \tag{6.3.9}$$

The plural modal response of the structure is assumed to be represented by the superposition of the first m orders of natural modals of the structure:

$$R=\Phi \mathrm{q} \tag{6.3.10}$$

where Φ represents the $n\times m$ orders natural modal matrix of the structure, n is the number of degrees of freedom, m is the natural modal order, and q is the generalized coordinate vector of the m^{th} row.

Substitute Equation (6.3.10) into Equation (6.3.9) and multiply by Φ^T on the left side:

$$\left(s^2 I+\omega^2 \overline{\mathrm{A}}_{se}+s\overline{C}+\Lambda\right)\mathrm{q}e^{st}=0 \tag{6.3.11}$$

where I is the unit matrix, $\overline{\mathrm{A}}_{se}=\Phi^T \mathrm{A}_{se}\Phi$, $\overline{C}=\Phi^T C\Phi$, Λ is the diagonal eigenvalue matrix of natural vibration characteristics analysis.

Since the damping ratio of the structure is generally small and the system damping ratio is 0 in the

flutter critical state, the frequency of the plural modal of the system can be taken as $\omega = -s\mathrm{i} = \omega + \xi \mathrm{i}$, which is substituted into Equation (6.3.11) and eliminated by ω to obtain the new generalized system characteristic equation:

$$\left(s^2\left(I + \overline{\mathrm{A}}_{se}\right) + s\overline{C} + \Lambda\right)\mathrm{q}e^{st} = 0 \tag{6.3.12}$$

Re-write the above characteristic equation in the form of the state space variable:

$$\left(\mathrm{A} - sI\right)\mathrm{Y}e^{st} = 0 \tag{6.3.13}$$

where $\mathrm{Y} = \begin{Bmatrix} \mathrm{q} \\ s\mathrm{q} \end{Bmatrix}$, $\mathrm{A} = \begin{bmatrix} 0 & I \\ -\overline{M}\Lambda & -\overline{M}\overline{C} \end{bmatrix}$, $\overline{M} = \left(I + \overline{\mathrm{A}}_{se}\right)^{-1}$.

Since $e^{st} \neq 0$, if there is a non-zero solution to Equation (6.3.13), the determinant of the coefficient matrix is 0, so the system plural modal characteristic analysis is transformed into a standard eigenvalue problem.

$$\mathrm{AY} = s\mathrm{Y} \tag{6.3.14}$$

where A is a plural matrix of $2m \times 2m$ orders and it contains only one variable, the reduced frequency, i.e. Equation (6.3.14) contains only two variables, s and K. Given a value of K, the corresponding $2m$ eigenvalues s and eigenvectors Y can be calculated as

$$s = (-\xi + i)\omega, \quad \mathrm{q} = \mathrm{a} + \mathrm{b}i \tag{6.3.15}$$

In the $2m$ eigenvalues, the m eigenvalues with positive imaginary parts are the plural frequencies of the system, and the corresponding eigenvectors Y with the upper part q is the generalized plural modal form of the system. The other m eigenvalues with negative imaginary parts and the corresponding eigenvectors have no real physical significance.

In the generalized plural modal of the structural system, the amplitude and phase of each natural modal of the structure are as follows:

$$|\mathrm{q}_k| = \sqrt{\mathrm{a}_k^2 + \mathrm{b}_k^2}, \quad \varphi = \tan^{-1}(\mathrm{b}_k / \mathrm{a}_k) \tag{6.3.16}$$

Due to the existence of aerodynamic coupling, the generalized plural modal of the system is the coupling of the natural modal of the structure. Therefore, when the damping ratios of all plural modals are greater than 0, the system is stable; when the damping ratio of any plural modal is equal to 0, the system is in the flutter critical state; when the damping ratio of any plural modal is less than 0, the system is unstable. In the process of flutter analysis, it is necessary to search for the reduced frequency K that makes the damping ratio of system equal to 0. At this point, the system is in the flutter critical state, and the corresponding frequency ω is the flutter circular frequency ω_f. Then, the critical flutter wind speed of the system $U_{cr} = B\omega_f / K$ can be calculated.

Within the appropriate search range of reduced wind speed $V^r (V^r = 2\pi / K)$, there may be multiple values of V^r such that the damping ratio of the system is equal to 0 for the flutter critical state. Among them, the wind speed corresponding to V^r which has the lowest reduced wind speed value,

may not be the lowest critical flutter wind speed. To solve this problem, the following single-parameter automatic search method is used to determine the lowest critical flutter wind speed for the structure.

The generalized modal coordinates $\mathrm{q}(t)$ and node displacements $X(t)$ of the structure in the flutter critical state are as follows:

$$\mathrm{q}(t) = \left\{ |\mathrm{q}_i| \sin(\omega_f t + \varphi_i) \right\} \tag{6.3.17a}$$

$$X(t) = \sum_{i=1}^{m} \phi_i |\mathrm{q}_i| \sin(\omega_f t + \varphi_i) = \mathrm{X}_0 \sin(\omega_f t + \bar{\varphi}) \tag{6.3.17b}$$

where ω_f is the flutter circular frequency, m is the number of modals involved in the analysis, ϕ_i is the i[th] order natural modal, X_0 is the amplitude of $X(t)$ and $\bar{\varphi}$ is the phase of $X(t)$.

The total energy E of the characteristic motion under flutter critical state is:

$$E = \frac{1}{2} \left\{ \dot{\mathrm{X}}_{\max} \right\}^T \mathrm{M} \left\{ \dot{\mathrm{X}}_{\max} \right\} = \frac{1}{2} \omega_f^2 \sum_{i=1}^{m} |\mathrm{q}_i|^2 \tag{6.3.18}$$

The energy E_i of any order natural modal is:

$$E_i = \frac{1}{2} \omega_f^2 |\mathrm{q}_i|^2 \tag{6.3.19}$$

The energy percentage of the i[th] natural modal is $e_i = E_i / E$, and the modal energy percentage represents the participation degree of each natural modal of the structure in flutter motion.

The above multi-modal flutter analysis method is a non-iterative single parameter search method, and the specific automatic search process for determining the critical flutter wind speed through this method is as follows:

(1) The first m orders natural frequencies and modal shapes of the structure required for flutter analysis are obtained through finite element calculation.

(2) Determine the search range for reduced wind speed (minimum search wind speed V_{low}^r and maximum search wind speed V_{high}^r) and the incremental V_{inc}^r for each step (V_{inc}^r can be set to 0 generally).

(3) Calculate the reduced wind speed V_i^r at the i[th] step, $V_i^r = V_{low}^r + (i-1)V_{inc}^r$.

(4) Obtain the reduced frequency at the i[th] step according to $K_i = 2\pi / V_i^r$, and determine the plural matrix A corresponding to this frequency.

(5) By solving the standard eigenvalue problem of Equation (6.3.14), the damping ratio and circular frequency corresponding to each plural modal of the system are obtained.

(6) Search for the damping ratio and circular frequency of each order plural modal. If the damping ratio of the k[th] order plural modal is less than 0, perform steps (7)~(8) and search for the minimum circular frequency $\omega_{\min}$ in the plural modals with the damping ratio greater than 0.

(7) For the k[th] order plural modal with the damping ratio less than 0, the secant method (as shown

in Figure 6.12) is used to approximate the value of reduced wind speed.

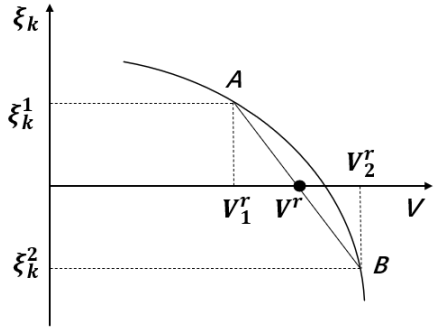

Figure 6.15: Architecture of the secant method

$$V^r = \frac{V_2^r \xi_k^1 - V_1^r \xi_k^2}{\xi_k^1 - \xi_k^2} \tag{6.3.20}$$

During the initial calculation, V_1^r and V_2^r are taken as V_{i-1}^r and V_i^r respectively, and ξ_k^1 and ξ_k^2 are the damping ratios corresponding to the k^{th} order plural modal.

(8) Perform steps (3)~(4), and if the absolute value $|\xi_k|$ of the k^{th} plural modal damping ratio is less than the allowable value, return to step (5); Otherwise, when $\xi_k > 0$, take $V_1^r = V^r$ and $\xi_k^1 = \xi_k$; When $\xi_k < 0$, take $V_2^r = V^r$ and $\xi_k^2 = \xi_k$. Repeat steps (7)~(8).

(9) Calculate the critical flutter wind speed corresponding to the zero damping ratio of the flutter plural modal in the i^{th} step, and select the minimum critical flutter wind speed $U_{\min}^{cr}$. Compare $U_{\min}^{cr}$ with $U_1 = \frac{1}{2\pi} B V_1^r \omega_{\min}$: If $U_{\min}^{cr} > U_1$, return to step (2); Loop again, if $U_{\min}^{cr} < U_1$, the loop ends and the search process ends.

(10) The critical flutter wind speed of the structure $U_{cr} = U_{\min}^{cr}$.

6.3.2 Critical flutter instability speed analysis with three-dimensional method

Like two-dimensional flutter analysis, the aerostatic coefficients predicted by EBP neural network and flutter derivatives predicted by GBDT are used for three-dimensional multi-modal flutter analysis. Still taking the Runyang suspension bridge as an example, Table 6.3 shows the prediction error of aerodynamic parameters of several closed box girder cross-sections, the two-dimensional and three-dimensional critical flutter wind speed calculation results and the error between the calculation and wind tunnel test, as well as the comparison between two-dimensional and three-dimensional. It can be seen that the prediction error of flutter derivatives will be weakened in the calculation of critical flutter wind speed, and the calculation results of two-dimensional and three-dimensional flutter numerical analysis are not significantly different. The result of two-dimensional flutter numerical analysis in this case is slightly closer to the result measured by sectional model wind tunnel test.

Table 6.3: Comparison of two-dimensional and three-dimensional flutter numerical calculations

Section No.	Prediction error of aerodynamic parameters		Critical flutter wind speed calculation result and error			
	Aerostatic coefficients	Flutter derivatives	Wind tunnel test	2D flutter numerical analysis	3D flutter numerical analysis	2D vs 3D
1	5.04%	15.2%	64.4m/s	Value: 63m/s Error: -2.17%	Value: 66m/s Error: 2.48%	4.55%
2	-	-	-	54m/s	54.4m/s	0.74%
3	-	-	-	45m/s	40.4m/s	-11.39%
4	-	-	-	74m/s	79.8m/s	7.27%
5	-	-	-	71m/s	74.8m/s	5.08%
6	-	-	-	74m/s	78.1m/s	5.25%
7	-	-	-	57m/s	59m/s	3.39%

6.3.3 Comparison of two-dimensional and three-dimensional evaluation results

In order to further compare three-dimensional flutter analysis with two-dimensional flutter analysis, sensitivity analysis of critical flutter wind speed is conducted again, which analyzes the variation pattern of critical flutter wind speed under different width to depth ratios, wind fairing angles and web inclined angles, respectively, and compares the distribution trend with the two-dimensional calculation result.

6.3.3.1 Ratio of width to depth

The same as the process of two-dimensional flutter numerical analysis, using the main girder cross-section of the Runyang Bridge as an example. Make the wind fairing angle and web inclined angle unchanged, and adjust the width to depth ratio only by changing the width of the cross-section. As shown in Figure 6.13, the critical flutter wind speed decreases with the increase of width to depth ratio, which is consistent with the trend obtained by two-dimensional flutter numerical analysis, and the magnitude of change is not much different. When $H/B<12$, the magnitude of change is significant; When $H/B>12$, the downward trend of critical flutter wind speed slows down with the increase of H/B.

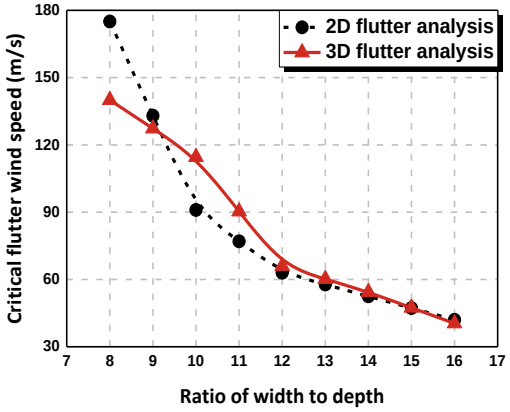

Figure 6.16: Comparison of critical flutter wind speed change with the ratios of width to depth

6.3.3.2 Wind faring angle

Figure 6.14 shows the variation pattern of critical flutter wind speed with the wind faring angle. It can be seen from the figure that in the range of $30°<\theta<90°$, the critical flutter wind speed increases and then decreases with the increasing wind faring angle, reaching a peak at around 60°. Although the specific critical flutter wind speeds are not the same for two-dimensional and three-dimensional calculations, the trend and change magnitude with the wind fairing angle are very similar.

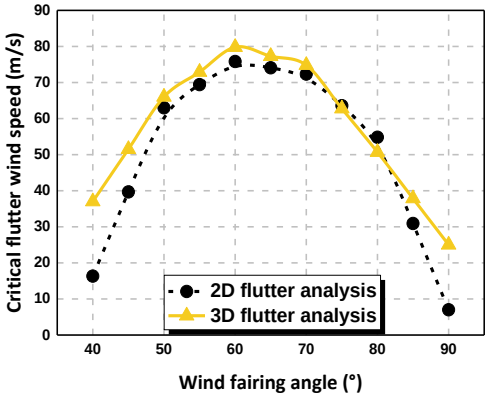

Figure 6.17: Comparison of critical flutter wind speed change with the wind fairing angles

6.3.3.3 Web inclined angle

For a closed box girder cross-section with a width to depth ratio of about 12, the critical flutter wind speed decreases when the web inclined angle changes from 10° to 25°, which is consistent with the result obtained by two-dimensional numerical analysis, and this trend is very close to linear (as shown in Figure 6.15). However, in practical engineering, it is not advisable to set the web inclined angle too small, as it would significantly increase the fabrication difficulty.

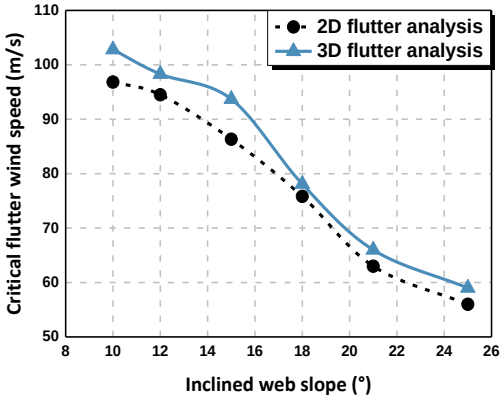

Figure 6.18: Comparison of critical flutter wind speed change with the web inclined angles

6.4 Conclusion

This chapter aims to analyze the wind-resistant stability of bridges with closed box girder based on three-dimensional numerical calculation theory, focusing also on the aerostatic instability and flutter instability, and the results were compared with two-dimensional wind-resistant stability analysis.

For a specific bridge structure, aerostatic response in the mid-span was calculated using a three-dimensional non-linear aerostatic stability analysis program. The variation patterns of lateral, vertical and torsional displacements at the mid-span of main girder with wind speed under different feature sizes of cross-section were given, showing that the aeroelastic instability pattern of closed box girder has the significant characteristic of spatially coupled deformation, where the displacement in each direction increases non-linearly with the increase of wind speed, and diverges at critical wind speed. The calculation results based on machine learning prediction are very close to the results based on wind tunnel test measurement. The sensitivity analysis of three-dimensional aerostatic stability shows that the critical wind speed of aerostatic instability roughly increases with the increase of width to depth ratio and wind fairing angle, but it is not very sensitive to the change of web inclined angle. In addition, the two-dimensional analysis often overestimates the aerostatic stability of the structure, and the results of three-dimensional aerostatic stability analysis are more reasonable.

In the analysis of three-dimensional flutter stability, the calculation results of two-dimensional and three-dimensional flutter numerical analysis are not significantly different. In order to further compare three-dimensional flutter analysis with two-dimensional flutter analysis, sensitivity analysis of critical flutter wind speed is conducted, which shows that the variation patterns of critical flutter wind speed with width to depth ratio, wind fairing angle and web inclined angle based on three-dimensional flutter numerical calculation are very similar to the calculation results obtained by two-dimensional flutter analysis. The critical flutter wind speed decreases with the increase of width to depth ratio, and it increases and then decreases with the increasing wind faring angle, reaching a peak at around 60°. When the web inclined angle changes from 10° to 25°, the critical flutter wind speed decreases.

CHAPTER 7

7 General conclusions and future developments

7.1 General conclusions

In order to rapidly analyze the wind-resistant performance of long-span bridges based on artificial intelligence, an aerodynamic parameter identification method of closed box girder based on multiple machine learning algorithms has been proposed. The predicted aerodynamic parameters have been successfully applied to two-dimensional and three-dimensional analysis of aerostatic stability and flutter stability. The influence of cross-sectional feature size on the wind-resistant performance of the structure was also analyzed, and the calculation results under various analysis methods were cross-validated. Major contributions of this study are summarized as follows:

(1) A specialized wind-resistance database including the experimental results of 99 long-span bridges from Tongji Wind Tunnel Laboratory has been built. The bridge types include: cable-stayed bridge, suspension bridge, arch bridge and rigid frame bridge. The spans of bridges range from 105m to 1688m. The types of cross-sections include closed box girder, π-shaped girder, cantilever box girder, slotted box girder, etc. All the data of each bridge were summarized into three modules: basic information, aerodynamic characteristics and aerodynamic parameters and stored in the Access database management system. The development of foreground visualization application was also carried out, which mainly implemented the functions of filtering, viewing, modifying and saving data. The foreground application is connected to the underlying database using a local protocol driven approach to achieve the independence of platform.

(2) Two types of sample sets have been established for machine learning modeling: hybrid dataset and pure numerical simulation dataset. The hybrid dataset includes 20 sets of wind tunnel test data of long-span bridges with closed box girders from the self-built wind-resistance database, 20 sets of numerical simulation data from open-source literature, and another 14 sets of supplementary data. All the data samples are re-calculated by CFD numerical simulation and checked to form the pure numerical simulation dataset, so as to obtain the better data condition and improve the effectiveness of machine learning training and prediction.

(3) The error back propagation neural network based on Levenberg-Marquardt algorithm was used to train and predict the aerostatic coefficients after the comparison of three machine learning methods. The machine learning models can obtain the potential input-output transfer relationship of training set since the fitting degree are all above 0.99. The models also have good extrapolation capability to the test set. The prediction errors of C_D are slightly larger than that of C_L *and* C_M, but the error mainly occurs under the large wind attack angles, and the prediction effect under small wind attack angle is good enough. The mean relative error of the best prediction result is only 0.0355, and the worst is 0.0778.

(4) The gradient boosting decision tree was selected to train and predict the flutter derivatives after comparison. The trained models can obtain the potential input-output transfer relationship of training

set, and the models are also able to predict the distribution of flutter derivatives in the test set to a large extent under current data condition. The mean relative error of the best prediction result is 0.1233 and the worst is 0.1970. Besides, the post-interpretation of models has been implemented, which enables the further explicit expression of machine learning black box.

(5) Two-dimensional aerostatic stability and flutter stability of the specific structure based on predicted aerodynamic parameters are evaluated. The error analysis and the sensitivity analysis of aerodynamic parameters and critical instability wind speed with the feature size change of the main girder cross-section further validate the feasibility of applying the machine learning methods to the wind-resistant performance analysis of bridges. The two-dimensional aerostatic stability analysis based on the Runyang suspension bridge shows that the shape of the main girder cross-section has a significant impact on the critical wind speed of torsional divergence. The error analysis of critical flutter wind speed reveals that the machine learning prediction error of flutter derivatives will be weakened in the numerical calculation of critical flutter wind speed, and the sensitivity analysis of flutter derivatives shows that A_1^*, A_2^*, A_3^* and H_3^* have great influence on critical flutter wind speed of closed box girder. The influence analysis of geometric shape on critical flutter wind speed demonstrates that the critical flutter wind speed decreases with the increase of width to depth ratio of the closed box girder; In the range of 30°-100° of wind fairing angle, the critical flutter wind speed first increases and then decreases with the increase of angle, and reaches the peak at around 60°; The critical flutter wind speed decreases with an increase in web inclined angle and is almost linear for a particular ratio of width to depth.

(6) Three-dimensional analyses of wind-resistant stability are also given, which mainly focuses on the influence of the cross-sectional feature size on the aerostatic performance and flutter performance, and the results are compared between two-dimensional and three-dimensional methods. The sensitivity analysis of three-dimensional aerostatic stability shows that the critical wind speed of aerostatic instability roughly increases with the increase of width to depth ratio and wind fairing angle, but it is not very sensitive to the change of web inclined angle. In addition, the two-dimensional analysis often overestimates the aerostatic stability of the structure, and the results of three-dimensional aerostatic stability analysis are more reasonable. The calculated critical flutter wind speed and the corresponding sensitivity analysis under two-dimensional and three-dimensional methods are slightly different but the overall variation trend is consistent.

7.2 Future developments

To improve and expand the current study, several topics can be continued for future research as follows:

(1) Efficient and high-precision intelligent identification methods for aerodynamic parameters are expected to be realized and ultimately unify wind tunnel test method and numerical simulation method, which depends on larger datasets and better data conditions. In addition, based on the post-interpretation, it is necessary to further study about the explicit expression of machine learning black box models.

(2) It is necessary to further improve the accuracy and robustness of intelligent identification of aerodynamic parameters. Besides, due to the existing data limitation, the current analysis of three-dimensional flutter stability can only be carried out based on the predicted 8 flutter derivatives by machine learning method and the other 10 flutter derivatives simplistically obtained by hydrostatic theory. More future works on three-dimensional flutter stability analysis based on predicted 18 flutter derivatives by machine learning are needed.

(3) At present, the sensitivity analysis of the critical wind speed for aerostatic instability and flutter instability with the shape of cross-sections only focuses on three feature dimensions: ratio of width to depth, wind fairing angle, and web inclined angle. In the future, it is expected to implement more refined research on the change of shape and even ancillary facilities of main girder, and expand the research to other types of main girder cross-sections. Based on it, universal conclusions or expressions on aerodynamic shape optimization can also be further studied.

Addendum

Appendix A: List of bridges in database

Table A.1: List of bridges included in self-built wind-resistance database

No.	Name	Type of bridge	Main span (m)	Type of girder
1	Angola Bridge	cable-stayed bridge	300	closed box girder
2	Anqing Yangtze River Bridge	cable-stayed bridge	495	closed box girder
3	Baguazhou Yangtze River Bridge	cable-stayed bridge	628	closed box girder
4	Beipan River Bridge	cable-stayed bridge	760	truss
5	Beishan Bridge	rigid frame bridge	200	cantilever box girder
6	Cuntan Yangtze River Bridge	suspension bridge	880	closed box girder
7	Damen Bridge	cable-stayed bridge	316	π-shaped girder
8	Dashengguan Yangtze River Bridge	cable-stayed bridge	648	closed box girder
9	Dongying Yellow River Highway Bridge	rigid frame bridge	220	cantilever box girder
10	East Sea Bridge	cable-stayed bridge	420	cantilever box girder
11	E'dong Yangtze River Bridge	cable-stayed bridge	926	closed box girder
12	E'huang Yangtze River Bridge	cable-stayed bridge	580	π-shaped girder
13	Erchong Floodway Bridge	cable-stayed bridge	200	closed box girder
14	Erqi Yangtze River Bridge	cable-stayed bridge	616	closed box girder
15	Feiyun River Bridge	cable-stayed bridge	240	closed box girder
16	Great Belt Bridge	suspension bridge	1624	closed box girder
17	Guangdong Jiujiang Bridge	cable-stayed bridge	160	cantilever box girder
18	Haihe Bridge	cable-stayed bridge	364	π-shaped girder
19	Hangzhou Bay Bridge	cable-stayed bridge	448	closed box girder
20	Hengqin Bridge	cable-stayed bridge	240	closed box girder
21	Hongguang Bridge	suspension bridge	380	closed box girder
22	Huai'an Bridge	cable-stayed bridge	370	π-shaped girder
23	Huaihe River Bridge	cable-stayed bridge	452	cantilever box girder
24	Humen Bridge	suspension bridge	570	closed box girder
25	Hong Kong-Zhuhai-Macao Jiuzhou Channel Bridge	cable-stayed bridge	693	cantilever box girder
26	Hong Kong-Zhuhai-Macao Qingzhou Channel Bridge	cable-stayed bridge	458	closed box girder

27	Jialing River Shimen Bridge	cable-stayed bridge	230	cantilever box girder
28	Jiangdong Bridge	suspension bridge	260	slotted box girder
29	Jiangjiehe Bridge	cable-stayed bridge	330	I-shaped girder
30	Jiangxi Jiujiang Yangtze River Bridge	cable-stayed bridge	818	closed box girder
31	Jiangyin Yangtze River Bridge	cable-stayed bridge	1385	closed box girder
32	Jiaozhou Bay Bridge	cable-stayed bridge	260	closed box girder
33	Jingyue Yangtze River Bridge	cable-stayed bridge	816	double box girder
34	Jingzhou Yangtze River Bridge (North Branch)	cable-stayed bridge	500	π-shaped girder
35	Jingzhou Yangtze River Bridge (South Branch)	cable-stayed bridge	300	π-shaped girder
36	Lijin Yellow River Highway Bridge	cable-stayed bridge	310	π-shaped girder
37	Lingdingyang East Channel Bridge	cable-stayed bridge	300	π-shaped girder
38	Lingdingyang West Channel Bridge	suspension bridge	920	closed box girder
39	Longtan River Bridge	rigid frame bridge	200	cantilever box girder
40	Luomazhou Bridge	cable-stayed bridge	133	closed box girder
41	Luomiao Bridge	cable-stayed bridge	270	π-shaped girder
42	Lupu Bridge	arch bridge	550	π-shaped girder
43	Ma'anshan Yangtze River Bridge (Left Branch)	suspension bridge	1080	closed box girder
44	Ma'anshan Yangtze River Bridge (Right Branch)	cable-stayed bridge	260	double box girder
45	Malinghe Bridge	cable-stayed bridge	360	flat plate
46	Maocaojie Bridge	arch bridge	368	T-shaped girder
47	Maogang Bridge	cable-stayed bridge	200	double box girder
48	Min River Bridge	cable-stayed bridge	605	π-shaped girder
49	Minpu Bridge	cable-stayed bridge	708	truss
50	Nan'ao Bridge	cable-stayed bridge	205	cantilever box girder
51	Nanjing Yangtze River Bridge	girder bridge	160	truss
52	Nanpu Bridge	cable-stayed bridge	423	cantilever box girder
53	Nansha Bridge	suspension bridge	1200	closed box girder

54	Nizhou Waterway Bridge	suspension bridge	1688	closed box girder
55	Puxi Bridge	cable-stayed bridge	300	cantilever box girder
56	Qiantang River Bridge	girder bridge	67	truss
57	Qingfeng Bridge	suspension bridge	280	closed box girder
58	Qixiashan Yangtze River Bridge	suspension bridge	1418	closed box girder
59	Queshi Bridge	cable-stayed bridge	518	double box girder
60	Runyang Yangtze River Bridge (North Branch)	cable-stayed bridge	406	closed box girder
61	Runyang Yangtze River Bridge (South Branch)	suspension bridge	1490	closed box girder
62	Shanghai Yangtze River Bridge	cable-stayed bridge	730	closed box girder
63	Shantou Bay Bridge	suspension bridge	452	cantilever box girder
64	Shennongxi Bridge	cable-stayed bridge	320	double box girder
65	Shiji Bridge	cable-stayed bridge	340	π-shaped girder
66	Shuangbei Jialing River Bridge	cable-stayed bridge	330	cantilever box girder
67	Shunfu Bridge	cable-stayed bridge	405	closed box girder
68	Siduhe Bridge	suspension bridge	900	truss
69	Stone Ditch Yangtze River Bridge	cable-stayed bridge	450	π-shaped girder
70	Suramadu Bridge	cable-stayed bridge	434	double box girder
71	Sutong Yangtze River Bridge	cable-stayed bridge	1088	closed box girder
72	The Second Fengdu Yangtze River Bridge	cable-stayed bridge	444	double box girder
73	Taoyaomen Bridge	cable-stayed bridge	580	closed box girder
74	The Second Minpu Bridge	cable-stayed bridge	250	truss
75	The Second Nujiang Bridge	cable-stayed bridge	155	closed box girder
76	The Second Ou'jiang Bridge	cable-stayed bridge	270	cantilever box girder
77	The Second Suyang Highway Bridge	cable-stayed bridge	120	cantilever box girder
78	The Second Wuhu Yangtze River Bridge	cable-stayed bridge	806	double box girder
79	The Second Wujiang River Bridge	cable-stayed bridge	340	cantilever box girder
80	The Third Qiantang River Bridge	cable-stayed bridge	168	cantilever box girder

81	Tieluoping Bridge	cable-stayed bridge	322	π-shaped girder
82	Tongling Yangtze River Bridge	cable-stayed bridge	432	flat plate
83	Weiliu Road Bridge	cable-stayed bridge	380	π-shaped girder
84	Wuhan Yangtze River Bridge	cable-stayed bridge	400	cantilever box girder
85	Xiangshangang Bridge	cable-stayed bridge	688	closed box girder
86	Xiasha Bridge	rigid frame bridge	232	cantilever box girder
87	Xihoumen Bridge	suspension bridge	1650	double box girder
88	Xinguang Bridge	arch bridge	428	cantilever box girder
89	Xupu Bridge	cable-stayed bridge	590	double box girder
90	Yangluo Bridge	suspension bridge	1280	closed box girder
91	Yangpu Bridge	cable-stayed bridge	602	cantilever box girder
92	Yichang Yangtze River Bridge	suspension bridge	960	closed box girder
93	Yingwuzhou Yangtze River Bridge	suspension bridge	850	I-shaped girder
94	Yingxiong Bridge	cable-stayed bridge	188	closed box girder
95	Yongjiang Bridge	cable-stayed bridge	105	cantilever box girder
96	Yuehu Bridge	cable-stayed bridge	232	three box girder
97	Yuyang Han River Bridge	cable-stayed bridge	414	closed box girder
98	Yuzui Yangtze River Bridge	suspension bridge	616	closed box girder
99	Zhanjiang Bay Bridge	cable-stayed bridge	480	closed box girder

Addendum

Appendix B: Datasets of closed box girder

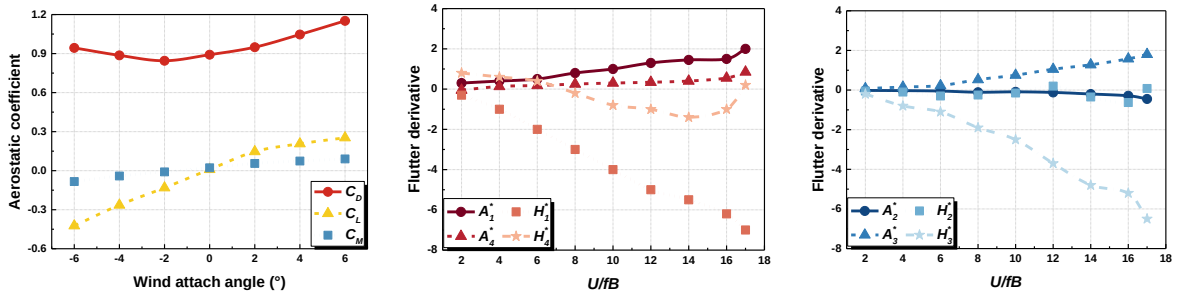

(1) Section 1

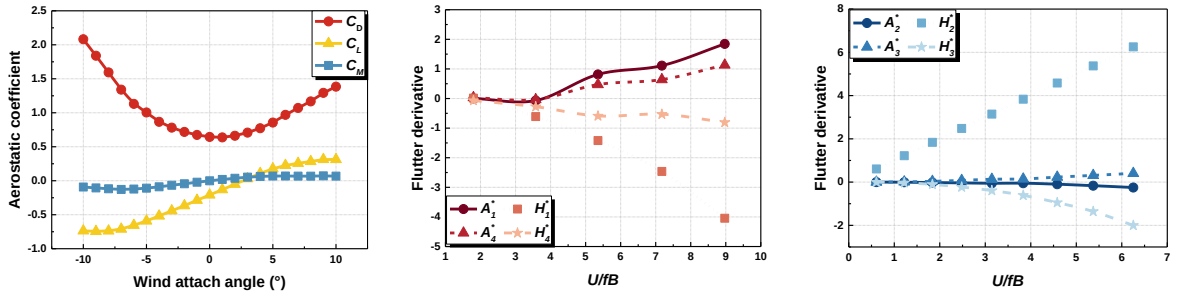

(2) Section 2

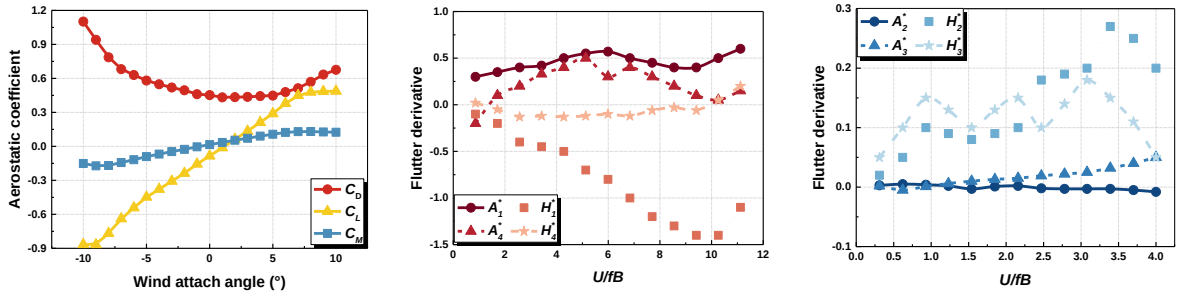

(3) Section 3

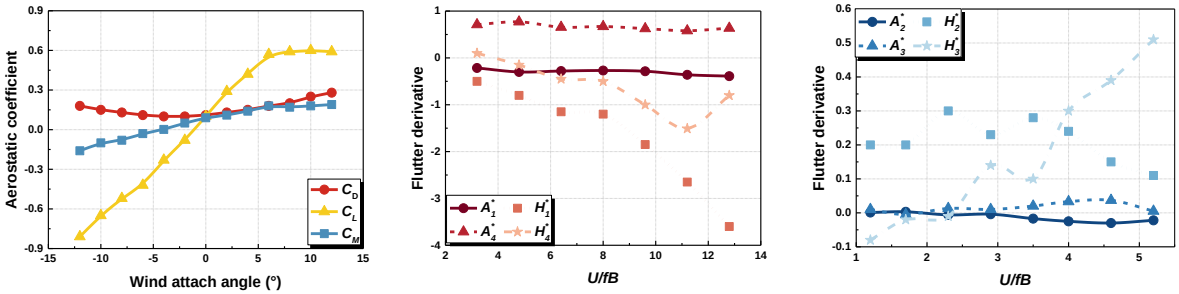

(4) Section 4

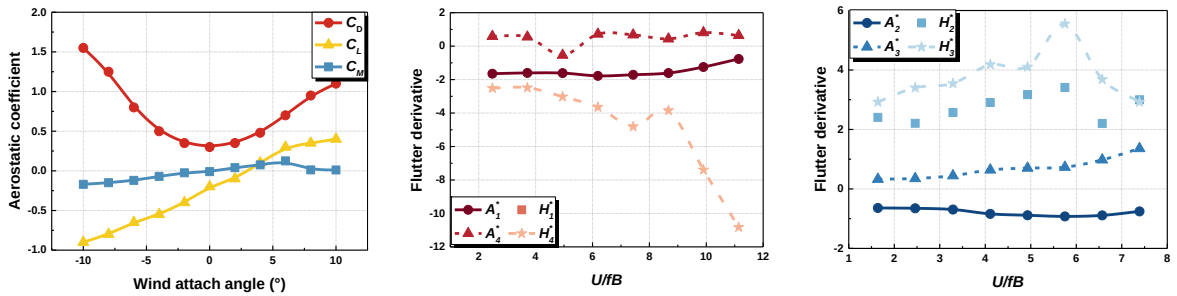

(5) Section 5

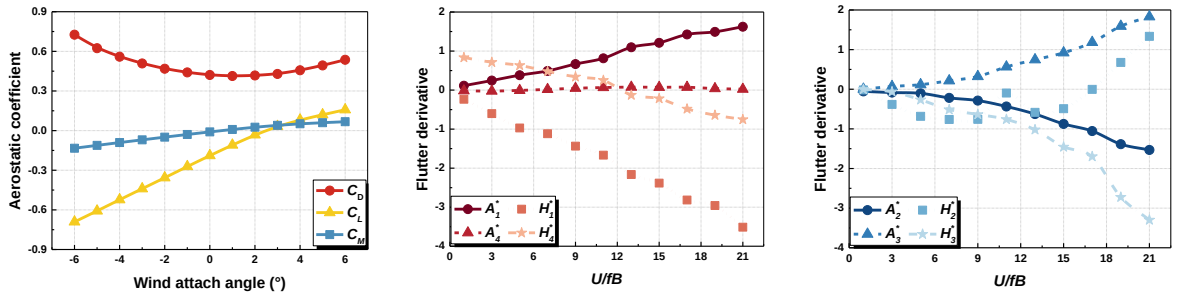

(6) Section 6

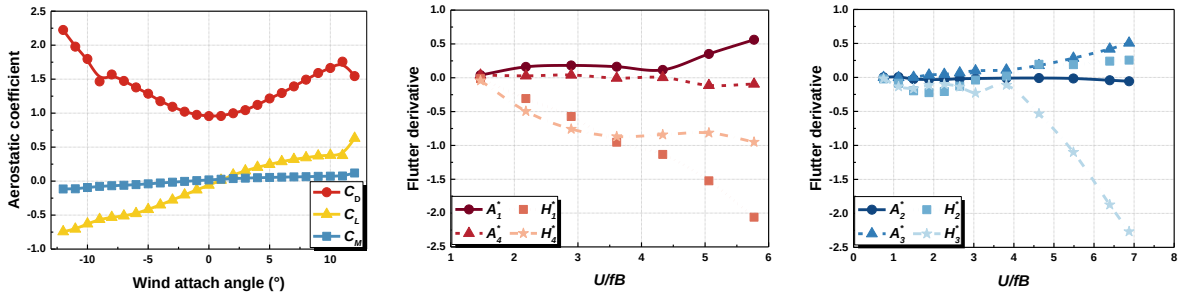

(7) Section 7

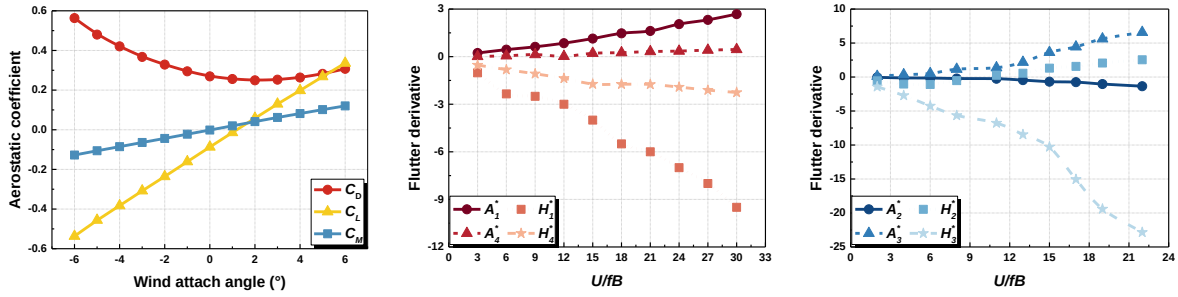

(8) Section 8

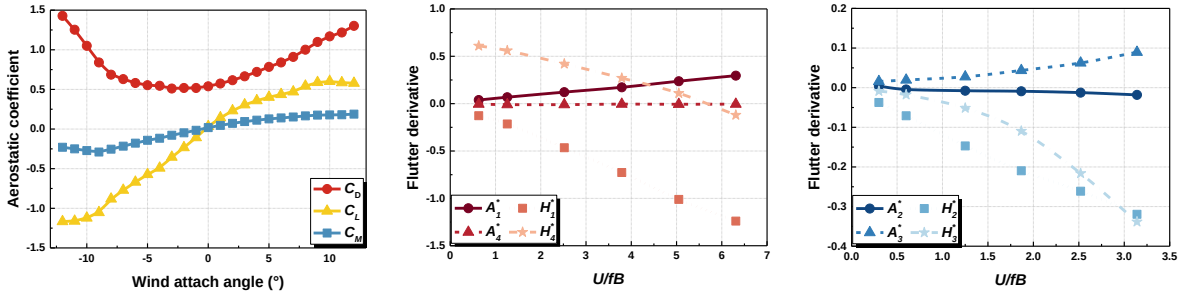

(9) Section 9

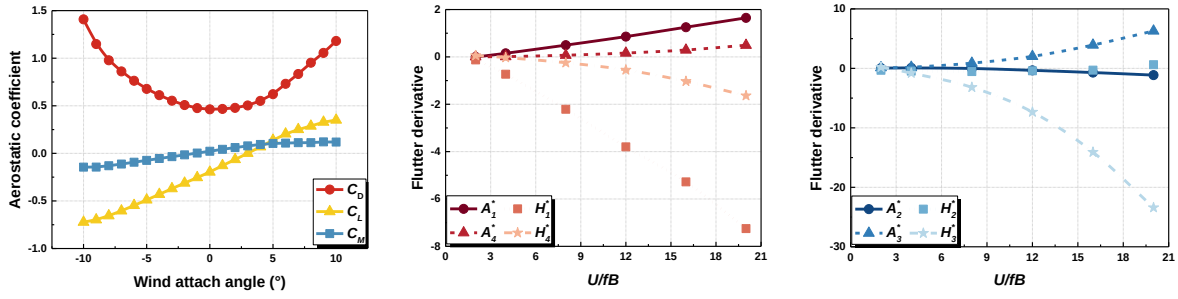

(10) Section 10

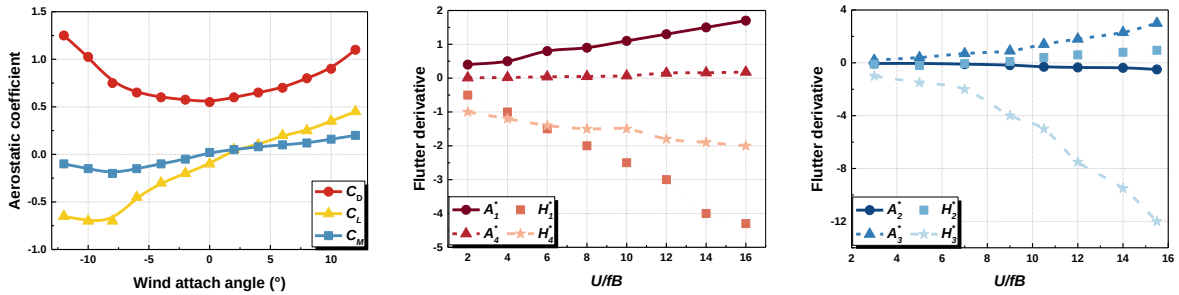

(11) Section 11

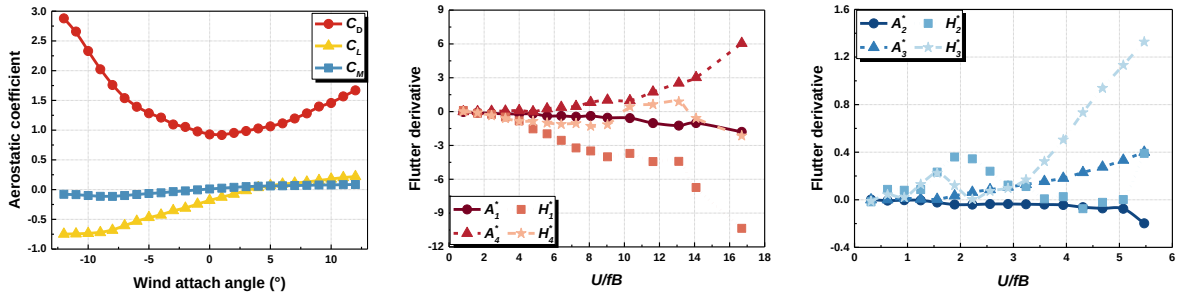

(12) Section 12

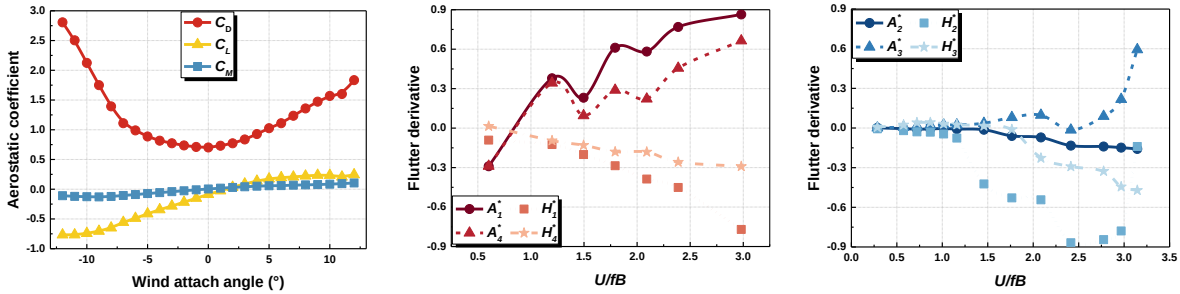

(13) Section 13

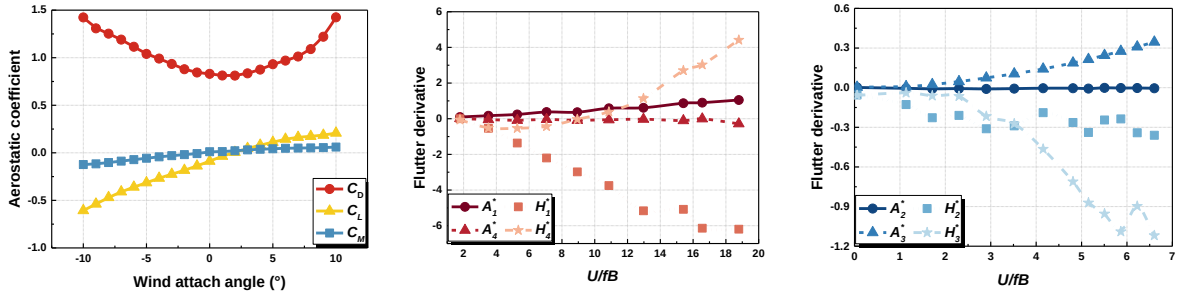

(14) Section 14

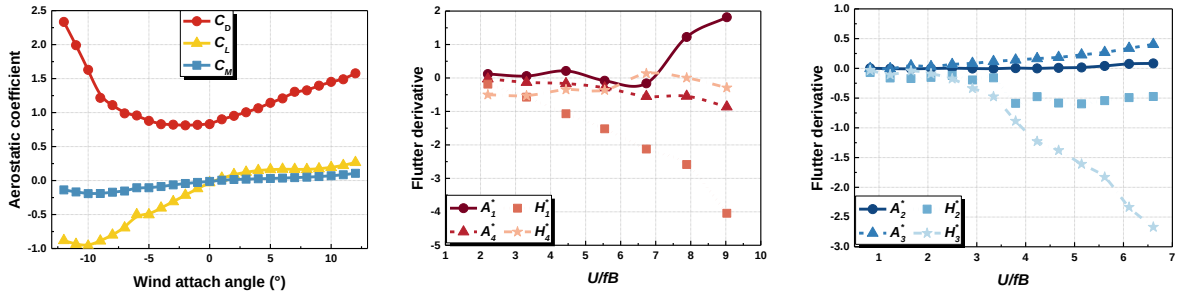

(15) Section 15

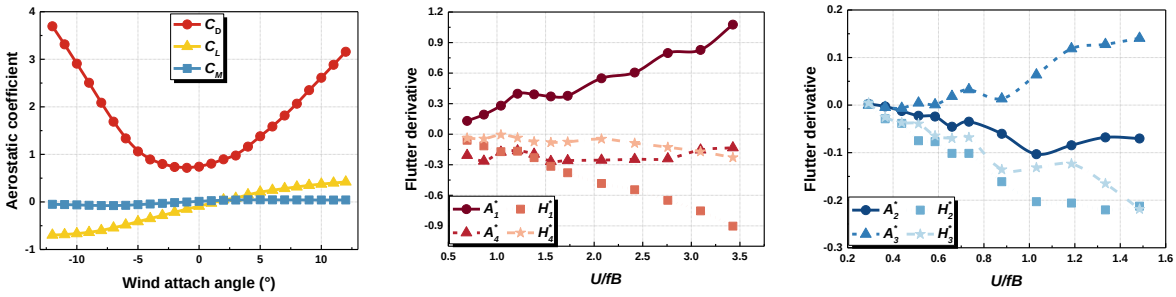

(16) Section 16

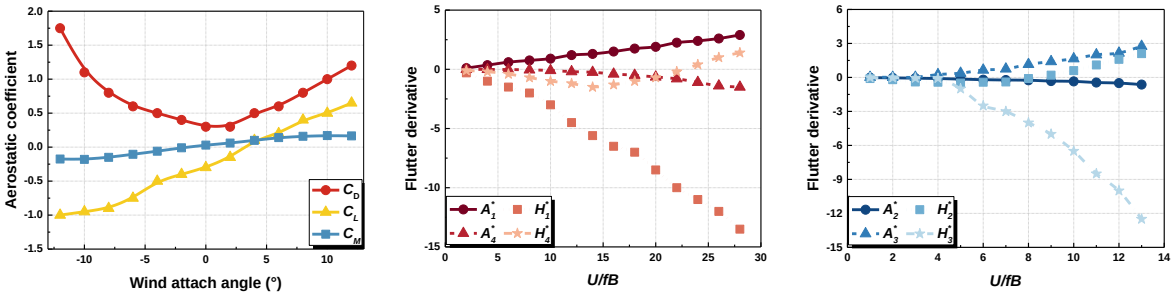

(17) Section 17

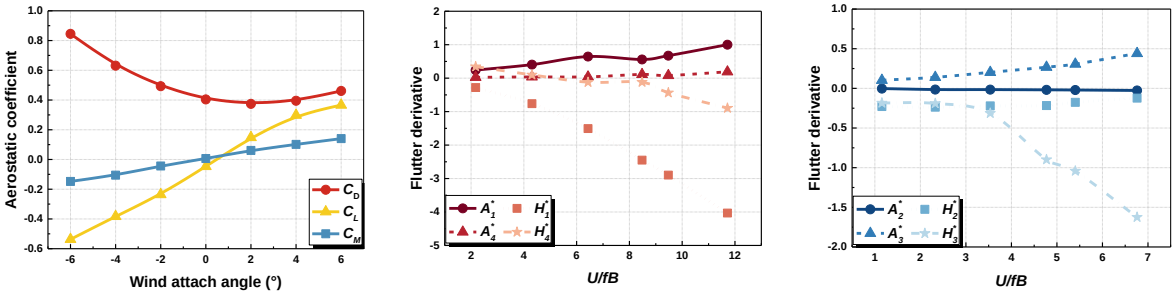

(18) Section 18

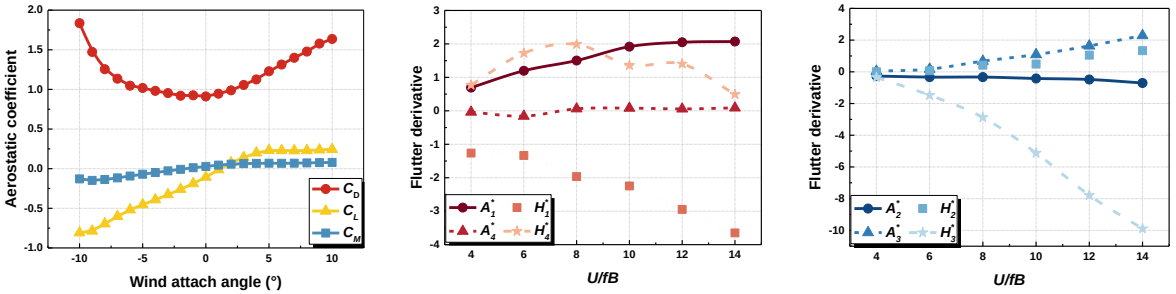

(19) Section 19

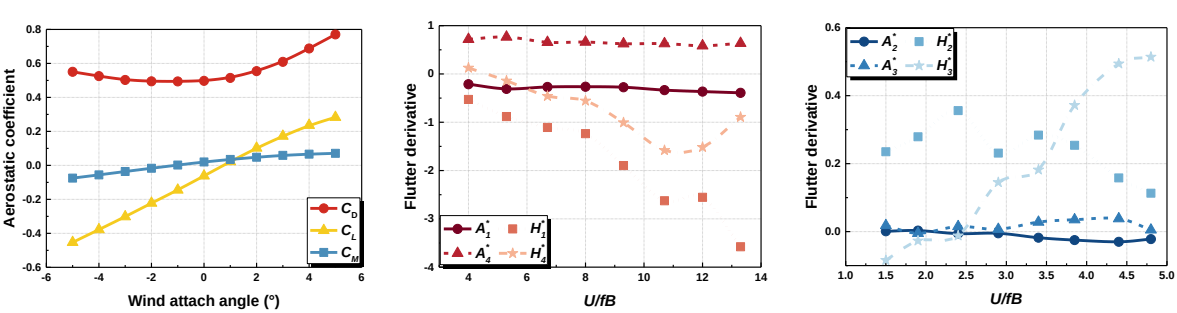

(20) Section 20

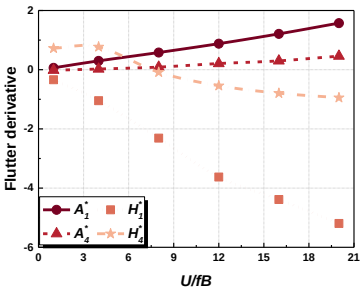

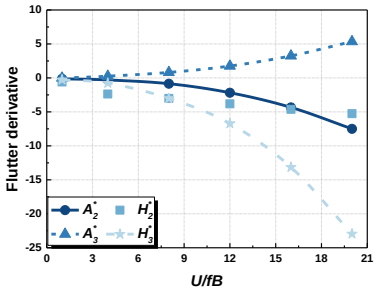

(21) Section 21

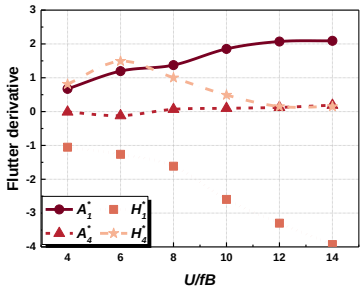

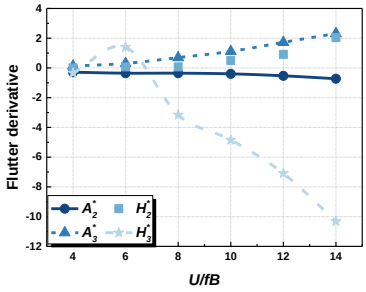

(22) Section 22

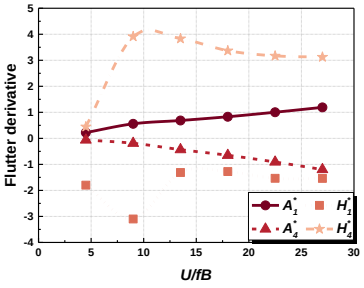

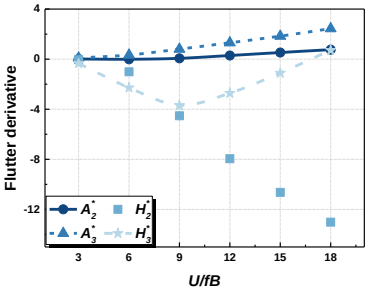

(23) Section 23

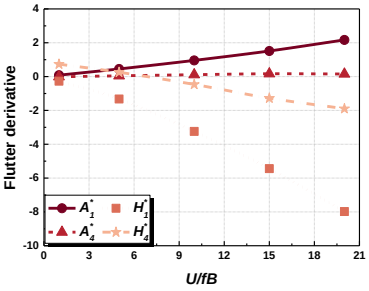

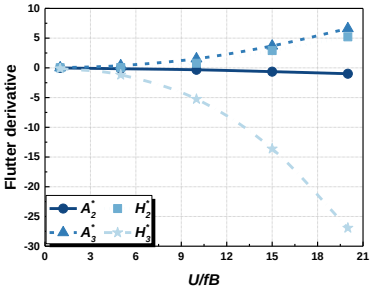

(24) Section 24

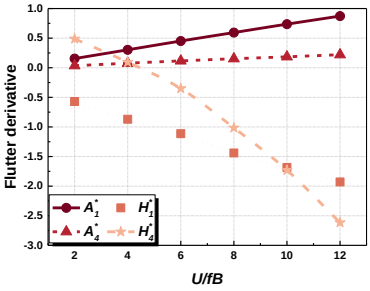

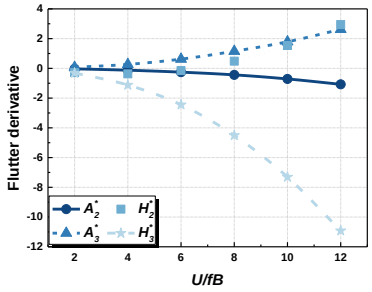

(25) Section 25

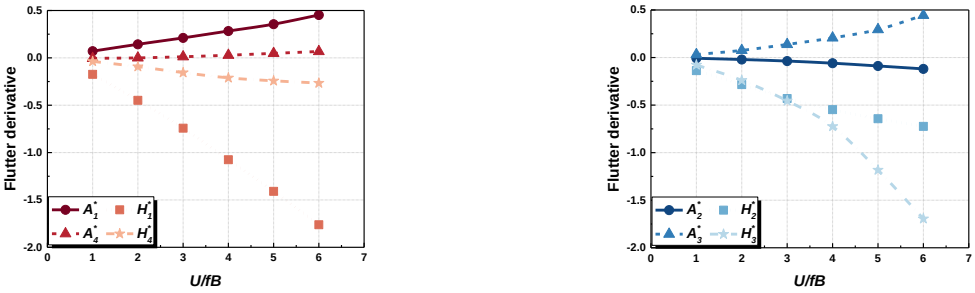

(26) Section 26

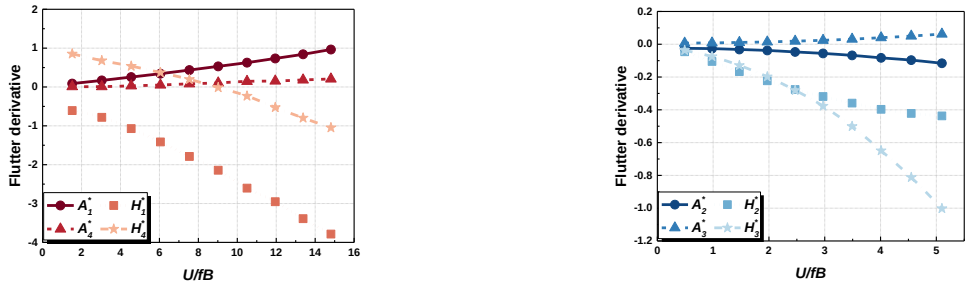

(27) Section 27

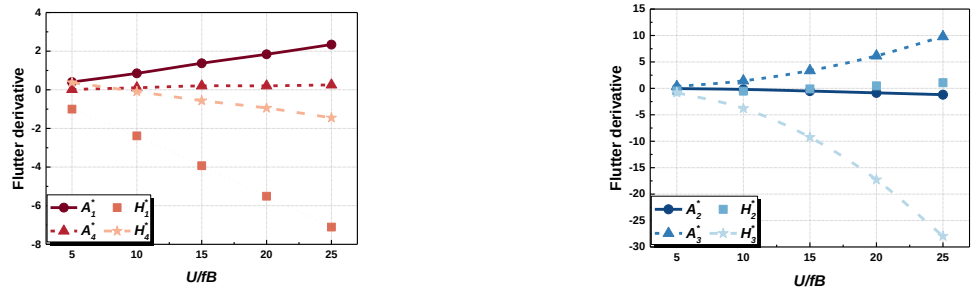

(28) Section 28

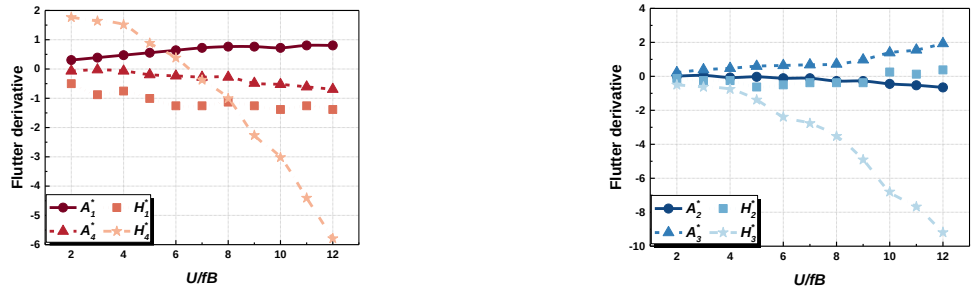

(29) Section 29

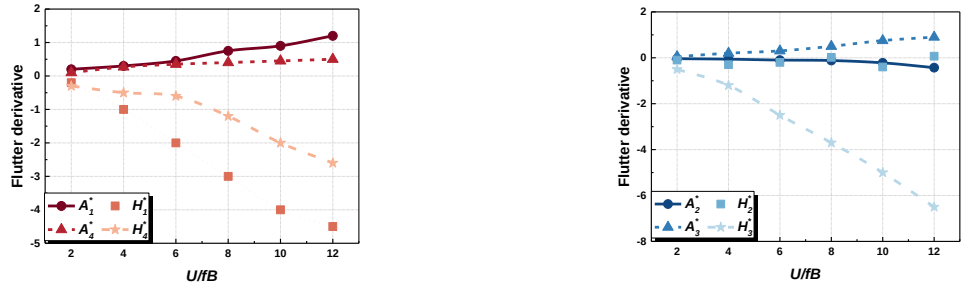

(30) Section 30

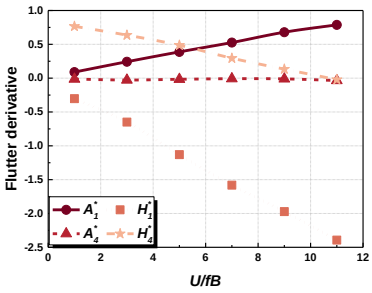

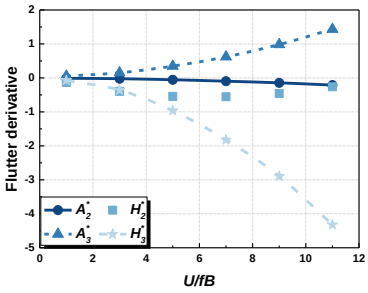

(31) Section 31

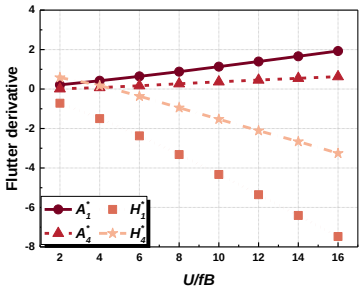

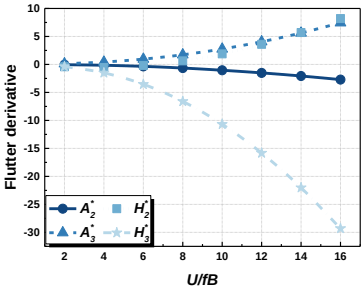

(32) Section 32

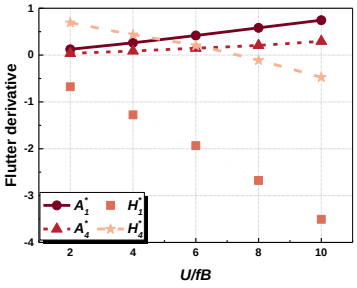

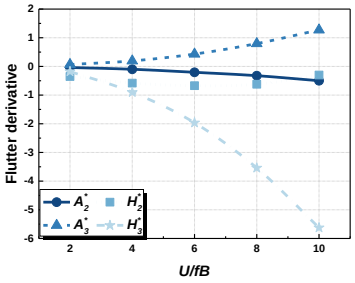

(33) Section 33

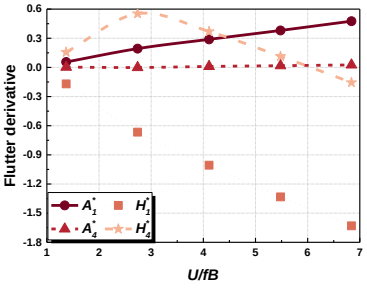

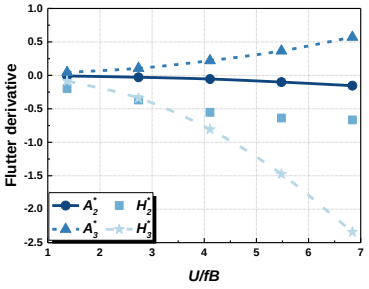

(34) Section 34

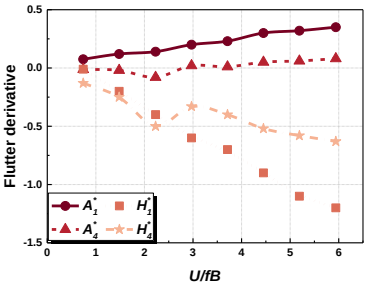

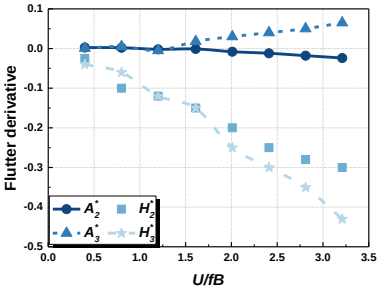

(35) Section 35

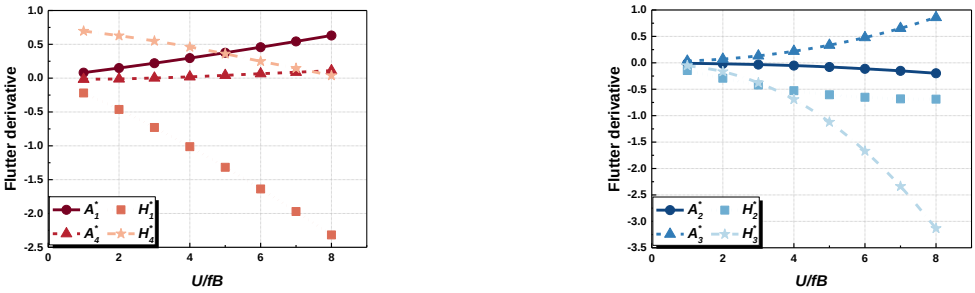

(36) Section 36

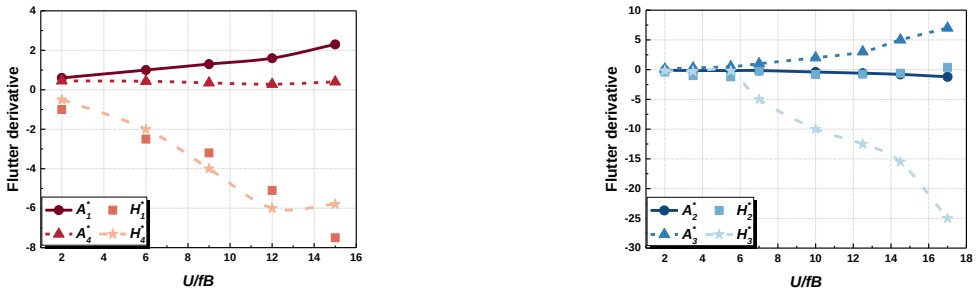

(37) Section 37

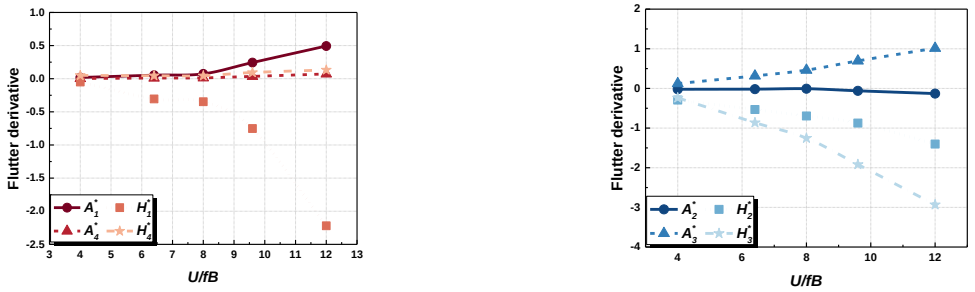

(38) Section 38

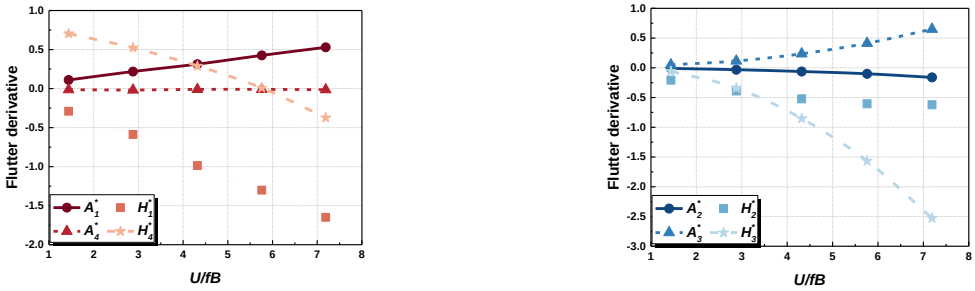

(39) Section 39

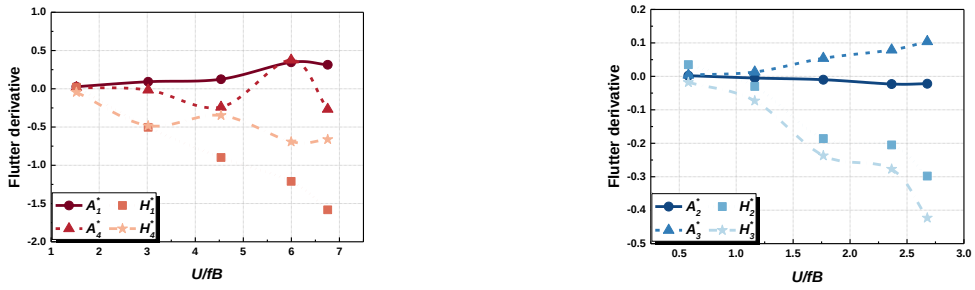

(40) Section 40

Figure B.1: Collected datasets of 40 closed box girders

Addendum

Appendix C: CFD numerical simulation results

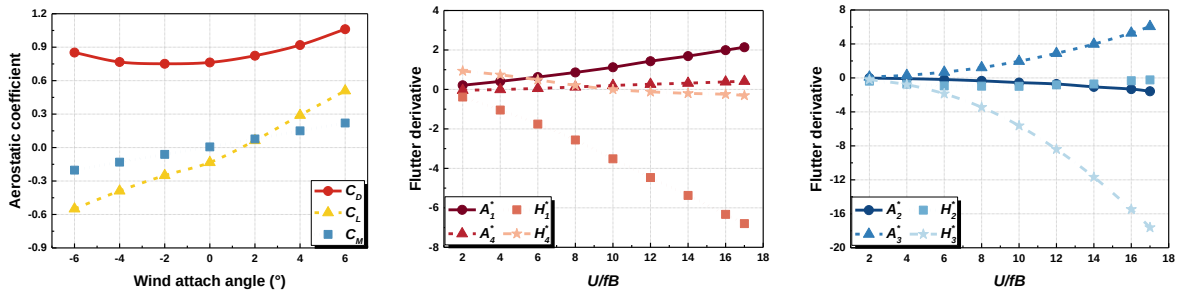

(1) Section 1

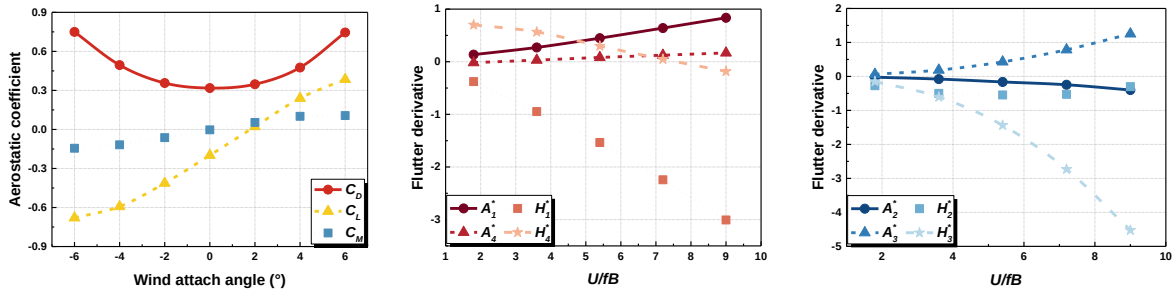

(2) Section 2

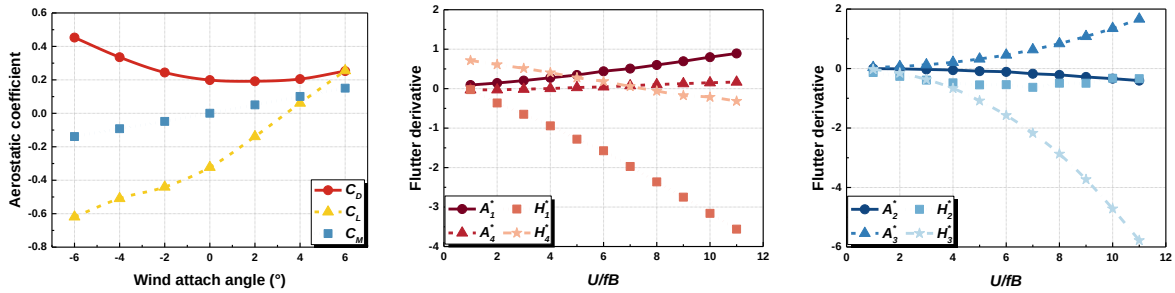

(3) Section 3

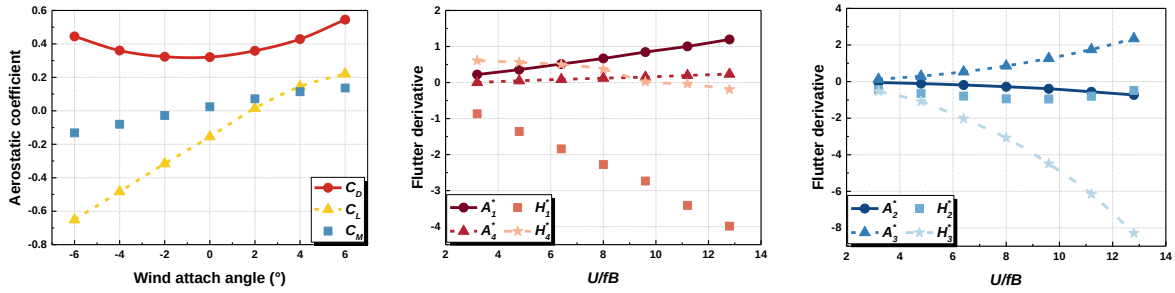

(4) Section 4

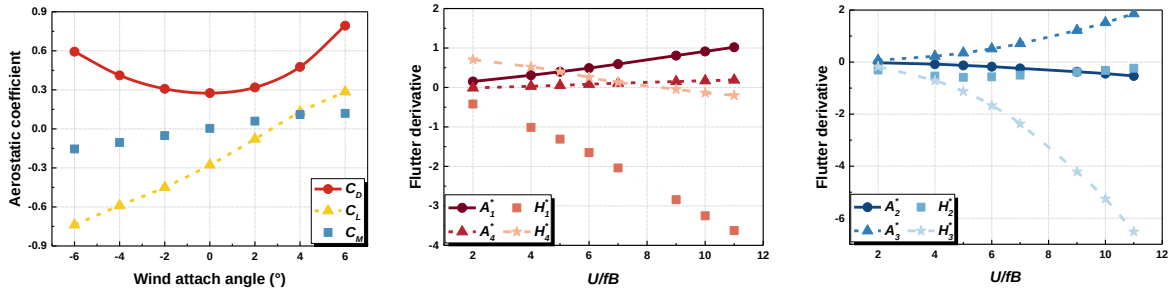

(5) Section 5

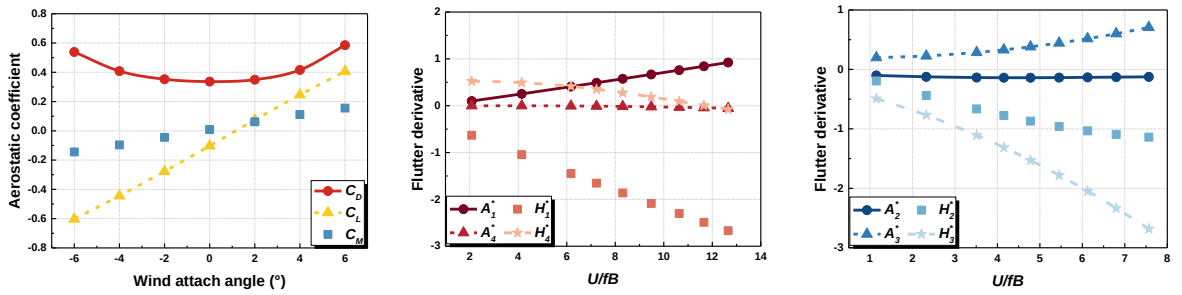

(6) Section 6

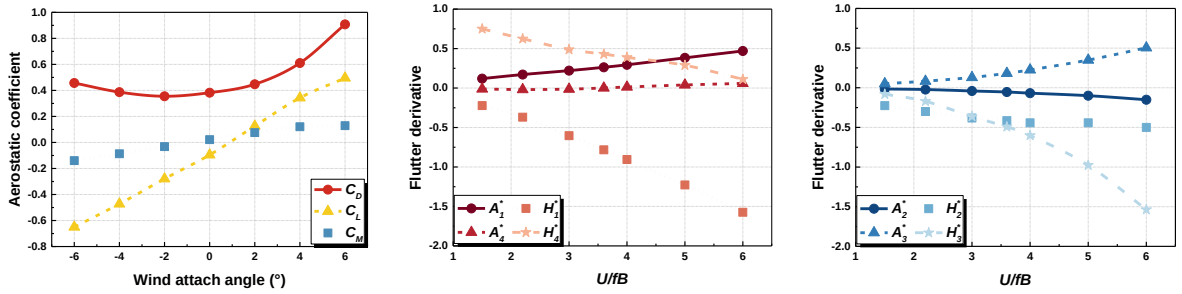

(7) Section 7

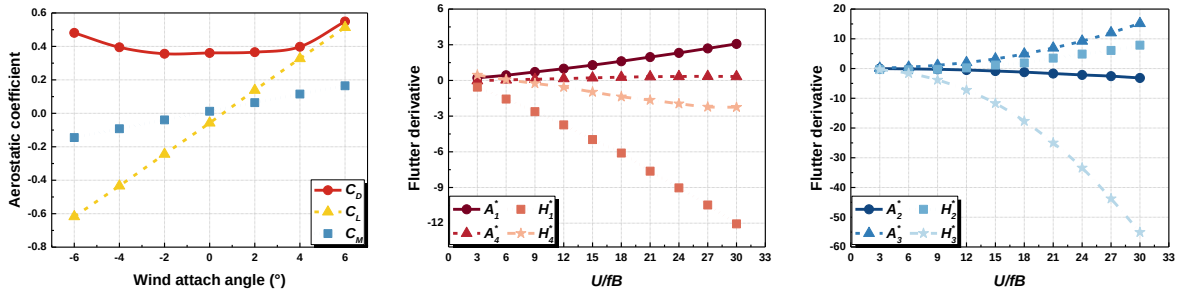

(8) Section 8

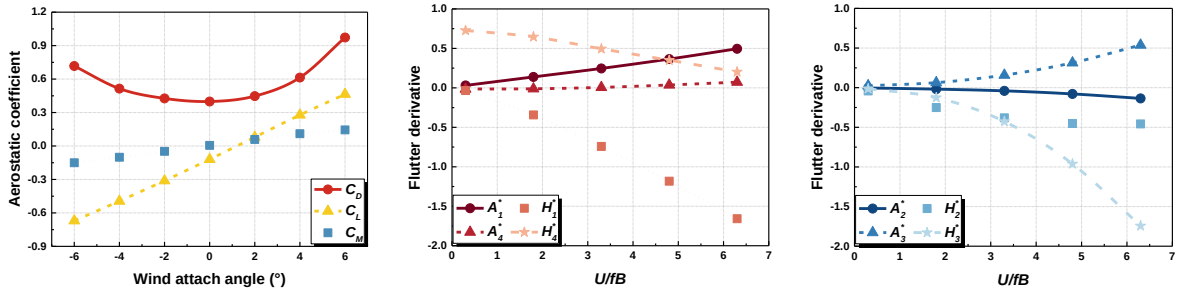

(9) Section 9

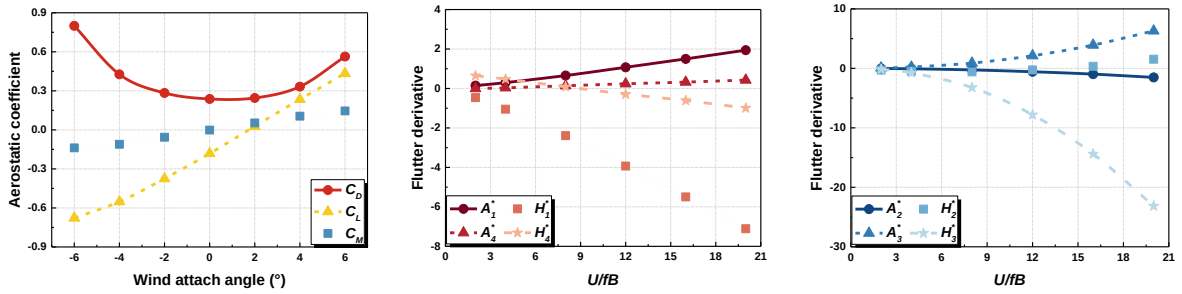

(10) Section 10

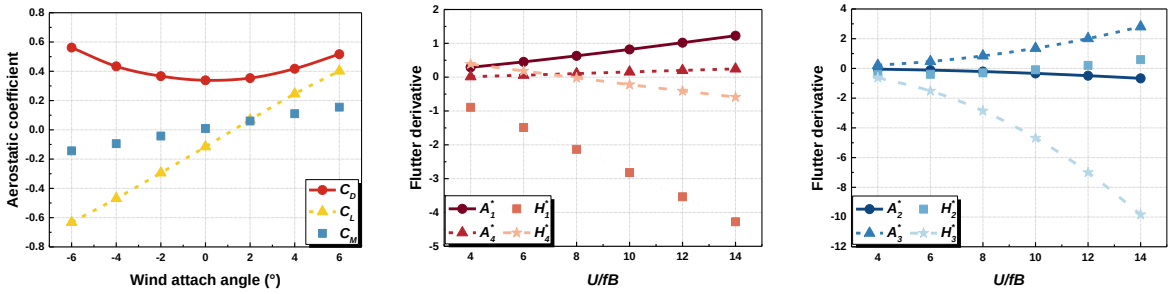

(11) Section 11

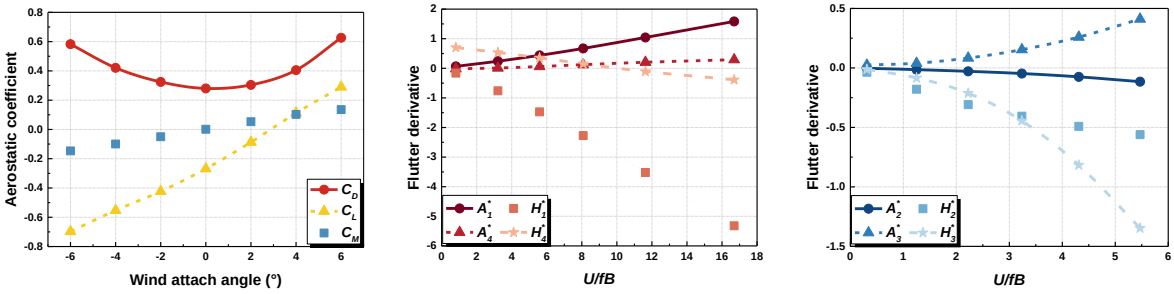

(12) Section 12

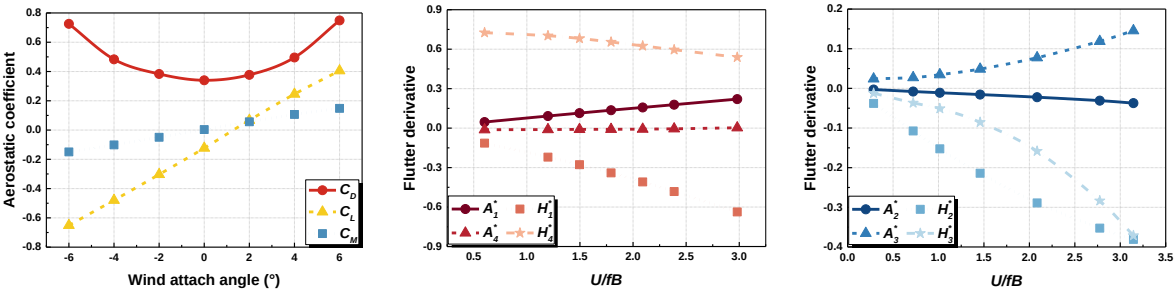

(13) Section 13

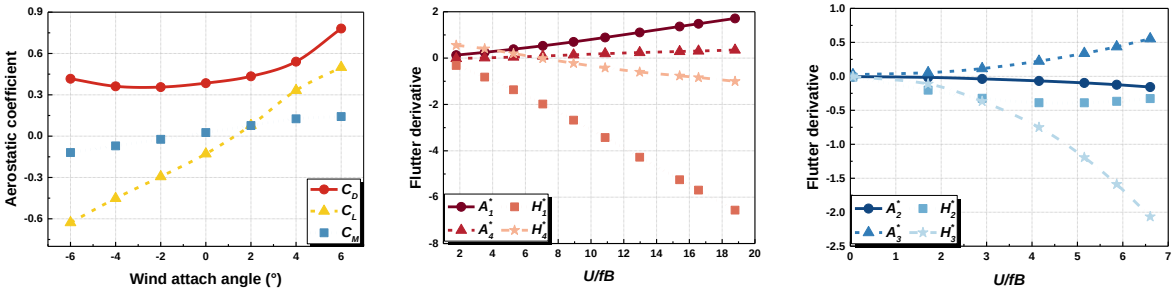

(14) Section 14

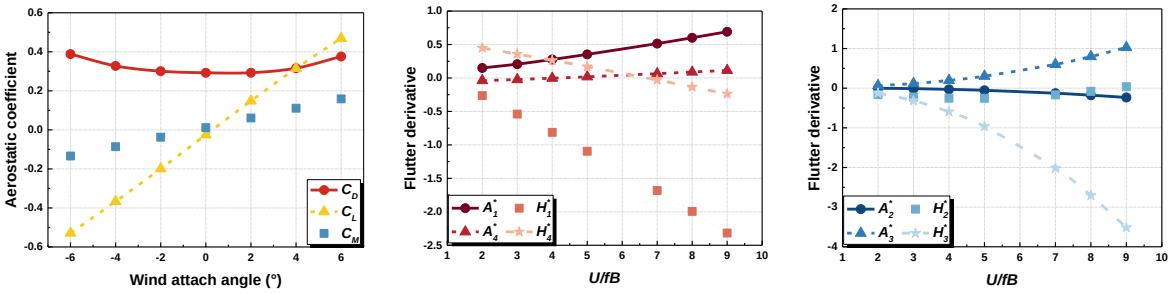

(15) Section 15

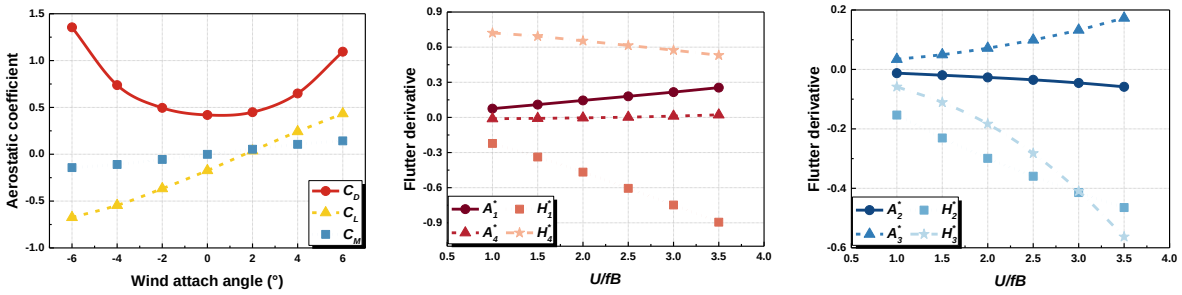

(16) Section 16

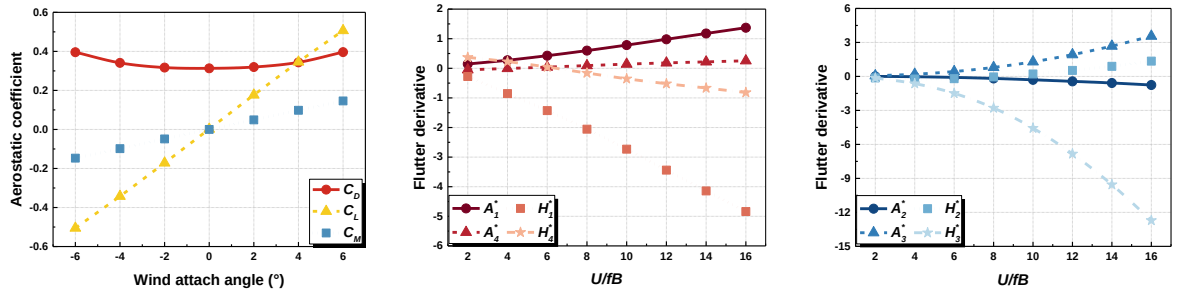

(17) Section 17

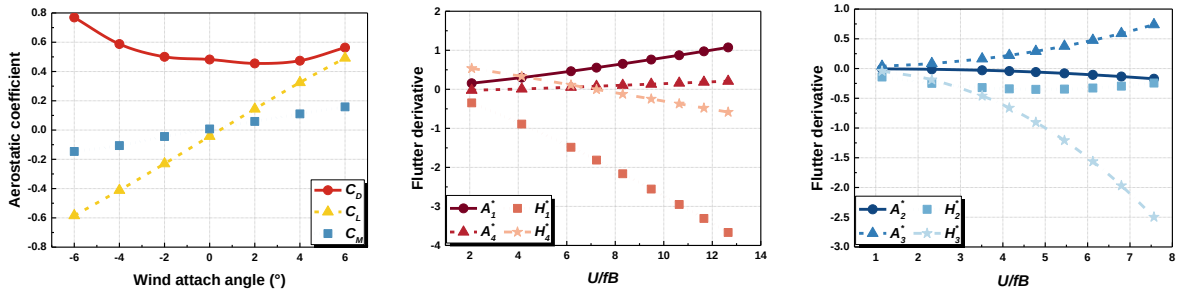

(18) Section 18

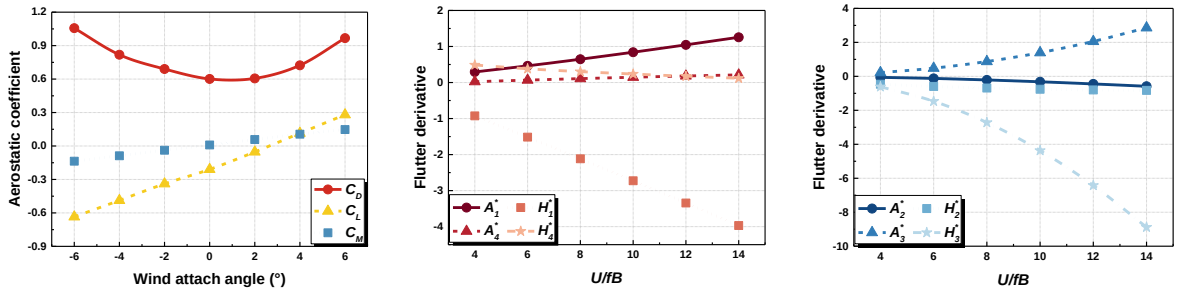

(19) Section 19

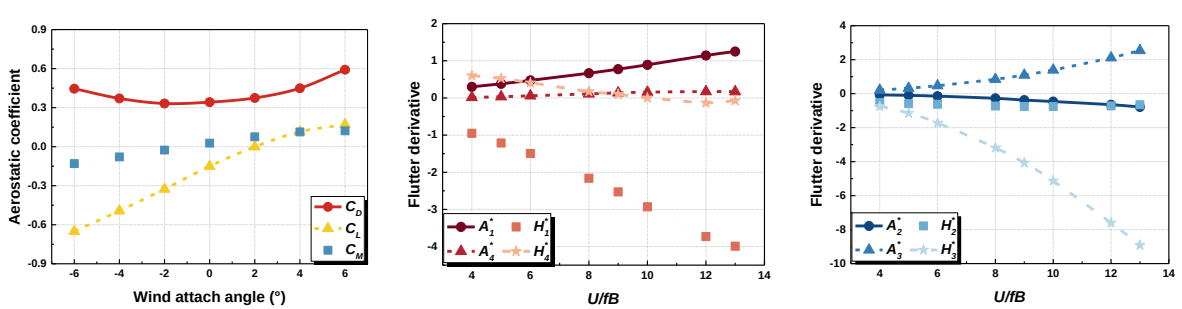

(20) Section 20

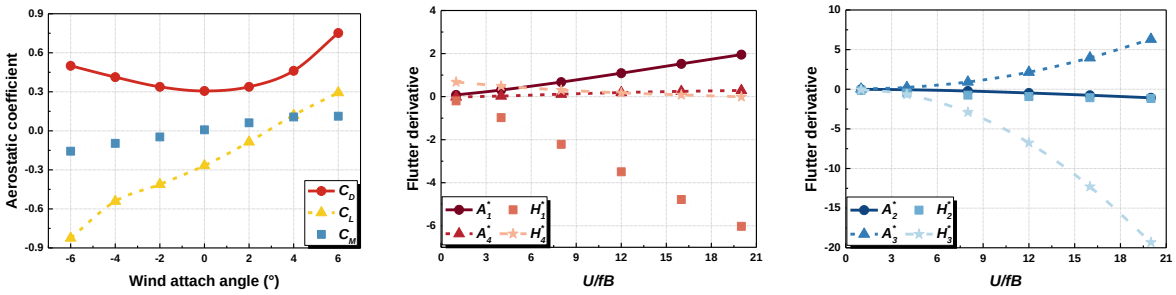

(21) Section 21

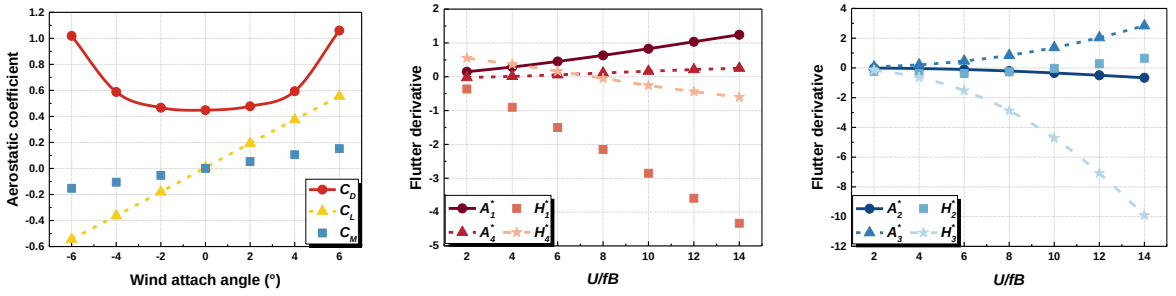

(22) Section 22

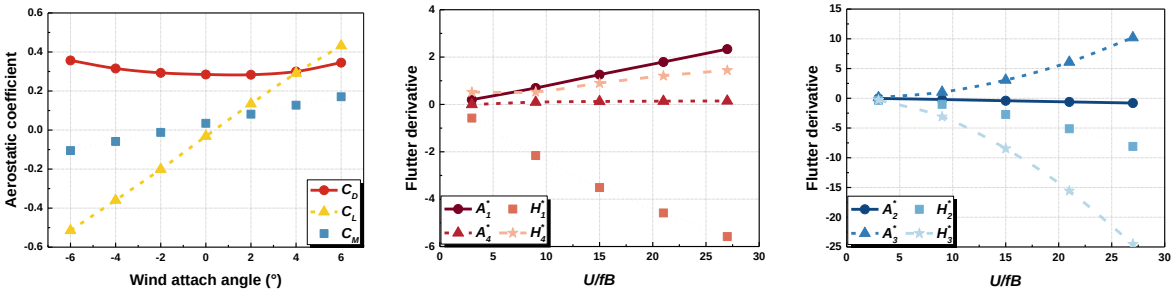

(23) Section 23

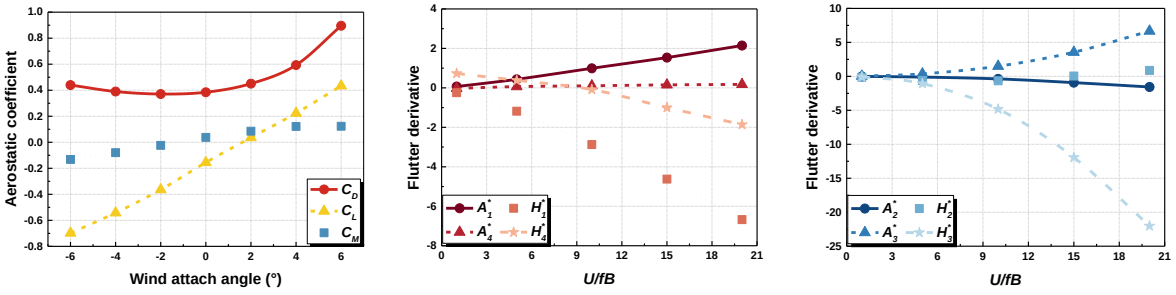

(24) Section 24

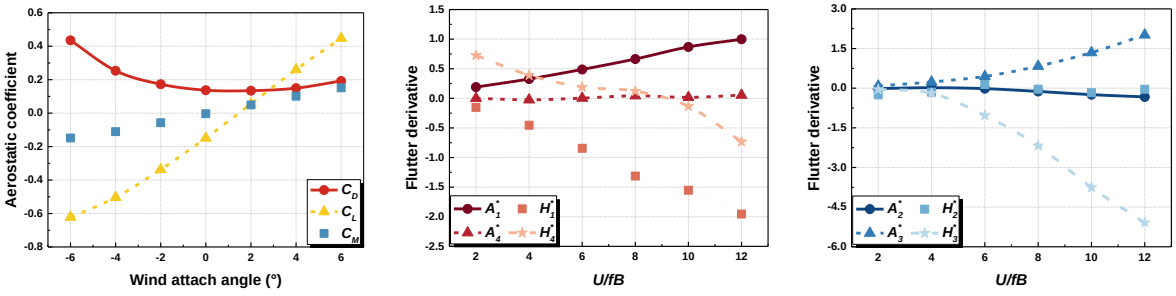

(25) Section 25

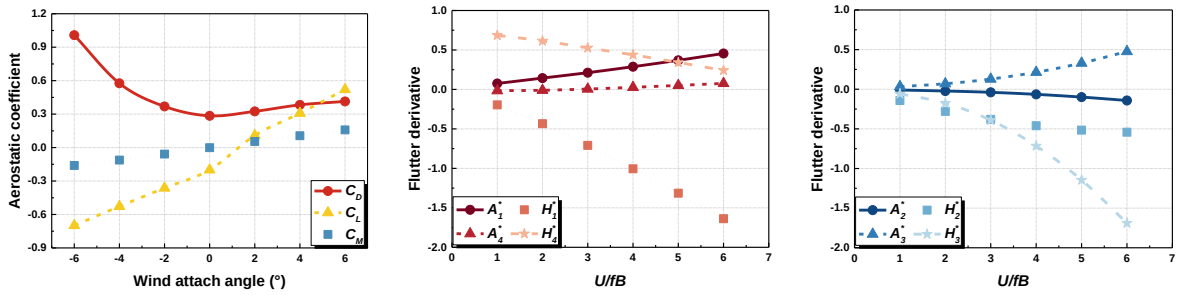

(26) Section 26

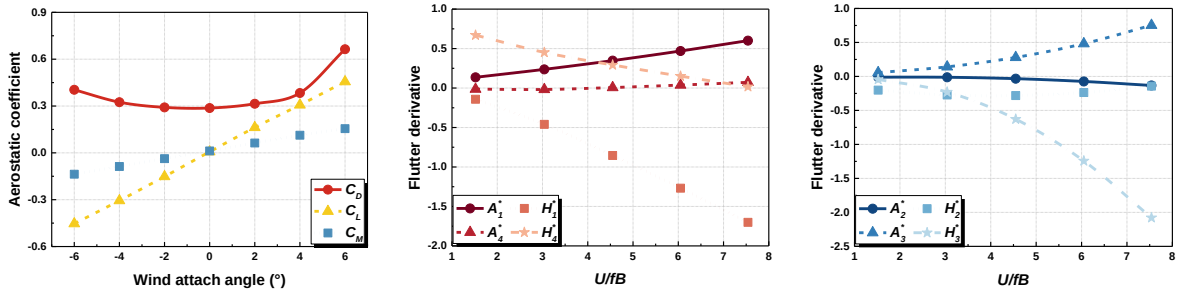

(27) Section 27

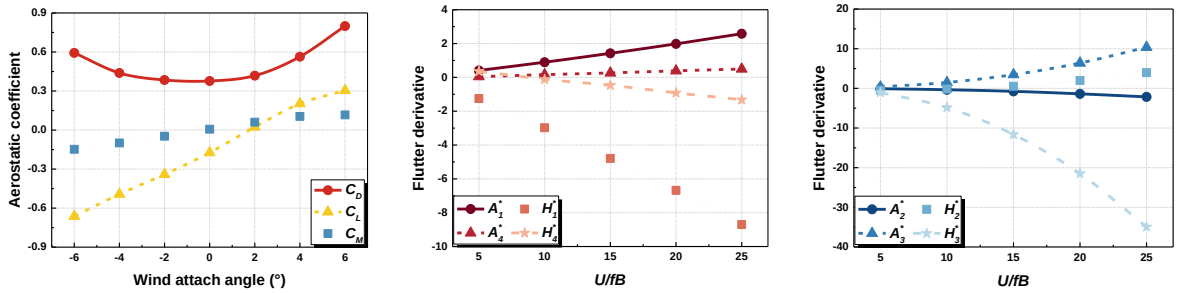

(28) Section 28

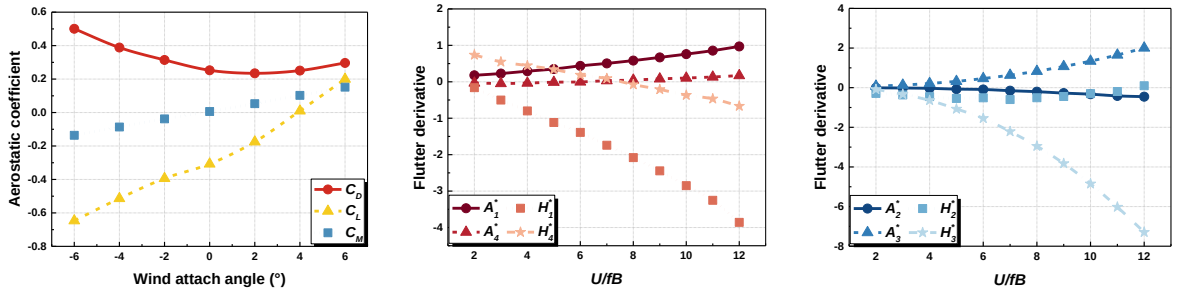

(29) Section 29

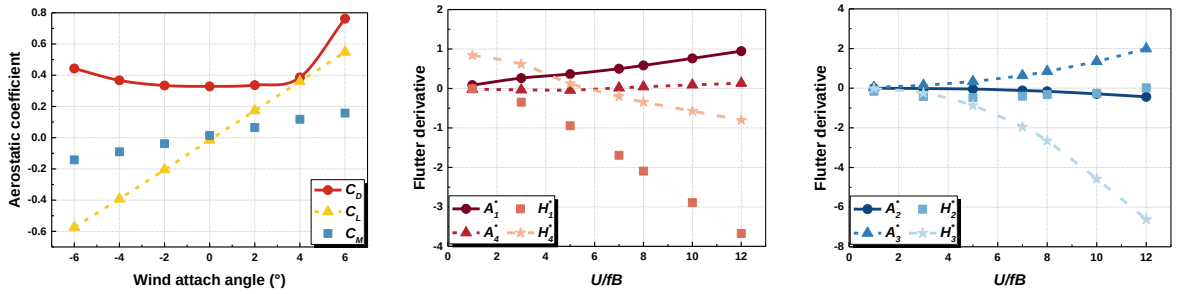

(30) Section 30

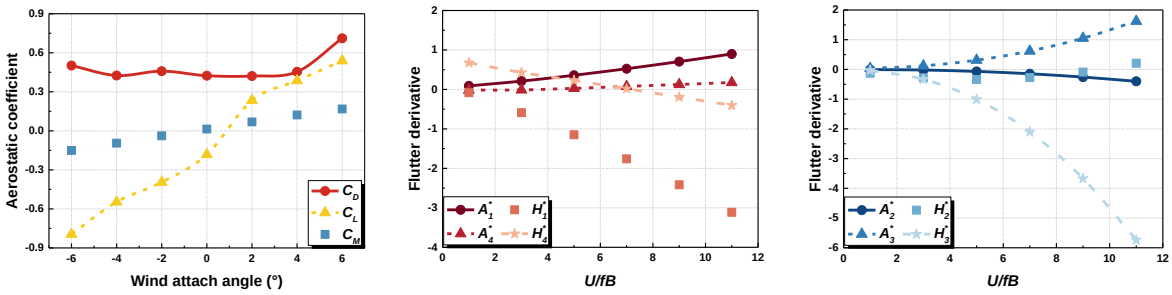

(31) Section 31

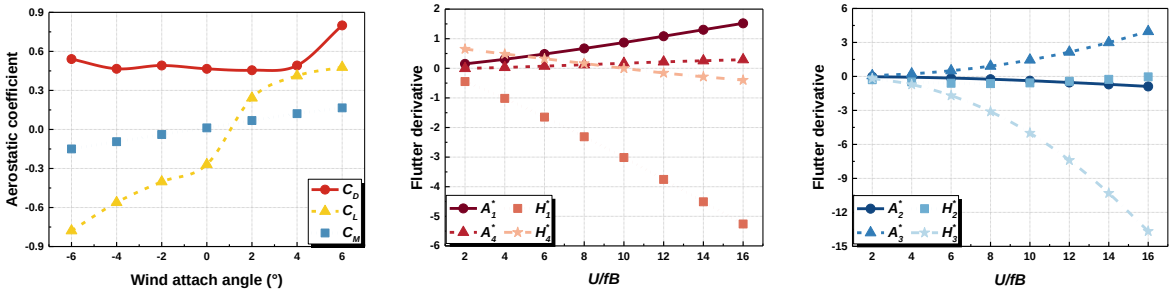

(32) Section 32

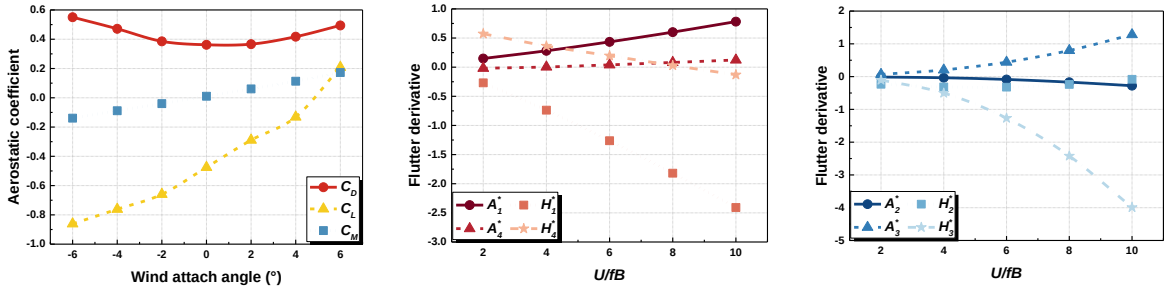

(33) Section 33

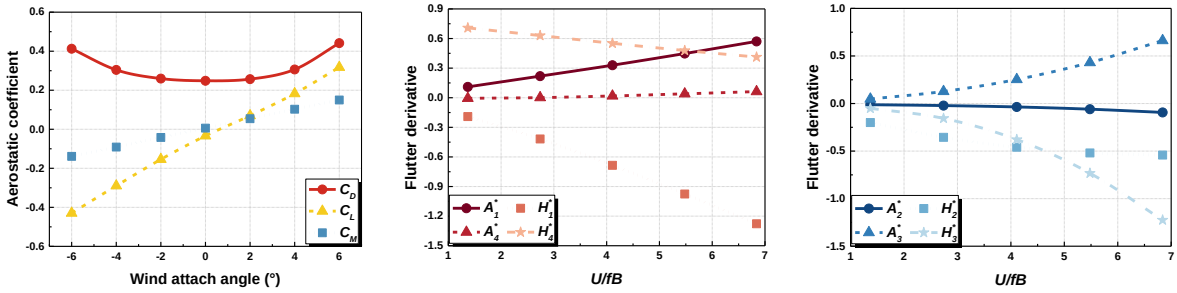

(34) Section 34

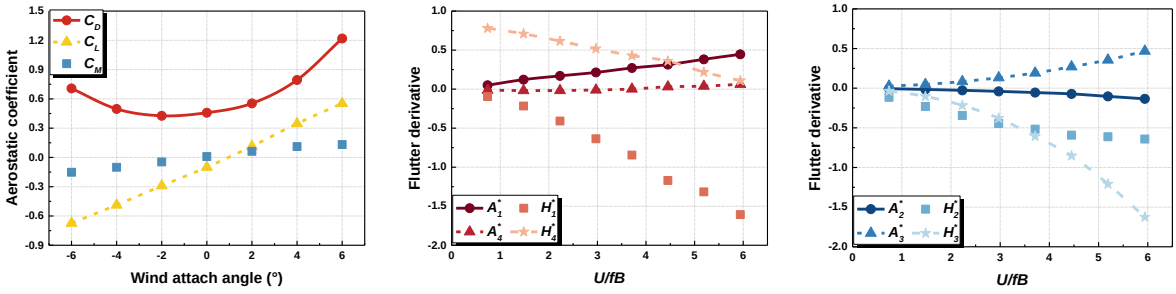

(35) Section 35

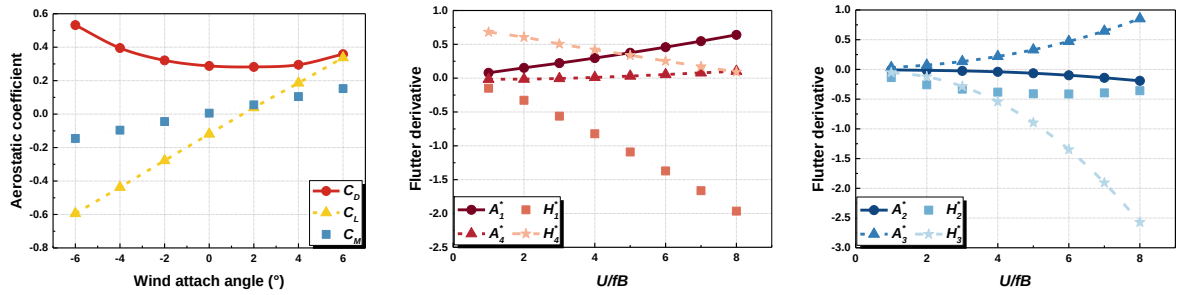

(36) Section 36

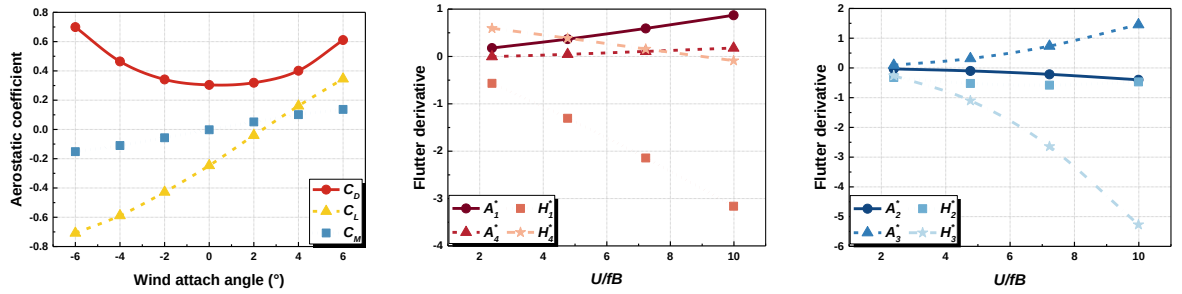

(37) Section 37

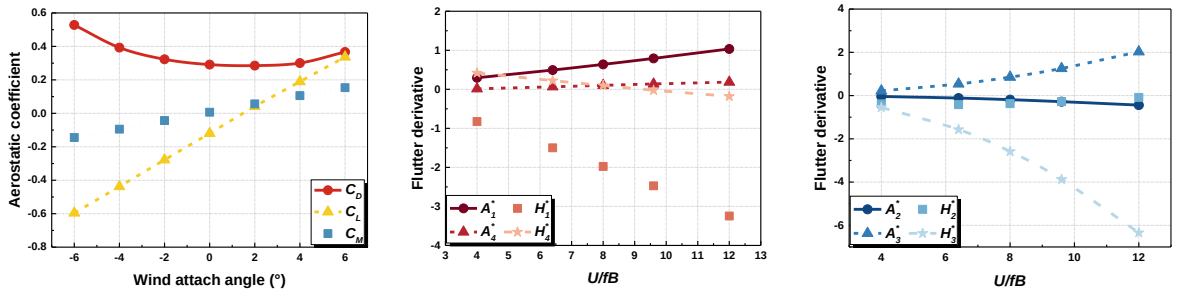

(38) Section 38

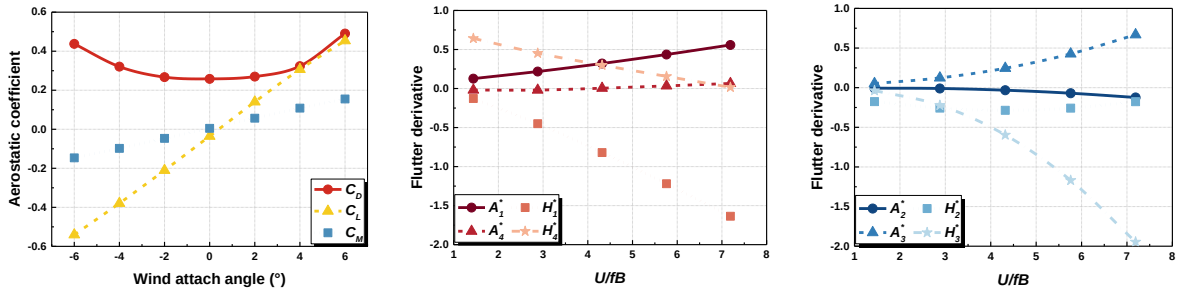

(39) Section 39

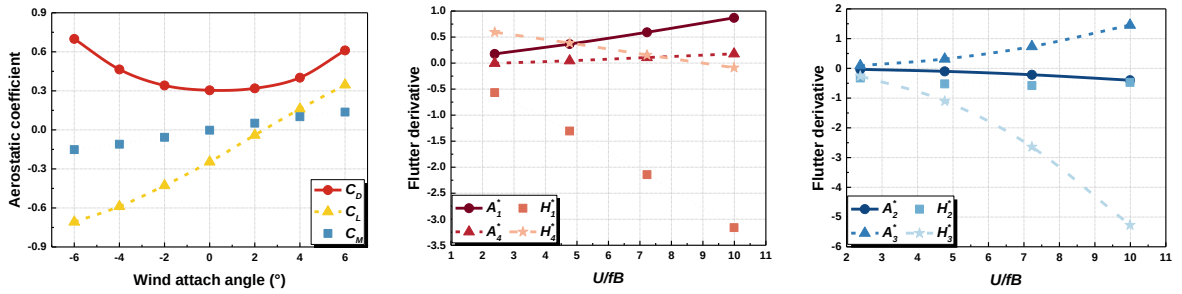

(40) Section 40

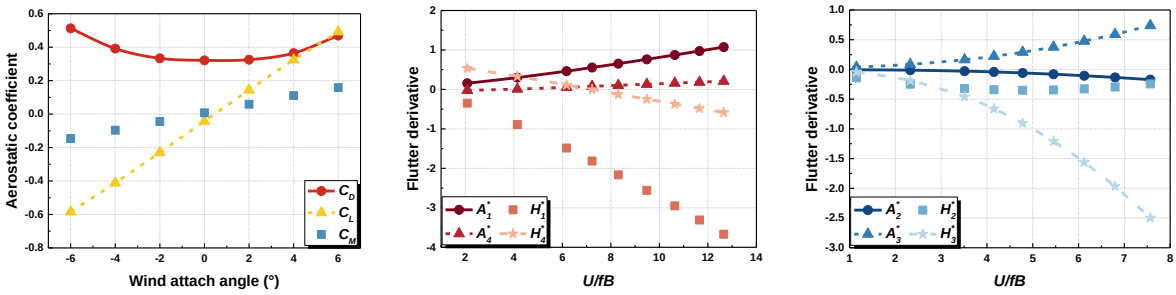

(41) Section 41

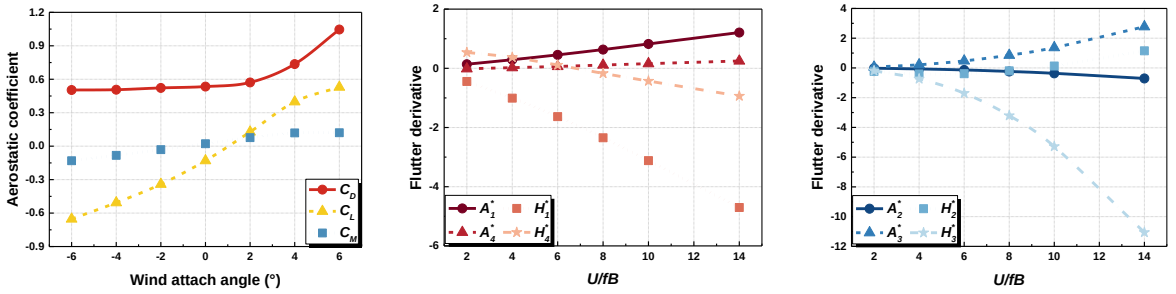

(42) Section 42

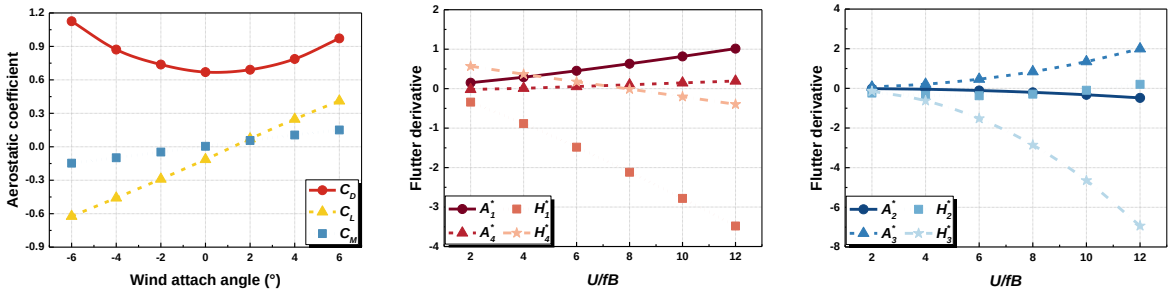

(43) Section 43

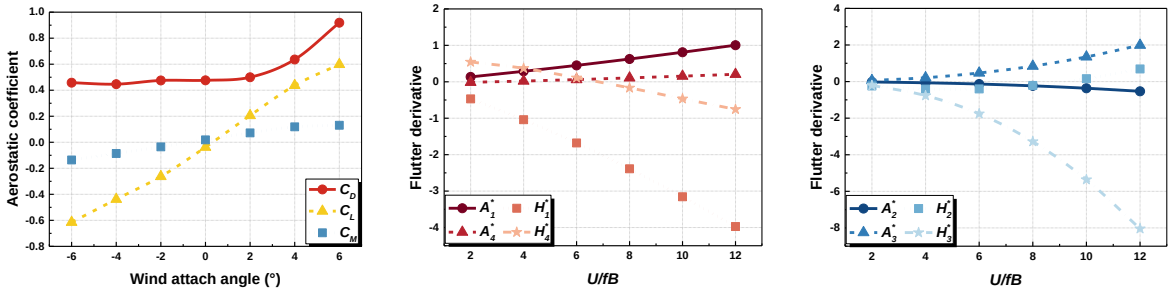

(44) Section 44

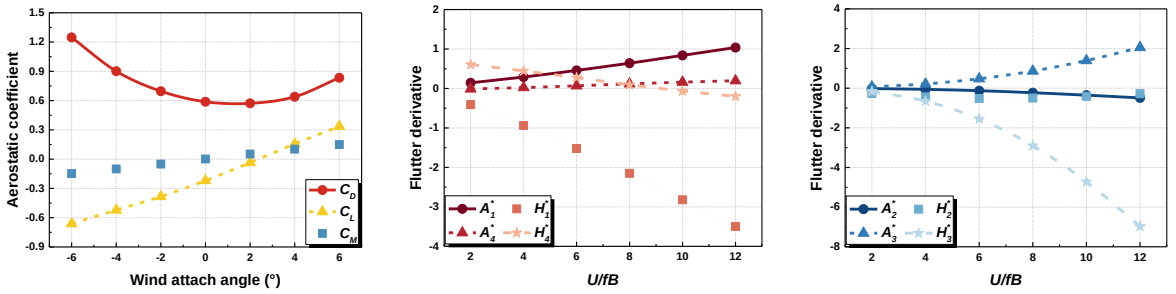

(45) Section 45

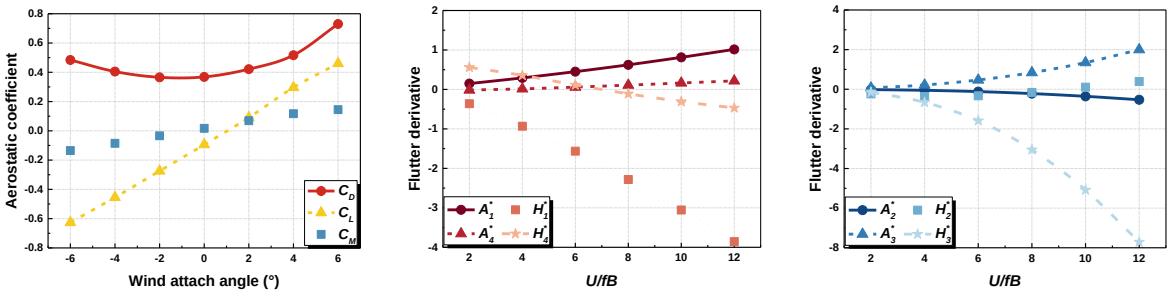

(46) Section 46

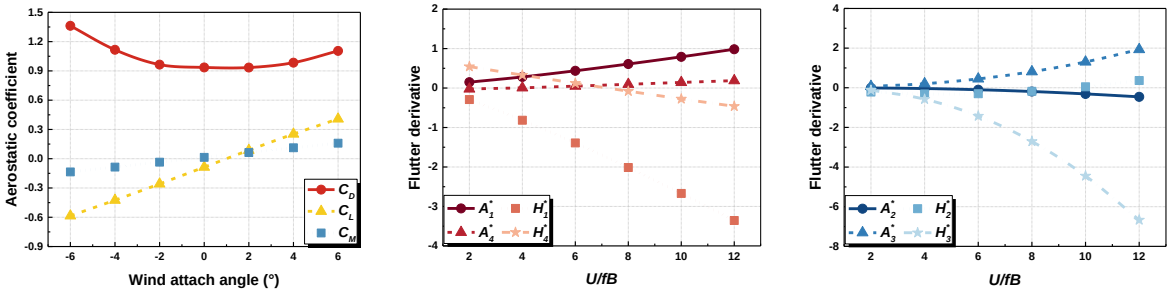

(47) Section 47

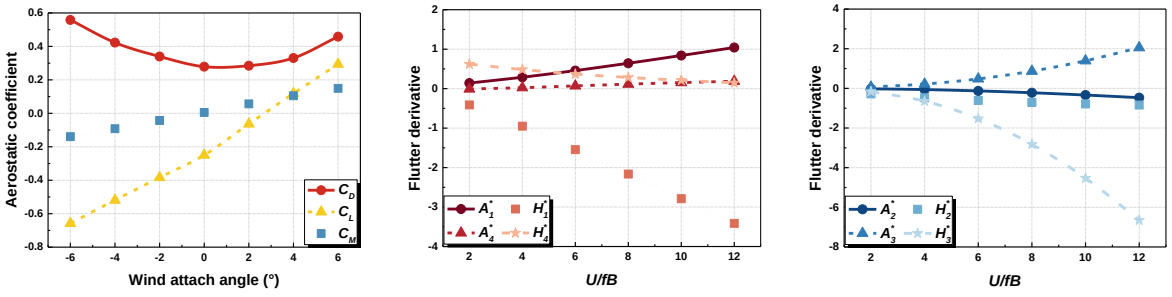

(48) Section 48

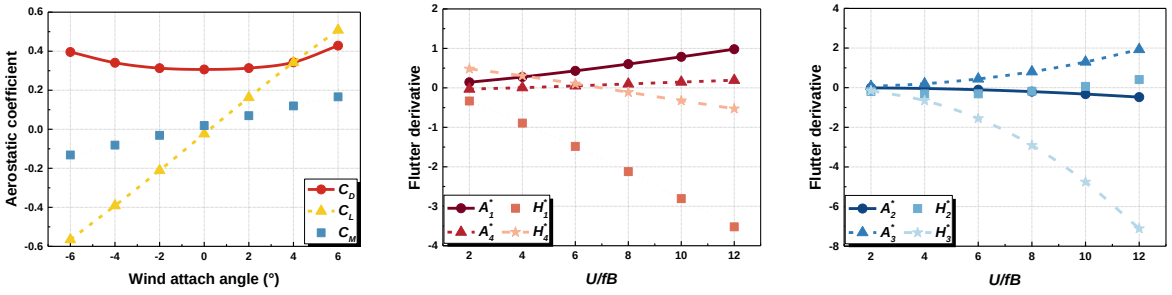

(49) Section 49

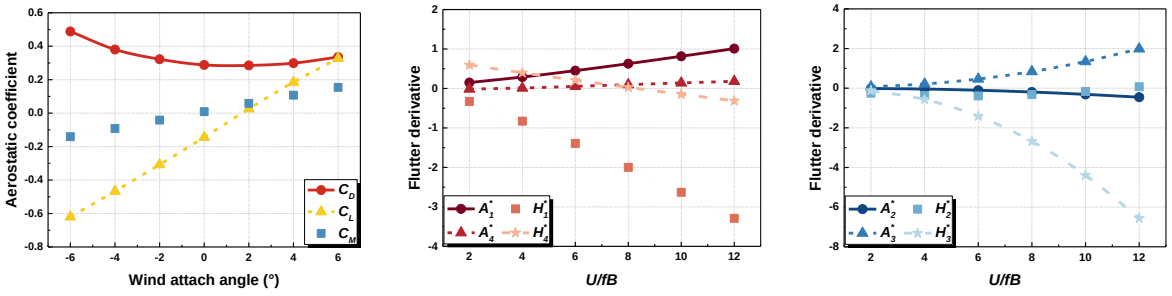

(50) Section 50

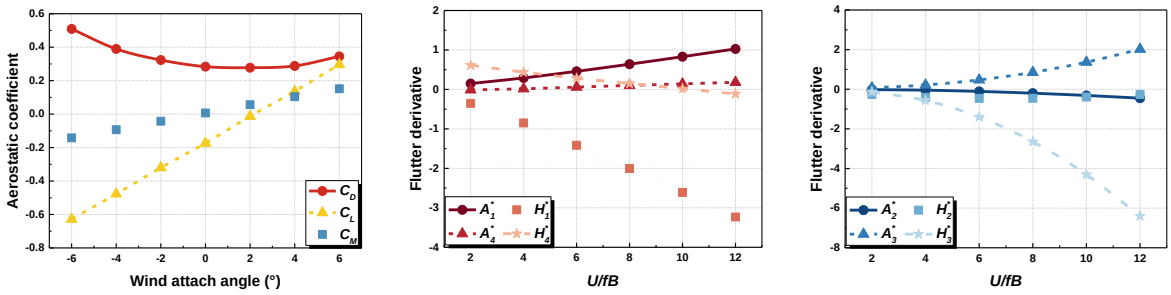

(51) Section 51

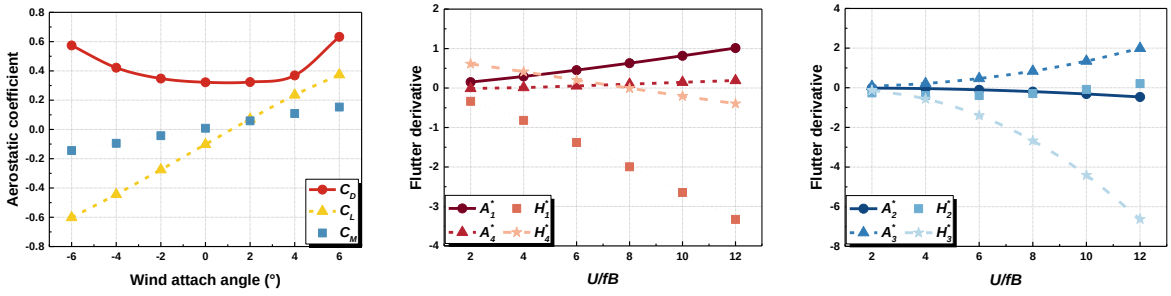

(52) Section 52

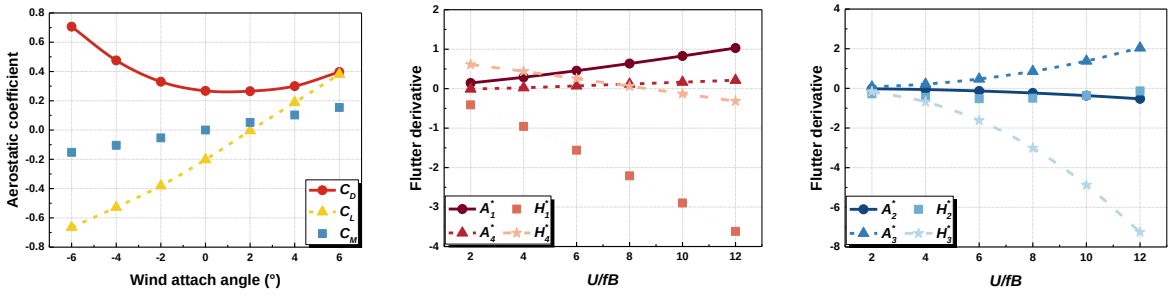

(53) Section 53

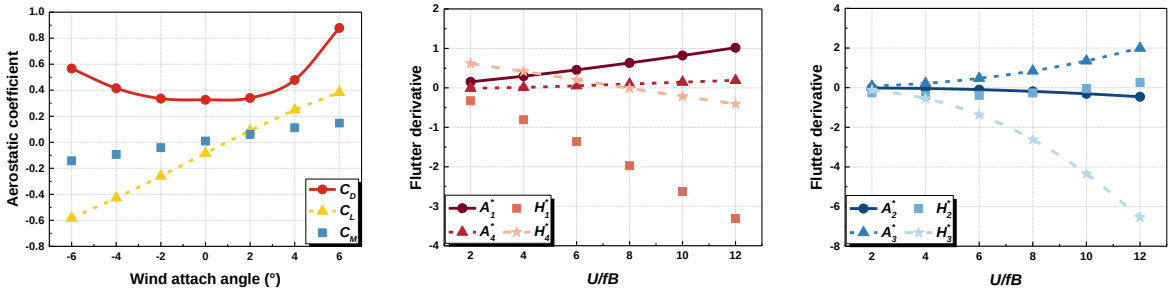

(54) Section 54

Figure C.1: CFD calculation results of 54 closed box girders

Bibliography

Abbas, T., Kavrakov, I., Morgenthal, G., Lahmer, T. (2020). Prediction of aeroelastic response of bridge decks using artificial neural networks. *Computers and Structures, 231, 106198.*

Aboshosha, H., Elshaer, A., Bitsuamlak, G.T., EI Damatty, A. (2015). Consistent inflow turbulence generator for LES evaluation of wind-induced responses for tall buildings. *Journal of Wind Engineering and Industrial Aerodynamics, 142, 198-216.*

Ayata, T., Arcakloglu, E., Yldz, O. (2018). Application of ANN to explore the potential use of natural ventilation in buildings in Turkey. *Applied Thermal Engineering, 27(1), 12-20.*

Bai, H., Xia, Y., Liu, J.X., Li, J.W. (2011). Numerical simulation for flutter stability of streamlined bridge decks. *Journal of Chang'an University (Natural Science Edition), 31(3), 45-50.* (in Chinese)

Bai, Y.L., Ou, J.P. (2009). Numerical simulation of flutter derivatives of CFRP streamlined box girders and determination of critical wind speed. *Proceedings of the 14th National Conference on Structural Wind Engineering*, Beijing, China. (in Chinese)

Bao, Y.Q., Li, H. (2020). Machine learning paradigm for structural health monitoring. *Structural Health Monitoring, 1475921720972416.*

Bartoli, G., Contri, S., Mannini, C., Righi, M. (2009). Toward an improvement in the identification of bridge deck flutter derivatives. *Journal of Engineering Mechanics, 135(8), 771-785.*

Billah, K.Y.R. (1989). *A study of vortex-induced vibration*. Ph.D. thesis, University of Princeton.

Bisplinghoff, R.L., Ashley, H., Halfman, R.L. (1957). *Aeroelasticity*. Cambridge: Addison-Wesley.

Bleich, F. (1949). Dynamic instability of truss-stiffened suspension bridges under wind action. *Transactions of the American Society of Civil Engineers, 114(1), 126-131.*

Boonyapinyo, V., Lauhatanon, Y., Lukkunaprasit, P. (2006). Nonlinear aerostatic stability analysis of suspension bridges. *Engineering Structures, 28(5), 793-803.*

Boonyapinyo, V., Yamada, H., Miyata, T. (1994). Wind-induced nonlinear lateral-torsional buckling of cable-stayed bridges. *Journal of Structural Engineering, 120(2), 486-506.*

Casero, R., Paredes, A., Sonnenschein, J. (1999). Complex notation in flutter analysis. *Journal of Structural Engineering, 124(8), 975-977.*

Castellon, D.F., Fenerci, A., Øiseth, O.A. (2020). Comparative study of wind-induced dynamic response models of long-span bridges using artificial neural networks, support vector regression and buffeting theory. *Journal of Wind Engineering and Industrial Aerodynamics, 209, 104484.*

Chao, C.R. (2015). *Research on flutter bridges with three towers and its whole process simulation*. Master's thesis, Southeast University. (in Chinese)

Chen, C.H., Wu, J.C., Chen, J.H. (2008). Prediction of flutter derivatives by artificial neural networks. *Journal of Wind Engineering and Industrial Aerodynamics, 96, 1925-1937.*

Chen, T., Guestrin, C. (2016). *XGBoost: a scalable tree boosting system.* 22nd International Conference on Knowledge Discovery and Data Mining, 785-794.

Chen, W. (1993). *Study on buffeting response spectrum of long-span bridges*. Ph.D. thesis, Tongji University. (in Chinese)

Chen, X., Kareem, A., Matsumoto, M. (2000). Aerodynamic coupling effects on flutter and buffeting of bridges. *Journal of Engineering Mechanics, 126(1), 17-26.*

Chen, X.Z., Matsumoto, M., Kareem, A. (2000). Time domain flutter and buffeting response analysis of bridges. *Journal of Engineering Mechanics, 126(1), 7-16.*

Chen, Y., Kopp, G. A., Surry, D. (2003). Prediction of pressure coefficients on roofs of low buildings using artificial neural networks. *Journal of Wind Engineering and Industrial Aerodynamics, 91(3), 423-441.*

Chen, Y.Q. (2016). *Aerodynamic shape optimization of central slotted box girders based on performance of wind-induced self-excited vibration*. Master's thesis, Tongji University. (in Chinese)

Chen, Z.Q. (2005). *Wind engineering of bridges*. Beijing: China Communications Press. (in Chinese)

Chen, Z.Q., Agar, T.J. (1994). Finite element-based flutter analysis of cable-suspended bridges. *Journal of Structure Engineering, 120(3), 1044-1046.*

Cheng, J., Xiao R.C. (2001). Discussion on methods of aerostatic stability analysis for long-span bridge and their improvement. *China Journal of Highway and Transport, 14(2), 30-32.* (in Chinese)

Cheng, J., Xiao, R.C., Xiang, H.F. (2000). Full range nonlinear analysis for long-span suspension bridge. *Journal of Tongji University (Natural Science), 6, 717-720.* (in Chinese)

Chowdhury, A.G., Sarkar, P.P. (2003). A new technique for identification of eighteen flutter derivatives using a three-degree-of-freedom section model. *Engineering Structures, 25(14), 1763-1772.*

Chung, J., Lee, S.W, Chang, S., Kim, Y.S. (2012). *Estimation of flutter derivatives of various sections using numerical simulation and neural network*. 2012 World Congress on Advances in Civil, Environmental, and Materials Research.

Costa, C., Borri, C. (2006). Application of indicial functions in bridge deck aeroelasticity. *Journal of Wind Engineering and Industrial Aerodynamics, 94: 859-881.*

Davenport, A.G. (1962). Buffeting of a suspension bridge by storm winds. *Journal of Structural Engineering, 88(3), 233-270.*

Diana, G., Resta, F., Belloli, M., Rocchi, D. (2006). On the vortex shedding forcing on suspension bridge deck. *Journal of Wind Engineering and Industrial Aerodynamics, 94(5), 341-363.*

Ding, Q.S. (2001). *Refinement of coupled flutter and buffeting analysis for long-span bridges*. Ph.D. thesis, Tongji University. (in Chinese)

Ding, Q.S., Chen, A.R., Xiang H.F. (2002). Coupled flutter analysis of long-span bridges by multimode and full-order approaches. *Journal of Wind Engineering and Industrial Aerodynamics, 90(12-15), 1981-1993.*

Ding, Q.S., Wang, J., Zhu, L.D. (2012). Coupled free vibration technique for identifying flutter derivatives of bridge decks. *Journal of Vibration and Shock, 31(24), 5-8+25.*

Ding, Q.S., Zhou, Z.Y., Zhu, L.D., Xiang, H.F. (2010). Identification of flutter derivatives of bridge decks with free vibration technique. *Journal of Wind Engineering and Industrial Aerodynamics, 98(12), 911-918.*

Du, B.S., Ge, Y.J., Li, Y.J. (2003). *Wake testing method for vortex-induced vibration of bridge cross-sections*. 11st National Conference on Structural Wind Engineering, 189-194. (in Chinese)

Elshaer, A., Bitsuamlak, G., EI Damatty, A. (2017). Enhancing wind performance of tall buildings using corner aerodynamic optimization. *Engineering Structures, 136, 133-148.*

Fang, G.S., Cao, J.X., Yang, Y.X., Zhao, L., Cao, S.Y., Ge, Y.J. (2020). experimental uncertainty quantification of flutter derivatives for a PK section girder and its application on probabilistic flutter analysis. *Journal of Bridge Engineering, 25(7), 04020034.*

Fu, J. (2016). *Wind tunnel experimental investigation and numerical simulation on the flutter characteristic of a long-span sus-pension bridge.* Master's thesis, Chongqing University. (in Chinese)

Fu, J.Y., Xie, Z.N., Ni, Z.H. (2002). Prediction of wind load on large span roof using fuzzy neural networks. *Journal of Building Structures, 23(1): 62-67*. (in Chinese)

Fung, Y. C. (1955). *An introduction to the theory of aeroelasticity*. New York: John Wiley & Sons.

Gao, W. (2013). *Flutter derivatives research of large span bridges under skew wind*. Master's thesis, Southwest Jiaotong University. (in Chinese)

Ge, Y.J. (2011). *Wind resistance of long span suspension bridges*. Beijing: China Communications Press. (in Chinese)

Ge, Y.J., Xiang, H.F., Tanaka, H. (2000). Application of a reliability analysis model to bridge flutter under extreme winds. *Journal of Wind Engineering and Industrial Aerodynamics, 86(2-3), 155-167.*

Gu, M., Zhang, R.X., Xiang, H.F. (2000). Identification of flutter derivatives of bridge decks. *Journal of Wind Engineering and Industrial Aerodynamics, 84(2), 151-162.*

Gu, M. Zhou, X.Y. (2003). Application of neural network in the prediction of wind load on long-span roofs. *Engineering Mechanics, 20(4), 99-103.* (in Chinese)

Hao, D. (2011). *The study of the effect of tuyere on bridge flutter stability*. Master's thesis, Chang'an University. (in Chinese)

Hasegawa, K., Fukami, K., Murata, T., Fukagata, K. (2020). Machine-learning based reduced-order modeling for unsteady flows around bluff bodies of various shapes. *Theoretical and Computational Fluid Dynamics, 34, 367-383.*

He, Y. (2016). *Conceptual design and wind stability analysis of a suspension bridge with span of 3500m.*

Master's thesis, Southwest Jiaotong University. (in Chinese)

Ho, T., Surry, D., Morrish, D., Kopp, G. (2005). The UWO contribution to the NIST aerodynamic database for wind loads on low buildings: part 1. archiving format and basic aerodynamic data. *Journal of Wind Engineering and Industrial Aerodynamics, 93, 1-30.*

Hong, C.J. (2019). *Numerical calculation method for flutter critical wind speed and flutter derivatives of long-span bridge streamlined steel box girder*. Master's thesis, Southwest Jiaotong University. (in Chinese)

Hong, G. (2012). *Identifying long-span bridge flutter derivatives via the free vibration method based on the flutter software*. Master's thesis, Chang'an University. (in Chinese)

Hong, L.Z. (2020). *Influence of wind barrier on flutter performance of bridge*. Master's thesis, Tongji University. (in Chinese)

Hu, G., Kwok, K.C.S. (2020). Predicting wind pressures around circular cylinders using machine learning techniques. *Journal of Wind Engineering and Industrial Aerodynamics, 198, 104099.*

Hu, X.L. (2006). *Analysis of buffeting and flutter vibration and aerostatic stability for long-span cable-stayed bridges*. Ph.D. thesis, Tongji University. (in Chinese)

Huang, D.M., He, S.Q., He, X.H., Zhu, X. (2017). Prediction of wind loads on high-rise building using a BP neural network combined with POD. *Journal of Wind Engineering and Industrial Aerodynamics, 170, 1-17.*

Huston, D.R. (1986). *The effects of upstream gusting on the aeroelastic behavior of long suspended-span bridges*. Ph.D. thesis, University of Princeton.

Jiao, L.N. (2009). *The effects of characteristics of mean wind and fluctuate wind on long-span bridge*. Master's thesis, Harbin Institute of Technology. (in Chinese)

Jin, X.W., Cheng, P., Chen, W.L., Li, H. (2018). Prediction model of velocity field around circular cylinder over various Reynolds numbers by fusion convolutional neural networks based on pressure on the cylinder. *Physics of Fluids, 30(4), 047105.*

Jung, S., Ghaboussi, J., Kwon, S.D. (2004). Estimation of aeroelastic parameters of bridge decks using neural networks. *Journal of Engineering Mechanics,130 (11), 1356-1364.*

Le, V., Caracoglia, L. (2020). A neural network surrogate model for the performance assessment of a vertical structure subjected to non-stationary, tornadic wind loads. *Computers and Structures, 231, 106208.*

Lecun, Y., Bengio, Y. (1995). Pattern recognition and neural networks. *Technometrics, 39(2), 233-234.*

Li, J.W., Fang, C., Hou, L.M., Wang, J. (2012). Sensitivity analysis for aerostatic stability parameter of a long-span bridge. *Journal of Vibration and Shock, 33(4), 124-130*. (in Chinese)

Li, L. (2003). *Identification of aerodynamic parameters of bridge section using artificial neural network*. Master's thesis, Southwest Jiaotong University. (in Chinese)

Li, Q., Yang, X.W. (2000). Artificial neural network method for analyzing the aerodynamic characteristics of main beam cross-section of bridge. *Highway Engineering, 25(3), 56-59.* (in Chinese)

Li, S.W., Laima, S.J., Li, H. (2018). Data-driven modeling of vortex-induced vibration of a long-span suspension bridge using decision tree learning and support vector regression. *Journal of Wind Engineering and Industrial Aerodynamics, 172, 196-211.*

Li, S.W., Li, S.C., Laima, S.J., Li, H. (2021). Data-driven modeling of bridge buffeting in the time domain

using long short-term memory network based on structural health monitoring. *Structural Control and Health Monitoring, 28(8), e2772.*

Li, T., Wu, T., Liu, Z. (2020). Nonlinear unsteady bridge aerodynamics: reduced-order modeling based on deep LSTM networks. *Journal of Wind Engineering and Industrial Aerodynamics, 198, 104116.*

Li, Y., Li, C., Liang, Y.D., Li, J.W. (2022). Fast prediction of the flutter critical wind speed of streamlined box girders by using aerostatic force coefficients and artificial neural networks. *Journal of Wind Engineering and Industrial Aerodynamics, 222, 104939.*

Li, Y.J., Ge, Y.J., Du, B.S. (2003). *Generalized nonlinear vortex-induced vibration model and its experimental study of long-span bridge*. 11st National Conference on Structural Wind Engineering, 229-234. (in Chinese)

Li, Y.L., Liao, H.L., Qiang, S.Z. (2003). Weighting ensemble least-square method for flutter derivatives of bridge decks. *Journal of Wind Engineering and Industrial Aerodynamics, 91(6), 713-721.*

Li, Z.G., Wang, Q., Liao, H.L., Wei, Y.F. (2018). Effects of inclined web slope on flutter performance of flat box girders and their quantification. *Journal of Vibration and Shock, 37(9), 17-24.* (in Chinese)

Lin, Y.K., Ariaratnam, S.T. (1980). Stability of bridge motion in turbulent winds. *Journal of Structural Mechanics, 8(1), 1-15.*

Lin, Y.K., Yang, J.N. (1983). Multimode bridge response to wind excitations. *Journal of Engineering Mechanics, 109(2), 586-603.*

Liu, S.Y. (2009). *Numerical evaluation and program of wind-resistant performance for highway bridges*. Bachelor's thesis, Tongji University. (in Chinese)

Lundberg, S.M., Lee, S.I. (2017). *A unified approach to interpreting model predictions*. 31st International Conference on Neural Information Processing Systems.

Lute, V., Upadhyay, A., Singh, K.K. (2009). Support vector machine based aerodynamic analysis of cable stayed bridges. *Advances in Engineering Software, 40(9), 830-835.*

Lv, L.S., Meng, Q.B., Li, T. (2011). Study on flutter derivative identification method based on MIMO system. *Bridge and Tunnel Engineering. 2, 42-47.* (in Chinese)

Mei, H.Y. (2021). *Deep neural network-based method for calculating nonlinear aerodynamic forces and responses of bridge section.* Ph.D. thesis, Southwest Jiaotong University. (in Chinese)

Miyata, T., Yamada, H. (1990). Coupled flutter estimate of a suspension bridge. *Journal of Wind Engineering and Industrial Aerodynamics, 33(1-2), 341-348.*

Nagai, M., Xie, X., Yamaguchi, H. (1998). Static and dynamic instability analyses of 1400-meter long-span cable-stayed bridges. *IABSE Reports, 79, 281-286.*

Namini, A., Albrecht, P., Bosch, H. (1992). Finite element-based flutter analysis of cable-suspended bridges. *Journal of Structure Engineering, 118(6), 1509-1526.*

Niu, H.W., Chen, Z.Q. (2014). Three degrees-of-freedom forced vibration method for identifying eighteen flutter derivatives of bridge decks. *China Civil Engineering Journal, 4, 75-83.* (in Chinese)

Oh, B.K., Glisic, B., Kim, Y., Park, H.S. (2019). Convolutional neural network-based wind induced response estimation model for tall buildings. *Computer Aided Civil and Infrastructure Engineering, 34, 843-858.*

Pang, W. (2007). *The identification of flutter derivatives for long-span bridges based on fluent*. Master's thesis, Southwest Jiaotong University. (in Chinese)

Peng, Y. (2012). *The numerical analysis for flutter stability on streamlined box girder and pneumatic control measures.* Master's thesis, Central South University. (in Chinese)

Phipps, G. (1999). Comparing observed bug and productivity rates for Java and C++. *Software Practice and Experience, 29(4), 345-358.*

Qi, Y.H. (2013). *Numerical analysis on 3D flutter instability of long-span suspension bridges and effects from active controlled wind barrier.* Master's thesis, Central South University. (in Chinese)

Qin, X.R., Gu, M. (2005). Stochastic system method for identification of aerodynamic derivatives of bridge decks in turbulent flow. *China Civil Engineering Journal, 38(4), 73-77.* (in Chinese)

Quan, Y., Tamura, Y., Matsui, M., Cao, S.Y. (2006). *Introduction to aerodynamic database of low buildings*. 7th National Conference on Wind Engineering and Industrial Aerodynamics. (in Chinese)

Rizzo, F., Caracoglia, L. (2020). Artificial neural network model to predict the flutter velocity of suspension bridges. *Computers and Structures, 233, 106236.*

Rumelhart, D.E., McClelland, J.L. (1986). *Parallel distributed processing: explorations in the microstructure of cognition*. Cambridge: MIT Press.

Sa, S.X., Tu, S. (1997). *Introduction to database system*. Beijing: Higher Education Press. (in Chinese)

Sarkar, P.P., Jones, N.P., Scanlan, R.H. (1994). Identification of aeroelastic parameters of flexible bridges. *Journal of Engineering Mechanics, 120(8), 1718-1742.*

Scanlan, R.H. (1974). Indicial aerodynamic functions for bridges decks. *Journal of Engineering Mechanics, 100, 657-672.*

Scanlan, R.H. (1978). The action of flexible bridges under wind-induced flutter theory. *Journal of Sound and Vibration, 1978, 60(2): 187-199.*

Scanlan, R.H., Tomko, J.J. (1971). Airfoil and bridge deck flutter derivatives. *Journal of Engineering Mechanics, 6, 1717-1737*.

Simiu, E., Scanlan, R.H. (1996). *Wind effects on structures: an introduction to wind engineering*. New York: Wiley Interscience.

Theodorsen, T. (1935). General theory of aerodynamic instability and the mechanism of flutter. *NACA Technical Reports.*

Tian, J., Gurley, K.R., Diaz, M.T., Fernandez-Caban P.L., Masters, F.J., Fang, R. (2020). Low-rise gable roof buildings pressure prediction using deep neural networks. *Journal of Wind Engineering and Industrial Aerodynamics, 196, 104026.*

Wang, D.L. (2003). *Numerical simulation of aeroelastic problems on bridges based on discrete vortex method*. Master's thesis, Tongji University. (in Chinese)

Wang, F.J. (2004). *Computational fluid dynamics analysis*. Beijng: Tsinghua University Publishing House. (in Chinese)

Wang, J., Cheng, C.M. (2017). Formulation of estimation models for wind force coefficients of rectangular shaped buildings. *Journal of Applied Science and Engineering, 20(1), 55-62.*

Wang, J.M., Cheng C.M., Tens P.T. (2003). *Design wind loads on tall buildings: a wind tunnel data based expert system approach*. 11th International Conference on Wind Engineering.

Wang, Q., Tao, Q., Liao, H.L. (2007). *Study on vortex-induced vibration characteristics of the large-scale*

sectional model test for the main beam of the E'dong bridge. 13rd National Conference on Structural Wind Engineering, 229-234. (in Chinese)

Wang, X. (2018). *Numerical simulation study on wind-induced vibration of long-span bridges*. Master's thesis, Guizhou University. (in Chinese)

Wang, X.J. (2008). *Identification of aerodynamic parameters of bridge decks by stochastic approaches*. Ph.D. thesis, Tongji University. (in Chinese)

Wang, X.Y., Chen, Z.Q., Huang, F.L. (2001). Identification of flutter derivatives of a bridge sectional model using neural network technique. *Journal of Hunan University of Science and Technology (Natural Science Edition), 16(3), 74-77.* (in Chinese)

Wang, Z. (2017). *Wind tunnel and numerical study on wind load characteristics of diffuser high-rise buildings*. Master's thesis, Zhejiang University of Technology. (in Chinese)

Wilde, K., Fujino, Y., Masukawa, J. (1996). Time domain modeling of bridge deck flutter. *Structure Engineering/Earthquake Engineering, 13(2), 93-104.*

Wu, T. (2013). *Nonlinear bluff-body aerodynamics*. Ph.D. thesis, University of Notre Dame.

Wu, T., Kareem, A. (2011). Modeling hysteretic nonlinear behavior of bridge aerodynamics via cellular automata nested neural network. *Journal of Wind Engineering and Industrial Aerodynamics, 99(4), 378-388.*

Xia, Y. (2011). *Numerical calculation of the flutter stability for long-span suspension bridge*. Master's thesis, Chang'an University. (in Chinese)

Xian, R., Liao, H.L. (2008). Wind tunnel test study of aerodynamic optimization measures for flutter stability of critical flat steel box girder. *World Bridges, 138(3), 44-47.* (in Chinese)

Xiang, H.F. (2002). Study on bridge wind engineering into 21st century. *Journal of Tongji University (Natural Science), 30(5), 529-532.* (in Chinese)

Xiang, H.F., Chen A.R. (2003). Recent advances in research on aerodynamics of extra long-span bridges. *China Civil Engineering Journal, 36(4), 1-8.* (in Chinese)

Xiang, H.F., Lin, Z.X., Bao, W.G. et al. (1996). *Wind-resistant design guidance for highway bridges*. Beijing: China Communications Press. (in Chinese)

Xie, Z.N., Gu, M., Ni, Z.H. (2004). Experimental investigations on static interference effects of tall buildings. *China Civil Engineering Journal, 37(6), 16-22.* (in Chinese)

Xu, F.Y. (2015). A direct approach to extract eighteen flutter derivatives of bridge decks and vulnerability analysis on identification accuracy. *Journal of Aerospace Engineering, 28.*

Xu, F.Y., Zhang, Z.B. (2017). Free vibration numerical simulation technique for extracting flutter derivatives of bridge decks. *Journal of Wind Engineering and Industrial Aerodynamics, 170, 226-237.*

Xu, F.Y., Zhu, L.D., Ge, X.M., Zhang, Z. (2014). Some new insights into the identification of bridge deck flutter derivatives. *Engineering Structures, 75(8), 418-428.*

Yakhot, V., Orszag, S.A. (1986). Renormalization group analysis of turbulence I basic theory. *Journal of Scientific Computing, 1(1), 3-51.*

Yamada, H., Katsuchi, H. (2004). Importance of wind tunnel verification and long-span bridges. *9th National Convention in Civil Engineering, 2(2), 23-32.*

Yamada, H., Miyata, T., Ichikawa, H. (1992). Measurement of aerodynamic coefficients by system identification methods. *Journal of Wind Engineering and Industrial Aerodynamics, 42(1-3), 1255-1263.*

Yang, X.W. (2000). *Application of artificial neural network in the analysis of aerodynamic characteristics of bridge cross-sections*. Master's thesis, Southwest Jiaotong University. (in Chinese)

Yang, Y.X. (2002). *Two-dimensional flutter mechanism and its application for long-span bridges*. Ph.D. thesis, Tongji University. (in Chinese)

Yu, C.J., Li, Y.L., Xiang, H.Y., Zhang, M.J. (2018). Data mining-assisted short-term wind speed forecasting by wavelet packet decomposition and Elman neural network. *Journal of Wind Engineering and Industrial Aerodynamics, 175, 136-143.*

Zhang, A., Zhang, L. (2004). RBF neural networks for the prediction of building interference effects. *Computers and Structures, 82(27), 2333-2339.*

Zhang, B.Y., Xiang, H.F. (1997). Development of the first bridge wind tunnel in China. *Acta Aerodynamica Sinica, 15(2), 161-168.* (in Chinese)

Zhang, H. (2018). *Estimation for critical flutter velocity of the bridge with flat box girder.* Master's thesis, Chang'an University. (in Chinese)

Zhang, Q. (2003). Review of atmospheric boundary layer meterology. *Journal of Arid Meteorology, 21(3), 74-78.* (in Chinese)

Zhang, Q. (2008). *Research on flutter derivatives of bridge girder sections by numerical simulation*. Master's thesis, Southwest Jiaotong University. (in Chinese)

Zhang, R.X. (1998). *Theoretical and experimental study on identification of aerodynamic parameters of bridges*. Ph.D. thesis, Tongji University. (in Chinese)

Zhang, X. (2007). Influence of some factors on the aerodynamic behavior of long-span suspension bridges. *Journal of Wind Engineering and Industrial Aerodynamics, 95(3), 149-164.*

Zhang, Z.B. (2016). *Numerical study on nonlinear aerodynamic forces on typical bridge decks*. Master's thesis, Dalian University of Technology. (in Chinese)

Zhang, Z.T., Ge, Y.J., Yang, Y.X. (2013). Torsional stiffness degradation and aerostatic divergence of suspension bridge decks. *Journal of Fluids and Structures, 40, 269-283.*

Zhao, B.L. (2007). *The wind load database system development based on Access platform*. Master's thesis, Harbin Institute of Technology. (in Chinese)

Zhao, J.H. (2005). *Java programming*. Beijing: China Machine Press. (in Chinese)

Zhou, H.P. (2012). *Numerical simulation study on wind field characteristics of large chassis high-rise building*. Master's thesis, Zhejiang University of Technology. (in Chinese)

Zhou, Y., Kijewski, T., Kareem, A. (2003). Aerodynamic loads on tall buildings: interactive database. *Journal of Structural Engineering, 129(3), 394-404.*

Zhu, A.D. (2014). *Wind-resistant performance analysis and experimental investigation on long-span cable-stayed bridges*. Master's thesis, Dalian University of Technology. (in Chinese)

Zhu, J., Zhang, W. (2018). Probabilistic fatigue damage assessment of coastal slender bridges under coupled dynamic loads. *Engineering Structures, 166, 274-285.*

Zhu, Y.Q. (2017). *Numerical simulation and experimental study on flutter characteristics of long span*

suspension bridge. Master's thesis, Southwest Jiaotong University. (in Chinese)

Zhang, Z.B. (2016). *Numerical study on nonlinear aerodynamic forces on typical bridge decks*. Master's thesis, Dalian University of Technology. (in Chinese)

Zhu, Z.W., Chen, Z.Q. (2004). Numerical simulations for aerodynamic derivatives and critical flutter velocity of bridge deck. *China Journal of Highway and Transport, 17(3), 41-45.* (in Chinese)

Zhu, Z.W., Chen, Z.Q., Gu, M. (2005). Evaluating flutter derivatives of the thin plate by applying the numerical simulation method. *Journal of Hunan University (Natural Sciences), 32(5), 11-15.* (in Chinese)

Zhu, Z.W., Gu, M. (2007). Wind tunnel and CFD study on identification of flutter derivatives of a long-span self-anchored suspension bridge. *Computer-Aided Civil and Infrastructure, 22, 541-554.*